Russian Journal of Earth Sciences

Vol. 24
Issue 1

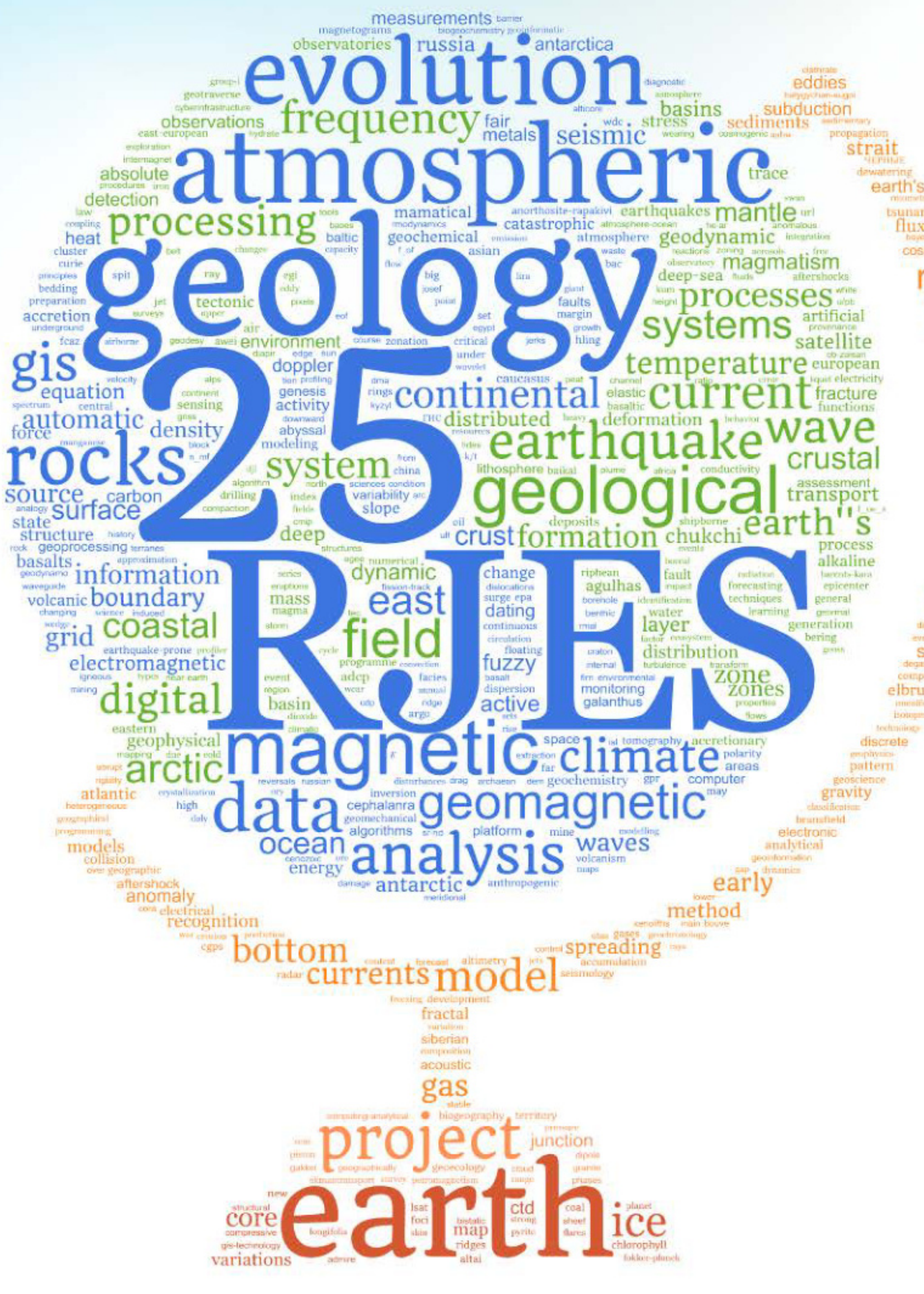

Russian Journal of Earth Sciences

Special Issue: "25th anniversary of the Russian Journal of Earth Sciences"

Seiche Dynamics in the Azov Sea Current System

G. G. Matishov[1,2], **K. S. Grigorenko**[1]

[1]Federal Research Centre the Southern Scientific Centre of the Russian Academy of Sciences, Rostov-on-Don, Russia

[2]Murmansk Marine Biological Institute, Kola Scientific Centre, Russian Academy of Sciences, Murmansk, Russia

* **Correspondence to:** Grigorenko Klim Sergeevich, klim_grig@mail.ru

Abstract: The paper presents new results of an investigations of the cyclic currents of the Azov Sea. Using offshore and onshore surveys at buoy ADCP-stations the separation of the characteristic features of water transport in different areas of the Taganrog Bay was shown. Expeditionary observations showed that despite of the drift-gradient nature, the resulting current has the direction of the Don runoff current. Direct coastal measurements showed that the runoff current significantly predominates on the spits of the southern coast of Taganrog Bay. Seiche pulsations manifest themselves as a two to three-hour slowdown of the main flow at diurnal intervals. The division of the areas of the Taganrog Bay according to the trajectories of water movement is noticeable. The eastern part has a predominantly river regime of water circulation. In the central part the meridional component of seiche currents plays an important role in water mixing. The marine regime of water mixing prevails in the western part of the Taganrog bay. Test calculations show that the classical tidal analysis program T_TIDE is applicable with caution for the Sea of Azov. The visually observed diurnal and semi-diurnal sea level rises represent a superposition of waves of different natures. The results of the work correspond to the known patterns of energy exchange between the atmosphere and the ocean. Even weak winds lead to the development of wave processes at eigen frequencies close to tidal ones. Increasing winds contribute to the intensification of wave fluctuations and significant transfer of water during strong surges.

Keywords: the Azov Sea, the Taganrog Bay, tideless basins, seiches, positive and negative water setups, ADCP-measurements, lithodynamics, sea currents.

Citation: Matishov G. G., Grigorenko K. S. (2024), Seiche Dynamics in the Azov Sea Current System, *Russian Journal of Earth Sciences*, Vol. 24, ES1001, https://doi.org/10.2205/2024ES000890

Research Article

Received: 15 October 2023
Accepted: 15 January 2024
Published: 29 February 2024

1. Introduction

The Azov Sea is the most remote inland sea in Eurasia. It is maximally isolated from the Atlantic Ocean, the basin of which it is part of. Tidal phenomena in their traditional form are indistinguishable here. Level fluctuations are caused primarily by the forcing effect of the wind field. As a result of the interference of the oncoming surge waves and the reflected surge waves, standing waves are formed – seiches. Under the influence of the Earth's rotation, they are strongly deformed and form a system of seiche currents and level fluctuations – an amphidromic region [*Zhukov*, 1976]. Seiche amphidromic systems are manifested both in cyclic changes in sea level and in current directions [*Matishov and Grigorenko*, 2023]. The eigen frequencies of the basin's oscillations are close to tidal ones. Numerous experimental observations show an obvious cyclicity of the diurnal and semi-diurnal periods, which can be explained primarily by meteorological factors [*Kurchatov*, 1925].

It is known that diurnal and semi-diurnal level maximum consist of many single components, which are formed due to different mechanisms. High-resolution spectral analysis shows significant influence of radiative tides in the tidal frequency range. It is believed that radiation tides in the Sea of Azov are formed under the influence of breeze circulation [*Korzhenovskaia et al.*, 2022]. However, the regularity of harmonics characteristic of tides is disrupted by the action of wind. Similar water level dynamics are observed in other water bodies, for example, large lakes [*Ivanov et al.*, 2019]. How closely are the seiches of the Sea of Azov related to the tides? The work also sets the task of separating cyclical fluctuations in sea level (seiches) from forced ones (surges), and thus calculating the magnitude of surges without the influence of seiches.

2. Materials and methods

The work is based on the results of the Southern Scientific Centre of the Russian Academy of Sciences expeditionary investigations. Researches in the Azov Sea was carried out using a Doppler current meter Aanderaa RCM 9 LW. The frequency of the instrument's acoustic signal is 2 MHz, which allows the high-precision measurements at shallow depths. The discreteness of recording environmental parameters is adjusted by the operator from 30 s to 2 hours. During this period of time, the recorder sends 600 pings and makes one record of an average measurement with a quality mark. The current meter is additionally equipped with temperature, salinity and pressure sensors. Measurement data with a period of 30 min wer used in the work.

Measurements were carried out on board the R/V Deneb in May 2018 (one station) and December 2021 (five observation stations) Coastal survey data were used on the spits of the southern coast of Taganrog Bay – Chumburskaya and Sazalnitskaya in May and August 2023, respectively. Totally, the results of the current parameters measurements at eight stations in the Taganrog Bay of the Azov Sea were used to analyze water transport

Data from coastal water-level meters in the cities Temryuk, Yeisk and Donskoy village for 2021 were used to calculate seiche parameters. The estimation of seiches part in the amplitude of surge level fluctuations was assessed using the classical harmonic analysis package T_TIDE, implemented in the Matlab environment [*Pawlowicz et al.*, 2002]. A set of algorithms collected in the package allows to analyze data for periods up to a year, taking into account specific tidal components using nodal corrections within established confidence intervals. The list of tidal components includes 45 astronomical and 101 shallow water components. In the general case, an automatic selection of the closest component algorithm is used. It is possible to manually set the most characteristic oscillation period. The isolation and relatively small size of the Azov Sea lead to the formation of oscillatory systems at different frequencies for different areas of the sea and their mixing. This specificity forces us to use the most general settings of the T_TIDE package without specifying specific frequencies of water level oscillations. For the calculations, data of the water level during a strong negative water setup (06.10.2015 – 06.11.2015) and positive water setup (01.12.2021 to 31.12.2021) were used. Changes in water level in the Don Delta are compared with the seaward part of the Taganrog Bay, which is not directly influenced by the Don runoff (Yeisk from May 1 to June 30, 2021). Algorithms of the T_TIDE package constructed a spectrum of water level fluctuations in the village of Donskoy and the city of Temryuk, taking into account and without taking into account cyclic changes.

3. Results and discussion

Previous studies have revealed in detail the role of seiches in the Azov Sea [*Matishov and Grigorenko*, 2023]. Basing on long-term databases of expeditions and coastal water-level meters, it is shown that this is a widespread, regime-forming phenomenon. There is also given an estimation that the direction of the current will change in 12 to 24 hours, regardless of the wind field. The most typical vector-progressive diagrams of currents (Figure 1), constructed according the expeditionary data of the R/V Deneb, show that despite of the drift-gradient nature, the resulting current has the direction of the Don runoff current.

It was expected during planning the research that in the distal parts of the spits a cyclic alternation of the direction and speed of currents should be observed [*Matishov et al.*,

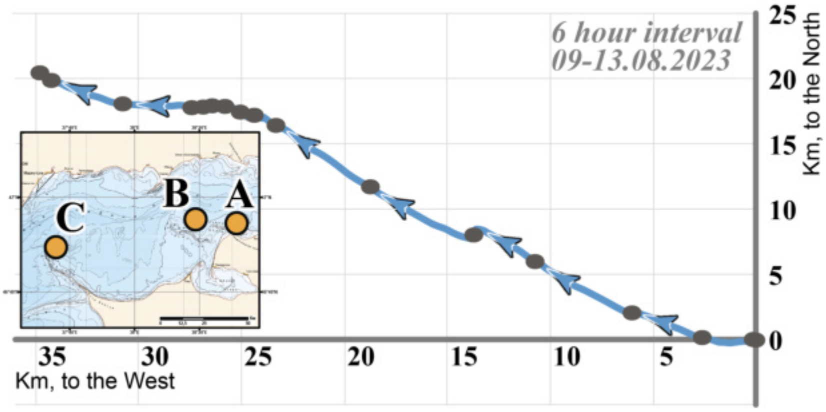

(a)

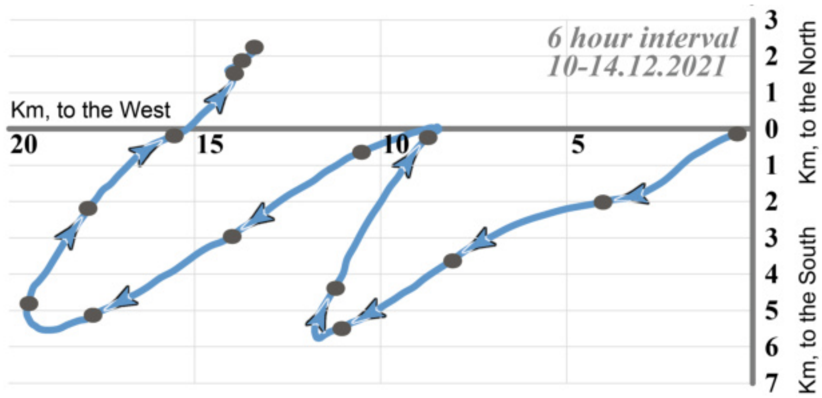

(b)

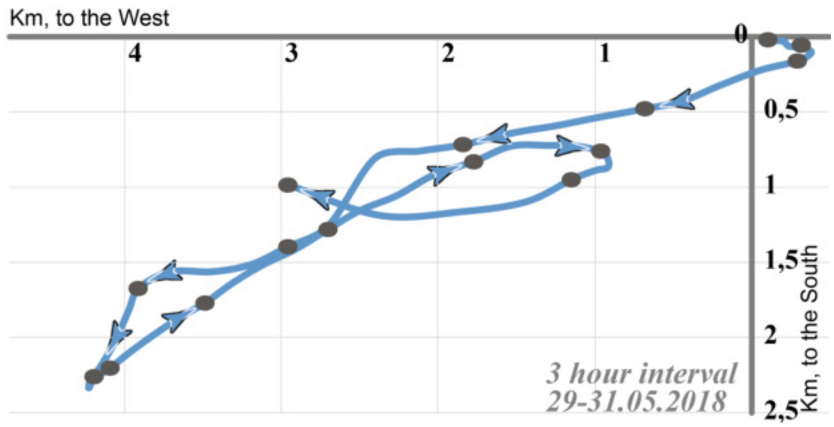

(c)

Figure 1. Vector-progressive diagrams of currents off the coast of the Sazalnitskaya Spit (a), in the seaward part of the Taganrog Bay (b) and in the seaward part of the Taganrog Bay near the Dolgaya Spit (c).

2022]. Direct measurements for a few days showed that the runoff current significantly predominates on the spits of the southern coast of Taganrog Bay (Figure 1a). Seiche pulsations manifest themselves as a two to three-hour slowdown of the main flow at diurnal intervals. The direction at this time changes to the opposite. This change is accompanied by minimal speeds, up to 10 cm/s. The establishment of a runoff current has the character of a breaking wave with a steep front slope close to collapse. During this phase, maximum velocities were measured – up to 60 cm/s on the Chumburskaya and Sazalnitskaya spits. After this, the speed levels out within 20–40 cm/s. The total movement of a water particle in a week under such conditions will reach 40 km.

In the central part of the Taganrog Bay, the meridional component of wave currents is noticeable (Figure 1b). The measurement under discussion was carried out during a strong three-day easterly wind, typical for the Azov region in winter. We will note that under the conditions of the strongest, during measurements, eastern wind (15–17 m/s), a northeastern current with a velocity of up to 25 cm/s was recorded. The maximum spatial transfer reached 20 km. However, the resulting movement of a water particle was reduced to 14 km, because the completion of measurements coincided with the compensatory stage of oscillations in the Azov Sea. In a week the transfer would be approximately 40 km.

The trajectory of water movement in the area of the Dolgaya Spit has a different appearance (Figure 1c). The measurements from the vessel were carried out at a distance approximately 15 km from the coast in almost calm conditions. The transfer was recorded strictly in the plane of the axis of the Dolzhansky Strait with a approximately diurnal period (21 hours). The range of fluctuations from east to west is relatively small, less than 5 km (about 35 km per week). We will note that the measurements were carried out for only a day, whereas in the cases described in Figures 1a and 1b – more than 3 days. All water exchange between the Taganrog Bay and the Sea of Azov itself occurs in the narrow strait between the Dolgaya and Belosarayskaya spits (Dolzhansky Strait). If we consider the long ridge of the underwater tip of the Dolgaya Spit, the width of the channel is only 20 km, while 30 km to the east the Taganrog Bay expands to 50 km. The narrowness helps to increase the currents. Even in calm conditions, a maximum speed 34 cm/s was noted. The average velocity of water movement of the entire Taganrog Bay in different areas to the west – the drainage direction of the Don, obtained from the results of measurements, is thus approximately 6 cm/s.

Let us consider the general scheme of water movement in the Taganrog Bay, constructed according to the results of current investigations at buoy stations since 2018 (Figure 2). For clarity, the movement of water particles is superimposed on a map of the Azov Sea bathymetry in the same scale. A vector-progressive diagram shows the distance and direction of movement of water particles at each time of measurement. Overlay on the map shows where a particle of water could move if there were no currents in the rest of the Taganrog Bay.

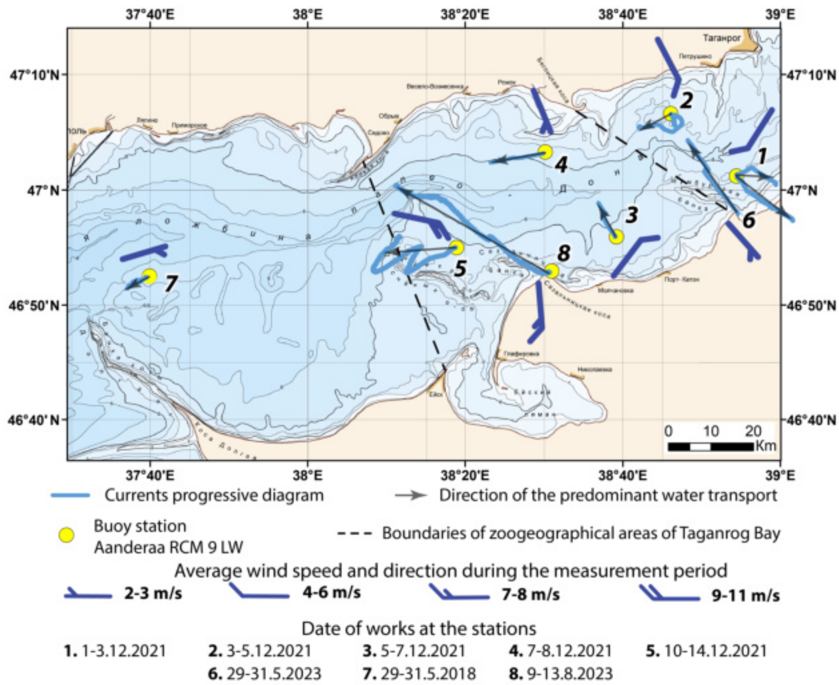

Figure 2. Vector-progressive diagrams of Taganrog Bay currents superimposed on a bathymetric map.

The division of the areas of the Taganrog Bay according to the trajectories of water movement is noticeable. The types of fluctuations are consistent with the known zoogeographical regions of the Taganrog Bay [*Gershanovich et al.*, 1991]. From the mouth of the Don to the cross-section of the Petrushinskaya spit – Chumburskaya bank, a predominantly river regime of water circulation operates. Salinity maximum during the absence of extreme surges do not exceed 5–7 p.s.u. The Don runoff current dominates in the water area; seiche transport is expressed in the periodic weakening of the runoff current. Movement of fresh current stream is possible from the southern to the northern shore. The biotic regime is close to the river one. The western border of the central region of Taganrog Bay is the cross-section between the Krivaya and Sazalnitskaya spits. Seiche currents of the meridional direction play an important role in water mixing. The central region is characterized by an average long-term location of the zoogeographic barrier for the habitat of freshwater fauna (5–7 p.s.u.). The western circulation volume of the Taganrog Bay is formed by the shallow ends of the Dolgaya and Belosarayskaya spits. The marine regime of water mixing prevails here. On the spectrum of level and salinity fluctuations, a pronounced 38-hour period of the 1-node seiche of the Sea of Azov is added [*Matishov and Inzhebeikin*, 2009]. Accordingly, the water area is characterized by sea salinity (more than 14 p.s.u. in modern times) and a corresponding distribution of bottom fauna. Due to the low water level of the Don, the runoff current in the Taganrog Bay has weakened. It is logical to correct the boundaries of zoogeographical regions to the east.

In direct form, the tides in the Azov Sea are weakly expressed. Researchers note a maximum theoretical value of up to 19.5 cm at the top of Taganrog Bay [*Korzhenovskaia et al.*, 2022]. Water-level meters show that the daily amplitudes of fluctuations in Yeysk and Donskoy sometimes exceed 1 m. Signal processing at specific periods is significantly difficult due to the mixing of different factors influencing on the level of the Azov Sea. A change in wind often leads to a change in the time of the characteristic onset of maximum and minimum levels. Using classical methods of harmonic analysis, an assessment of the interaction of radiation tides, seiches and surge water transport in the system of level fluctuations in the Sea of Azov was obtained (Figure 3).

The reasons and conditions for the formation of extreme surges are discussed in detail in [*Matishov and Grigorenko*, 2017]. The initial observation period, October 6–10, 2015 (Figure 1a), was accompanied by a drop in level to one m and had a strict daily cycle. The weakening of the surge wind was accompanied by the restoration of the shape of the level surface and three daily peaks of up to 0.2 m. The minimum phase of the surge was reached on October 15 with a drop in level of 1.5 m. Moreover, without taking into account cyclic fluctuations, the drop in level should have been only 0.2–0.25 m. The actual increase in water level to the initial level occurred from October 15 to October 20. At 20:00 on October 21, the second minimum level was reached – less than 1.2 mBS. The level recovered at 5:20 on October 23. Over the next four days, the level maximums gradually increased at daily intervals until they reached 0.3 mBS at 1:20 on October 27. With a regular daily period, the water surface decreased until 22:00 on October 31. Then, it sharply rose by 22:00 on November 2, 2015 to 0.5 mBS. The next minimum was recorded at 17:20 on November 3.

The absence of daily harmonics would lead to the formation of three surge maxima (up to 0.5 mBS) and minima (up to −0.5 MBS) of the level with an interval of 3–4 days. Changes in water level without taking into account wave dynamics would not lead to extreme surges.

Diurnal dynamics significantly influence the course of water levels in the east of Taganrog Bay during surges (Figure 1b). A cyclic series of small (up to 0.7 m) surges from the first to the fourth of December 2021 had a strict diurnal frequency. The maximum was reached around two o'clock in the morning, the minimum – around 14:00 – 15:00 daily.

The subsequent difference between adjacent maxima lasted 40 hours. The amplitude reached 1 m. Until December 10, a pronounced diurnal variation was not observed. In the spectra of level fluctuations in the Sea of Azov (Figure 4a and 4b) there is a peak with a period of about 13–14 days. Apparently, it corresponds to the characteristics of the

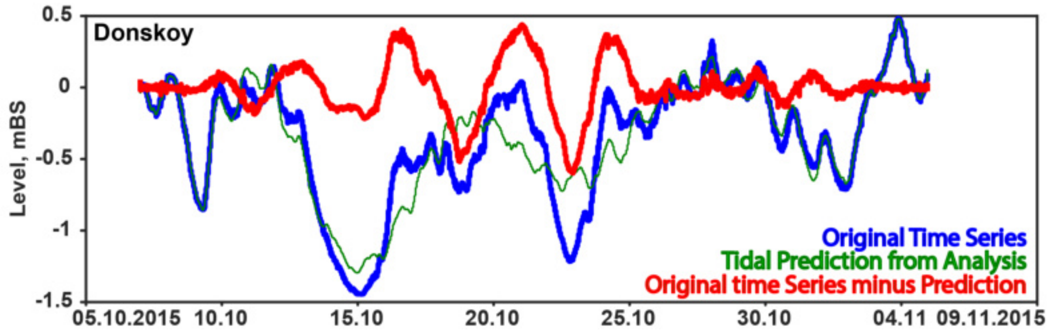

(a)

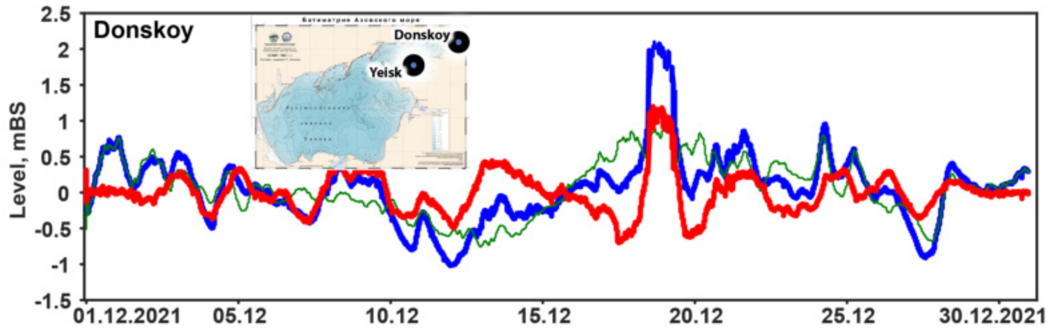

(b)

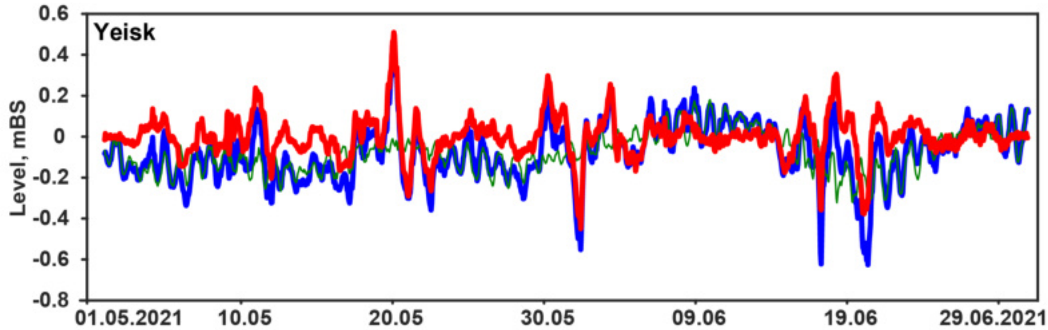

(c)

Figure 3. Results of processing data of water level in the Azov Sea using harmonic analysis methods. a) period of heavy wind negative water setup 10/06/2015 – 11/06/2015 in the Don delta; b) a period containing both daily fluctuations and a positive water setup more than 2 m from 12/01/2021 to 12/31/2021 in the Don delta; c) area of the Taganrog Bay, not directly influenced by the Don runoff (water-level meter in Yeisk) from 01.05 to 30.06.2021.

cyclonic circulation of the atmosphere in the Azov region. All extreme negative setups were recorded during two-week phases of decreasing levels. There are positive water setups, respectively, during long-term semi-monthly maximums. An example of such level dynamics is shown in Figure 3b and 3c. In particular, Figure 3b shows a negative water setup about 1 m on December 13th. After which the positive water setup wind phase began with a peak of water level at 14:50 on December 19 of 2.3 mBS. The diurnal periodicity of the oscillations appeared on December 25 during the phase of level decline during the two-week oscillation. Against the background of two-week fluctuations, the diurnal periodicity is not clearly expressed. At the same time, it is shown that the negative water setup on December 28 and the positive water setups on December 25 and 26 occurred because of a wave nature, without taking into account which the range of fluctuations would not have been 2 m, but about 0.5 m. The long-term stay of high waters on December 19 after filtering the semi-monthly periodicals would lead to an increase in the level up to half a meter higher relative to the actual one on December 14 and a decrease in the positive water setup on the 19th by more than 1 m.

The water-level meter in Yeisk is not directly influenced by the variability of the Don runoff. At the same time, Figure 3b shows both long-term cycles of increase and decrease in the level of the Taganrog Bay with a duration of about two weeks, and daily waves, well smoothed by software methods. The amplitude is significantly smaller compared to the Don delta. A number of positive and negative water setups were identified that did not have a distinct daily periodicity. At 2:00 on May 20, with a level of 0.4 mBS, at 6:00 on May 30 and a level of 0.2 mBS, at 9:00 on June 3, with a level of 0.3 mBS. Over the next 12 days, the daily amplitude of about 0.2 m is smoothed out. Fluctuations from June 14 to June 24 had approximately daily periods, but were mixed due to a general two-week decrease in water levels.

The spectra of surface level fluctuations were constructed for the Donskoy (Figure 4a) and Temryuk (Figure 4b) points, located on the opposite borders of the Sea of Azov. Similar patterns are observed in diurnal and semi-diurnal periods. The elongated shape of the Taganrog Bay contributes to an increase in wave energy, which is proven by deep decreases in the density of the filtered spectral signal relative to the original one at tidal periods. Both observation stations are also characterized by a two-week cycle of level oscillations. The nature of level changes in Temryuk is distinguished by small daily amplitudes, only 20–40 cm. The highest positive water setup in 2021 reached the level of 1.1 mBS (12/01/2021), and the negative water setup −0.6 mBS (10/06/2021), i. e. e. the total level difference throughout the year did not exceed 1.7 m. The Azov Sea in Temryuk is characterized by a 7-hour period of level fluctuations. This period is poorly recognized by the T_TIDE package, because it differs from the nearest tidal component (M4, with a period of 6.21 hours). The wide peak at this frequency is a local seiche of the Temryuk Gulf or a four-node seiche of the Azov Sea, the estimated period of which is 8.8 hours [*Matishov and Inzhebeikin*, 2009]. The maximum of the spectral signal at a frequency close to the period of a single-node seiche corresponds to a period of 35 hours. This value is also far from the nearest tidal ones, so the peak is lost in the spectrum, relative to the daily one.

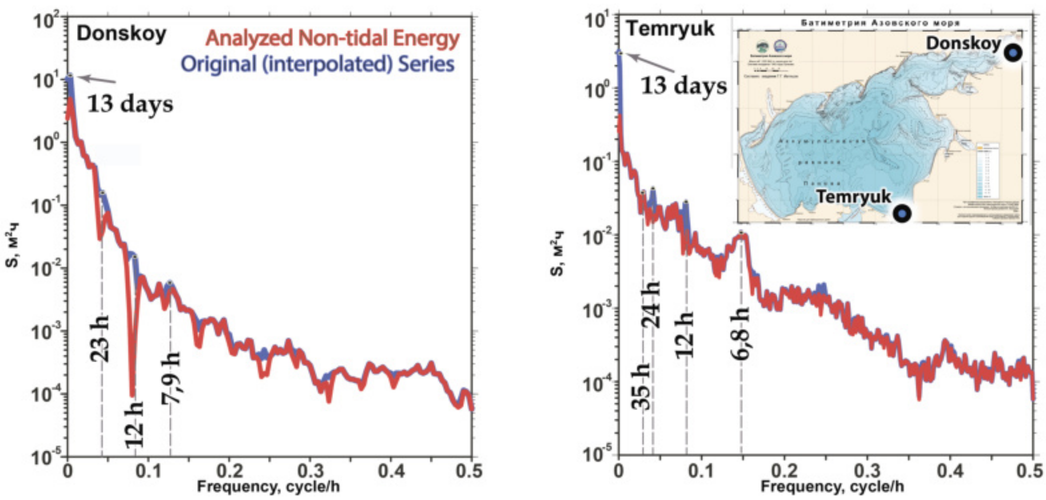

(a) (b)

Figure 4. a) spectrum of level fluctuations in the village of Donskoy, taking into account and without taking into account cyclical fluctuations in water level in 2021; b) spectrum of level fluctuations in the city of Temryuk, taking into account and without taking into account cyclical fluctuations in water level in 2021.

4. Conclusions

The paper presents new results of an investigations of currents in the Azov Sea. It has been shown that water transport characteristics are very different in different areas of the sea. The dominance of runoff transport, despite of the pronounced wave nature of the current field, complements the estuarine characteristics of the Taganrog Bay. According to measurements (Figure 1 and 2), the eastern transport is observed in the areas of greatest depths of the bay and weakens towards the shores. Near the northern [*Matishov et al.*, 2022] and southern coasts, at near-zero levels and during negative water setups, the western current dominates. The current regime corresponds to the generally accepted zoogeographical zoning of the Taganrog Bay. The depth of location and height of accumulative sediments in the Azov Sea spit system depends on the maximum water level. For example, underwater banks (Sand Islands of the Sazalnitskaya Spit) with an upper edge at a depth of about 1 m are formed by a flow at a water level not lower than the normal one. Numerous shallows at the ends of the spits in the near-surface layer line up at near-zero water levels. Thus, the shallows of the underwater ends of the spits are stressed by the daily effects of seiche oscillations. Positive water setups of 2 m or more occur during extreme winds of the westerly component and are accompanied by high current speeds. The energy of one powerful surge is enough to significantly change the shape of the coastal topography of spits and islands.

This means that basing on the shape and age of accumulative bodies, it is possible to restore the hydrodynamic conditions of coastal zones in earlier eras.

Continuous fluctuations in the level of the Azov Sea contributed to the formation of the spits in their modern form. The regular nature of changes in the direction of alongshore currents leads to the accumulation of sediments at the ends of the spits. Catastrophic wind surges lift them, completing the body of the spit.

The isolation of the Azov Sea from tidal basins leads to the formation of a complex system of sea surface level fluctuations. Tides are directly discernible only using high-frequency spectral analysis [*Korzhenovskaia et al.*, 2022]. The visually observed diurnal and semi-diurnal sea level rises represent a superposition of waves of different natures. These include both lunar and solar tides, as well as radiation tides associated with winds. The bathymetric compartments of the Taganrog Bay are separated from each other by the underwater ends of the spits, which impede water exchange. Each compartment is characterized by its own oscillation systems – seiches. When eigen oscillations come into resonance with tidal ones, coastal level gauges record pronounced daily and semi-diurnal dependences of the water level.

Test calculations show that the classical tidal analysis program T_TIDE is applicable with caution for the Sea of Azov. Ocean tides have the character of forced waves, the period of which strictly corresponds to the period of the forcing forces. Regular rises in the level of the Azov Sea are formed by a combination of free oscillations at eigen frequencies. The share of regular, compelling, tidal forces that significantly feed seiches remains to be calculated. Changes in the wind regime reshape the periods of regular oscillations. For example, today the period of level peaks is 12 hours, tomorrow it can decrease to 9, and the day after tomorrow it can rise to 13 hours. At the same time, a general characteristic pattern is observed: the maximum water level at the top of the Taganrog Bay (Donskoy village) is observed in between 21:00 pm and 2:00 am. In conditions of constant wind with a speed of up to 5–7 m/s, or after a strong wind (more than 10 m/s) weakening, fluctuations in water level with an amplitude of up to 2 m can be completely explained by seiche dynamics. Single-node seiches of the Sea of Azov in the Taganrog Bay are observed infrequently. They are accompanied by extreme surges and maximum saturation of amphidromic sea systems with energy. In this case, the proportion of wave dynamics during level changes decreases. When the surge winds weaken, the diurnal dynamics of the level and currents are built. Accurate estimates require continued observations, filtering out low-frequency, biweekly fluctuations, and calculating the sea's energy balance.

The results of the work correspond to the known patterns of energy exchange between the atmosphere and the ocean. Even weak winds lead to the development of wave processes at eigen frequencies close to tidal ones. Increasing winds contribute to the intensification of wave fluctuations and significant transfer of water during strong surges.

Acknowledgments. The publication was prepared as part of the implementation of the research work of the State task of the Southern Scientific Center of the Russian Academy of Sciences No. 122103100027-3 "Investigation of the hydroclimatic features of periodically drying up water areas of southern Russia in the context of the global carbon cycle"; 123071900007-8 "Development of a system of climatic and environmental monitoring of the Azov Sea and ensuring its functioning"; and agreement No. 72-223/VIPGZ-23 dated 04/03/2023 between IO RAS and SSC RAS within the framework of Consortium 2.

References

Gershanovich, D. E., N. P. Goptarev, B. M. Zatuchnaya, and A. I. Simonov (Eds.) (1991), *Hydrometeorology and hydrochemistry of the seas of the USSR. Volume V. Sea of Azov*, Gidrometeoizdat, Saint Petersburg (in Russian).

Ivanov, V. A., N. I. Palshin, and Y. V. Manilyuk (2019), Seiches in Petrozavodsk Bay, Lake Onega, *Water Resources*, *46*(5), 709–717, https://doi.org/10.1134/S0097807819050117, EDN: URYYEX.

Korzhenovskaia, A. I., I. P. Medvedev, and V. S. Arkhipkin (2022), Tidal Sea Level Oscillations in the Sea of Azov, *Oceanology*, *62*(5), 585–596, https://doi.org/10.1134/s0001437022050095, EDN: NOIVBT.

Kurchatov, I. V. (1925), Seiches in the Black and Azov Seas, pp. 149–158 (in Russian).

Matishov, G. G., and K. S. Grigorenko (2017), Causes of salinization of the Gulf of Taganrog, *Doklady Earth Sciences*, *477*(1), 1311–1315, https://doi.org/10.1134/S1028334X17110034, EDN: XXKUPJ.

Matishov, G. G., and K. S. Grigorenko (2023), Seiche Currents in the Sea of Azov Based on Field Observations, *Oceanology*, *63*(1), 27–34, https://doi.org/10.1134/S00014370230100095 (in Russian).

Matishov, G. G., and Y. I. Inzhebeikin (2009), Numerical study of the Azov Sea level seiche oscillations, *Oceanology*, *49*(4), 445–452, https://doi.org/10.1134/S0001437009040018, EDN: MWRZDZ.

Matishov, G. G., V. V. Polshin, V. V. Titov, K. S. Grigorenko, K. S. Sushko, and S. A. Misirov (2022), New data on the structure of the Beglitskaya spit, *Science in the South of Russia*, (3), 13–20, https://doi.org/10.7868/S25000640220302.

Pawlowicz, R., B. Beardsley, and S. Lentz (2002), Classical tidal harmonic analysis including error estimates in MATLAB using T_TIDE, *Computers & Geosciences*, *28*(8), 929–937, https://doi.org/10.1016/S0098-3004(02)00013-4.

Zhukov, L. A. (1976), *General oceanology*, Gidrometeoizdat, Leningrad (in Russian).

Russian Journal of Earth Sciences

Special Issue: "25th anniversary of the Russian Journal of Earth Sciences"

Accumulation of Technogenic and Natural Radionuclides in the Don Delta Sediments

G. G. Matishov[1,2], G. V. Ilyin[2], V. V. Polshin[*,1], I. S. Usyagina[2]

[1]Federal Research Centre The Southern Scientific Centre of the Russian Academy of Sciences, Rostov-on-Don, Russia

[2]Murmansk Marine Biological Institute of the Russian Academy of Sciences, Murmansk, Russia

* **Correspondence to:** Vladimir V. Polshin, email: vlad0220vlad@mail.ru

Abstract: The study of current sedimentation processes and radioactive contamination in the total area of the Don Delta is the research goal. The presented paper contains data analysis of radio-ecological and lithologic studies on bottom sediments, sampled in the northern part of the Don Delta in 2022. Based on the research results obtained, the authors provide the characteristics of the current conditions of sedimentation and specific activity of artificial and natural radionuclides in fluvial deposits, as well as indicate that similar in characteristics sandy-silty aleurites and sandy aleurite-clayish silts with inclusions of plant and shell detritus compose the bottom sediments of numerous braided channels. The authors determined the zonal accumulation character of both ^{137}Cs technogenic and ^{226}Ra, ^{40}K, and ^{232}Th natural radionuclides which conditions their accumulation and content increase from the lower delta to the upper delta areas. The velocity of currents in the braided channels (bayous) and related sedimentation conditions of suspended matter, as well as the lithotype of the bottom ground determine the indicated regularity. We assume that unlike ^{137}Cs the distribution of natural radionuclides (^{40}K, ^{226}Ra, and ^{232}Th) mainly depends on the mineral content of sediments entering the delta with the river runoff. Relatively low indices – on average *ca.* 9 Bq/kg of dry weight (d.w.) – characterise the current range of ^{137}Cs radioisotope concentrations in the sediments of the Northern Don Delta. Such a level of specific activity is of no danger to the regional ecosystem.

Keywords: Don Delta, braided channels (bayous), river runoff, current velocity, technogenic and natural radioisotopes, bottom sediments.

Citation: Matishov G. G., Ilyin G. V., Polshin V. V., Usyagina I. S. (2024), Accumulation of Technogenic and Natural Radionuclides in the Don Delta Sediments, *Russian Journal of Earth Sciences*, Vol. 24, ES1002, https://doi.org/10.2205/2024ES000891

Research Article

Received: 15 October 2023
Accepted: 15 January 2024
Published: 29 February 2024

1. Introduction

The necessity of studying the dynamics of technogenic radionuclides inflow from the Don and Dnieper rivers water catchment areas determines the relevance of research on the radioactive contamination in the Sea of Azov – Black Sea basin. The geochemical circulation of artificial radioisotopes, which entered the environment after the accident at the Chernobyl Nuclear Power Plant, is still typical of the considered territory [*Bulgakov et al.*, 2021; *Buryakova et al.*, 2021; *Kryshev et al.*, 2021]. Besides, the danger of aggravating the armed conflict situations in the Rostov, Novovoronezh, and Zaporozhye NPP operation areas enhances the urgent necessity to study the dynamics of radiation background variability in the region.

A significant element of migration of artificial radioisotopes which are of the potential threat to the Sea of Azov is the Don River water catchment system as the river forms braided delta when flowing into the Taganrog Bay. The delta's sediments accumulate considerable part of the solid, organogenic, and chemical runoffs.

Despite the fact that the radionuclides accumulation process in the Sea of Azov bottom sediments has been studied rather intensively and extensively during the last years, these studies have barely covered the Don Delta area. Our previously obtained results on the specific activity of artificial radioisotopes in the Sea of Azov indicate that the granulometric composition of the bottom sediments is one of the most significant parameters controlling the level of radioactive contamination of aquatic ecosystem. The content of radionuclides in sea bottom sediments increased with the decrease in size of the particles of bottom ground and reached the maximum indices in clayish silts of the Central Sea of Azov [*Matishov et al.*, 2020].

Considering the above stated, the main goal of the study was the formation of objective ideas about the current radiation background and the role of the Don Delta in the transit of radionuclides along the river – the Sea of Azov system. New data on typization of the Don Delta bottom sediments allow obtaining the general view of geographic conditions of artificial and natural radionuclides sedimentation and studying their accumulation patterns in the delta's various areas.

2. Materials and methods

Radio-ecological and lithologic studies in the Don Delta total area were implemented in 2022 in the Northern Don Delta located aside the busy transport routes between the Mertvyi Donets channel (bayou) in the North and Bolshaya Kuterma channel (bayou) in the South. Sampling of the ground surface layer (0–2 cm) was applying the Van Veen Grab (Figure 1).

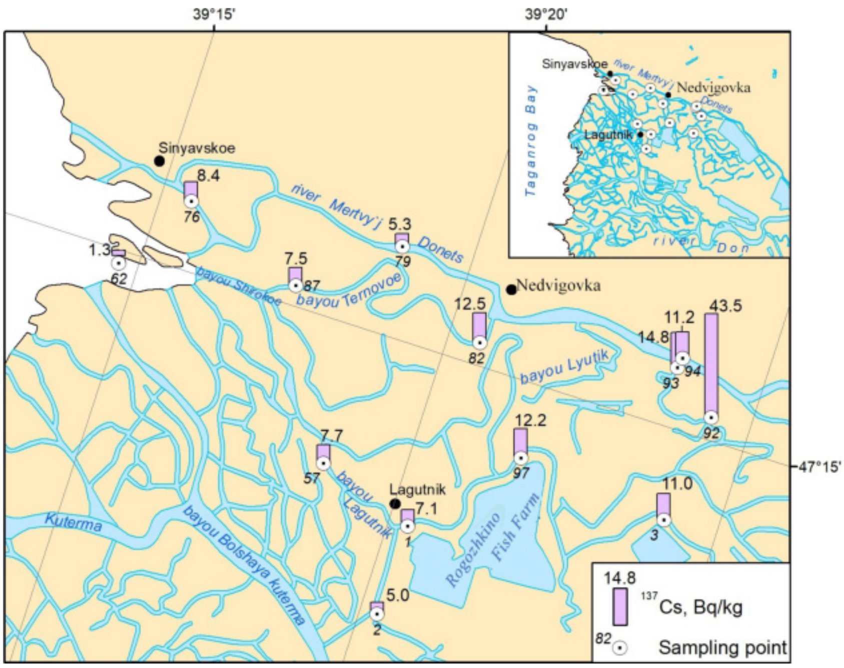

Figure 1. Bottom sediments' sampling scheme and ^{137}Cs specific activity values (Bq/kg of d.w.) in the Don Delta, 2022.

The primary lithologic description of bottom sediments samples was during the field studies. The samples then were placed into hermetically sealed containers and transported for further laboratory research. The subsequent preparation, treatment, and radiometric analysis of samples to determine the ^{137}Cs, ^{40}K, ^{226}Ra, ^{232}Th, ^{210}Pb specific activities were at the analytical laboratory of Murmansk Marine Biological Institute RAS. Preparation, treatment, and measuring procedures were according to the "Manual on Gamma-Ray Emitting Radionuclides Activity (Specific Activity) Measurements in Test Samples Using the *CANBERRA* Gamma-Ray Spectrometer with *GENIE 2000* Software" [*Federal Information Foundation for Ensuring the Uniformity of Measurements*, 2015].

The research at that stage covered the following activities: determination of natural humidity of bottom sediments samples and their dehydration, which prevents the loss of organic matter, and two-time weighing, grinding, and composing of test samples, which meet the radiometric measurements requirements.

The measurements of specific activity of radionuclides in test samples were at the multichannel gamma-ray spectrometer for measuring X-ray and gamma radiation BE5030 (*Canberra Semiconductors NV*, Olen, Belgium) with lead screen protection of the HPGe detector *Ekran-2P* manufactured by *Aspekt* (Dubna, Russia). Spectra processing took place and the *Genie-2000* Software (version 3.3) was used to identify the technogenic and natural radionuclides. The measurement time of each sample was 24 hours minimum. We calculated the specific activity of radionuclides in the studied sample per one unit of dry weight.

3. Sedimentation conditions

According to I. V. Samoilov, the Don Delta is a multi-channel (braided) delta with the shallow front-estuary [*Samoilov*, 1952]. According to the genesis, the tectonic depression of the delta belongs to the Rostov Ledge of the Ukrainian Shield of the East European Platform [*Sidorenko et al.*, 1970]. The accumulative formations of fluvial sedimentary material at the mouth of the delta are pushed into the limits of the sea bay. Its current conditions were formed during the last 4.5 thousand years with the Sea of Azov level being unstable. The sea level fluctuations were typical of the Sea of Azov. The sedimentary cover was formed in the area during the Holocene, which thickness may reach 20 m in some places [*Berkovich and Timofeeva*, 2007; *Zaitsev and Zelenshchikov*, 2009].

The current Don Delta begins where the Mertvyi Donets separates from the Don River main channel and is a flat alluvial plain composed of isles separated by numerous channels and bayous. The height of the isles land areas rarely exceeds 1 m in relation to the river low-water level. The length of the delta is *ca.* 30 km and the width between the utmost channels in the near seashore areas is more than 20 km [*Samokhin*, 1958].

The sea level changes, tidal fluctuations and surges, caused by strong and long-duration winds, impact the estuary area morphology significantly. They also impact the delta hydrological and sedimentary rocks accumulation conditions.

The intensive anthropogenic transformation of the river runoff, which began in the 20th century, significantly changed the environmental conditions in the Lower Don basin. The launch of the Tsymlyansk Water Storage Reservoir in 1952 considerably influenced the hydrological and sedimentation conditions in the Don Delta and the launch of operations along the Azov-Don Seaway Canal (in 1927) – the redistribution of the river runoff between the delta's channels. These anthropogenic intrusions resulted in the reduction of the Don River solid runoff by more than 10 times since the middle of the 20th century. The volume of the river runoff in the Southern Don Delta via the Peschanyi bayou (continuation of the Staryi (Old) Don channel) via which the canal route runs increased by 4–5 times. At the same time, its volume in the smaller bayous in the indicated area decreased by 1.5 to 12 times. The velocity of runoff currents also decreased resulting in silting and gradual dying out of some of them [*Polshin et al.*, 2021].

The change of solid runoff fraction composition took place. The content of sandy dimension particles decreased in the fluvial suspension and, vice versa, the content of pelite fraction increased. The abundance of sand in the suspended matter in the river water of the braided Don Delta by the early 21st century was slightly higher than 3 % and of clayish particles – *ca.* 75 % [*Bessonov et al.*, 2009].

The studies we conducted indicate that the spatial distribution of bottom sediments in the Northern Don Delta depends on the morphologic composition of numerous channels and bayous, their depth, as well as currents velocity. Admixture of sandy material, which content increases in areas with intensive flow, is typical of the fluvial deposits in the studied area. The accumulation of silts of various granulometric compositions of dark-grey and black colours is more typical of seashore and front-estuary areas overgrown with aquatic vegetation. Periodically and due to the strong wind impact, the grounds composing the upper part of the layer can become stirred up and be transported to the Taganrog Bay area.

Overall, sedimentation conditions in the northern part of the delta determine the accumulation of deposits of relatively similar granulometric composition. These are mainly sandy-silty aleurites with inclusions of plant and shell detritus and sandy aleurite-clayish silts also containing detritus of organic origin. We observed changes in the sediments composition in close proximity to the confluences of channels and the Taganrog Bay and in wide channels and bayous with strong flow. The silty fine and middle-size sands, which also contain inclusions of shells and shell detritus, replace the silt deposits in these areas (Table 1).

4. Radionuclides in the delta bottom sediments

The accident at the Chernobyl NPP resulted in the subsequent contamination of water catchment basin of the Sea of Azov and its main freshwater stream flow – the Don River. However, there was no radiation monitoring of the vast delta aquatic system during that period. The main focus was on observations made directly in the Sea of Azov water area. According to research data of 1986, the specific activity of ^{137}Cs in the Taganrog Bay deposits varied from 2 to 90 Bq/kg. And the level of isotope accumulation depended on the type of bottom ground. The maximum values of ^{137}Cs content were registered in fine-dispersed clayish silts. The specific activity of ^{139,140}Pu radioisotopes in fine-aleurite silts along the axis line of the Taganrog Bay was 1.5 Bq/kg. The silty sediments in the Central Sea of Azov contained on average up to 75–85 Bq/kg of ^{137}Cs radioisotope [*Bufetova*, 2002; *Vakulovsky et al.*, 1994].

The sea area radioactive contamination began to decrease in the early 2000s. However, there are still sites with high ^{137}Cs specific activity (50–65 Bq/kg) in clay and aleurite-clay silts of the Central Sea of Azov at the depth of 10–13 m. The concentration of ^{137}Cs in the Taganrog Bay aleurite-clay silts is 20–45 Bq/kg. The change of the bottom ground lithotype to the sandy-silty aleurites in the Eastern Taganrog Bay condition the decrease of ^{137}Cs concentration to 11 Bq/kg [*Matishov et al.*, 2020].

Thus, the river runoff within the Don – Taganrog Bay – the Sea of Azov aquatic system sustains the existing local background of technogenic radioactivity and ensures the circulation of radionuclides, of ^{137}Cs in particular. However, both the radio-ecological conditions of the Don Delta and radiation characteristics of the runoff remain insufficiently studied. There are only single observations in the mouth part of the river.

The studies we conducted in 2022 also indicate a relatively low level of radioactive contamination of bottom sediments in some areas of the Don Delta. The specific activity of technogenic ^{137}Cs ranges within 5–43.5 Bq/kg of d.w. (Table 1).

Table 1. Specific activity of radionuclides in the bottom sediments of the Don Delta, 2022.

№	Cs-137 (Bq/kg)	K-40 (Bq/kg)	Ra-226 (Bq/kg)	Th-232 (Bq/kg)	Bottom sediments characteristics
1	7.1±0.4	602±23	17.9±0.8	21.0±1.2	Fine aleurite-silty sand with inclusions of plant and shell detritus.
2	5.0±0.3	453±22	19.1±0.9	20.1±1.0	Sandy-silty aleurite with inclusions of plant and shell detritus.
3	11.0±0.8	383±31	13.6±1.1	18.3±1.5	Sandy aleurite-clay silt with single inclusions of plant and shell detritus. Flooded. Colour: dark grey.
57	7.7±0.6	678±35	25.3±1.3	28.9±1.6	Sandy aleurite-clay silt of gray-green colour with inclusions of plant and shell detritus.

Continued on next page

Table 1. Specific activity of radionuclides in the bottom sediments of the Don Delta, 2022. (Continued)

№	Cs-137 (Bq/kg)	K-40 (Bq/kg)	Ra-226 (Bq/kg)	Th-232 (Bq/kg)	Bottom sediments characteristics
62	1.3±0.2	299±19	13.4±0.7	13.7±0.8	Silty fine sand, flooded. Inclusions of shell material. Colour: grey.
76	8.4±0.4	446±22	18.4±0.9	23.6±1.1	Aleurite-clay silt with large content of shell material (ca. 50 %).
79	5.3±0.3	318±17	15.8±0.7	14.0±0.6	Sandy aleurite silt with inclusions of plant material and shells. Colour: dark grey.
82	12.5±0.5	659±28	25.7±1.0	29.5±1.1	Sandy aleurite-clay silt with inclusions of plant and shell detritus. Flooded. Colour: dark grey.
87	7.5±0.6	590±31	24.4±1.2	24.3±1.2	Sandy-silty aleurite with inclusions of plant and shell detritus. Colour: dark grey.
92	43.5±2.2	754±43	27.4±1.6	33.3±2.1	Sandy-silty aleurite with inclusions of plant and shell detritus. Colour: grey-green.
93	14.8±0.4	875±36	29.8±1.3	29.1±1.3	Sandy aleurite-clay silt with inclusions of plant and shell detritus. Flooded. Colour: dark grey.
94	11.2±0.9	1217±85	37.0±2.5	51.7±3.8	Aleurite-clayish silt. Registered inclusions of shell material. Colour: dark grey.
97	12.2±1.4	776±49	34.0±2.3	39.5±2.5	Clayish silt. Registered inclusions of shell material. Colour: from dark grey to black.

There are no pronounced changes of sediments lithotype in numerous channels and weakly flowing bayous. As a rule, the bottom sediments are similar in their granulometric composition sandy-silty aleurites and sandy aleurite-clayish silts with inclusions of plant and shell detritus. However, there is a pronounced specific activity increase towards the top of the delta and the main channel of the Don River within the radioisotope distribution in the aquatic system (Figure 1).

In this particular case the change of currents velocities and intensity of suspended matter deposition in the bayous of the Don Delta mainly influence the ^{137}Cs accumulation. The Don River runoff containing suspended matter contaminated with caesium enters the upper delta areas where its redistribution into streams and bayous takes place at the decreased velocities of the runoff flows thus conditioning the deposition of suspended matter and zoning in the redistribution of technogenic radioisotopes.

This trend is less distinct when it comes to the redistribution of natural radioisotopes – ^{40}K, ^{226}Ra, and ^{232}Th. The mineral composition of deposit particles determines the content of these radionuclides to the greater degree, not their fraction sizes (Table 1).

It is noteworthy that the cases of relatively increased activity of ^{137}Cs in single samples of the ground similar to the deposition of the hot particle are possible in the sediments of the top of the delta (Figure 2a, Sampling Point 92).

The change of lithotype expectedly takes place only in the seashore and front-estuary areas (Sampling Point 62). Hydrodynamics in the seashore and front-estuary areas conditions the replacement of aleurite silts with sands of various sizes with inclusions of shells and shell detritus. The ^{137}Cs concentration in sediments decreases significantly under such conditions (Figure 2). The currents transport radionuclides related to pelite-aleurite fraction of sediments to the sediments accumulation areas located in the Taganrog Bay and the Central Sea of Azov. According to the data of the previous field studies of 2018-2021, the ^{137}Cs specific activity in the seashore and front-estuary areas was registered at the level of 2 Bq/kg [*Matishov et al.*, 2022], which corresponds to the values we obtained in 2022. The

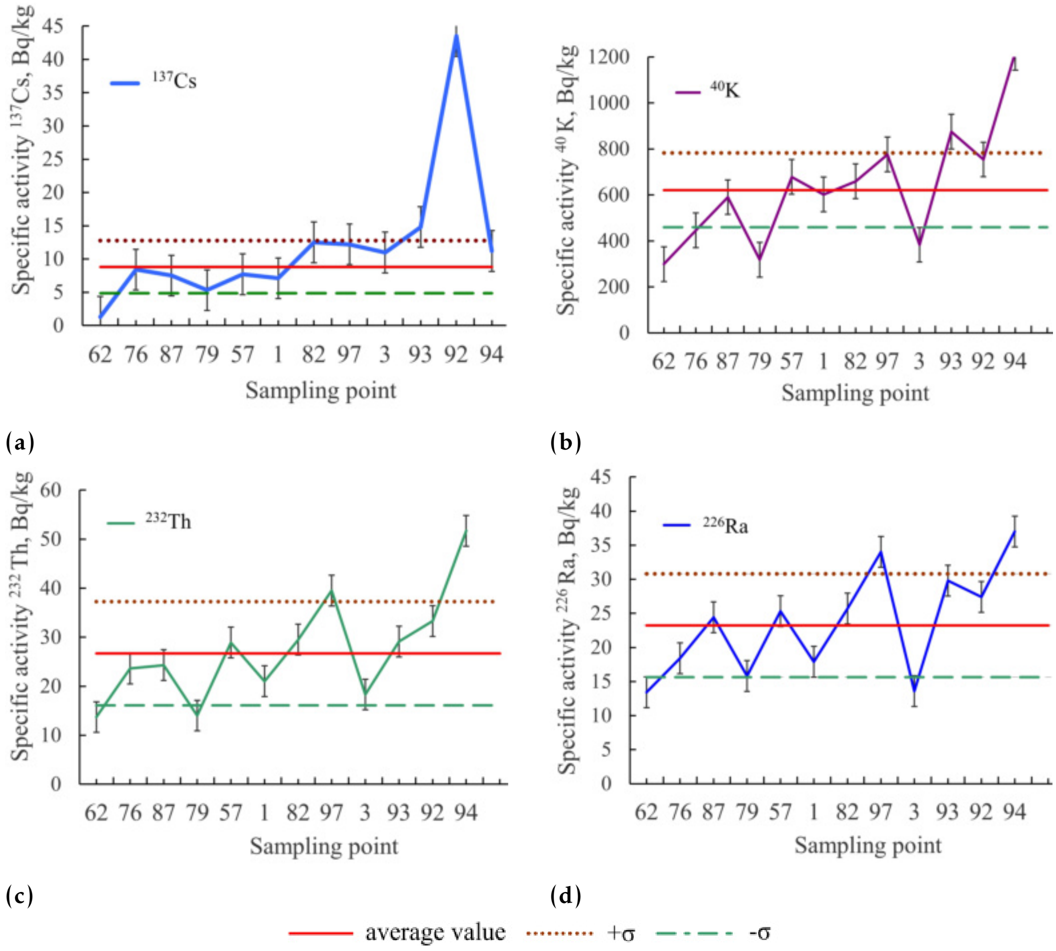

Figure 2. Profile of specific activity of radionuclides in the bottom sediments of the Don Delta, 2022.

change of sediments lithotype also causes the decrease of ^{226}Ra and ^{232}Th radioisotopes concentrations. The content of ^{40}K remains at the mean value level.

Table 2 presents the averaged values of specific activity of technogenic and natural radionuclides and its variability in the Don Delta landscape. The averaged value of activity of potentially hazardous technogenic ^{137}Cs radioisotope equal to 8.8±1.2 Bq/kg allows assessing the general radio-ecological situation in the studied delta areas.

5. Conclusions

The studies indicate that the current range of ^{137}Cs radioisotope concentrations in the Northern Don Delta bottom sediments is characterised by a relatively low specific activity – *ca.* 9 Bq/kg d.w. on average. The distribution of both technogenic ^{137}Cs and natural ^{226}Ra and ^{232}Th radioisotopes follows a certain zonal pattern related to the radionuclides specific activity increase from the seashore and front-estuary areas towards the top of the delta. This pattern depends on velocities of the runoff flows and currents in delta and related changes in sedimentation conditions of suspended matter inflowing with the river runoff.

Periodic washout and roiling of bottom ground in the shallow near-shore areas of the Sea of Azov result in the formation of the bottom sediments lithotype different from the delta one – fine silty sand, which contains insignificant quantity of ^{137}Cs, ^{40}K, ^{226}Ra, and ^{232}Th. However, unlike technogenic ^{137}Cs, the mineral composition of suspended matter transported from the delta is of greater significance for the natural radioisotopes distribution in these areas.

There are single cases of the peak values of ^{137}Cs specific activity in the top of the delta, supposedly related to remote sources of radioactive suspended matter sporadically transported from the Don River water catchment area. Overall, the concentration of

Table 2. Statistical characteristics of the distribution of technogenic and natural radionuclides in the bottom sediments of the Don Delta, 2022.

Characteristics	Radionuclide, Bq/kg dry weight				
	Cs-137	Ra-226	Th-232	Pb-210	K-40
Average	8.81	23.22	26.69	75.34	620.67
Minimum	1.30	13.40	13.70	23.80	299.00
Maximum	14.80	37.00	51.70	123.00	1217.00
Standard uncertainty	1.20	2.11	2.93	8.84	76.78
Standard deviation	3.97	7.59	10.58	26.52	265.96
Statistical dispersion	15.77	57.61	111.93	703.57	70734.97

technogenic ^{137}Cs radionuclide in the studied area is currently of no danger for the biota and nature resources exploitation.

The data obtained may be applied to the situation analysis of radio-ecological processes in the Sea of Azov aquatic ecosystem, as well as when analysing the general patterns of radionuclides geochemistry in the river – delta – seashore areas aquatic system.

Acknowledgments. The study was within the themes of SSC RAS State Task No. 122101100083-5 entitled "Analysis of Historical Data to Provide the Grounds for the Biogeochemical Cycles Monitoring System in the Sea of Azov Basin Considering the Specific Regional Features" and No. 122011900166-9 entitled "The Impact of Global Paleo-Ecological and Paleo-Geographic Events on the Status of Biogeocenoses and Human Populations in the Southern Regions of Northern Eurasia in the Late Cainozoic", MMBI RAS State Task, as well as RSF Grant No. 22-17-00243.

The authors would also like to express their gratitude to Roman G. Mikhalyuk (SSC RAS) for the English Language assistance.

References

Berkovich, K. M., and V. V. Timofeeva (2007), Morphology and directed deformations of the Lower Don River channel, *Geomorphology*, *3*, 54–62 (in Russian), EDN: IAYPQL.

Bessonov, O. A., M. G. Davydov, G. V. Zelenshchikov, and L. N. Kaz'mina (2009), Behaviour of terrigenous sedimentation matter in the Tsymlyansk Water Storage Reservoir – Lower Don – Taganrog Bay system, in *Geology, geography and ecology of the ocean. International Scientific Conference dedicated to 100-year birth anniversary of D. G. Panov (Rostov-on-Don, 8–11 June 2009)*, pp. 32–36, SSC RAS Publishers, Rostov-on-Don (in Russian).

Bufetova, M. V. (2002), Radioactive contamination of the Sea of Azov with long-lived 90Sr and 137Cs radionuclides, phdthesis, Murmansk (in Russian), EDN: QDQFOP.

Bulgakov, V. G., A. D. Uvarov, V. D. Gnilomedov, M. N. Katkova, A. O. Epifanov, and S. M. Vakulovsky (2021), Results of the study of radioactive contamination of the soils of the Bryansk Region, in *Radio-ecological consequences of radiation accidents – to the 35-year anniversary of the accident at the Chernobyl NPP: collection of presentations at the International Scientific and Practical Conference (Obninsk, 22–23 April 2021)*, pp. 46–48, FSBSI VNIIRAE, Obninsk (in Russian), EDN: AYMVGV.

Buryakova, A. A., I. I. Kryshev, N. N. Pavlova, and M. N. Katkova (2021), Current state of radioecological situation on the territory of the Chernobyl radioactive trace in the Bryansk Region, in *Radio-ecological consequences of radiation accidents – to the 35-year anniversary of the accident at the Chernobyl NPP: collection of presentations at the International Scientific and Practical Conference (Obninsk, 22–23 April 2021)*, pp. 48–51, FSBSI VNIIRAE, Obninsk (in Russian), EDN: WSLUAR.

Federal Information Foundation for Ensuring the Uniformity of Measurements (2015), Manual on Gamma-ray emitting radionuclides activity (specific activity) measurements in test samples using the CANBERRA Gamma-ray spectrometer with the GENIE 2000 Software (FR.1.38.2016.23695), https://fgis.gost.ru/fundmetrology/registry16/items/302615 (in Russian), (access date: 04/07/2023).

Kryshev, I. I., A. A. Buryakova, N. N. Pavlova, T. G. Sazykina, and A. I. Kryshev (2021), Environmental risk assessment of the Chernobyl accident in contaminated areas of Russia (1986–2020), in *Radio-ecological consequences of radiation accidents – to the 35-year anniversary of the accident at the Chernobyl NPP: collection of presentations at the International Scientific and Practical Conference (Obninsk, 22–23 April 2021)*, pp. 88–90, FSBSI VNIIRAE, Obninsk (in Russian), EDN: QXOOEW.

Matishov, G. G., V. V. Polshin, G. V. Ilyin, and I. S. Usyagina (2020), Dynamics of Background Radiation in Russian Seas (New Data on the Sea of Azov), *Doklady Earth Sciences*, *493*(2), 640–644, https://doi.org/10.1134/S1028334X20080127.

Matishov, G. G., V. V. Polshin, G. V. Ilyin, and I. S. Usyagina (2022), Influence of gas aerosol emissions of the Rostov Nuclear Power Plant on the radiation background of southern waters, *Doklady Earth Sciences*, *503*(2), 220–225, https://doi.org/10.31857/S2686739722040119 (in Russian).

Polshin, V. V., I. V. Tolochko, K. S. Sushko, A. Y. Moskovets, and S. V. Biryukova (2021), Changes in paleo-landscapes during the Holocene under the influence of natural and anthropogenic processes (the case of the Taganrog Bay water area and adjacent section of the Don River Delta), *Science in the South of Russia*, (2), 49–56, https://doi.org/10.7868/S25000640210205 (in Russian).

Samoilov, I. V. (1952), *Mouths of rivers*, Geografgiz, Moscow (in Russian).

Samokhin, A. F. (1958), *Don River and it's tributaries*, RSU, Rostov-on-Don (in Russian).

Sidorenko, A. V., F. A. Belov, A. I. Egorov, and N. I. Pogrebnov (1970), *Geology of the USSR. Volume 46. Rostov, Volgograd, Astrakhan regions and Kalmyk ASSR*, Nedra, Moscow (in Russian).

Vakulovsky, S. M., A. I. Nikitin, V. B. Chumichev, I. Y. Katrich, O. A. Voitsekhovich, V. I. Medinets, V. V. Pisarev, L. A. Bovkum, and E. S. Khersonsky (1994), Cesium-137 and strontium-90 contamination of water bodies in the areas affected by releases from the chernobyl nuclear power plant accident: an overview, *Journal of Environmental Radioactivity*, *23*(2), 103–122, https://doi.org/10.1016/0265-931X(94)90055-8.

Zaitsev, A. V., and G. V. Zelenshchikov (2009), Holocene of the Don Delta, in *Geology, geography and ecology of the ocean. International Scientific Conference dedicated to 100-year birth anniversary of D.G. Panov (Rostov-on-Don, 8-11 June 2009)*, pp. 124–126, SSC RAS Publishers, Rostov-on-Don (in Russian).

Russian Journal of Earth Sciences

Special Issue: “25th anniversary of the Russian Journal of Earth Sciences”

High Resolution Seismicity Smoothing Method for Seismic Hazard Assessment

I. A. Vorobieva[1], E. M. Grekov[1], K. V. Krushelnitskii[*,1], P. A. Malyutin[1], P. N. Shebalin[1]

[1] Institute of Earthquake Prediction Theory and Mathematical Geophysics RAS, Moscow, Russian Federation

* **Correspondence to:** K. Krushelnitskii, kirillkrush@mail.ru

Abstract: A high resolution smoothing method is proposed for performing local estimates of the parameters of the Gutenberg-Richter law (GR). Using this method, the smoothing radius can be chosen large enough to ensure that the condition of applicability of GR law is met, while the distinguished areas of high activity align well with the distribution of epicenters and there is no “smearing” of narrow areas of really high seismic activity into wider zones, which are not actually active at the edges.

Keywords: seismicity, seismic hazard, smoothing method, Gutenberg-Richter law, interpolation.

Citation: Vorobieva I. A., Grekov E. M., Krushelnitskii K. V., Malyutin P. A., Shebalin P. N. (2024), High Resolution Seismicity Smoothing Method for Seismic Hazard Assessment, *Russian Journal of Earth Sciences*, Vol. 24, ES1003, https://doi.org/10.2205/2024ES000892

Research Article

Received: 15 October 2023
Accepted: 15 January 2024
Published: 29 February 2024

1. Introduction

The problem of reliable assessment of seismic hazard and its application in practice has intensified after the catastrophic earthquakes on February 6 and 7, 2023 $Mw = 7.8$ and 7.5 on the border of Turkey and Syria and the earthquake on September 8, 2023 $Mw = 6.8$ in Morocco. In Turkey, like in Russia and in most countries located in earthquake-prone regions, seismic hazard assessments are used in earthquake-resistant construction standards (building codes) in order to minimize the number of casualties and economic loses in case of a devastating earthquake. Unfortunately, as it has happened in most cases of catastrophic earthquakes [*Wyss and Kossobokov*, 2012], the seismic hazard in the epicentral zones of these earthquakes is significantly underestimated.

Seismic hazard assessment is understood as an assessment of the probability of exceeding a seismic effect of a certain value in a certain location over a certain time period. The impact effect is usually measured in terms of macroseismic intensity or in units of ground acceleration. There are two main approaches to assessing seismic hazard – deterministic and probabilistic. In the deterministic approach, the possibility of exceeding a certain effect over a very long time interval (tens of thousands of years) is assessed. This approach is usually based on active tectonic faults data, paleo- and archaeoseismological studies, and data on instrumentally recorded large earthquakes. The goal of the probabilistic approach is to estimate the probability or recurrence of exceeding a certain effect over a certain time interval. Both, data on active faults and statistical analysis of instrumentally recorded earthquakes are typically used in this approach. Commonly, the abbreviations DSHA (Deterministic Seismic Hazard Analysis) and PSHA (Probabilistic Seismic Hazard Analysis) are used.

Usually, seismic hazard assessment is presented in the form of maps called seismic zoning maps. In Russia, depending on the detail of the scale, maps are classified as general (GSZ), detailed (DSZ) and microseismic (MSZ) zoning maps. GSZ maps are used on a state scale. The actual earthquake impact may depend on ground conditions (on rocky grounds, other things being equal, the impact is weaker than on soft or water-saturated soils), so GSZ maps are designed for average grounds.

The first seismic zoning maps were based on the deterministic approach, so traditionally GSZ maps are constructed in the form of zones of the maximum expected impact – macroseismic intensity in the MSK-64 scale [*Medvedev et al.*, 1964]. In the framework of PSHA, several versions of maps are constructed with estimates of the expected maximum impact for different time intervals (for example, 500, 5000, 10000 years).

Seismic hazard assessment consists of modeling the seismic regime or zones of possible earthquake sources (PES) and the impact of earthquakes on objects at a distance from the earthquake source. The seismic regime is a set of earthquakes considered in space and time, taking into account their magnitude [*Riznichenko*, 1958, 1968]; in fact, this is more general concept than PES zones. In PSHA, PES zones imply sources of earthquakes in the form of points (epicenters), lines (active faults), and areas ("domains"), which are considered as near-homogeneous seismogenic zones.

Nowadays, despite the apparent complexity, significant progress has been made in the world seismology in solving the problem of accurate modeling the impact of earthquakes compared to modeling PES zones. The errors in seismic hazard assessments are usually associated with inaccurate forecasting of the future earthquake source locations and their magnitudes. Many cases of earthquakes are known, that occurred in places where no one expected them to be such a magnitude. The most striking recent example is the magnitude $Mw9.0$ Tohoku earthquake near the coast of Japan on March 11, 2011. A very recent example is the September 8, 2023, $Mw = 6.8$, earthquake in Morocco.

In the USSR and then in the CIS many earthquakes were a surprise from the point of view of the GSZ maps used at that time: Gazli, 1976, $M = 7.0$ in Uzbekistan, Spitak, 1988, $M = 6.8$ in Armenia, Zaysan, 1990, $M = 6.9$ in Kazakhstan, Rachi, 1991, $M = 7.0$ in Georgia, Sususamyr, 1992, $M = 7.5$ in Kyrgyzstan, Khailin, 1991, $M = 7.0$ in Koryak and Neftegorsk, 1995, $M = 7.6$ in Sakhalin. Large earthquakes occurred after the development of the GSZ-97 map set for the territory of Russia also demonstrated significantly larger impact than expected: Olyutor, 2006, $M = 7.6$ in Koryak, Tuva, 2012, $M = 6.9$, Ilin-Tass (Abyisky), 2013, $M = 6.7$ in Yakutia, Katav-Ivanovsk, 2018, $M = 5.4$ in the Urals, etc.

Another type of errors is a significant overestimation of seismic hazard over large areas. [*Shebalin et al.*, 2022] showed that in most regions of Russia the seismic hazard is overestimated by at least 10 times. The analysis was carried out by comparison of the areas expected in accordance with the map of the OSR-97A zones, and the total isoseismal areas from earthquakes that occurred in the period after the publication of the OSR-97 maps.

The main contribution to such errors is the overestimation of the recurrence rate of earthquakes over large areas. Thus, the inaccurate model of PES zones is the main source of errors in GSZ maps, both target misses and false alarms.

In modern world practice, as a rule, a combined seismic regime model is used for the purposes of general seismic zoning. The model includes seismicity along linear structures – "lineaments" (active tectonic faults), on area structures – "domains," as well as individual potential earthquake sources. It is assumed that within a structure unit, seismic events have an equally probable epicenter location, and the same recurrence rate and frequency-magnitude distribution.

The transition from PES zones to GSZ maps is the construction of model of the earthquake impact propagated from the source to a point on the surface of the Earth may be performed either using a "classical" analytical method proposed by [*Cornell*, 1968] or by forming of a synthetic earthquake catalog. In the latter method at each location the impact of different magnitudes is calculated integrating the impacts of all synthetic events.

This approach was used to develop maps of the general seismic zoning of Russia GSZ-97, GSZ-2015, GSZ-2016, which were used as normative ones for design of earthquake-resistant construction in seismic regions. The model was created by a large group of authors under the leadership of V. I. Ulomov and was called the lineament-domain-focal (LDF) model [*Ulomov and The GSHAP Region Working Group*, 1999]. It should be noted that it is incorrect to interpret the creation of such a model as an innovation first implemented in Russia, as it is often noted in Russian sources. At the international scope, this approach was used within the framework of the international project GSHAP (Global Seismic Hazard Assessment Program), operated from 1992 to 1999 [*Giardini et al.*, 1999]. Nevertheless, this model was a step forward in the practice of seismic hazard zoning. For the first time, probabilistic maps began to be used, intended for engineering of the earthquake-resistant constructions of different categories of vulnerability and length life.

However, the approach to design GSZ maps based on the LDF model can only conditionally be called probabilistic. The determining of lineaments and domain boundaries, as well as the additional identification of potential sources, is highly subjective, thus, the location of epicenters and recurrence rate in the model are significantly predetermined by this human factor. The division of seismic zones into linear and areal structures in the LDF model historically appeared as an addition to the deterministic model, which included only linear structures - active faults, and was first proposed by S. A. Cornell [*Cornell*, 1968]. Such approach was justified in the era of limited computing capacities, when analytical solutions could greatly reduce the amount of calculations. The analytical solutions of S. A. Cornell, thanks to the assumption of spatial homogeneity of earthquake sources within each structure, made it possible to relatively quickly calculate the recurrence of impacts at a given point from potential earthquakes with sources in lineament and domains.

Nowadays, it is no longer necessary to use Cornell's analytical solutions. The PES zone model can be represented in the form of a synthetic catalog of earthquakes. Then, direct calculations at a given point of the impacts from each synthetic earthquake and, accordingly, the rate of impacts of a certain intensity are possible. Of course, it is possible to create a synthetic catalog based on an LDF-type model, but this will not eliminate subjective factors in determining the boundaries of the structural elements of the LDF model that significantly affect the modeling results. Therefore, frequent disagreements among researchers regarding the boundaries of linear and areal structures, criticism of the "characteristic earthquakes" model underlying the identification of individual potential sources have led in many countries to the use of smoothed seismicity – a representation of a seismic regime in which no zone boundaries are needed [*Akinci et al.*, 2018; *Helmstetter and Werner*, 2012]. The smoothed seismicity approach models the variability between the spatiotemporal distribution of past and future seismicity and provides a much more spatially accurate prediction than zoning models.

Smoothed seismicity models require a significantly larger number of earthquake observations for a detailed and accurate assessment of seismic regime parameters. A quarter of a century has passed since the creation of the GSZ-97 maps, and during this period a huge amount of data on earthquakes has been accumulated, making it possible to move from zoning models to smoothed seismicity models.

The synthetic catalog is formed based on a seismic regime model that determines the recurrence of earthquakes of a certain magnitude at different points in the region under consideration. A common practice is to use recorded earthquakes. It is assumed that the locations of smaller earthquakes are representative of the locations of larger earthquakes. In this case, to estimate the frequency of earthquakes of greater magnitude, the Gutenberg-Richter law is used [*Gutenberg and Richter*, 1945], which establishes the ratio of the number of events of different magnitudes. The specific details of which magnitudes are used depend on the quality of the earthquake catalog and may change over time. It is generally believed that the reliability of a forecast is related to the length of the catalog, which can vary from decades to centuries.

The choice of smoothing method can be based solely on expert judgment or can be decided on the basis of statistical optimization of forecast accuracy using past earthquakes (e. g. [*Petersen et al.*, 2015; *Stirling et al.*, 2012]). Common practice includes fixed smoothing radius methods (for example, [*Frankel*, 1995]), and so-called adaptive methods, in which the smoothing radius increases as the density of observed earthquakes decreases [*Akinci* *et al.*, 2018; *Helmstetter and Werner*, 2012; *Pisarenko and Pisarenko*, 2021; *Stock*, 2002]. In both approaches, the value of the estimated parameter is assigned to the center of the circle. This always leads to a significant decrease in the spatial resolution of the assessment results: in the most seismically active areas, the activity inevitably turns out to be underestimated, and at the edges of these areas – overestimated. An additional underestimate of activity is caused by the fact that during normalization per unit area, the fractal structure of the seismicity distribution is not taken into account [*Kosobokov and Mazhkenov*, 1992].

Adaptive estimates provide a more contrasting picture of the distribution of seismicity compared to the constant radius methods, however, excessive detail may not be entirely justified due to the significant spatiotemporal clustering of earthquakes, which persists even after declustering of the earthquake catalog. Another drawback of this model is that the assessment of the intensity of the flow of events per time unit and per area unit is based on the assumption of homogeneity, although the method is aimed specifically at identifying the details of the spatial heterogeneity of the seismicity distribution.

Both constant radius and adaptive estimates must take into account the limits of applicability of the Gutenberg-Richter law [*Gutenberg and Richter*, 1945]. The geological basis of this law is the fractal structure of the support of seismicity – the fault system [*Sadovsky*, 1979]. Therefore, when assessing the parameters of the GR law, it is incorrect to consider narrow areas, since this takes into account events only in the "root" part of the fractal structure and thereby predetermines the excess of stronger events. It is also incorrect to consider compact areas (for example, circles) with a radius comparable to the linear size of the source of the strongest earthquake in the area [*Main*, 2000; *Molchan et al.*, 1997; *Romanowicz*, 1992]. Thus, it is necessary to consider areas of a sufficiently large size, but this can lead to an unjustified "smearing" of seismic activity over space.

In this paper, we propose a high-contrast smoothing method in which estimated values are assigned not to the center of the circle, but to the average position of the earthquake epicenters used in the calculations, and in which areal normalization is performed taking into account fractal property of seismicity.

2. Method

We propose a modified version of the smoothing method with circles of a fixed radius, which gives significantly more contrasting results compared to the standard method and does not contain the disadvantages of the adaptive method described above. The choice of smoothing radius can be determined taking into account the applicability of the Gutenberg-Richter law.

The study region is scanned by circles with a constant radius R. The centers of the circles are located at the nodes of a regular grid with a given step D_{lat} in latitude and D_{lon} in longitude. It is well known that seismicity has a fractal structure in space [*Kosobokov and Mazhkenov*, 1992], which must be taken into consideration when normalizing the intensity of the flow of events. This is taken into account in our method. In each circle under consideration, an estimate $\nu(M)$ of the number of earthquakes with a magnitude $m \geq M$ earthquakes in the spatial cell $D_{\mathrm{lat}} \times D_{\mathrm{lon}}$ is made, normalized to the duration of the catalog

$$\nu(M) = N(M)\frac{S_{\mathrm{cell}}^{d_f}}{S_{\mathrm{circle}}^{d_f}}. \tag{1}$$

Here $N(M)$ is the number of earthquakes with magnitudes $m \geq M$ in a circle, $S^{d_f}_{\text{cell}}$ and $S^{d_f}_{\text{circle}}$ are the areas of the cell and the circle in d_f-dimensional space:

$$S^{d_f}_{\text{circle}} = R^{d_f} \frac{\pi^{\frac{d_f}{2}}}{\Gamma(1+\frac{d_f}{2})};$$

$$S^{d_f}_{\text{cell}} = D^{d_f} \cos^{\frac{d_f}{2}}(\varphi),$$

where Γ is the gamma function, R is the circle radius, D is the linear size of cell in degrees, φ is the latitude of the center of the circle, d_f – fractal dimension of the spatial distribution of the epicentres.

In the modified method proposed here, we will assign the value not to the center of the circle, but to the average position of the earthquakes in the sample. As a result of this operation, there will be several activity values in some cells $0.1^\circ \times 0.1^\circ$. For each such cell, we will choose a single value of ν corresponding to the maximum activity estimate. In those cells that did not contain a single value, we will restore activity using the built-in "Surface" interpolation procedure of the Generic Mapping Tool (GMT) package [*Wessel et al.*, 2019].

The interpolation method used in the "Surface" function of the GMT package is a modification of the minimum curvature method from [*Briggs*, 1974]. The main problem of interpolation methods when mapping data is getting unreasonable outliers in the results that do not fit well into the real picture (for example, sharp changes in elevation on a plain in terrain maps, etc.). This is caused by the fact that the values in the intervals between points with known data are not constrained by anything [*Grain*, 1970]. The so-called methods of mathematical surfaces, in which the solution is sought in the form of a single function for the entire surface, and the coefficients are found by solving equations for each point, seem to suffer most from this effect. The problem can be partially solved by dividing the surfaces into separate parts (piecewise), but this increases the computation time and also causes problems with discontinuities at the boundaries [*Grain*, 1970].

More advanced from this point of view are the methods of numerical surfaces, which can generally be divided into two groups: methods with weights and methods of finite differences. In the first case, the interpolated value is determined by the weighted average of the surrounding points. The further away the point is, the less its weight. However, this method produces poor results when the data density varies greatly. Areas of high density will be smoothed, while areas of low density will be interpolated rather unevenly [*Grain*, 1970]. It should be noted that in problems of seismicity smoothing, exactly this situation is realized.

The principle underlying finite difference methods is the assumption that the solution surface satisfies some differential equation. This equation is then approximated by finite differences and solved iteratively. In the simplest case, Laplace's equation can be used:

$$\frac{\delta^2 z}{\delta^2 x} + \frac{\delta^2 z}{\delta^2 y} = 0$$

In this case the value at the point z_{ij} will be determined by four other values at the neighboring points [*Grain*, 1970].

In [*Briggs*, 1974], a more complex equation is proposed. Specifically, the equation of displacement of a thin metal plate being bent by forces acting at points such that the displacement at these points is equal to the observed value. In this case, the value at point z_{ij} will be determined by twelve values at the neighboring points. It is also shown that such an equation fulfills the condition of minimizing the squared surface curvature. That is, the integral of the squared curvature is proportional to the total elastic energy of the plate and therefore the solution with the minimum energy corresponds to the surface with the minimum squared curvature [*Smith and Wessel*, 1990]. That is, thereby, the interpolated values between points with known data are constrained, and a physical justification for these constraints is provided.

However, as shown in [*Smith and Wessel*, 1990], even such a method can still produce unreasonable fluctuations in surface curvature after interpolation. The authors found out that if horizontal forces are added to the plate equation from [*Briggs*, 1974], which were excluded there to simplify the calculations, unwanted outliers and unnecessary inflection points can be avoided by controlling the tension parameter.

The method from [*Smith and Wessel*, 1990], implemented in the "Surface" procedure, has become widespread in solving problems of interpolation of geographical, geological, and geophysical data.

3. Application examples

The figure shows a map for assessing variations in seismic activity in the regions of southern Siberia using the described method. The value $R = 100$ km was used, which is about 10 times the size of the earthquake source with magnitude $M = 6.0$. The map is based on the data from the earthquake catalog for 1982–2021, obtained by combining catalogs from the yearbooks "Earthquakes in the USSR" for 1982–1991 (digitized version is available on the link http://www.wdcb.ru/sep/seismology/cat_USSR.ru.html), yearbooks "Earthquakes in Northern Eurasia" (1992-2021) (http://zeus.wdcb.ru/wdcb/sep/hp/seismology.ru/cat_N_Eurasia.ru.html) and the catalog of the International Seismological Center ISC (http://www.isc.ac.uk). Duplicates in the catalog were identified and removed according to the methodology of [*Gvishiani et al.*, 2022; *Vorobieva et al.*, 2022]. The catalog was also declustered using the methodology of [*Shebalin et al.*, 2020]. The resulting catalog is available on the link https://clck.ru/39T8k6. Local estimates of magnitude of completeness for the catalog according to the methodology of [*Vorobieva et al.*, 2013] (map is available at https://clck.ru/39T8oy) allow us to accept the value $Mc = 3.5$ as a regional estimate. The study region is scanned using circles with a constant radius $R = 100$ km (diameter $D = 200$ km). Value $a = \log_{10} \nu(3.5)$, where $\nu(3.5)$ is an estimate of the number of earthquakes in a cell with magnitude $M \geq 3.5$, calculated using the formula (1). Two versions of estimates can be compared: 1) values are assigned to the centers of the circles, and then interpolation is not carried out, 2) values are assigned to the average position of the epicenters and interpolation is carried out using the method described above. The results for the first option are shown in Figure 1, for the second one – in Figure 2.

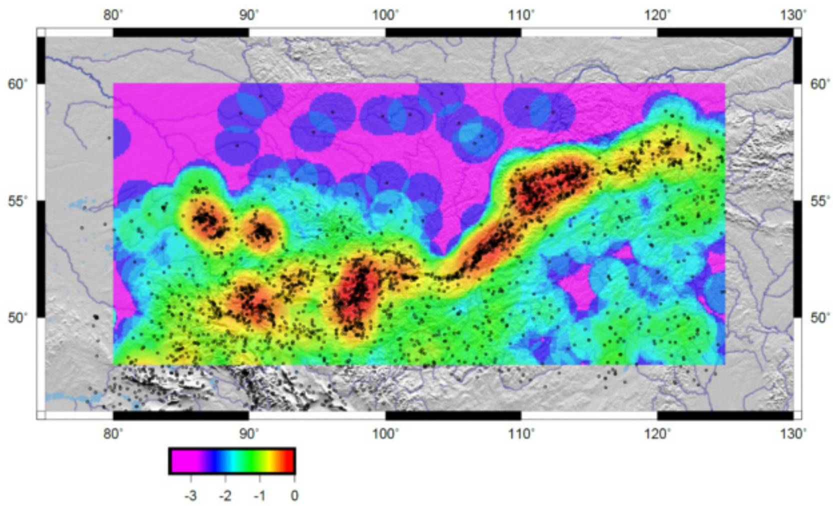

Figure 1. Variations in seismic activity $a = \log_{10} \nu(3.5)$, ν is the estimate of the number of earthquakes with magnitude $M \geq 3.5$, calculated using the formula (1). Earthquake epicenters are shown as black dots. The values are assigned to the centers of the scanning circles.

As it can be seen from Figure 2, when using the second approach, the activity corresponds well to the spatial distribution of the epicenters. If we use the traditional option,

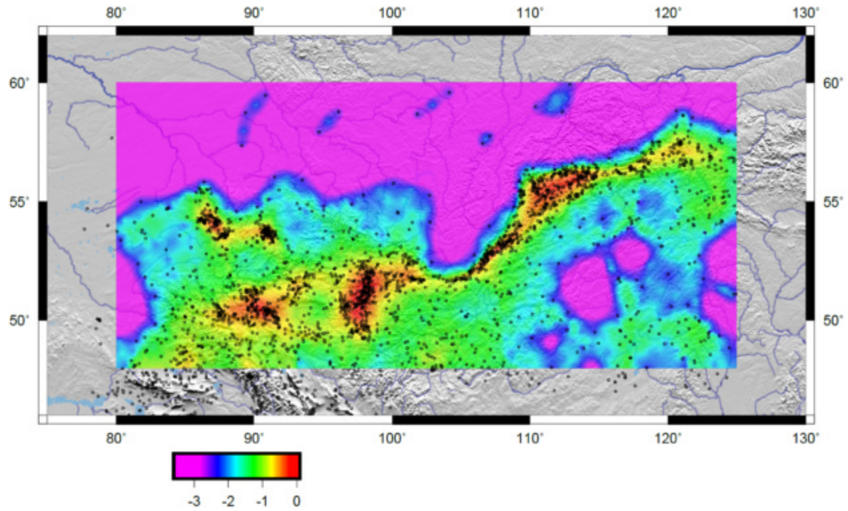

Figure 2. Variations in seismic activity $a = \log_{10} \nu(3.5)$. Earthquake epicenters are shown as black dots. The values are assigned to the average position of the epicenters in the scanning circles. The values at the grid points are calculated using interpolation.

assigning values to the centers of the circles, then the areas of high activity turn out to be significantly "smeared". Thus, the proposed method, while retaining the advantages of the smoothing method with circles of constant radius, provides a significantly more contrasting activity map, reflecting in detail the distribution of earthquake epicenters.

We propose to use a similar approach for local estimates of the b-value parameter. Since earthquakes of magnitude 7 have been observed in the region, to estimate the b-value parameter we use an increased value of $R = 200$ km, which corresponds to the conditions for the applicability of the Gutenberg-Richter law. The b-value is calculated using the Bender method [*Bender*, 1983], which, unlike the widely used Aki method [*Aki*, 1965], gives an unbiased value on small samples. The minimum sample size is 50 events; if the number of events in the circle is less than 50, we assign the corresponding cell the regional value of b.

Similar to the activity maps (Figure 1 and Figure 2), we compare two options for mapping the b-value: 1) values are assigned to the centers of circles (Figure 3), 2) values are assigned to the average position of the epicenters with subsequent interpolation (Figure 4).

As it can be seen from the figures, the use of our method actually leads to a significantly more contrasting picture of the distribution of the b-value: the areas of anomalously large and anomalously small values of the parameter turn out to have much smaller area. At the same time, unlike the activity maps, areas of homogeneous parameter values show low correlation with the density of epicenters and do not have an elongated shape.

4. Discussion and conclusion

In this paper, we proposed a high-contrast smoothing method for local estimation and mapping of seismic regime parameters determined by the Gutenberg-Richter law. When using this method, on the one hand, the conditions for the applicability of this law are controlled (a fairly large smoothing radius), and on the other hand, narrow areas of really high seismic activity are not "smeared" into wider zones that are not actually active at the edges.

The proposed approach allows to obtain local estimates of the parameters of the Gutenberg-Richter law with arbitrary detail. We used a scanning step of 0.1 degrees by latitude and longitude. For comparison, the detail of estimates when constructing GSZ-97, GSZ-2015, GSZ-2016 was 0.25 degrees. As the analysis of the obtained results shows, there is no need to further increase the detail, since the obtained estimates in neighboring grid cells differ, as a rule, by no more than 30%. If necessary, a technical increase in detail can be achieved using linear interpolation.

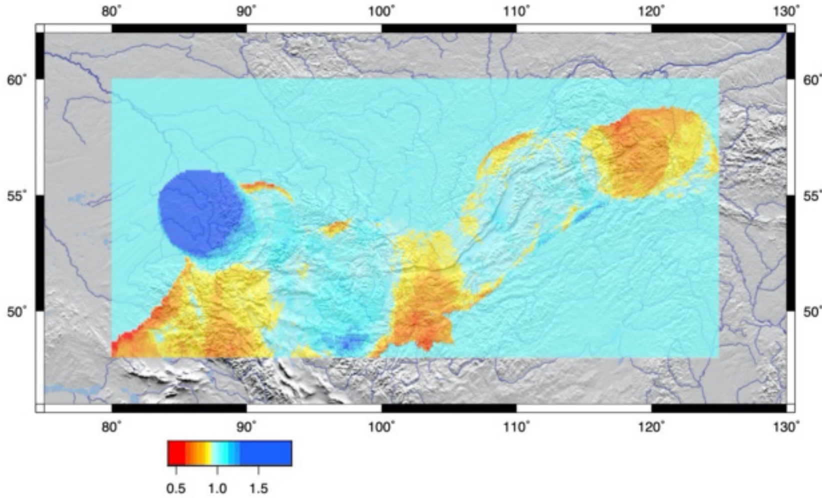

Figure 3. Variations of the b-value parameter. The values are assigned to the centers of the scanning circles.

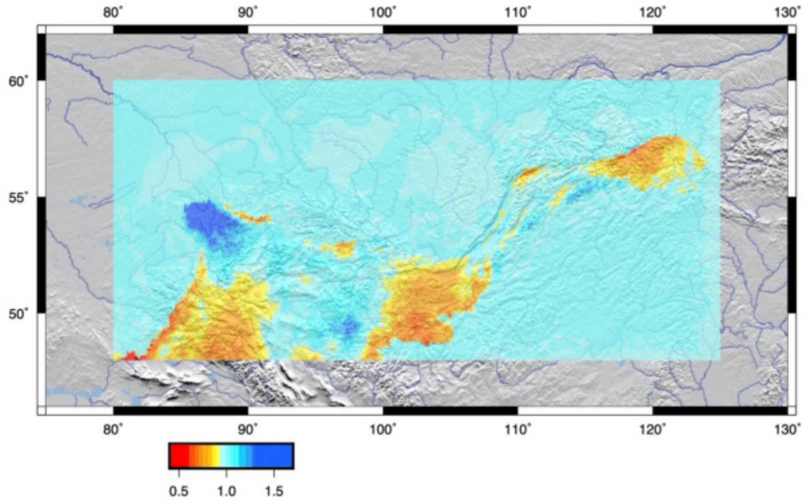

Figure 4. Variations of the b-value parameter. The values are assigned to the average position of the epicenters in the scanning circles. The values at the grid points are calculated using interpolation.

The local estimates of the parameters of the Gutenberg-Richter law obtained using our method can be used to construct a synthetic catalog of earthquakes. To do this, it is necessary to estimate the parameters of the Gutenberg-Richter law for the entire simulated region. This will allow to generate a sequence of seismic events with determined times (based on the Poisson model) and magnitudes. To generate the coordinates of the epicenter, it is enough to use local estimates of a and b-value to construct a probability distribution for the occurrence of an event of a given magnitude in cells of a regular grid and, using this distribution, select the appropriate cell using a random number generator. For the epicenters of the strongest earthquakes, additional constrains can be introduced using some model of the places where strong earthquakes may occur. Modeling of background earthquakes that follow the Poisson distribution can be supplemented with a synthetic catalog of clustered events, generated as sequences of aftershocks from background events, aftershocks of aftershocks, etc.

The approach to constructing a synthetic catalog described above does not require any subjective decisions other than choosing the boundaries of the region. This is its main advantage compared to LDF-type models. However, like the LDF model, this is just one of the possible solutions. To evaluate which approach is more effective, a quantitative comparison of different models with a catalog of recorded earthquake is necessary. The methodological foundation for such a comparison can be tests based on the likelihood function [*Zechar et al.*, 2010]. Comparison with the catalog that was used to build the model will only indicate the internal compatibility of the method and data. To compare the efficiency of different models a test on independent data is necessary. One can, for example, consider strong earthquakes for the period preceding the start date of the used part of the catalog.

Acknowledgments. The study was supported by a grant from the Russian Science Foundation (project No. 20-17-00180-p).

References

Aki, K. (1965), Maximum likelihood estimate of b in the formula $\log N = a - bM$ and its confidence level, *Bulletin of the Earthquake Research Institute*, *43*, 237–239.

Akinci, A., M. P. Moschetti, and M. Taroni (2018), Ensemble Smoothed Seismicity Models for the New Italian Probabilistic Seismic Hazard Map, *Seismological Research Letters*, *89*(4), 1277–1287, https://doi.org/10.1785/0220180040.

Bender, B. (1983), Maximum likelihood estimation of b values for magnitude grouped data, *Bulletin of the Seismological Society of America*, *73*(3), 831–851, https://doi.org/10.1785/BSSA0730030831.

Briggs, I. C. (1974), Machine contouring using minimum curvature, *GEOPHYSICS*, *39*(1), 39–48, https://doi.org/10.1190/1.1440410.

Cornell, C. A. (1968), Engineering seismic risk analysis, *Bulletin of the Seismological Society of America*, *58*(5), 1583–1606, https://doi.org/10.1785/BSSA0580051583.

Frankel, A. (1995), Mapping Seismic Hazard in the Central and Eastern United States, *Seismological Research Letters*, *66*(4), 8–21, https://doi.org/10.1785/gssrl.66.4.8.

Giardini, D., G. Grünthal, K. M. Shedlock, and P. Zhang (1999), The GSHAP Global Seismic Hazard Map, *Annals of Geophysics*, *42*(6), https://doi.org/10.4401/ag-3784.

Grain, I. K. (1970), Computer interpolation and contouring of two-dimensional data: A review, *Geoexploration*, *8*(2), 71–86, https://doi.org/10.1016/0016-7142(70)90021-9.

Gutenberg, B., and C. F. Richter (1945), Frequency of earthquakes in California, *Nature*, *156*(3960), 371–371, https://doi.org/10.1038/156371a0.

Gvishiani, A. D., I. A. Vorobieva, P. N. Shebalin, B. A. Dzeboev, B. V. Dzeranov, and A. A. Skorkina (2022), Integrated Earthquake Catalog of the Eastern Sector of the Russian Arctic, *Applied Sciences*, *12*(10), 5010, https://doi.org/10.3390/app12105010.

Helmstetter, A., and M. J. Werner (2012), Adaptive Spatiotemporal Smoothing of Seismicity for Long-Term Earthquake Forecasts in California, *Bulletin of the Seismological Society of America*, *102*(6), 2518–2529, https://doi.org/10.1785/0120120062.

Kosobokov, V. G., and S. A. Mazhkenov (1992), On Similarity in the Spatial Distribution of Seismicity, in *Computational Seismology and Geodynamics*, pp. 6–15, American Geophysical Union, https://doi.org/10.1029/CS001p0006.

Main, I. (2000), Apparent Breaks in Scaling in the Earthquake Cumulative Frequency-Magnitude Distribution: Fact or Artifact?, *Bulletin of the Seismological Society of America*, *90*(1), 86–97, https://doi.org/10.1785/0119990086.

Medvedev, S., W. Sponheuer, and V. Kárník (1964), Neue seismische Skala Intensity scale of earthquakes, 7. Tagung der Europäischen Seismologischen Kommission vom 24.9. bis 30.9.1962, *Institut für Bodendynamik Und Erdbebenforschung in Jena*, *77*, 69–76.

Molchan, G., T. Kronrod, and G. F. Panza (1997), Multi-scale seismicity model for seismic risk, *Bulletin of the Seismological Society of America*, *87*(5), 1220–1229, https://doi.org/10.1785/BSSA0870051220.

Petersen, K., S. Vakkalanka, and L. Kuzniarz (2015), Guidelines for conducting systematic mapping studies in software engineering: An update, *Information and Software Technology*, *64*, 1–18, https://doi.org/10.1016/j.infsof.2015.03.007.

Pisarenko, V. F., and D. V. Pisarenko (2021), A Modified k-Nearest-Neighbors Method and Its Application to Estimation of Seismic Intensity, *Pure and Applied Geophysics*, *179*(11), 4025–4036, https://doi.org/10.1007/s00024-021-02717-y.

Riznichenko, Y. V. (1958), On the study of seismic regime, *Izv. Academy of Sciences of the USSR. Ser. geophysics*, (9), 1057–1074 (in Russian).

Riznichenko, Y. V. (1968), Energy model of seismic regime, *Izv. Academy of Sciences of the USSR. Ser. geophysics*, (5), 3–19 (in Russian).

Romanowicz, B. (1992), Strike-slip earthquakes on quasi-vertical transcurrent faults: Inferences for general scaling relations, *Geophysical Research Letters*, *19*(5), 481–484, https://doi.org/10.1029/92GL00265.

Sadovsky, M. A. (1979), Natural Lumpiness of Rocks, *Reports of Academy of Sciences*, *227*(4), 829–834 (in Russian).

Shebalin, P. N., C. Narteau, and S. V. Baranov (2020), Earthquake productivity law, *Geophysical Journal International*, *222*(2), 1264–1269, https://doi.org/10.1093/gji/ggaa252.

Shebalin, P. N., A. D. Gvishiani, B. A. Dzeboev, and A. A. Skorkina (2022), Why Are New Approaches to Seismic Hazard Assessment Required?, *Doklady Earth Sciences*, *507*(1), 930–935, https://doi.org/10.1134/s1028334x22700362.

Smith, W. H. F., and P. Wessel (1990), Gridding with continuous curvature splines in tension, *GEOPHYSICS*, *55*(3), 293–305, https://doi.org/10.1190/1.1442837.

Stirling, M., G. McVerry, M. Gerstenberger, N. Litchfield, R. V. Dissen, and other (2012), National Seismic Hazard Model for New Zealand: 2010 Update, *Bulletin of the Seismological Society of America*, *102*(4), 1514–1542, https://doi.org/10.1785/0120110170.

Stock, C. (2002), Adaptive Kernel Estimation and Continuous Probability Representation of Historical Earthquake Catalogs, *Bulletin of the Seismological Society of America*, *92*(3), 904–912, https://doi.org/10.1785/0120000233.

Ulomov, V. I., and The GSHAP Region Working Group (1999), Seismic hazard of Northern Eurasia, *Annals of Geophysics*, *42*(6), 1023–1038, https://doi.org/10.4401/ag-3785.

Vorobieva, I., C. Narteau, P. Shebalin, F. Beauducel, A. Nercessian, V. Clouard, and M.-P. Bouin (2013), Multiscale Mapping of Completeness Magnitude of Earthquake Catalogs, *Bulletin of the Seismological Society of America*, *103*(4), 2188–2202, https://doi.org/10.1785/0120120132.

Vorobieva, I. A., A. D. Gvishiani, B. A. Dzeboev, B. V. Dzeranov, Y. V. Barykina, and A. O. Antipova (2022), Nearest Neighbor Method for Discriminating Aftershocks and Duplicates When Merging Earthquake Catalogs, *Frontiers in Earth Science*, *10*, https://doi.org/10.3389/feart.2022.820277.

Wessel, P., J. F. Luis, L. Uieda, R. Scharroo, F. Wobbe, W. H. F. Smith, and D. Tian (2019), The Generic Mapping Tools Version 6, *Geochemistry, Geophysics, Geosystems*, *20*(11), 5556–5564, https://doi.org/10.1029/2019GC008515.

Wyss, M., and A. N. V. Kossobokov (2012), Errors in expected human losses due to incorrect seismic hazard estimates, *Natural Hazards*, *62*(3), 927–935, https://doi.org/10.1007/s11069-012-0125-5.

Zechar, J. D., M. C. Gerstenberger, and D. A. Rhoades (2010), Likelihood-Based Tests for Evaluating Space-Rate-Magnitude Earthquake Forecasts, *Bulletin of the Seismological Society of America*, *100*(3), 1184–1195, https://doi.org/10.1785/0120090192.

Russian Journal of Earth Sciences

Special Issue: "25th anniversary of the Russian Journal of Earth Sciences"

Current Issues Problems of Geoinformatics

I. N. Rozenberg[1], **S. K. Dulin**[2]

[1]Russian University of Transport (MIIT), Moscow, Russian Federation
[2]Institute of Informatics Problems, Federal Research Center "Computer Science and Control" of the Russian Academy of Sciences, Moscow, Russian Federation
* **Correspondence to:** Igor N. Rozenberg, i.rozenberg@geosc.ru

Abstract: Geoinformatics is a scientific discipline that focuses on natural, technical, and socio-economic spatial systems studied through computer modeling of localized objects and phenomena. The main goals of geoinformatics as a science are visualization, localization, and decision-making regarding spatial transformations of the environment. The structure of geoinformatics includes such sections as geosystem modeling, spatial analysis, and applied geoinformatics itself. The development of technologies for collecting, storing, converting and exchanging spatial and temporal data has led to the rapid development of GIS technologies and the emergence of a wide variety of industrial GIS aimed at processing geodata in order to make informed decisions. Currently, geoinformatics in many industries is perceived as a geoinformation industry, which implies the presence of its own equipment, the development of commercial software products such as GIS, a staff of experienced expert analysts and the organization of marketing. The paper highlights three of the most pressing problems faced by researchers in the field of geoinformatics over the past two decades: interoperability, digital transformation, and geodata fusion. The characteristic features of these problems and some aspects of their solution are considered.

Keywords: geoinformatics, GIS, geointeroperability, digital transformation, geodata fusion.

Citation: Rozenberg I. N., Dulin S. K. (2024), Current Issues Problems of Geoinformatics, *Russian Journal of Earth Sciences*, Vol. 24, ES1004, https://doi.org/10.2205/2024ES000893

1. Introduction

The current stage of geoinformatics development is characterized by solving three most pressing problems: ensuring geointeroperability, bringing informatization to the level of digital transformation, and synthesizing geodata [*Rozenberg and Dulin*, 2021]. A detailed review of these problems reveals that they are quite closely interrelated, and success in solving each of them has a significant impact on solving the rest. The ability to share geodata has been one of the main requirements since the development of the first GIS. Despite the fact that the past two decades have been very productive in terms of the development of geointeroperability, which facilitates the sharing of geographical data, geointeroperability has not yet become generally significant. Although the standards developed by ISO/TC 211 and the Open Geospatial Consortium (OGC) Inc. [*Open Geospatial Consortium*, 1999] provided the basis for its development, and in international organizations (Canadian Geospatial Data Infrastructure (CGDI), National Spatial Data Infrastructure (NSDI), Infrastructure for Spatial Information in Europe (INSPIRE), Global Spatial Data Infrastructure (GSDI) spatial data infrastructures emerged, geointeroperability is still in its early stages of implementation.

On the other hand, the Internet and the Web have developed tremendously over the past two decades. Currently, the Web is being upgraded to Semantic Web (or Web 3.0), evolving from Web documents to Web data, becoming an international open database.

Research Article

Received: 15 October 2023
Accepted: 15 January 2024
Published: 29 February 2024

2. Geointeroperability

The International Organization for Standardization ISO 19119 offers the following definition (https://www.iso.org/standard/53998.html): "Interoperability is the ability to connect, execute programs, or transmit data among various functional modules in a way that does not require the user to have knowledge of the characteristics of these modules."

For a geographical area, the following description of the term "geographic interoperability" applies (https://www.iso.org/standard/57465.html): "Geographical interoperability is the ability of information systems to 1) freely exchange all types of spatial information about the Earth and about objects and phenomena on, above and below the Earth's surface; and 2) share network software for managing such information."

It should be noted that this definition does not assume that each component uses the same data format (the coincidence of formats corresponds to the usually incorrect perception of interoperability by many people), but rather proclaims the ability to understand each other's format(s).

Semantic interoperability corresponds to human-level collaboration, and deals with the flow of work, the establishment of partnerships and collaborations, and the need to remove existing (national, local, organizational) barriers [*Dulin et al.*, 2014]. In other words, semantic interoperability becomes the ability of a collection of system components to (a) distribute information and (b) process it according to publicly available operational semantics in order to achieve a specific goal in a given context.

In the context of geoinformation, interoperability is directly related to GIS, which is the main environment for implementing geointeroperability.

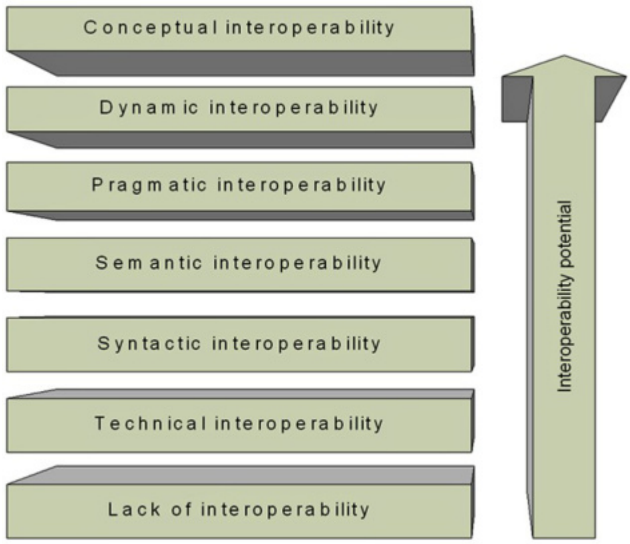

Figure 1. Interoperability levels.

Research in the field of geoinformatics points to the need to create interoperability models that can ensure that interoperability is established between systems in accordance with different goals and contexts [*Makarenko et al.*, 2019].

There are several approaches to the formation of GIS through interoperability models [*Makarenko et al.*, 2019]. Each approach has advantages and disadvantages in terms of achieving interoperability in a particular context. The main advantages of interoperability models are the ability to (a) define a common vocabulary that ensures consistency of semantics and analysis, (b) provide alternatives to suggestions regarding the structure of solutions, and finally (c) evaluate new ideas and add different options.

Examples of interoperability models that have been successfully applied in the GIS domain are – the Levels of Conceptual Interoperability Model (LCIM) and the Intermodel5. These models are mainly used at the highest levels of organizational interoperability out of the traditional seven levels: zero interoperability level, technical, syntactic, semantic, pragmatic, dynamic, and conceptual levels (Figure 1) [*Mohammad Saied et al.*, 2015].

3. Semantic Geointeroperability and Semantic Web

Geographic databases and user representations of real phenomena are characterized by high heterogeneity, which hinders effective geointeroperability. As a rule, heterogeneity is decomposed into four levels: system, syntactic, structural, and semantic.

Establishing semantic geointeroperability goes beyond simply being able to access geographic database information on a display or printed on paper. It requires more time, and the exact dictionary of geographical databases must be known in advance in order to get the relevant information [*Dulin et al.*, 2016].

Semantic interoperability is a key factor that allows interacting systems to understand data and process it based on this understanding. Interoperable systems represent components and tools in the lifecycle of product manufacturing and service delivery. Standards are one of the means to achieve semantic interoperability because they provide well-defined and consistent data requirements, although they are often so narrowly defined that they cannot provide the complete information model required for interoperability [*Gulyayev et al.*, 2012]. However, models related to standards can be easily integrated, providing a fairly broad domain model. The standards provide the necessary foundation for any interoperability. Creating intelligent infrastructures requires a more holistic exchange of information between different subject areas, which requires universal interoperability based on common semantic and ontological foundations with an unconditional availability of understanding.

Along with the problem of understanding in general, there is the problem of understanding the semantics of geodata [*Tarasov*, 2015].

Among the definitions of the concept of understanding for interoperability problems, the most appropriate is the following:: "Understanding (assimilation) – correlation, comparison of newly received information (text, image, speech, behavior, phenomenon, etc.) with already known, accumulated and structured information (i. e., basic knowledge) by means of cognitive structures, behavior patterns, concepts and categories of concepts; and its evaluation from certain positions, based on based on a certain sample, standard, norm, principle, etc. for example, the accumulated experience or circumstances in which the process of perception and understanding occurs, the features of the cognitive system/ cognitive style of a person" [*Tarasov*, 2015].

Misunderstanding is most often caused by the unfounded, non-obvious or lack of such a standard, and can also be caused by the emerging cognitive dissonance (in the terminology of information systems – a violation of the integrity of existing knowledge), as well as, in the case of the human understanding process, by subjective perception factors (unfavorable conditions for perception and understanding/assimilation of information). In the latter case, understanding may also occur with a delay rather than immediately, for example:

- after a certain period of time – there was time to "think" or favorable conditions were created for reflection;
- when conditions change – additional information was received, for example, certain events occurred, which supplemented, "pushed" previously misunderstood information, "put everything in its place".

Understanding (or more precisely, meaningful knowledge) makes it possible to perform actions with new objects based on already established skills and abilities; as well as reflect on the understood / learned information (knowledge), deduce various consequences from it.

Regarding the process of understanding (interpretation), we can formulate the following: the author (generator) expresses his subjective images or judgments in a formalized form (text, speech), and the interpreter restores this image or judgment in his own subjective context. This subjective context is determined by the subject's previous experience and the current circumstances in which the interpretation occurs. Thus, the language acts as a "universal ontology", which ensures the interoperability of subjects-native speakers (more precisely, users of the language).

For the generator, there is no (rather, it is invisible to it) problem of homonymy of words/terms (ambiguity of the word/term used), since it knows the meaning implied by it. But the interpreter faces such a problem and is forced to solve it either by relying on the context of the message, and if this does not help, then it is forced to use probabilistic (frequency) or fuzzy estimates (such as "the author probably meant the following" or "the author could have meant either this or that"'). The search for implicitly / vaguely expressed content occurs as a result of accessing knowledge relevant to this text (Figure 2).

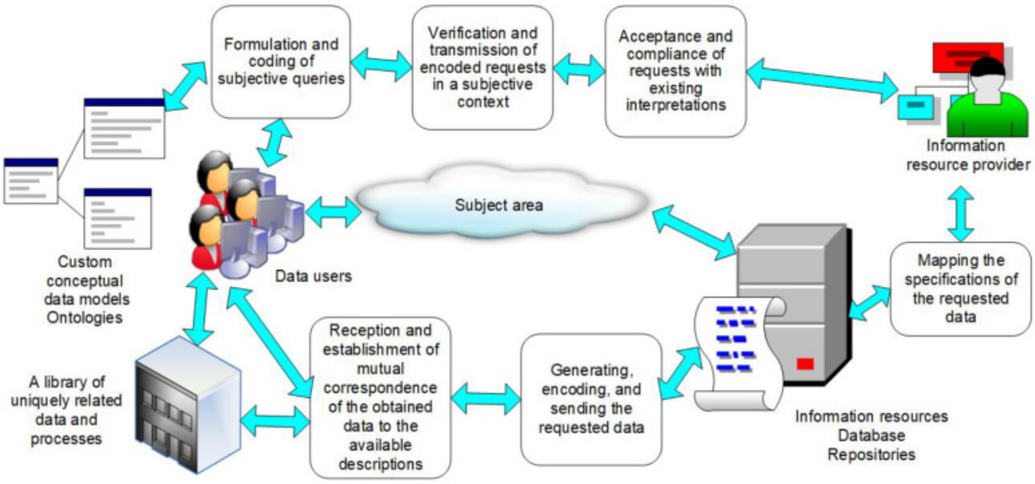

Figure 2. Structure of semantic interoperability.

Semiotic communication involves the participation of the sender and recipient of an information message, and in the process of communication, each of them acts as a generator or interpreter of the message.

Modeling semantics [*Dulin et al.*, 2016] is deeply embedded in the geointeroperability framework and thus provides a comprehensive description of semantic geointeroperability in general, which underlies the development of Semantic spatial data infrastructure and Semantic Web geospatial information.

Geointeroperability is the foundation for the development and implementation of Spatial Data Infrastructures (SDIs) [*Dulin et al.*, 2019]. The purpose of SDIs is to coordinate the useful exchange and sharing of geographic information using appropriate services.

In 2001 Berners-Lee the idea of Semantic Web was put forward. It was based on a proposal to modernize the Web from the document level to the data and information modeling level.

Semantic Web requires logical statements, classification of concepts, formal models, rules, and protocols of security and trust. The Semantic Web architecture has been described in detail in many publications. It is based on Uniform Resource Identifiers (URIs), Universal Character Set (Unicode), and eXtensible Markup Language (XML).

The idea of creating a geospatial Semantic Web was first introduced Egenhofer in 2002. It should expand the concept of Semantic Web, improving the semantic interoperability of geodata on the Web. But most importantly, establishing semantic geointeroperability requires that users and providers have a relevant understanding of the semantics of requests and responses. In the context of the Semantic Web, this feature is becoming more and more accessible.

During this time, efforts to standardize ISO / TC 211 and OGC and the development of geoinformatics provided a large part of the foundation for the creation of the geospatial Semantic Web. The international standards ISO / TC 211 have defined an ontology of geospatial concepts that are independent of applications. This ontology is the basis for describing geographic information, which includes concepts for describing geometry, topology, temporal information, spatial reference information systems, features, characteristics, behavior, relationships, quality, metadata, and services.

4. Aspects of digitalization

Currently, there is an intensification of digitization of geographic information and processing of digitized geographic information by GIS tools. Digital geodata, as experience shows, ensure the improvement of the activities of any company. However, most modern geodata are not interoperable: they are stored in isolated geodata databases, non-interoperable systems, and are used in restricted access programs. This makes it difficult to exchange geodata, and it is often impossible to analyze and interpret them.

Digitization, digitalization and digital transformation [*Hewlett Packard Enterprise*, 2023] – these are different processes that are used differently in different industries. However, in the field of IT, they usually mean the following:

- digitization means the transformation of some information resource from an analog representation to a digital one. For example, scanning manuscripts and storing them in an electronic library.
- digitalization means the introduction of a technological process in the field of technology and related software. The online shopping service on the Internet is an example of a digital business process that combines electronic purchase and delivery.
- digital transformation means that software-based processes are created that can evolve to increase the company's flexibility and competitiveness. The following definition can be given: "Digital transformation is the process of integrating digital technologies into all aspects of business activities, requiring fundamental changes in technology, culture, operations, and the principles of creating new products and services" [*Hewlett Packard Enterprise*, 2023].

When it comes to digital transformation, understanding the processes in the problem domain takes a significant amount of time and is much more difficult than simply adapting them to new digital technologies. In digital transformation, new solutions are being sought, as problems arise that are being solved with the help of new technologies. For example, a document is not just digitized, but processed and analyzed, and the question of whether a specific process is needed or whether it can be simplified using a new technology is studied.

Therefore, digital transformation is nothing more than solving problems with the best technical means. To a certain extent, this also applies to topics such as "agile design thinking", "brainstorming" and other creative ways of working, since they are necessary in order to expand the view of problems. You can solve them by technical means using new technologies only if you have an understanding of these problems.

Digitalization has led to the emergence of digital content. This content can be processed by digital processes, and new technologies will lead to the development of a digital business strategy. But digital transformation provides much more. Of course, digital content, digital processes, and a digital business model are essential, but digital transformation takes into account all aspects of production. Digital transformation is a work that needs to be carefully planned and takes a long time (3–5 years). Unlike digitalization, digital transformation does not just require enterprises to apply a large number of advanced technologies in their activities and cannot be completed in a single project.

The implementation of digital transformation development can be represented in the idea of three stages: I. Implementation of an information technology and service management system, II. Development and implementation of a service for analyzing the use, evaluation, and efficiency of digital technologies, III. Transition from a digital service to a service based on artificial intelligence, machine learning, and big data for managing digital technologies.

Complex GIS software can be roughly described as layers of spreadsheets containing data representing real geographical and spatial features, combined with tools for visualizing this data, as well as tools for manipulating data and creating new relationships and subsets of data. The Esri GIS system, in particular, supports three main views when working with geodata [*ESRI*, 2002] (Figure 3).

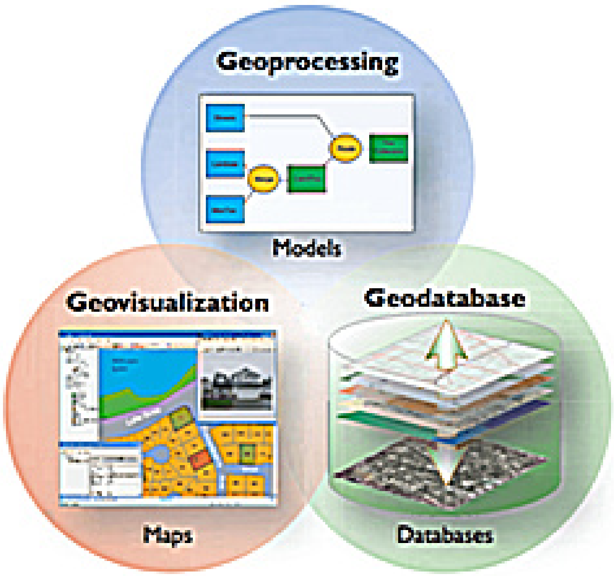

Figure 3. Three main views of geodata.

Geo data representation: GIS includes a BGA with geo data sets that contain geographical information in terms of supporting the general GIS data model (functions, rasters, topologies, networks, etc.).

Geovisualization View: GIS is a set of smart maps and other descriptions that show features of relationships between objects on the Earth's surface. Various map views of basic geographic information can be used as a "window to the geodata database" to support querying, analyzing, and editing information.

Geoprocessing View: GIS is a set of information transformation tools that form new sets of geodata from existing sets of geodata. These geoprocessing functions take information from existing geo sets, apply analytical functions, and place the results in new derived geo sets.

Since digital transformation involves the use of technologies to radically improve productivity, the digitization of all three representations should provide an appropriate level of software technology. Digital transformation means that we have managed to introduce a technology that starts completely new processes, and not just a new way of processing geodata [*Naseer et al.*, 2015].

Digital transformations have a significant impact on how specialists using geo-resources interact with each other within the existing geointeroperability, which is a key condition for implementing digital transformation [*Rozenberg et al.*, 2021].

Implementation of digital transformation of geodata provides at least four benefits: reduces the cost of maintaining the structure and consistency of geodata, improves the accuracy and adequacy of generated queries, increases the speed of executed transactions, and makes working with geodata more meaningful and efficient.

Digital transformation of geodata, which is possible only in the presence of semantic geointeroperability, requires preliminary digitalization of all geoinformation resources, which is complicated by the inherent heterogeneity of geodata. This requires accurate and up-to-date geodata about the location of spatial features, their properties and characteristics, their movement or change over time, and their interaction with other features. In other words, we are not talking about expanding attribute data, but about creating a spatial basis for digital transformation. The geographic information solutions obtained on this basis will allow both to organize and organize various information flows, as well as receive independent timely analytical reports on various spatial features and events taking place on the map [*Rozenberg et al.*, 2022].

Digitized geodata can be obtained as a result of using modern technical means of satellite scanning, sensing and positioning, or using aviation means of aerial photography of the earth's surface. Photogrammetry and mobile laser scanning make a significant contribution to the formation of geocontent [*Ruiz et al.*, 2011].

5. Geodata fusion

Fusion of spatial data from various sources available on the Web is the main task for modern applications that use information search on the web and are aimed at making decisions based on geodata [*Stankute and Asche*, 2012].

The rapid development of the Web from a data-driven variant to structures for serving a wide range of queries, along with the widespread adoption of mobile location-based devices, has greatly affected the understanding, availability, and use of geodata. As a result, the number of geodata available through the network is continuously increasing. Successful analysis of geodata sets requires methods for establishing relationships and combining geodata obtained from a variety of sources. It is becoming clear that once web services provide the fusion of spatial information from an arbitrary number of geodata sources, there will be a much greater processing potential than today's Spatial Data Infrastructures (SDIs)provide [*Dulin et al.*, 2019], which act only as spatial data delivery platforms available over the network. Spatial data fusion techniques play an important role in creating an integrated representation of distributed spatial data sources in the network. Since flexibility and interoperability are key factors in such geo-data integration, the use of standards is an indisputable requirement. Therefore, in addition to the geospatial standards established by the Open Geospatial Consortium (OGC) [*Percivall*, 2013], semantic web standards published by the World Wide Web Consortium (W3C) regarding related geodata [*Percivall*, 2023], are a good addition for formalizing and managing relationships between object characteristics as part of the fusion process. Although the SDIs and Semantic Web architectures are very different in terms of the applied technological processes and standards, they can complement each other.

The term “Data Fusion” is widely used in the field of electronic data processing and includes many different definitions and classifications. In 2010, when studying standards, information data fusion was defined as [*Stankute and Asche*, 2012] “the act or process of combining or combining data or information relating to one or more objects that are considered in an explicit or implicit knowledge structure in order to improve the ability (or reveal a new opportunity) to detect, identify, or characterize the objects in question.” Although research was initially focused on solving military intelligence tasks, synthetic decision-making has proven to be applicable in business, urban planning, and many other applied areas.

Open standards-based interoperability radically changes the role of data fusion in classical application domains, creating new ways to identify relationships in small-structure data.

In this paper, spatial data fusion is considered in relation to a variety of sources to extract meaningful information related to a particular application context. Therefore, understanding the geodata fusion proposed here includes what others describe as a fusion [*Huang et al.*, 2023], geo data integration [*Al-Bakri and Fairbairn*, 2012] or geo data concatenation [*López-Vázquez and Manso Callejo*, 2013].

Many fusion processes can be implemented in a closed architecture with a single software and hardware provider. However, without the use of open standards, many geodata and services are difficult to automate and scale. Standardized data, applications, and services provide an automated and interoperable geodata fusion environment, supporting secure geo sharing and transparent reuse of services for processing large volumes of geodata and unpredictable analytical queries.

Some elements of the preferred open structure of geographic information fusion based on geostandards are already being distributed to users. For example, Web Map Service [*Randall*, 2014] (WMS) provides map fusion. WMS presents maps as illustrated layers of images obtained from various sources in order to use the geographical overlay to create aggregated maps that meet the needs of users (Figure 4).

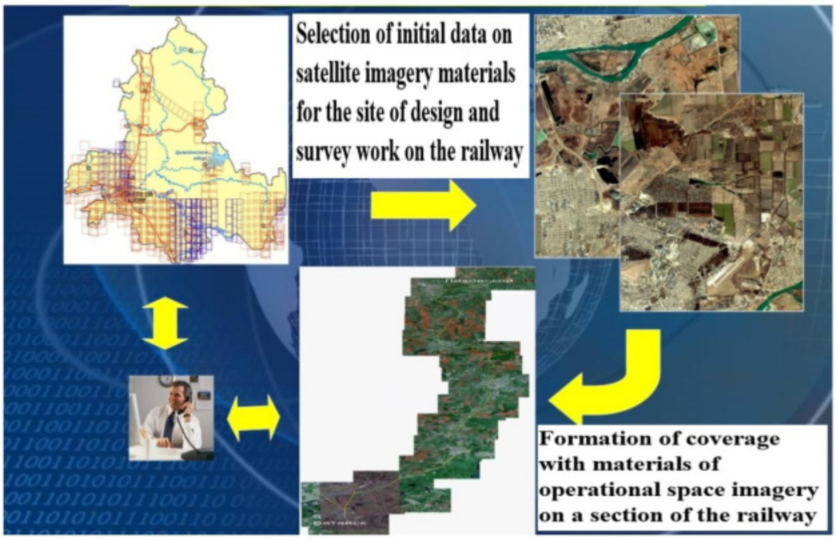

Figure 4. An example of geographic information fusion based on WMS the standard OGC. The map image is represented by sequentially generated levels of geospatial information synthesized into a single visualization.

In the study of geodata fusion, it is customary to consider three categories: comparison of observations and measurements (Observation Fusion); comparison of phenomena (Feature Fusion) and fusion of solutions (Decision Fusion) [*Ciuonzo and Salvo Rossi*, 2014].

As a result of the fusion of observations, multiple sensor measurements of the same phenomena are combined into a combined observation. Processes mappings thus, a combination of different sensor measurements is formed in the form of a well-described observation, while taking into account the inherent uncertainties of this process (for example, analyzing the client's signature or recognizing his face from different angles).

Basic requirements for mappings observations and sensor measurements include [*Ciuonzo and Salvo Rossi*, 2014]:

1. Build a system of sensors, necessary observations, and surveillance processes that meet the needs of users.
2. Determination of sensor capabilities and measurement quality.
3. Availability of sensor parameters that allow you to automatically determine the location of observations.
4. Determination of real-time observations in standard encodings, including encoding of measurement uncertainty, and parameters required for processing measurements.
5. Configure sensors to make observations of interest.
6. Generate and publish alerts that will be issued by sensors or sensor services based on certain criteria.
7. Object identification and classification.
8. Enabling it mappings observations and measurements provide access to the processing mechanisms and necessary information about the object.

Information for performing fusion can be obtained from both sensor observations and from people. Information as a result of observation can serve as input to processes mappings observations and dimensions, or it can be used to identify recognized objects whose characteristics are processed as input to the fusion process. Standards for mappings, observations and measurements have been used for a long time and have proven their viability.

Comparison of phenomena involves processing observations at a higher level of semantic properties of phenomena. This improves the understanding of the operational situation and clarifies the assessment of potential threats and impacts, allowing you to more correctly identify, classify, link and combine objects of interest. The processes of comparing phenomena include their generalization and aggregation. Aggregation technology includes useful options that allow you to work with imperfect, heterogeneous, contradictory, and duplicated geodata.

Service-oriented architecture (SOA) [*Naseer et al.*, 2015] it is well suited for supporting distributed services of phenomenon aggregation rules. Comparison of phenomena allows you to work with more powerful, flexible and accurate information resources than with those obtained from original sources.

Recommendations for comparing phenomena should be taken into account:

- To achieve a level of semantic interoperability, user profiles must be taken into account when processing geodata.
- Designing user profiles is a task that concerns not only the selection of appropriate input and output type definitions, but also the selection of appropriate classifications.
- Metadata in user profiles is required for registering in directories OGC, to quickly find and establish links with standardized structures.

Decision fusion initiates processes that support a person's ability to make a decision, providing an interoperable network service environment for situation assessment and decision support, using information from various sensors and information already processed.

Solution Fusion provides analysts with an environment where they can access interoperable tools using a single client interface to find, process, and use different types of data from different sensors and databases. Decision fusion involves the use of information from corporate geocommunities, which allows you to assess the overall situation and take advantage of the overall operational situation. Therefore, we can say that the information available for decision fusion is a collection of information from intellectual corporate capital. Sources of such information are people, documents, equipment, or technical sensors.

This information can be grouped as follows:

- Information received from people.
- Geospatial information accumulated in the form of geo resources.
- Information in the form of sensor signals.
- Information in the form of measurement data for various parameters.
- Information about open access geodata in any format.
- Information about scientific and technical intelligence geodata.

The development of decision fusion requires the development of standards for structured information, such as schema mapping methods with appropriate identification of mapping rules, and an increased emphasis on association processing, since the identification of associations between objects is at the heart of fusion. The most efficient environment for implementing these categories of fusion is an architecture with distributed databases and services based on a common core of geodata formats, algorithms, and applications [*Naseer et al.*, 2015].

Figure 5 shows an example of decision fusion that involves analyzing flood trends and causes in the Kargasok city area based on geodata from multiple sources. The decision fusion carried out in this study is a large-scale operation that includes both geodata received from a person from a mobile device, and geodata of the general situation from the center of the Ministry of Emergency Situations.

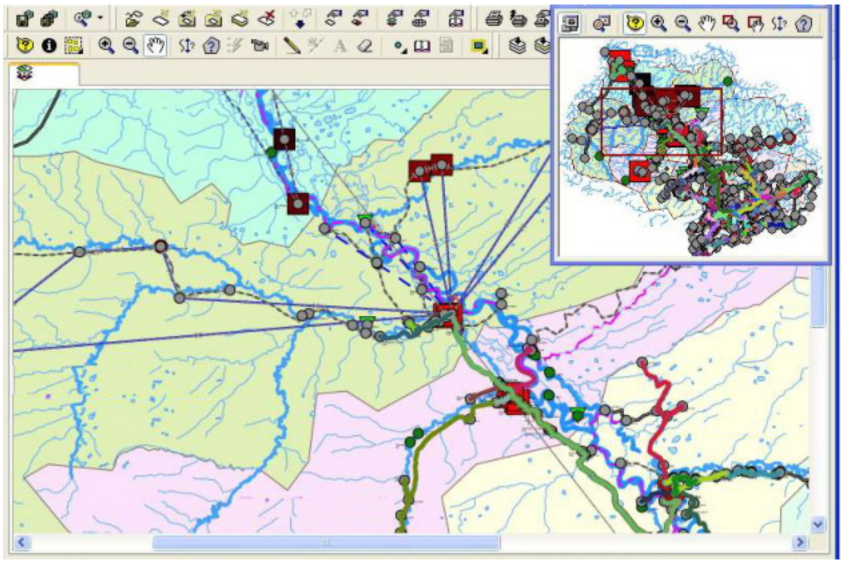

Figure 5. Fusion of solutions based on switching geodata from various sources.

6. Conclusion

Increasing requirements for joint processing of spatial data for various applications have revealed an urgent need for GIS scalability with supported geointeroperability.

To achieve semantic geointeroperability, it is necessary to develop both a geo-description matching system and a set of related services to ensure an efficient bidirectional communication process, where the user and the geodata provider interact through requests and responses, understanding each other through their knowledge and reasoning processes.

Digital geodata ensure the improvement of any company's operations. This period is marked by a large-scale digital transformation, and here we should note the need for geointeroperability to conduct digital transformation of geodata and the leading role of GIS in providing users with access to digitized geo-resources and in the process of integrating digital technologies.

Fusion of spatial data from various sources available in Web, is the main task for modern applications that use information search in the network and are aimed at making decisions based on geodata. Geodata fusion in distributed information environments with open standards-based interoperability radically changes the classical areas of data fusion, offering completely new ways to represent relationships.

References

Al-Bakri, M., and D. Fairbairn (2012), Assessing similarity matching for possible integration of feature classifications of geospatial data from official and informal sources, *International Journal of Geographical Information Science*, *26*(8), 1437–1456, https://doi.org/10.1080/13658816.2011.636012.

Ciuonzo, D., and P. Salvo Rossi (2014), Decision Fusion With Unknown Sensor Detection Probability, *IEEE Signal Processing Letters*, *21*(2), 208–212, https://doi.org/10.1109/LSP.2013.2295054.

Dulin, S. K., N. G. Dulina, and P. V. Yermakov (2014), Intellectualization of access to geodata based on semantic geointeroperability, *Journal Information-measuring and Control Systems*, *12*(8), 41–47 (in Russian).

Dulin, S. K., N. G. Dulina, and D. A. Nikishin (2016), Problems of maintenance of semantic geointeroperability and coordination of understanding of geodata semantics, *Systems and Means of Informatics*, *26*(1), 86–108, https://doi.org/10.14357/08696527160107 (in Russian).

Dulin, S. K., N. G. Dulina, and O. S. Kozhunova (2019), Synthesis of geodata in spatial infrastructures based on related data, *Informatics and Applications*, *13*(1), 82–90, https://doi.org/10.14357/19922264190112 (in Russian).

ESRI (2002), *Geodatabase Workbook. GIS by ESRI*, ESRI, USA.

Gulyayev, Y. V., E. E. Zhuravlev, and A. Y. Oleynikov (2012), Standardization methodology to ensure the interoperability of information systems of a wide class, *Journal of Radioelectronics*, *3*, 1–40 (in Russian).

Hewlett Packard Enterprise (2023), What is digital transformation?, https://www.hpe.com/emea_europe/en/what-is/digital-transformation.html, (accessed September, 2023).

Huang, Z., S. Sun, J. Zhao, and L. Mao (2023), Multi-modal policy fusion for end-to-end autonomous driving, *Information Fusion*, *98*, 101,834, https://doi.org/10.1016/j.inffus.2023.101834.

López-Vázquez, C., and M. A. Manso Callejo (2013), Point- and curve-based geometric conflation, *International Journal of Geographical Information Science*, *27*(1), 192–207, https://doi.org/10.1080/13658816.2012.677537.

Makarenko, S. I., A. Y. Oleynikov, and T. E. Chernitskaya (2019), Models of interoperability of information systems, *Control systems, communications and security*, *4*, 215–245, https://doi.org/10.24411/2410-9916-2019-10408 (in Russian).

Mohammad Saied, A., A. Abdel-Hamid, and Y. El-Sonbaty (2015), An Interoperability Framework for Identity Federation in Multi-Clouds, *International journal of Computer Networks & Communications*, *7*(5), 67–82, https://doi.org/10.5121/ijcnc.2015.7506.

Naseer, A., H. I. Aldoobi, and B. Y. Alkazemi (2015), A Service-oriented Architecture for GIS Applications, in *Proceedings of the 10th International Conference on Software Paradigm Trends*, pp. 151–155, SCITEPRESS - Science and Technology Publications, https://doi.org/10.5220/0005556501510155.

Open Geospatial Consortium (1999), OGC Standards, http://www.opengeospatial.org/standards/, (accessed September, 2023).

Percivall, G. (2013), Geodata fusion study by the Open Geospatial Consortium, in *Geospatial InfoFusion III*, edited by M. F. Pellechia, R. J. Sorensen, and K. Palaniappan, SPIE, https://doi.org/10.1117/12.2016226.

Percivall, G. (2023), Fusion Standards Study, Part 2: Decision Fusion, https://www.ogc.org/initiatives/fusion-2/, (accessed September, 2023).

Randall, A. (2014), Web Map Service (WMS) Introductionfor Science On a Sphere, https://sos.noaa.gov/media/downloads/wms_tutorial.pdf, (accessed September, 2023).

Rozenberg, I. N., and S. K. Dulin (2021), Development of geoinformation technologies, *Automation*, *Communications*, *Informatics*, *11*, 12–17, https://doi.org/10.34649/AT.2021.11.11.004 (in Russian).

Rozenberg, I. N., S. K. Dulin, and N. G. Dulina (2021), Interoperability as a key condition for the implementation of digital transformation, *Systems and Means of Informatics*, *31*(3), 49–60, https://doi.org/10.14357/08696527210304 (in Russian).

Rozenberg, I. N., S. K. Dulin, and N. G. Dulina (2022), Geographic information system is a tool for digital transformation of geodata, *Systems and Means of Informatics*, *32*(1), 46–54, https://doi.org/10.14357/08696527220104 (in Russian).

Ruiz, J. J., F. J. Ariza, M. A. Ureña, and E. B. Blázquez (2011), Digital map conflation: a review of the process and a proposal for classification, *International Journal of Geographical Information Science*, *25*(9), 1439–1466, https://doi.org/10.1080/13658816.2010.519707.

Stankute, S., and H. Asche (2012), A Data Fusion System for Spatial Data Mining, Analysis and Improvement, in *Lecture Notes in Computer Science*, pp. 439–449, Springer Berlin Heidelberg, https://doi.org/10.1007/978-3-642-31075-1_33.

Tarasov, V. B. (2015), The problem of understanding: the present and the future of artificial intelligence, *Open Semantic Technologies for Intelligent Systems (OSTIS-2015)*, *5*, 25–42 (in Russian).

R of J E S

Russian Journal of Earth Sciences

Special Issue: “25th anniversary of the Russian Journal of Earth Sciences”

Информационное обеспечение геомеханических расчетов устойчивости подработанного породного массива со сложным тектоническим строением

А. А. Барях*[,1], И. А. Санфиров[1], М. В. Дьяконов[2], С. Ю. Лобанов[1], А. И. Никифорова[1]

[1]Горный институт УрО РАН, г. Пермь, Россия
[2]ПАО «Уралкалий», г. Березники, Россия
* **Контакт:** Александр Абрамович Барях, bar@mi-perm.ru

На примере Тюбегатанского месторождения калийных солей (Узбекистан) рассмотрен комплекс геофизического и геомеханического обеспечения безопасности горных работ в условиях сложного тектонического строения подработанного породного массива. Геофизические исследования включали наземные сейсморазведочные наблюдения по системе профилей в сочетании с «легкими» стандартными методами электро- и гравиразведки. По результатам этих работ производилось построение физико-геологической модели участков месторождения с локализацией ослабленных зон и разрывных нарушений. В рамках содержательной интерпретации физико-геологическая модель трансформировалась в геомеханическую расчетную схему, которая отражала основные горно-геологические и горнотехнические условия разработки и базировалась на модели упругопластического деформирования соляных пород. Калибровка геомеханической модели производилась по результатам радарной интерферометрической съемки. Фактор времени учитывался в соответствии с разработанной модификацией известного метода переменных модулей деформации. Формирование зон пластичности в физическом выражении отождествлялось с образованием областей трещиноватости в водозащитной толще, определяющих опасность нарушения ее сплошности. Численная реализация геомеханической модели методом конечных элементов позволила обосновать оптимальные параметры камерной системы разработки, обеспечивающие сохранность водозащитной толщи, включая и зоны разрывных нарушений.

Ключевые слова: калийные месторождения, водозащитная толща, тектоника, разрывные нарушения, геофизические исследования, геомеханика, математическое моделирование, численная реализация.

Цитирование: Барях А. А., Санфиров И. А., Дьяконов М. В., Лобанов С. Ю., Никифорова А. И. Информационное обеспечение геомеханических расчетов устойчивости подработанного породного массива со сложным тектоническим строением // Russian Journal of Earth Sciences. — 2024. — Т. 24. — ES1012. — DOI: 10.2205/2024es000894

Получено: 15 октября 2023 г.
Принято: 15 января 2024 г.
Опубликовано: 29 февраля 2024 г.

Введение

В современных условиях глобального дефицита продовольствия активизируется разработка месторождений калийных руд в сложных горно-геологических условиях [*Рыльникова и др.*, 2023; *Pumjan et al.*, 2022; *Rauche*, 2015]. Для подобного типа месторождений общеизвестны повышенные риски, связанные с геологическим строением водоупорных пород, перекрывающих продуктивную толщу, и опасностью прорыва пресных вод в горные выработки [*Барях и Евсеев*, 2019; *Рудковский и др.*, 2011; *Gendzwill and Brehm*, 1993; *Prugger and Prugger*, 1991]. В этой связи особую значимость при разработке месторождений минеральных солей приобретает геомеханическая оценка влияния горных работ на сохранность водозащитных толщ (ВЗТ), отделяющих водоносные горизонты от выработанного пространства.

Традиционно в качестве информационного обеспечения геомеханических расчетов, основанных на современных численных методах математического моделирования [*Барях и др.*, 2017; *Беляков и Беликов*, 2022; *Karasev et al.*, 2022] и критериях разрушения [*Baryakh and Tsayukov*, 2022; *The ISRM Suggested Methods for Rock Characterization, Testing and Monitoring: 2007-2014*, 2015; *You*, 2011], используются: данные о физико-механических свойствах горных пород, пространственные физико-геологические модели разрабатываемых участков шахтных полей, параметры ведения горных работ, результаты инструментальных измерений деформаций в горных выработках и оседаний земной поверхности. Из всех перечисленных составляющих наиболее неустойчивой в плане достоверности является физико-геологическая модель.

В простых горно-геологических условиях, без значимой латеральной изменчивости строения и свойств породного массива, модельные построения теоретически могут базироваться только на результатах геологоразведочного бурения. Общемировая практика эксплуатации месторождений водорастворимых полезных ископаемых [*Барях и др.*, 2009] показывает, что подобная ситуация наблюдается крайне редко. Необходимой является повышенная пространственная дискретизация опробования структурно-физических параметров разрабатываемого интервала породного массива. С этой целью применяются различные геофизические исследования, обычно в виде определенного комплекса методов. Содержание комплекса определяется особенностями строения объекта изучения. Для месторождений минеральных солей пластового типа наибольшее распространение получили сейсмо-, электро- и гравиразведка. В качестве параметрического обеспечения интерпретационных заключений по данным наземных наблюдений выполняются и скважинные геофизические исследования [*Болгаров и Рослов*, 2009; *Глебов*, 2004; *Nolet*, 2008; *Yilmaz*, 2008].

На крупнейшем в Европе Верхнекамском месторождении калийных и магниевых солей для информационного обеспечения геомеханических расчетов применяется сейсморазведка на отраженных волнах с привлечением интерференционных систем регистрации по методике многократных перекрытий [*Барях и др.*, 2017].

Подобное методическое решение обусловлено благоприятными сейсмогеологическими условиями, заключающимися в адекватности слоистой квазипараллельной модели реальным средам и подходящих для проведения наземных сейсморазведочных наблюдений поверхностных условиях. Наличие аналогичных условий определило ведущую роль сейсморазведочных наблюдений и на крупнейшем в мире Саскачеванском месторождении (Канада) [*Gendzwill and Stead*, 1992; *Halabura (Steve) and Hardy*, 2007].

Благоприятное сочетание физико-геологических свойств объекта изучения и условий для проведения сейсморазведочных исследований характерно не всем месторождениям калийно-магниевых руд. В случае их залегания в условиях горного рельефа необходимая плотность сейсморазведочных наблюдений не всегда достижима и возможности требуемой детализации физико-геологической модели разрабатываемой толщи в пределах всего месторождения весьма ограничены. В подобных случаях возможно районирование территории месторождения на основе сочетания более «легких» методов с сейсморазведочными исследованиями. На основании результатов районирования производится детализация наиболее неблагоприятных участков с разработкой по сейсморазведочным данным типовых физико-геологических моделей основных геологических «опасностей».

В качестве «легких» методов возможно применение стандартных электро- и гравиразведочных технологических решений. Например, вертикальное электрическое зондирование и однократные гравиметрические наблюдения.

Реализация комплекса информационного обеспечения геомеханических оценок опасности нарушения сплошности водозащитных толщ в условиях сложного тектонического строения иллюстрируется на примере Тюбегатанского месторождения калийных солей.

1. Общая характеристика Тюбегатанского месторождения и условий его отработки

Тюбегатанское месторождение калийных солей находится на границе Республики Узбекистан (Кашкадарьинская область) и Республики Туркменистан (Чарджоуская область) и разделяется пограничной рекой Шордарья на две части. Месторождение расположено в юго-западных отрогах Гиссарского хребта, являющегося юго-западным ответвлением Тянь-Шаньской горной системы. Максимальные высотные отметки гряды в северной части структуры — 1443 м (г. Тюбегатан), а на юге — 1325 м (г. Карачгат). Относительные превышения горных вершин над дном продольных долин достигают 300–400 м. Склоны гряд изрезаны сетью поперечных ущелий.

В геоморфологическом отношении в пределах Тюбегатанского месторождения калийных солей развит куэстовый рельеф с асимметричным строением: пологими западными и крутыми восточными склонами. В нижней части таких куэстовых площадок развиты глубоко врезанные саи овражистого типа, которые являются водосборниками пресных вод со всей территории Тюбегатанской возвышенности (рис. 1).

В геологическом строении месторождения принимают участие осадочные породы юрской, меловой, неогеновой и четвертичной систем [*Поздеев и др.*, 2010] (рис. 2).

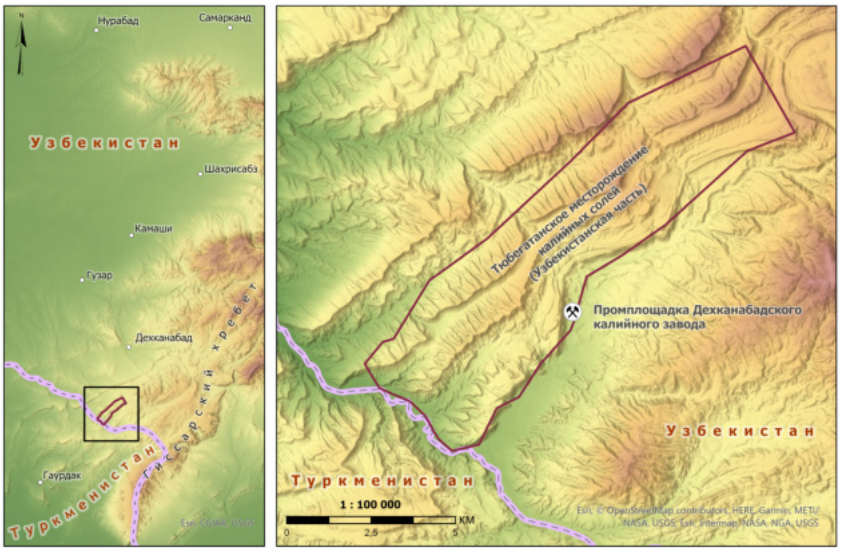

Рис. 1. Обзорная карта Тюбегатанского месторождения калийных солей.

Узбекская часть Тюбегатанского месторождения приурочена к Тюбегатанской брахиантиклинали Гаурдак-Тюбегатанской антиклинальной зоны (рис. 3) и характеризуется крайне сложным тектоническим строением.

Разработка Тюбегатанского месторождения на территории Республики Узбекистан начата в 2010 году (рис. 4). Участок первоочередной отработки расположен в северной части и представляет собой многоугольник, вытянутый в северном направлении на 3 км при ширине до 1,8 км.

Как и на большинстве калийных и соляных месторождений здесь применяется камерная система разработки с поддержанием вышележащей толщи на ленточных междукамерных целиках. Очистные работы ведутся по двум сильвинитовым пластам: Нижний IIа (ширина камер $a = 5{,}5$ м, ширина целиков $b = 3$ м, вынимаемая мощность $m = 5$ м) и Нижний IIб (ширина камер $a = 5{,}5$ м, ширина целиков $b = 3$ м, вынимаемая мощность $m = 3{,}1$ м). Промышленные пласты характеризуются пологим залеганием с углом падения на северо-запад 10–15°. Порядок движения фронта горных работ — обратный: от юго-восточной границы в северо-западном направлении. На настоящий

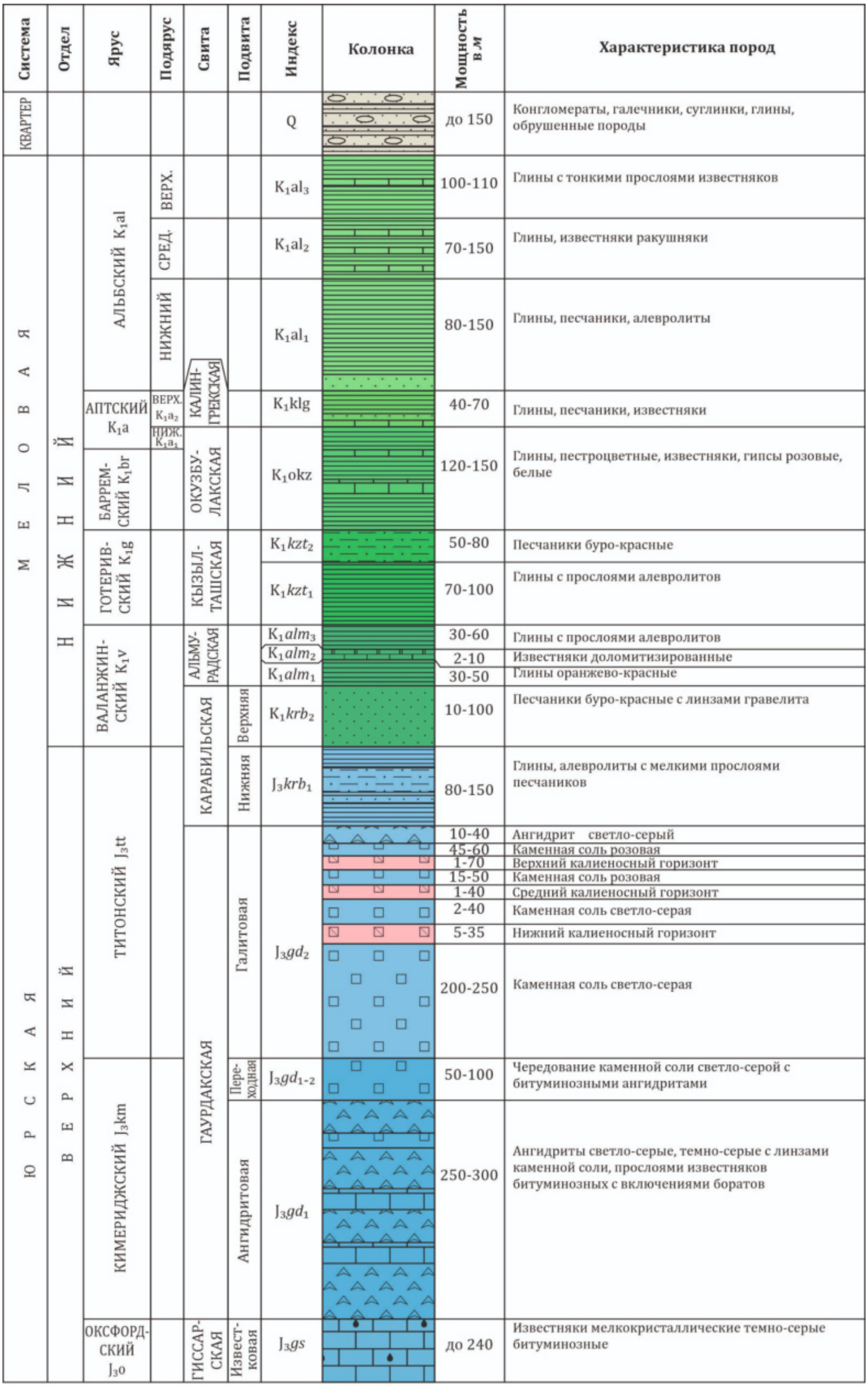

Рис. 2. Стратиграфическая колонка района Тюбегатанского месторождения калийных солей.

момент времени состояние горных выработок на участке первоочередной отработки оценивается как неудовлетворительное: камеры «задавлены» обрушенными породами.

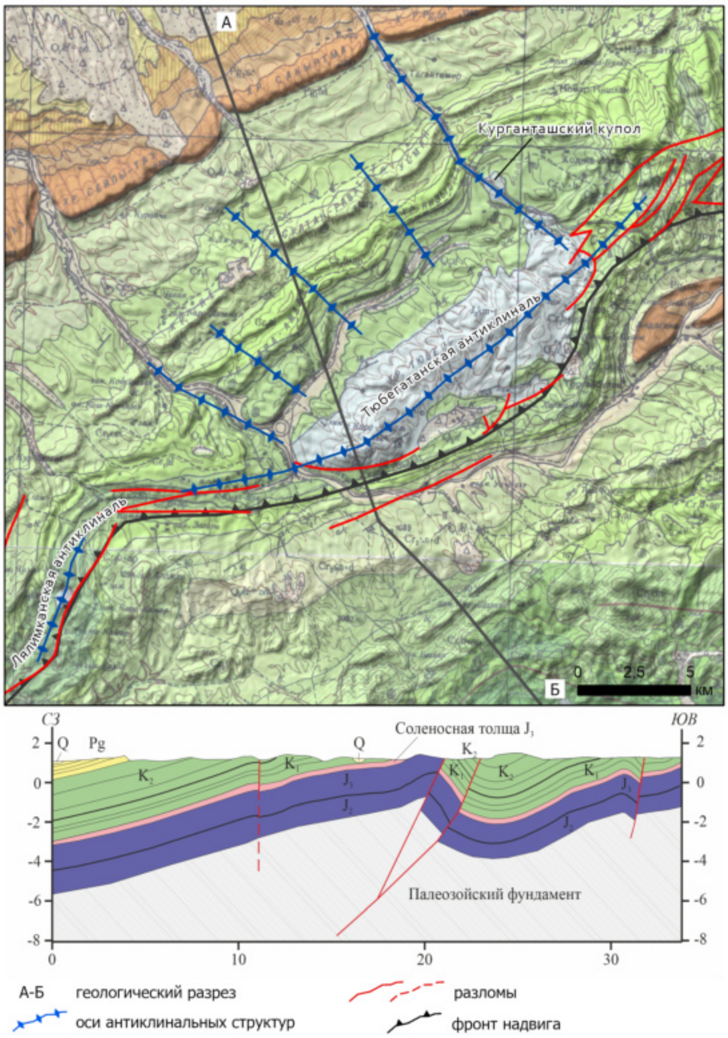

Рис. 3. Геологическая карта района Тюбегатанской антиклинали с элементами тектоники.

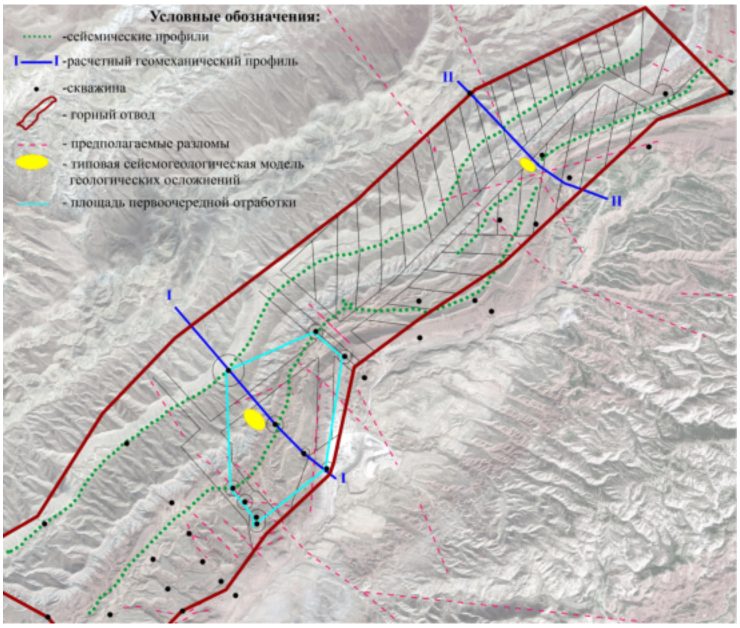

Рис. 4. Схема шахтного поля Дехканабадского калийного завода.

2. Комплексные геофизические исследования

В рамках параметрического обеспечения геомеханических расчетов выполнены площадные гравиразведочные и профильные сейсмо- и электроразведочные исследования.

По совокупности негативных изменений геофизических параметров в пределах горного отвода Тюбегатанского месторождения наиболее достоверно выделяются три участка (рис. 5):

1. на северо-востоке — зоны 1 и 2 сейсморазведочных аномалий, которые характеризуются пониженными значениями скорости и плотности, а также удельного электрического сопротивления;
2. в центре на участке первоочередной отработки — зона 4 сейсморазведочных аномалий с аналогичными признаками по негативным изменениям всех трех составляющих;
3. на юго-западе площади работ, где отмечается снижение значений упругих параметров при противоречивом поведении электрометрических показателей от незначительного понижения к преобладающему повышению значений.

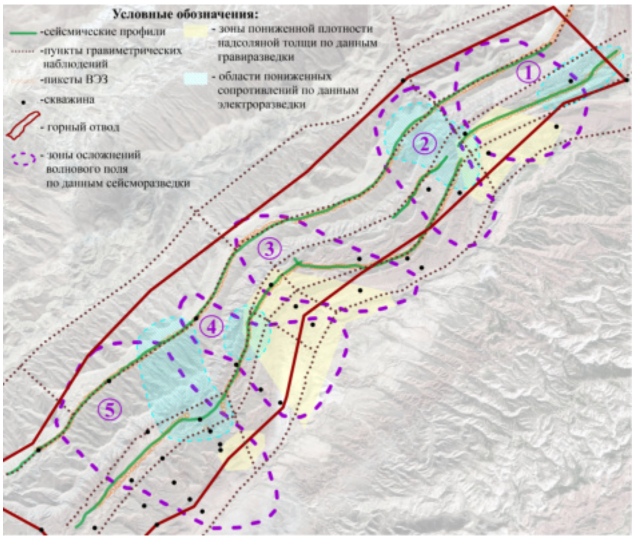

Рис. 5. Схема комплексных результатов геофизических исследований.

Подобные сочетания рассматриваемых геофизических параметров позволяют предположить понижение прочностных свойств в целом для надсоляной и соляной толщ на всех трех участках, при этом на первых двух имеет место реализация негативных гидрогеологических процессов, а для третьего пока нет. Геологическая природа данных зон связана с зонами наиболее активного проявления подземного выщелачивания, расслоения и обрушения. Наиболее наглядно они проявляются на результатах цифровой обработки сейсморазведочных данных (рис. 6).

На временных разрезах отмечается ряд наиболее динамически выраженных осей синфазности, которые соответствуют целевым сейсмическим отражающим горизонтам (ОГ), относящимся к конкретным границам.

Согласно геологической модели месторождения и установленному скоростному закону по результатам сейсмических скважинных исследований, основные отражающие горизонты, выделяемые на временных разрезах, имеют следующую геологическую привязку: ОГ Krb — кровля Карабильской свиты (K_1krb_2); ОГ BC — кровля солей Гаурдакской свиты (J_3gd_2); ОГ H2 — кровля продуктивного пласта Нижний II.

При цифровой обработке оцениваются следующие параметры волнового поля:

1. структура волновой картины, представленная на временном разрезе по общей глубинной точке (рис. 6, а);

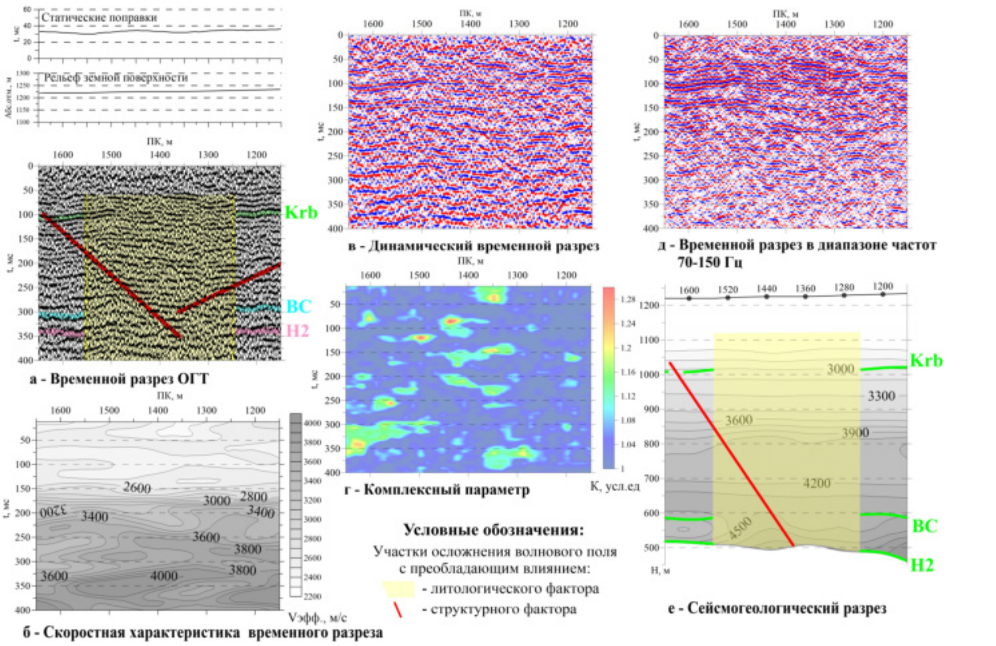

Рис. 6. Результаты цифровой обработки.

2. кинематическая составляющая, оцениваемая по скоростной характеристике (рис. 6, б), представляющей распределение эффективных скоростей во временной области;
3. интенсивность, оцениваемая по динамическому временному разрезу и его модификациям в частотном (рис. 6, в) и высокочастотном (рис. 6, д) диапазонах обработки.

По нарушениям структуры волновой картины, снижению интенсивности и значениям скоростной характеристики на профильных линиях выделяются участки осложнений волнового поля. При их локализации учитывалась согласованность негативных изменений анализируемых сейсмических параметров, представленная на разрезах комплексного параметра (рис. 6, г). Расчет его значений основан на совместном использовании независимых количественных характеристик волнового поля: частота, эффективная скорость, амплитуда, отношение сигнал/помеха. Функции, описывающие поведение указанных характеристик вдоль профиля, преобразуют в промежуточные величины, принимающие значение 0 или 1. Промежуточной функции присваивают 0, если на данном пикете исходная функция не выходит за доверительный интервал, и 1 — если выходит. «Комплексный параметр» представляет собой нормированную сумму промежуточных результатов [*Санфиров и др.*, 2013].

В итоге формируется количественная оценка негативных изменений упругих и структурных параметров исследуемого интервала геологического разреза (рис. 6, е), учитываемая при геомеханических расчетах.

В качестве типовых сейсмогеологических моделей для оценки геомеханических рисков выбраны участки в пределах зон № 1 и № 2 (рис. 5), где отмечаются наиболее контрастные негативные изменения геофизических параметров. Выделенные типовые геофизические аномалии представляют собой ослабленные по механическим свойствам зоны, которые могут быть связаны с тектоническими разрывными нарушениями.

3. Геомеханическая оценка и прогноз состояния водозащитной толщи

По результатам геофизических исследований с учетом данных бурения геологоразведочных скважин построены характерные для месторождения физико-геологические модели, которые трансформированы в геомеханические расчетные схемы по двум разрезам: I-I и II-II. Их положение показано на рис. 4. Профиль I-I пересекает участок первоочередной отработки, профиль II-II приурочен к площади перспективной выемки запасов. Отметим, что сейсморазведочная аномалия, расположенная в пределах профиля I-I, представлена ослабленной зоной без осложнения тектоническим нарушением; выделенная в районе расчетного профиля II-II связана с тектоническим нарушением. Все сейсморазведочные аномалии, в соответствии с имеющейся геологической информацией, имеют природное происхождение. Оценка степени снижения прочностных и деформационных свойств пород в пределах ослабленных зон производилась на основе анализа изменения параметров волнового поля [*Барях и др.*, 2017; *Жикин и др.*, 2023].

Геомеханическая оценка и прогноз изменения напряженно-деформированного состояния породного массива под воздействием горных работ основывались на численном математическом моделировании. Методика расчетов достаточно подробно изложена в работе [*Барях и др.*, 2017] и базируется на модели идеальной упруго-пластической среды, которая в области действия напряжений сжатия реализуется в варианте параболического критерия Кулона-Мора [*Wang et al.*, 2019], а в области напряжений растяжения упругое деформирование ограничивается пределом прочности при растяжении. Отметим, что в физическом выражении формирование зон пластических деформаций в областях сжатия и растяжения связывается с процессами трещинообразования, соответственно за счет развития трещин сдвига и отрыва.

Геомеханическая расчетная схема отражала весь комплекс горнотехнических и горно-геологических факторов (глубину горных работ, количество отработанных пластов, параметры системы разработки, порядок отработки, угол падения пластов, установленные по результатам геофизических особенности строения подработанного массива и др.). В рамках принятой схемы математического моделирования временной фактор учитывался в соответствии с разработанной модификацией известного метода переменных модулей деформации [*Барях и Самоделкина*, 2005].

Граничные условия определялись следующим образом: на боковых границах горизонтальные смещения, а на нижней границе вертикальные — принимались равными нулю. Верхняя граница (дневная поверхность) — свободная от усилий. Учет собственного веса пород проводился посредством задания массовых сил интенсивностью γ_i. (γ_i — удельный вес i-го элемента геологического разреза). Исходное напряженное состояние ненарушенного горными работами соляного массива считалось гидростатическим:

$$\sigma_x^0 = \sigma_y^0 = \gamma H, \tau_{xy}^0 = 0.$$

В расчетных схемах учтены выделенные по результатам геофизических работ области пониженных механических свойств пород. Разрывные тектонические нарушения моделировались проницаемой субвертикальной нарушенной зоной со свойствами уменьшенными в 10 раз по отношению к ненарушенному массиву. Исходное вертикальное напряжение по всему разрезу, включая и области сейсморазведочных аномалий, принималось равным γH. В геомеханической модели выработанное пространство отражалось средой с пониженными по отношению к породам соответствующего пласта механическими свойствами. Степень снижения механических свойств определялась принятыми параметрами камерной системы разработки.

Параметрическое обеспечение геомеханических расчетов основывалось на результатах механических испытаний пород, представленных в геологическом разрезе Тюбегатанского месторождения.

В связи с отсутствием системы маркшейдерских наблюдений за оседаниями земной поверхности на шахтном поле рудника калибровка геомеханической модели по профилю I-I производилась по результатам радарной интерферометрической съемки спутника Sentinel-1A[1]. Полученные оценки среднегодовых скоростей оседания земной поверхности составили: в 2021 году — 200 мм/год, в 2022 — 300 мм/год. Эти величины приняты в качестве ориентира при калибровке геомеханической модели по оседаниям земной поверхности. Численная реализация геомеханической модели основывалась на известных алгоритмах метода конечных элементов [*Borst et al.*, 2012; *de Souza Neto et al.*, 2008; *Zienkiewicz et al.*, 2014].

Выполненные геомеханические расчеты показали, что на участке первоочередной отработки (рис. 7) уже на сегодняшний момент времени в ВЗТ сформированы зоны субвертикальной трещиноватости, которые могут служить каналами для поступления пресных вод в выработанное пространство рудника. Причем, в данных условиях отработки нарушение сплошности ВЗТ обусловлено не наличием выделенной аномалии (ослабленная зона без осложнения разрывным нарушением), а в большей степени связано с реализованными параметрами очистной выемки.

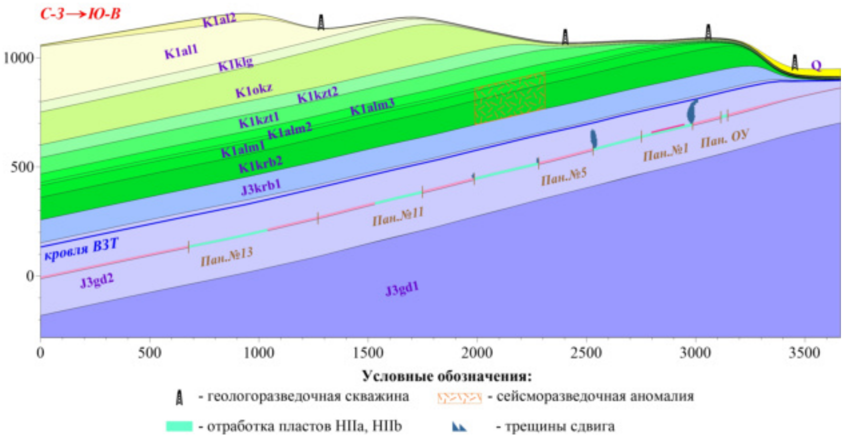

Рис. 7. Характер формирования зон техногенной нарушенности в водозащитной толще (ВЗТ) в пределах отработанного участка (профиль I-I) на момент 2022 года.

При оценке опасности нарушения сплошности ВЗТ на участке перспективной выемки запасов сильвинитовой руды (профиль II-II, рис. 8) установлено, что сквозное ее разрушение при сохранении принятых ранее параметров разработки наступает уже через 10 лет после начала горных работ.

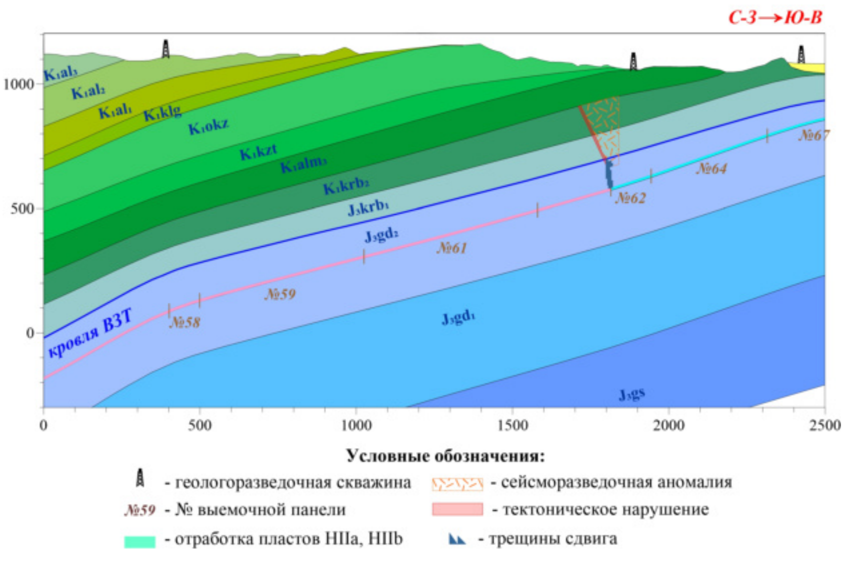

Рис. 8. Характер формирования зон техногенной нарушенности в ВЗТ в районе перспективной отработки (профиль II-II) через 10 лет после начала горных работ.

В этом случае зона субвертикальной нарушенности локализуется непосредственно в районе разрывного нарушения. Таким образом, можно констатировать, что в условиях Тюбегатанского месторождения основная опасность прорыва пресных вод в горные выработки связана с наличием разрывных тектонических нарушений.

В целях обеспечения потенциальной возможности отработки запасов Тюбегатанского месторождения в условиях сложного тектонического строения выполнены расчеты с изменениями параметров камерной системы разработки. При сохранении ширины очистных камер и вынимаемой мощности на обоих рабочих пластах соблюдалось следующее требование: вне зависимости от глубины горных работ степень нагружения междукамерных целиков не должна превышать 0,4, т. е. запас их несущей способности не менее 2,5. При соблюдении этих условий безопасные условия подработки ВЗТ обеспечиваются вплоть до завершения процесса сдвижения.

4. Заключение

Комплексные геофизические и геомеханические исследования, выполненные в районе Тюбегатанского месторождения, позволили сделать некоторые общие выводы, направленные на обеспечение безопасности горных работ в условиях сложного тектонического строения разрабатываемого соляного массива:

1. Наряду с традиционными геологоразведочными работами, на стадии подготовки месторождения к отработке необходимо предусмотреть комплекс геофизических исследований, ориентированный на пространственную локализацию аномальных зон, особенно связанных с разрывными нарушениями.
2. Результаты геофизических исследований должны быть представлены в виде физико-геологических моделей для последующей их трансформации в геомеханические расчетные схемы.
3. Обязательным элементом разработки калийных месторождений в сложных горно-геологических условиях является сопроводительный мониторинг состояния подработанного массива, который включает режимный геофизический комплекс исследований, сейсмологический контроль процессов разрушения, инструментальные и/или радарные интерферометрические наблюдения за развитием оседаний земной поверхности, измерения в гидронаблюдательных скважинах. Геомеханическая интерпретация результатов мониторинга позволит получить более достоверную оценку устойчивости водозащитной толщи и повысит качество обеспечения безопасности горных работ.

Благодарности. Исследования выполнены сотрудниками Института физики Земли им. О. Ю. Шмидта РАН под руководством члена-корреспондента РАН В. О. Михайлова. Работа частично выполнена при финансовой поддержке гранта РНФ № 19-77-30008.

Список литературы

Барях А. А., Евсеев А. В. Ликвидация калийных рудников и соляных шахт: обзор и анализ проблемы // Горный информационно-аналитический бюллетень. — 2019. — Т. 9. — С. 5—29. — DOI: 10.25018/0236-1493-2019-09-0-5-29.

Барях А. А., Красноштейн А. Е., Санфиров И. А. Горнотехнические аварии: затопление Первого Березниковского калийного рудника // Вестник Пермского научного центра. — 2009. — № 2. — С. 4—9. — EDN: PYWAJJ.

Барях А. А., Самоделкина Н. А. Об одном подходе к реологическому анализу геомеханических процессов // Физико-технические проблемы разработки полезных ископаемых. — 2005. — № 6. — С. 32—41. — EDN: PFHADT.

Барях А. А., Санфиров И. А., Федосеев А. К. *и др.* Сейсмо-геомеханический прогноз состояния водозащитной толщи на калийных рудниках // Физико-технические проблемы разработки полезных ископаемых. — 2017. — № 6. — С. 10—22. — DOI: 10.15372/FTPRPI20170602.

Беляков Н. А., Беликов А. А. Прогноз целостности водозащитной толщи на Верхнекамском месторождении калийных руд // Горный информационно-аналитический бюллетень (научно-технический журнал). — 2022. — № 6—2. — С. 33—46. — DOI: 10.25018/0236_1493_2022_62_0_33.

Болгаров А. Г., Рослов Ю. В. Межскважинная сейсмическая томография для решения инженерно-геологических задач // Технологии сейсморазведки. — 2009. — № 1. — С. 105—111. — EDN: NCGHRJ.

Глебов С. В. Геофизическое обеспечение разработки Верхнекамского месторождения солей // Горный информационно-аналитический бюллетень. — 2004. — № 9. — С. 89—92. — EDN: IFAPOR.

Жикин А. А., Санфиров И. А., Фатькин К. Б. Классификация волновых образов типовых геологических неоднородностей соляной толщи Верхнекамского месторождения калийных и магниевых солей // Проблемы недропользования. — 2023. — Т. 3, № 38. — С. 118—128. — DOI: 10.25635/2313-1586.2023.03.118.

Поздеев А. А., Земсков А. Н., Ибрагимов Г. И. Некоторые аспекты освоения Тюбегатанского месторождения калийных солей // Рудник Будущего. — 2010. — № 1. — С. 6—10. — EDN: POEHWH.

Рудковский Р. Р., Трофимов В. Л., Хазиев Ф. Ф. Блуждающие рассолы соляных толщ и мероприятия по защите горных выработок от их затопления // Разведка и охрана недр. — 2011. — № 1. — С. 63—72. — EDN: LVFAKN.

Рыльникова М. В., Есина Е. Н., Сахаров Е. М. *и др.* Закономерности геодинамических явлений при освоении глубокозалегающих сложноструктурных месторождений калийно-магниевых солей // Горная промышленность. — 2023. — № 1. — С. 89—94. — DOI: 10.30686/1609-9192-2023-1-89-94.

Санфиров И. А., Степанов Ю. И., Фатькин К. Б. *и др.* Малоглубинные геофизические исследования на Верхнекамском месторождении калийных солей // Физико-технические проблемы разработки полезных ископаемых. — 2013. — № 6. — С. 71—77. — EDN: RRUGXL.

Baryakh A., Tsayukov A. Justification of fracture criteria for salt rocks // Frattura ed Integrità Strutturale. — 2022. — Vol. 16, no. 62. — P. 585–601. — DOI: 10.3221/IGF-ESIS.62.40.

Borst R. de, Crisfield M. A., Remmers J. J. C., *et al.* Non-Linear Finite Element Analysis of Solids and Structures. — Wiley, 2012. — DOI: 10.1002/9781118375938.

de Souza Neto E. A., Perić D., Owen D. R. J. Computational Methods for Plasticity: Theory and Applications. — Wiley, 2008. — DOI: 10.1002/9780470694626.

Gendzwill D. J., Brehm R. High-resolution seismic reflections in a potash mine // GEOPHYSICS. — 1993. — Vol. 58, no. 5. — P. 741–748. — DOI: 10.1190/1.1443459.

Gendzwill D. J., Stead D. Rock mass characterization around Saskatchewan potash mine openings using geophysical techniques: a review // Canadian Geotechnical Journal. — 1992. — Vol. 29, no. 4. — P. 666–674. — DOI: 10.1139/t92-073.

Halabura (Steve) S. P., Hardy M. P. An overview of the geology of solution mining of potash in Saskatchewan // Fall 2007 Conference 8–9 October 2007. — Halifax, Nova Scotia, Canada : Solution Mining Research Institute, 2007.

Karasev M. A., Protosenya A. G., Katerov A. M., *et al.* Analysis of shaft lining stress state in anhydrite-rock salt transition zone // Rudarsko-geološko-naftni zbornik. — 2022. — Vol. 37, no. 1. — P. 151–162. — DOI: 10.17794/rgn.2022.1.13.

Nolet G. A Breviary of Seismic Tomography: Imaging the Interior of the Earth and Sun. — Cambridge University Press, 2008. — DOI: 10.1017/CBO9780511984709.

Prugger F. F., Prugger A. F. Water problems in Saskatchewan potash mining - what can be learned from them? // CIM Bulletin. — 1991. — Vol. 84, no. 945. — P. 58–66.

Pumjan S., Long T. T., Loc H. H., *et al.* Deep well injection for the waste brine disposal solution of potash mining in Northeastern Thailand // Journal of Environmental Management. — 2022. — Vol. 311. — P. 114821. — DOI: 10.1016/j.jenvman.2022.114821.

Rauche H. Die Kaliindustrie im 21. Jahrhundert. — Springer Berlin Heidelberg, 2015. — DOI: 10.1007/978-3-662-46834-0.

The ISRM Suggested Methods for Rock Characterization, Testing and Monitoring: 2007-2014 / ed. by R. Ulusay. — Springer International Publishing, 2015. — DOI: 10.1007/978-3-319-07713-0.

Wang D.-J., Tang H., Shen P., *et al.* A Parabolic Failure Criterion for Transversely Isotropic Rock: Modification and Verification // Mathematical Problems in Engineering. — 2019. — Vol. 2019. — P. 1–12. — DOI: 10.1155/2019/8052560.

Yilmaz Ö. Seismic Data Analysis: Processing, Inversion, and Interpretation of Seismic Data. Volume I, II. — Society of Exploration Geophysicists, 2008. — 2027 p.

You M. Comparison of the accuracy of some conventional triaxial strength criteria for intact rock // International Journal of Rock Mechanics and Mining Sciences. — 2011. — Vol. 48, no. 5. — P. 852–863. — DOI: 10.1016/j.ijrmms.2011.05.006.

Zienkiewicz O. C., Taylor R. L., Fox D. The Finite Element Method for Solid and Structural Mechanics. — Seven. — Elsevier, 2014. — 624 p. — DOI: 10.1016/C2009-0-26332-X.

Russian Journal of Earth Sciences

Information Support for Geomechanical Calculations of Stability of the Undermined Rock Mass With a Complex Tectonic Structure

A. A. Baryakh*[,1], I. A. Sanfirov[1], M. V. Dyakonov[2], S. Yu. Lobanov[1], A. I. Nikiforova[1]

[1]Mining Institute, Ural Branch of RAS, Perm, Russia
[2]Uralkali, Berezniki, Russia
****Correspondence to:** A. A. Baryakh, bar@mi-perm.ru

Using the example of the Tyubegatan potash deposit (Uzbekistan), a complex of geophysical and geomechanical safety assurance for mining operations in conditions of the complex tectonic structure of the undermined rock mass is considered. Geophysical research included ground-based seismic surveys using a profile system in combination with «light» standard electro- and gravimetric techniques. Based on the results of these works, a physical and geological model of the deposit areas was built with the weakened zones and faults localization. As part of the meaningful interpretation, the physical and geological model was transformed into a geomechanical calculation scheme, which reflected the main mining-geological and mining-technical condition of development and was based on a model of elastoplastic deformation of salt rocks. The geomechanical model was calibrated from radar interferometric surveys. The time factor was taken into account in accordance with the developed modification of the well-known method of variable deformation modules. The formation of plasticity zones in physical terms was identified with the formation of fracturing areas in the water protection layer, which determine the danger of violating its continuity. Numerical implementation of the geomechanical model using the finite element method made it possible to substantiate the optimal parameters of the chamber development system, ensuring the safety of the water protection layer, including fault zones.

Received: 15 October 2023
Accepted: 15 January 2024
Published: 29 February 2024

Keywords: potash deposit, water protection layer, tectonic, fault, geophysical research, geomechanical, mathematical modeling, numerical implementation.

Citation: Baryakh A. A., Sanfirov I. A., Dyakonov M. V., Lobanov S. Yu., Nikiforova A. I. (2024), Information Support for Geomechanical Calculations of Stability of the Undermined Rock Mass With a Complex Tectonic Structure, *Russian Journal of Earth Sciences*, 24, ES1012, https://doi.org/10.2205/2024es000894

References

Baryakh A., Tsayukov A. Justification of fracture criteria for salt rocks // Frattura ed Integrità Strutturale. — 2022. — Vol. 16, no. 62. — P. 585–601. — DOI: 10.3221/IGF-ESIS.62.40.

Baryakh A. A., Evseev A. V. Closure of potash and salt mines: Review and analysis of the problem // Mining Informational and analytical bulletin. — 2019. — Vol. 9. — P. 5–29. — DOI: 10.25018/0236-1493-2019-09-0-5-29.

Baryakh A. A., Krasnoshtein A. E., Sanfirov I. A. Mining accidents: flooding of the First Bereznikovsky potash mine // Bulletin of the Perm Scientific Center. — 2009. — No. 2. — P. 4–9. — EDN: PYWAJJ.

Baryakh A. A., Samodelkina N. A. Rheological analysis of geomechanical processes // Journal of Mining Science. — 2005. — No. 6. — P. 32–41. — EDN: PFHADT.

Baryakh A. A., Sanfirov I. A., Fedoseev A. K., *et al.* Seismic-Geomechanical Prediction of Water-Impervious Strata State in Potassium Mines // Journal of Mining Science. — 2017. — No. 6. — P. 10–22. — DOI: 10.15372/FTPRPI20170602.
Belyakov N. A., Belikov A. A. Prediction of the integrity of the water-protective stratum at the Verkhnekamskoye potash ore deposit // Mining informational and analytical bulletin. — 2022. — No. 6–2. — P. 33–46. — DOI: 10.25018/0236_1493_2022_62_0_33.
Bolgarov A. G., Roslov Y. V. Inter-well seismic tomography for solving engineering-geological problems // Seismic technologies. — 2009. — No. 1. — P. 105–111. — EDN: NCGHRJ.
Borst R. de, Crisfield M. A., Remmers J. J. C., *et al.* Non-Linear Finite Element Analysis of Solids and Structures. — Wiley, 2012. — DOI: 10.1002/9781118375938.
de Souza Neto E. A., Perić D., Owen D. R. J. Computational Methods for Plasticity: Theory and Applications. — Wiley, 2008. — DOI: 10.1002/9780470694626.
Gendzwill D. J., Brehm R. High-resolution seismic reflections in a potash mine // GEOPHYSICS. — 1993. — Vol. 58, no. 5. — P. 741–748. — DOI: 10.1190/1.1443459.
Gendzwill D. J., Stead D. Rock mass characterization around Saskatchewan potash mine openings using geophysical techniques: a review // Canadian Geotechnical Journal. — 1992. — Vol. 29, no. 4. — P. 666–674. — DOI: 10.1139/t92-073.
Glebov S. V. Geophysical support for the development of the Verkhnekamskoye salt deposit // Mining informational and analytical bulletin. — 2004. — No. 9. — P. 89–92. — EDN: IFAPOR.
Halabura (Steve) S. P., Hardy M. P. An overview of the geology of solution mining of potash in Saskatchewan // Fall 2007 Conference 8–9 October 2007. — Halifax, Nova Scotia, Canada : Solution Mining Research Institute, 2007.
Karasev M. A., Protosenya A. G., Katerov A. M., *et al.* Analysis of shaft lining stress state in anhydrite-rock salt transition zone // Rudarsko-geološko-naftni zbornik. — 2022. — Vol. 37, no. 1. — P. 151–162. — DOI: 10.17794/rgn.2022.1.13.
Nolet G. A Breviary of Seismic Tomography: Imaging the Interior of the Earth and Sun. — Cambridge University Press, 2008. — DOI: 10.1017/CBO9780511984709.
Pozdeev A. A., Zemskov A. N., Ibragimov G. I. Some aspects of the development of the Tyubegatan potassium salt deposit // Mine of the Future. — 2010. — No. 1. — P. 6–10. — EDN: POEHWH.
Prugger F. F., Prugger A. F. Water problems in Saskatchewan potash mining - what can be learned from them? // CIM Bulletin. — 1991. — Vol. 84, no. 945. — P. 58–66.
Pumjan S., Long T. T., Loc H. H., *et al.* Deep well injection for the waste brine disposal solution of potash mining in Northeastern Thailand // Journal of Environmental Management. — 2022. — Vol. 311. — P. 114821. — DOI: 10.1016/j.jenvman.2022.114821.
Rauche H. Die Kaliindustrie im 21. Jahrhundert. — Springer Berlin Heidelberg, 2015. — DOI: 10.1007/978-3-662-46834-0.
Rudkovsky R. R., Trofimov V. L., Khaziev F. F. Errant brines in salt sections and actions to take to study the brines // Exploration and protection of subsoil. — 2011. — No. 1. — P. 63–72. — EDN: LVFAKN.
Rylnikova M. V., Esina E. N., Sakharov E. M., *et al.* Regularities in geodynamic phenomena in mining deep-lying potassium-magnesium salt deposits with complex structure // Mining Industry Journal. — 2023. — No. 1. — P. 89–94. — DOI: 10.30686/1609-9192-2023-1-89-94.
Sanfirov I. A., Stepanov Y. I., Fatkin K. B., *et al.* Shallow geophysical exploration of the upper Kama potash salt deposit // Journal of Mining Science. — 2013. — No. 6. — P. 71–77. — EDN: RRUGXL.
The ISRM Suggested Methods for Rock Characterization, Testing and Monitoring: 2007-2014 / ed. by R. Ulusay. — Springer International Publishing, 2015. — DOI: 10.1007/978-3-319-07713-0.
Wang D.-J., Tang H., Shen P., *et al.* A Parabolic Failure Criterion for Transversely Isotropic Rock: Modification and Verification // Mathematical Problems in Engineering. — 2019. — Vol. 2019. — P. 1–12. — DOI: 10.1155/2019/8052560.
Yilmaz Ö. Seismic Data Analysis: Processing, Inversion, and Interpretation of Seismic Data. Volume I, II. — Society of Exploration Geophysicists, 2008. — 2027 p.
You M. Comparison of the accuracy of some conventional triaxial strength criteria for intact rock // International Journal of Rock Mechanics and Mining Sciences. — 2011. — Vol. 48, no. 5. — P. 852–863. — DOI: 10.1016/j.ijrmms.2011.05.006.
Zhikin A. A., Sanfirov I. A., Fatkin K. B. Classification of wave patterns of typical geological heterogeneities of the salt strata of the Verkhnekamskoye deposit of potassium and magnesium salts // Problems of Subsoil Use. — 2023. — Vol. 3, no. 38. — P. 118–128. — DOI: 10.25635/2313-1586.2023.03.118.
Zienkiewicz O. C., Taylor R. L., Fox D. The Finite Element Method for Solid and Structural Mechanics. — Severn. — Elsevier, 2014. — 624 p. — DOI: 10.1016/C2009-0-26332-X.

Special Issue: "25th anniversary of the Russian Journal of Earth Sciences"

The Polymetallic Deposits of the Western European Plate and Structure of the Earth's Crust According to GOCE Gravity Data

A. L. Galyamov[1], A. V. Volkov[1], K. V. Lobanov[1]

[1]Institute of Geology of Ore Deposits, Petrography, Mineralogy and Geochemistry of the Russian Academy of Sciences, Moscow, 119017, Staromonetny lane, 35

* **Correspondence to:** A. L. Galyamov, a-galyamov@yandex.ru

Abstract: For the first time, the results of modern studies of the earth's crust based on gravity data from the GOCE satellite Project are used for a comparative regional metallogenic analysis of the geodynamic settings of the formation of polymetallic deposits in Western Europe and the Mediterranean segment of the Tethys belt. It is shown that exhalative sulfide deposits (SEDEX) and cuprous sandstones and shales (SSC) are mainly located in the earth's crust with a predominant development of the lower "basalt" layer of the earth's crust. Pyrite copper and lead-zinc deposits in volcanogenic rocks (VMS), as well as some occurrences of the SEDEX type, are found in supra-subduction island-arc and accretionary crustal settings with a predominant development of the middle "granite" layer. Lead-zinc ores of the Mississippi type (MVT) are localized in deep pericratonic sedimentary basins with petroleum-bearing specialization on the shelf and continental slope, regardless of the stratification of the earth's crust. The results obtained can be used for regional forecasting and metallogenic constructions, prospecting and assessment of new deposits.

Keywords: Western Europe, Tethys, lithosphere, Earth's crust, base metal, deposit, SEDEX, MVT, VMS, SSC.

Citation: Galyamov A. L., Volkov A. V., Lobanov K. V. (2024), The Polymetallic Deposits of the Western European Plate and Structure of the Earth's Crust According to GOCE Gravity Data, *Russian Journal of Earth Sciences*, Vol. 24, ES1006, https://doi.org/10.2205/2024ES000895

Research Article

Received: 15 October 2024
Accepted: 15 January 2024
Published: 29 February 2024

1. Introduction

Lead-zinc deposits, widespread in the world, are one of the most important sources of strategic metals: Cu, Pb, Zn, Ag, Au, PGE, Te, Se, Ge, Ga, Bi, Cd, In, Re, REE [*Bortnikov et al.*, 2016; *Galyamov et al.*, 2021]. Such large Pb-Zn deposits are known in the world as Red Dog, Green Creek (Alaska, USA), Selwyn, Howard Pass, Pine Point (Canada), Broken Hill, McArthur River (Australia), Sullivan, Kidd Creek, Faro, Brunswick in Canada, Citronen in Greenland, Rio Tinto in Spain, Falun in Sweden, Anguran in Iran, Kholodninskoye, Ozernoye, Sardana and Pavlovskoye in Russia, as well as many others. The bulk of the world's reserves of lead and zinc (60%) are in pyrite-polymetallic deposits in terrigenous and carbonate-terrigenous formations (SEDEX type); reserves of lead-zinc deposits in carbonate formations (MVT type) and pyrite-polymetallic deposits in volcanogenic formations (VMS type) are about 20% each [*Dergachev and Eremin*, 2008]. Moreover, more than 40% of the reserves and about half of the resources come from SEDEX-type objects in Precambrian rocks.

In Western Europe, about four hundred lead-zinc and copper objects are known, including two dozen large deposits. Pyrite deposits are located in the Caledonides and Alps-Kristineberg, Garpenbergsfaltet, Renstrom, Boliden (Sweden), Rammelsberg (Germany), Rio Tinto, Angostura (Spain), Horni Kalna, Kostalov (Czech Republic). Stratiform deposits are known in the Hercynian and Alpine complexes of Poland (Upper Silesia, Miedziana, Pomorzany, etc.), Italy (Iglesiente), Sweden (Horntraskviken, etc.), Ireland (Navan, etc.) (Figure 1). Vein polymetallic (including silver) deposits are located in the Alpides and Hercynides of Bulgaria (Madan, etc.), North Macedonia (Sasa, etc.), Slovakia (Banska Stiavnica, etc.), France (L'Argentiere, etc.)

The origin of large concentrations of base metals and, especially, their sources are of great interest for forecasting and identifying new deposits. Modern forecasting and metallogenic studies are impossible without Earth remote sensing materials; generalization and analysis of geological, geotectonic, geochemical and other spatial data, as well as information on metallogeny [*Volkov et al.*, 2020].

Previous studies [*Blundell et al.*, 2007] show that the location of polymetallic deposits in Europe is closely related to geodynamic settings that correspond to deep processes in the earth's crust-subduction, rifting and orogenesis. The features of the deep structure of the earth's crust are of significant interest to study the geodynamic conditions of the formation of deposits in the lithosphere. This article used a global geophysical model of the earth's crust, the CRUST1.0 model, compiled from the results of remote gravitational measurements from space within the framework of the GOCE project [*Laske et al.*, 2013; *Reguzzoni and Sampietro*, 2015]. The modern ideas about the structure and geodynamic development of the earth's crust were taken into account.

Figure 1. Location of polymetallic deposits in Europe (based on materials from [*Asch*, 2003]).
1–7 – Types of deposits: 1 – copper-pyrite in volcanogenic-sedimentary rocks, 2 – lead-zinc volcanic-carbonate stratiform, 3 – pyrite-polymetallic in terrigenous rocks, 4 – lead-zinc stratiform in carbonate rocks, 5 – polymetallic vein, 6 – cuprous sandstones and shales, 7 – silver-polymetallic vein.
8–12 – Age of geological formations: 8 – Cenozoic, 9 – Mesozoic, 10 – late Paleozoic (D-P), 11 – early Paleozoic (Cm-S), 12 – Precambrian.

This article continues the study of global and regional trends of location of lead-zinc deposits [*Galyamov et al.*, 2021, 2022, 2023] and focuses on the spatial relationships of polymetallic ores and features of the deep structure of the earth's crust within Western Europe and the Mediterranean segment of the Tethys belt.

2. Model of the deep structure of the Earth's crust CRUST1.0

Currently, a huge amount of material has been accumulated as a result of seismic studies of the earth's crust using the DSS (deep seismic sounding) and MOV-CDP (reflected wave – common depth point) methods. The DSS method makes it possible to determine the thickness of the earth's crust, identify seismic boundaries, deep faults, etc. in its thickness. In Western Europe, seismic studies at the end of the last century were carried out on a variety of profiles with an average profile density (4.5 linear km) per thousand km^2, providing study of the earth's crust and upper mantle [*Fountain et al.*, 1993; *Hasterok et al.*, 2022].

Currently, one of the most complete and spatially distributed modern systems of remote sensing data on the earth's crust, based on measurements over a uniform network, are the results of space gravimetric measurements under the GOCE (Gravity Field and Steady-State Ocean Circulation Explorer) project. The GOCE spacecraft (weighing 1 ton) was launched from the Russian Plesetsk cosmodrome by the Rokot launch vehicle into low-Earth sun-synchronous orbit on March 17, 2009. GOCE is a satellite of the European Space Agency (ESA), combining gravity reconnaissance and GPS tracking to determine the average gravitational field of the Earth with unprecedented accuracy and spatial resolution [*Klyuykov*, 2018]. To ensure the highest possible accuracy of measurements, a very low orbit was chosen – 260 km above the Earth's surface.

Based on the results of the GOCE mission, the shape of the planet was determined in more detail, the gravitational force in various regions and the density of the Earth's crust were measured, and a new global gravitational map of the Earth was compiled. The maximum resolution of GOCE gravimetry is 50 km; in general, for many parameters, the resolution is 100 km. But the GOCE equipment made it possible to measure field values over a uniform network, which made it possible to build global models of seismic surfaces, and additional parameters - a rheological model of the upper mantle to a depth of 100 km.

The gravimetric data stimulated the development of global models of the deep structure of the earth's crust and upper mantle (GEMMA1.0, CRUST1.0), which contributed to the understanding of the metallogenic specialization of large ore regions and provinces. The GEMMA (GOCE Exploitation for Moho Modeling and Applications) project, also funded by ESA, based on GOCE data, carried out an updated assessment and significantly detailed the boundaries of the Moho [*Reguzzoni and Sampietro*, 2015].

The global model CRUST1.0 is based on a uniform one-degree network and is the most complete and combines data on the depth of the Moho (half-degree network GEMMA), a three-layer sedimentary cover, as well as the upper, middle and lower layers of the consolidated crust [*Laske et al.*, 2013]. We used this model to explain the spatial patterns of the location of polymetallic deposits in the structure of the earth's crust. In addition, the GEMMA model was used – the density and thermal regime of the upper mantle [*Cammarano and Guerri*, 2017]. According to the model, the total thickness of the earth's crust on the continents ranges from 16 km to 72 km. On 95% of the area of all continents, the thickness of the continental crust varies in the range of 22–57 km.

The sedimentary cover forms the uppermost layer of the earth's crust [*Laske et al.*, 2013]. Its thickness varies from zero on shields to more than 20 km in deep sedimentary basins. The rocks of the sedimentary cover are often metamorphosed and seismically indistinguishable from the crystalline basement rocks. In many regions, metamorphosed Paleozoic sediments are included in the upper crystalline crust. The upper horizon, up to 2 km thick, represented by the least dense and weakly metamorphosed sedimentary complexes, has the widest distribution (more than 500 million km^2), occupying vast oceanic spaces. Its complexes make up individual deep troughs confined to oil and gas provinces (for example, the North Sea-German, Cis-Carpathian, Transylvanian, etc.). In general, hydrocarbon specialization is much weaker in the oceanic and continental sediments of this horizon [*USGS*, 2012].

Oil and gas bearing formations are most often confined to the deepest parts of the sedimentary crust, to areas of development of strata of the middle and lower horizons. The middle horizon, up to 4 km thick, has a relatively smaller distribution (about 100 million km^2) and covers many hydrocarbon provinces (the Arabian Peninsula, South America, Western Siberia, etc.) and their frame. The lower horizon of the sedimentary layer of the lithosphere, the least widespread in the world (less than 20 million km^2), is composed of the most powerful complexes (over 14 km), to which the central sections of the large hydrocarbon provinces of the world are confined.

The consolidated crust, according to the CRUST1.0 model, consists of three layers. The upper and middle layers of the continental crust are composed mainly of metamorphic complexes, gneisses, granites and granodiorites. The boundary between the upper "metamorphic" and middle "granite" layers is often conditional and runs along the velocity section of about 6.3 km/s. The lower "basaltic" crust is believed to be composed of rocks of the amphibolite facies, although it is possible that the lower crust may be composed of andesites and dacites [*Hacker et al.*, 2015].

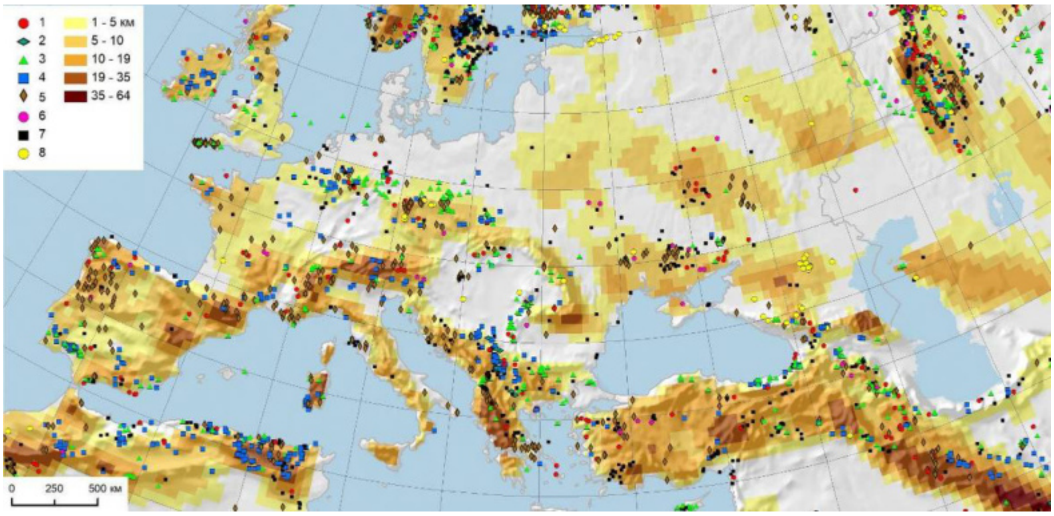

Figure 2. Local thickening of the earth's crust (in km) and location of ore deposits (using materials from [*Laske et al.*, 2013]).

1–8 – deposits: 1 – precious metals, 2 – copper-nickel, 3 – copper, 4 – lead-zinc, 5 – base (W, Sn, etc.), 6 – rare, 7 – ferrous and 8 – radioactive metals.

Seismological and geological-geophysical studies have shown that the lower, middle and upper layers of the consolidated crust are inconsistent in thickness. The deformation of the crustal layers is expressed in the form of contrasting protrusions and depressions of the Moho surface, anomalous swelling and thinning of the lower and middle crust. Among such deep areas, geodynamic areas of different ranks and different types according to the mechanism of formation are distinguished. They are associated with mantle processes, on the one hand, and tectonic horizontal movements during the interaction of lithospheric plates and terranes. Mantle processes, the trigger of the geodynamic situation in the near-surface region of the crust, cause new deformations in the latter, expressed by uplifts, troughs and flexures.

Local thickenings – structures of the second and higher orders, are reflected on maps in the form of stripes and individual areas (Figure 2), identified by calculating average values in a sliding window. Local areas of increased thickness are clearly distributed throughout the world, often have linear outlines and most likely highlight the nature of plate interactions. The thickening of the crust reflected in the seismic section is explained as a result of the decompression of the upper mantle material and the corresponding lowering of its upper boundary.

Local thickening of the earth's crust and its layers is characterized by variability. Sharp variability is often explained by the block structure of the section, features of rifting and other tectonic and rheological reasons and is revealed by a sharp change in the slope of the Moho surface. General spatial statistics show that within zones of local crustal thickening, significantly more than half of all the world's deposits and occurrences of noble, non-ferrous, rare, ferrous and radioactive metals are located.

3. Deep structure of the Earth's crust of Western Europe and location of polymetallic deposits

The Western European young platform has, in general, a Paleozoic folded basement and a Mesozoic-Cenozoic cover. It is characterized by a distinct block structure: massifs (Bohemian, Rhine, Armorican, Central), ancient protrusions (Harz, Vosges, Black Forest) and superimposed depressions (Polish-German, North German, Parisian, Aquitaine, Thuringian, Sub-Hercynian).

Cenozoic (Rhine) and Mesozoic (North Sea) intracratonic rift systems are developed. The largest oil and gas deposits are associated with the latter, and deposits of rock and potassium salts are confined to the fields of development of Late Permian deposits, and deposits of hard and brown coal are confined to the Carboniferous, Permian and Neogene territories.

The crust of Western Europe differs from the crust of the East European Platform [*Belousov and Pavlenkova*, 1989; *Galyamov et al.*, 2023]. Its greatest thickness (average 30 km) does not exceed 48 km compared to 57 km (average 39 km) in the east of the European continent. Average speeds there are also somewhat lower: 6.3–6.4 km/s compared to 6.5–6.6 km/s on the ancient platform. The consolidated crust is divided into three layers – upper ("granite-gneiss"), middle ("granite") and lower ("mafic"). A feature of the crust of Western Europe is the reduced average thickness of its layers and significant stratification of the lower layer (based on materials from CDP profiles). Spatial analysis also shows that the ancient highs (Bohemian, Armorican and Central) are confined to areas of thickened lower "mafic" layer of the crust, while areas of the Alpine orogeny are spatially associated with areas of increased thickness of the upper (Pontids and Taurids in Turkey) and, in part, middle layer.

The basement of the Western European Platform was formed during the Baikal, Caledonian and Hercynian eras of orogenesis (Figure 3). Ancient consolidated elements of the earth's crust, complicated by the development of rift structures, repeatedly experienced orogenesis; ultimately, the age and contours of the main geodynamic regions of Western and Central Europe are determined by recent orogenic processes that caused extensive metamorphic restructuring and magmatism [*Plant et al.*, 2005]. In the areas of the British Isles, the North Sea and the Norwegian Sea shelf, the northern part of the North German Basin and the border of the East European Platform, the basement is Caledonian age mainly.

In the southern part of the platform, the basement in the form of protrusions (Armorican, Central, Vosges, Black Forest and Bohemian massifs) is composed of Hercynian complexes. These formations also compose Ardennes, the Rhine Slate Mountains, Harz, Thuringian Forest, Ore Mountains, Sudetenland, and in the western and central parts of the Iberian Peninsula [*Plant et al.*, 2005]. The development of Cenozoic extended grabens of the European rift system, 1100 km long, in the Alpine foreland complicates the modern tectonic activity of the Hercynides. The Rhine Grabens remain seismically active currently.

Polymetallic deposits are unevenly distributed in the geological structure (Figure 3). In general, on the territory of Western Europe, within volcanic and magmatic arcs, the VMS deposits of Sweden (Renstrom, Kristineberg, Boliden, etc.) and Finland (Pyhasalmi, Outokumpu, Vihanti, Pirttilampi, Verttuunjärvi, Korppisjärvi, Muittari, etc.) predominate (more than 30% of the number of polymetallic occurrences).

In orogenic areas, VMS pyrite-volcanogenic deposits (more than 20%) of Norway (Tverrfjellet, Fosdalen, Sel, Nordre Gjetryggen, Grimsdalen, etc.) and Spain (Arinteiro, Bama, Filon Sur-Esperanza, Vuelta Falsa, etc.) are predominantly widespread, as well as exhalative (about 15%) deposits (Germany – Rammelsberg, Meggen, etc.). Next to them, in the clastic and clay redbed facies, there are stratiform deposits of cuprous sandstones and shales (SSC) – in Germany (Leitmar, Korbach, Konrad), in Poland (Lubin, Malomice), in Spain (Granada, Menorca, Santomera) , in France (Bancairon, Cap Garonne, Cerisier).

Carbonate formations of the Paleozoic basement and Mesozoic-Cenozoic cover contain MVT type deposits (about 15%) in Ireland (Navan, Abbeytown, Ballinalack, Tatestown, etc.),

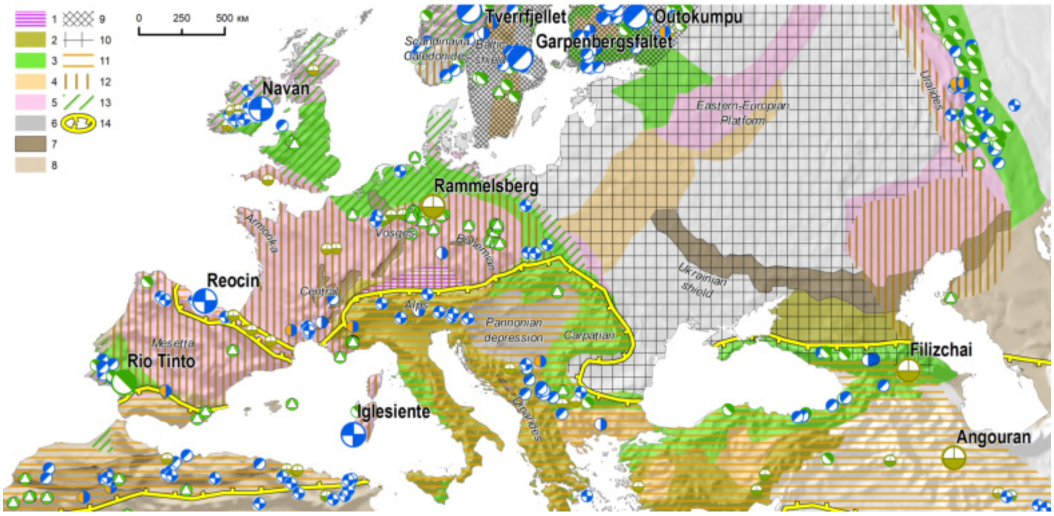

Figure 3. Location of polymetallic deposits and geodynamic regions of Europe (based on materials from [*Hasterok et al.*, 2022; *Richards*, 2015]).
1 – foredeeps, 2 – accretionary complexes, 3 – island arcs, 4 – magmatic arcs, 5 – orogenic belts, 6 – superimposed basins, 7 – rifts, 8 – passive margin, 9 – shields, 10 – cratons; 11–13 – age of orogenesis: 11 – Alpides (Ap, MZ-KZ basins), 12 – Hercynides (Hz, Hz+Ap), 13 – Caledonides (Kd); 14 – contours of the Tethys belt.

Belgium (Verviers), Poland (Upper Silesian basin, Pomorzany), Spain (Reocin, Rubiales, Picos de Europa, Troya). Some small this type deposits occur in Early Paleozoic formations on the periphery of the Hercynian block massifs (Central French, Mesetta, Czech, etc.). The stratiform occurrencesare mostly transformed into skarnoids (Svardsjo, Lovasfaltet, Kalvbacksfaltet).

Within shields with a Precambrian age of orogenesis, there are predominantly copper and polymetallic VMS deposits (more than 30%), occurring in ancient metamorphosed island-arc volcanogenic-sedimentary deposits and metamorphic complexes of volcanic and magmatic arcs (Kristineberg, Renstrom, Boliden, Outokumpu, Vihanti, etc.) .

The depth of the Moho surface within the Precambrian protrusions of the Baltic Shield fluctuates on average about 44 km (Figure 4), the maximum value is 48–50 km, the temperature of the upper mantle at a depth of 60 km is reduced to 500 °C [*Reguzzoni and Sampietro*, 2015].

The concentration of pyrite volcanogenic deposits in Sweden and Finland occurs in areas of the thickened upper “metamorphic” layer of the consolidated crust, as well as in areas of increased thickness of the middle layer and decreased thickness of the lower layer. Similar patterns of crustal structure and placement of VMS ores are also noted in the frame of the East European and Siberian platforms [*Galyamov et al.*, 2023]. This feature of the deep structure of the earth's crust is also observed in the Norwegian Caledonides zone in the north of the Scandinavian Peninsula.

In the areas of the Caledonian orogeny of Europe, pyrite-base metal VMS ores occur mainly in metamorphosed complexes of Norway (Bjornefjell, Espelandsmyr, Solberg, etc.) and Sweden (Fosdalen, Joma, Grimeli, Rostvangen, Hersjo, Killingdal, etc.). Along with them, isolated SEDEX pyrite exhalation occurrences are known (Laisvall in Sweden, Mofjellet and Bleikvassli in Norway, Ben Eagach in Great Britain, etc.), occurring in terrigenous and carbonate formations of the Riphean-Vendian and Early Paleozoic, as well as stratiform MVT deposits of Ireland (Navan, Gortdrum, Garrycam, Abbeytown, Ballinalack, etc.). The depth of the Moho here is characterized by shallower depths within 20 km on the Iberian Peninsula and 32–38 km on the British Isles and Norway (Figure 4), while the temperature of the upper mantle at a depth of 60 km is increased to 900–1000 °C [*Reguzzoni and Sampietro*, 2015].

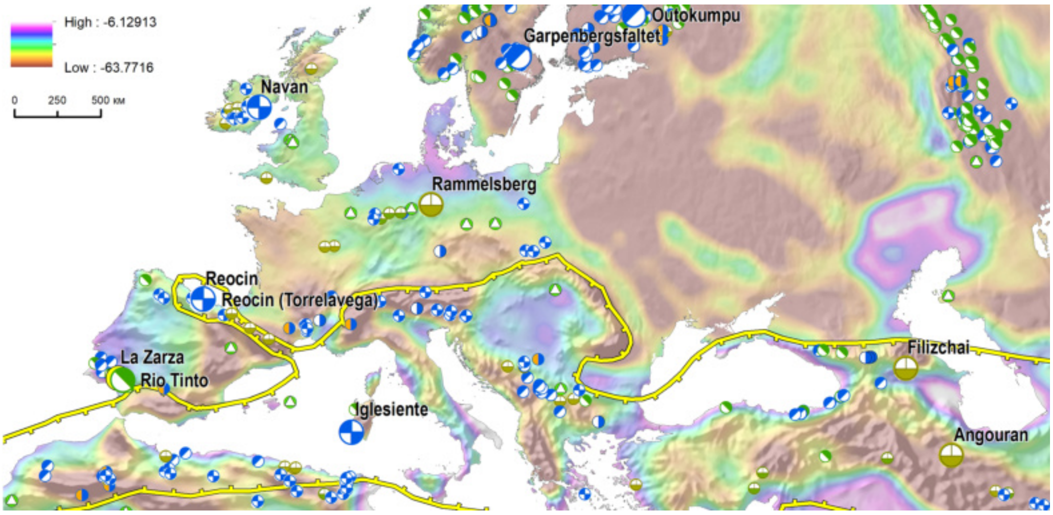

Figure 4. Polymetallic deposits of Western Europe and Moho depth in km (based on materials from [*Reguzzoni and Sampietro*, 2015]). Symbol see Figure 1, Figure 3.

VMS-type deposits predominate both in areas of the Hercynian volcanic belts (Spain – Angostura, Rio Tinto, Cueva de la Mora, San Telmo, San Miguel, etc.) and in accretionary complexes of supra-subduction zones (Serbia – Zimovnik, Tisovik, Brskovo Zuta Prla, Koporic, etc.).

The Iberian (Iberian) pyrite belt is one of the world's largest concentrations of volcanogenic deposits of non-ferrous metals – Angelita, Esperanza and San Miguel. Polymetallic mineralization here was probably formed under pre-arc extensional conditions [*Blundell et al.*, 2007]. Previous collisional and lateral movements contributed to the opening of weakened zones in the earth's crust, where deep magmas and anomalous heat flows were intruded. Large pyrite-volcanogenic deposits formed in the back-arc basins at the epicenter of these anomalies. The most intense metal content of the belt appeared with the end of syn-collisional extension, immediately before post-collisional extension during granulitization of the lower crust. The most likely source of metals is lower crustal granulites [*Blundell et al.*, 2007].

In the Hercynides of Central Europe, especially in areas of widespread development of rift structures (Rhine Grabens, Vosges, Hesse and Eger), exhalation SEDEX deposits of Germany (Rammelsberg, Meggen, etc.), France (Bodennec, Porte Aux Moines) and occurrencea of cuprous sandstones and SSC type shales – Konrad, Korbach, etc. (Germany), Nowy Kosciol, Sierozovice, etc. (Poland) and France (Cerisier, Giordannet, Liouc, etc.). This also includes numerous hydrothermal polymetallic deposits associated with the Hercynian and younger granite intrusions of the Rudnoga polymetallic province.

Of the Mississippian-type deposits in Paleozoic and Mesozoic carbonate rocks, the French Villemagne and Malines, the Spanish Antonina and Rubiales, karst-type deposits (Iglesiente and Monteponi in Italy, Upper Silesian objects in Poland, the Belgian Pb-Zn deposit Schmalgraf, as well as lead-zinc deposits in Ireland) are known .

The Irish Navan, Tynagh, Silvermines, Lisheen and Galmoy deposits, which occur in Early Carboniferous carbonate layers, contain a large number of strata deposits, formed partly in the muds of the coastal zone, but generally during diagenesis (dolomitization and brecciation), sometimes against a background of volcanic activity.

Stratified deposits of the Upper Silesian ore district occur in shallow Triassic limestones and dolomites and belong to the type of replacement of cavities, veins and mineralized breccias [*Vos et al.*, 2005]. Under conditions of folding and faulting deformations during the formation of stratiform deposits of this type, the development of karst occurred together with the redeposition of sulfides and barite with productive ore deposition at the end of the Hercynian orogeny [*Boni and Amstutz*, 1982]. In southwestern Poland there are deposits of cuprous sandstones and shales, possibly of exhalative origin. The ores of these deposits were formed as a result of the movement of brine through permeable zones in the basement during the Triassic rifting period [*Blundell et al.*, 2007].

A significant part of the Hercynian belts of Western Europe is covered by the Mesozoic-Cenozoic cover, with the exception of the Paleozoic block massifs (Parisian, Czech, etc.). The Moho surface within the massifs is distinguished by significant depth, compared with the areas hidden under the Mesozoic-Cenozoic cover (Figure 1). In general, the Hercynides are characterized by a thick lower "mafic" layer of the earth's crust, within the block massifs its thickness is one and a half to two times or more greater than that of the middle and upper layers (Figure 5). A significant part of the SEDEX and SSC deposits in Germany, Belgium, Poland and the Czech Republic are located on the periphery of the Vosges and Czech massifs, above areas of thickening of the lower crustal layer, relative to the middle layer (Figure 6).

Alpine activation in Western Europe is manifested mainly in the form of active zones of the Mediterranean segment of the Tethys belt. The axis of the belt segment is located between the southern continental margin of Eurasia and the Afro-Arab plate. To the north, as a result of stretching of the Hercynian crust, the rift system of Western Europe developed, accompanied by alkali-basalt and alkaline volcanism [*Trifonov*, 2017].

The Tethys volcanic belts host numerous small and large porphyry Cu-Mo-Au deposits and associated epithermal Au-Cu occurrences. The Tethys Belt also hosts stratiform and exhalative polymetallic deposits, accompanied by skarn and epithermal polymetallic and silver occurrences.

The vast majority of polymetallic deposits here occur in Mesozoic complexes. The most represented lead-zinc deposits of the Mississippian type are in Spain (Reocin, Troya), Italy (Salafossa, Raibl and Gorno), as well as Slovenia, Switzerland and Austria. There are also exhalative occurrences of lead and zinc in France (Arrens), Spain (Arditurri) and cuprous sandstones and shales (Granada and Santomera in Spain, Darno-Hegy in Hungary, Giordannet in France, etc.).

Within the Tethyan belt, the depth of the Moho varies between 35–45 km, while the depth of the Pannonian Basin, which is part of the belt, is 22 km [*Reguzzoni and Sampietro*, 2015]. The temperature of the upper mantle within the belt is characterized by elevated values, varying around 1100°C, in some places exceeding 1300 °C. The thickness of the lower layer of crust in the Tethys belt on average does not exceed 15 km; in areas conjugating with the Hercynian blocks, the values rarely exceed 25 km (Figure 5). The middle layer has a more uniform thickness within the range of 8–15 km, while the thickness within the Pannonian Basin is reduced to 7–8 km.

The belt also shows a correlation between the placement of deposits of VMS and SEDEX types, depending on the ratio of the thickness of the lower and middle layers of the earth's crust. In areas with a layer thickness ratio of 1.5–2:1, exhalation deposits are common (Figure 6), and in areas with a layer thickness ratio of 0.5:1, VMS ores are predominant. The upper layer of the crust, in general, has an increased thickness (about 15–20 km), but in the Pannonian Basin the values do not exceed 8 km.

4. The discussion of the results

4.1. Thickening of the earth's crust, types, causes and consequences

The main reasons for the increase in the volume of the earth's crust are: tectonic interaction of plates and thermochemical mantle influence, accompanied by magmatism, underplating and separation of the crust and mantle. The main consequence of crustal thickening is delamination, convection, metasomatism and subsequent decompression of the crust and upper mantle, which is accordingly reflected in the form of thickening on seismic sections.

Tectonic thickening of the earth's crust is usually associated with collision processes during collision, subduction of plates, etc. (African and Eurasian). During the collision, an almost doubling of the thickness of the earth's crust is noted, which is expressed in the relief by intense folded-block uplifts (Pyrenees, Alps, Apennines, Dinarides, Carpathians).

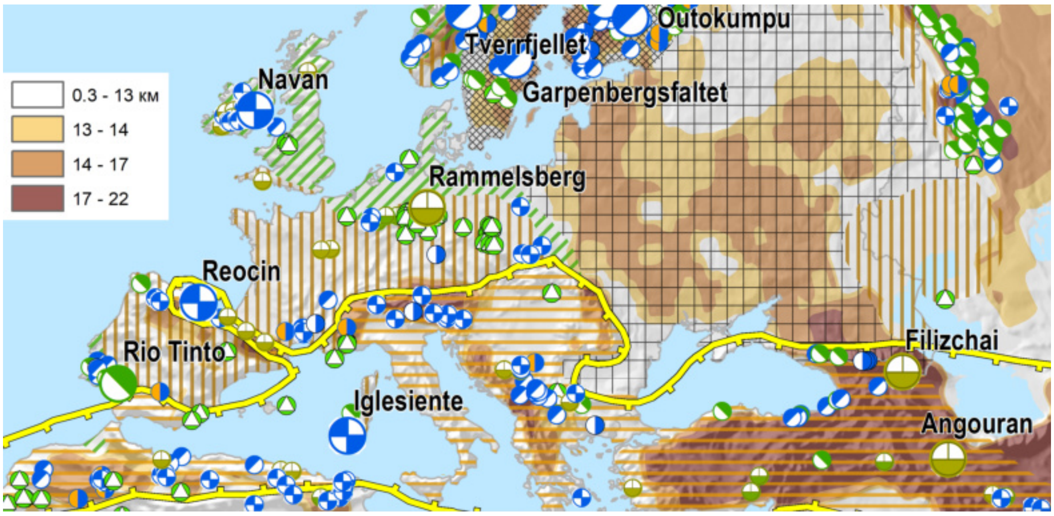

(a)

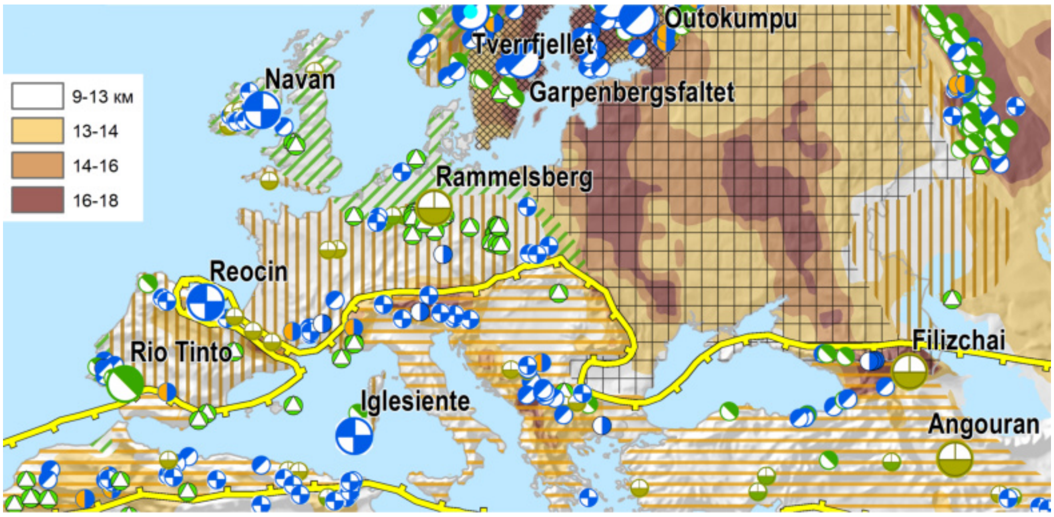

(b)

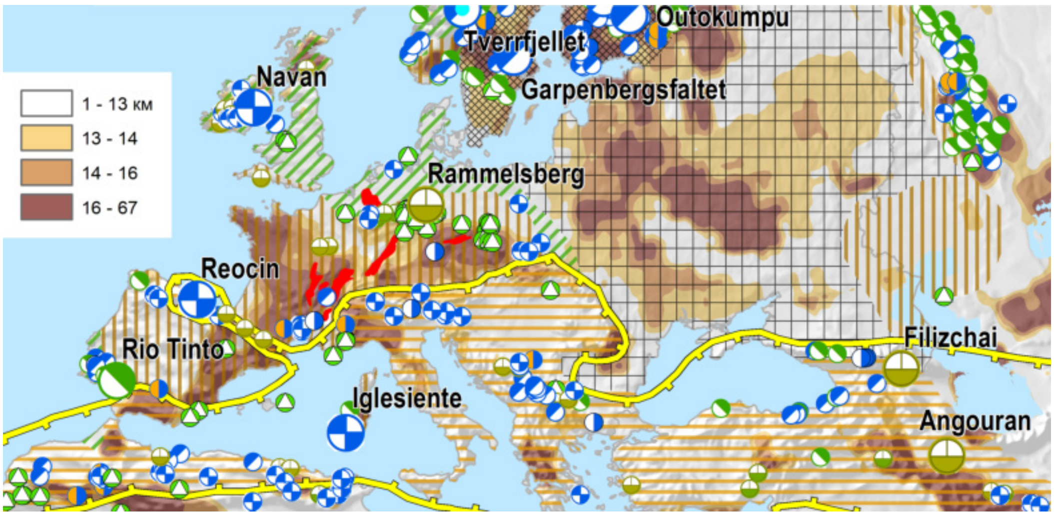

(c)

Figure 5. Thickness of the upper (a), middle (b) and lower (c) layers of the earth's crust and the location of polymetallic deposits in Western Europe (using materials from [*Laske et al.*, 2013]). Rifts are shown in red, rest. conventional designation see Figure 1, Figure 3.

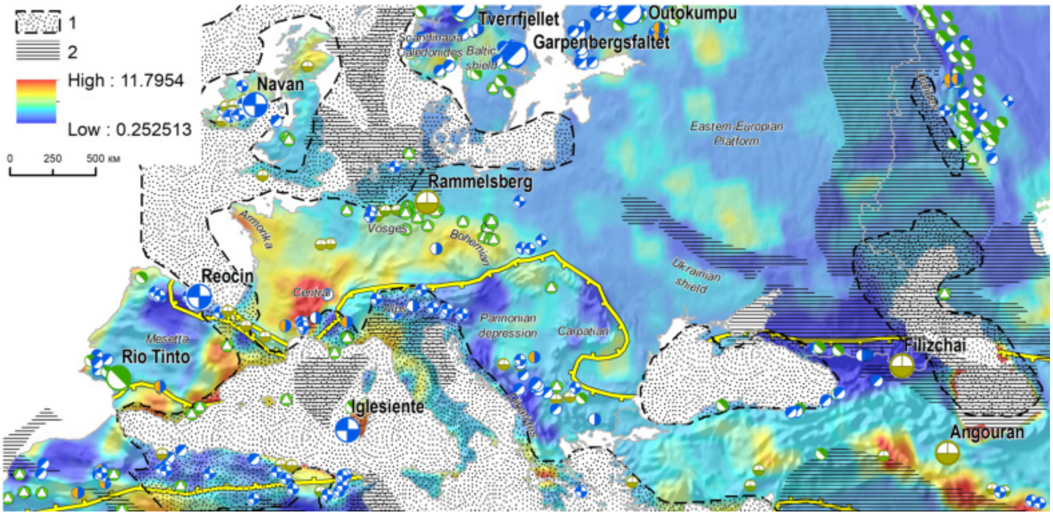

Figure 6. Polymetallic deposits of Europe and the ratio (from 4:1 to 1:11) of the lower and middle layers of the earth's crust (based on materials from [*Laske et al.*, 2013; *Richards*, 2015; *USGS*, 2012]). 1 – troughs of the sedimentary crust, 2 – oil and gas provinces.

As a result of orogenic thickening of the crust, thermal erosion occurs [*Zhang*, 2007] and delamination, in which the lower "mafic" crust and the underlying lithospheric mantle are stratified into blocks of varying buoyancy, the denser of which sink into the asthenosphere [*Hacker et al.*, 2015; *Houseman and Molnar*, 1997; *Pirajno*, 2009]. This leads to a rapid compensatory rise of the less dense asthenospheric mantle, followed by decompression melting [*Luchitskaya*, 2014], mafic underplating, and partial melting of lower crust materials [*Artemieva and Meissner*, 2012; *Pirajno*, 2009] and intraplate basaltic magmatism [*Mo et al.*, 2007]. All this leads to a general decompression of the crust and thickening in seismic imaging. This is evidenced by the results of geophysical studies, according to which decompression of the crust and upper mantle under the Central Tien Shan has been established, which is associated with retrograde metamorphism of rocks [*Makarov*, 2005]. A decrease in the speed of seismic waves due to decompaction is also observed under mountainous areas (Tibet, the Caucasus, the Carpathians and the Alps).

4.2. Subduction, accretion and VMS deposits

The thickness of the upper "granite-gneiss" crust can also be increased due to subduction, obduction, accretion and magmatism during collisional orogenesis [*Artemieva and Meissner*, 2012]. This is reflected in the existence of a thick "felsic" middle crust beneath deformed complexes of volcanic arcs and accretionary prisms. This feature is clearly manifested in the structure of the Dinarides and Western Alps system (Figure 5b).

The subduction paleothethic island arc process in the Alps determined back-arc spreading, rifting, and ophiolite formation in the Devonian period [*Graciansky et al.*, 2010]. Later, the formation complexes that had formed by this time were accreted to the subduction and obduction zone under the Apulian-African plate. The continuation of the collision of the European and African plates led to a thickening of the accretionary prism.

The Dinarides, like the Alps, are a fold-and-thrust belt that extends from the Southern Alps in the northwest to the Hellenides in the southeast [*van Unen et al.*, 2019]. The main structural elements of the Dinarides are manifested in Early-Middle Triassic rift troughs and accompanying magmatism [*Huismans et al.*, 2002; *Robertson et al.*, 2009]. Subduction and subsequent decompression of the continental crust led to the formation of a back-arc basin with ophiolitic melange, the influence of which is associated with the formation of VMS (Cypriot) type pyrite deposits in the Serbo-Macedonian volcanic belt.

It should also be mentioned that VMS pyrite deposits are confined to areas of thickening of the middle crust in the Svecofennian accretionary orogen [*Balagansky et al.*, 2016]. The Svecofennian orogenic block was formed as a result of the subduction of oceanic crust under the Karelian craton, the subsequent formation of island arcs containing numerous pyrite volcanogenic deposits, and their accretion. The multi-stage nature of accretion determined the complex nature of the Svecofennian accretionary structures and the subsequent rifting of the Karelian craton, which determined intraplate magmatism and the accompanying copper-nickel mineralization.

At the same time, there is no evidence of thickening of the middle crust in the Iberian pyrite belt, which hosts VMS and SEDEX pyrite ores of the Cadomian and Hercynian age. The Hercynian metallogenesis of the belt was caused by transpressional deformations of the crust [*Tornos et al.*, 2004], which represented an active continental margin. With subsequent movements, it was transformed into a collision zone, which could have affected the thickening of the upper and middle crust relative to the lower crust. However, recent seismic studies have shown that at a depth of 10–15 km, under the Ossa Morena zone, a large flat and dense magmatic body is found, possibly of mafic-ultrabasic composition and Hercynian age (Figure 5b). The parameters and properties of this body could have caused a general increase in the density of this part of the middle layer and a corresponding upward displacement of the seismic roof of the lower crust.

4.3. Rifting and SEDEX and SSC deposits

The process of thickening of the earth's crust associated with mantle influence is usually accompanied by diapirism of the asthenosphere [*Mazukabzov et al.*, 2011], basification (in the understanding of Academician V. V. Belousov) and eclogitization [*Pavlenkova et al.*, 2016]. The thickness of the crust also increases during the formation of large igneous provinces [*Artemieva and Meissner*, 2012]. The thickness of the earth's crust within the provinces averages about 40 km, while the lower crust, due to powerful basaltic magmatism, has an increased thickness (20 km), sometimes due to the reduction of the overlying "granite-gneiss" layer.

The consequence of thickening, layering and decompression of the earth's crust is rifting [*Pirajno*, 2009], the development of which is associated with the formation of many deposits (Carlinsky, stratiform, epithermal and other types). In general, rifting is also characterized by thinning of the middle "acidic" layer and thickening of the "mafic" layer of the earth's crust [*Artemieva and Shulgin*, 2019].

Confinement of polymetallic SEDEX deposits to areas of back-arc and continental-margin rifting is a common phenomenon in the world [*Groves and Bierlein*, 2007]. At the same time, for riftogenic areas, a feature of the deep structure of the earth's crust is noted – a local thickening of its lower "mafic" layer (Figure 5b). Thickening of the lower "mafic" crust is observed mainly in broad areas of spreading and rifting of the continental margin.

In the Western Alps, where local thickening of the lower crust is noted (Figure 5b), rifting occurred in the Early Cretaceous period and was caused by stretching and thinning of the continental lithosphere [*Graciansky et al.*, 2010]. Early phases of extension are associated with the development of Tethys in the Eastern Mediterranean.

The deposits of Central Europe (Rammelsberg, Bieber, etc.) were formed during the early rift phase of the development of the passive continental margin [*Leach et al.*, 2005]. The position of pyrite lead-zinc ores gravitates to the area of thickening of the lower crust (Figure 5b), on the passive continental margin with rift structures (Limanskaya, Bresskaya, Rhine, etc.), among organic-rich Middle Devonian siliceous-clastic rocks.

In areas of rifting there are also deposits of cuprous sandstones and shales (France, Germany, Poland). The currently accepted model for the formation of these ores during the period of diagenesis. Copper sandstone and shale (SSC) occurrences occur in Zechstein rocks in the Permian basin, extending from Great Britain through the southern North Sea, northern Germany and Poland to Lithuania. The basin is an inland trough and contains carboniferous sediments with thick coal deposits. The role of metalliferous fluids was played by seawater, which migrated down through the sediments into the basement [*Blundell et al.*, 2007]. In areas of Triassic rifting and elevated thermal conditions, ore-bearing fluids migrated upward along faults and fractures.

The Iberian Axial Zone in the northeast of the Iberian Peninsula, which hosts Ordovician lead-zinc deposits of the SEDEX type, is part of the Alpine orogeny associated with the collision between the Iberian block and the European plate. This fold belt is characterized by local thickening of the Earth's crust, with thickening of the lower crust covering larger areas (Figure 5b). The earlier history of the development of the Zone affects the Late Jurassic rifting in the Northern Iberian and Sub-Pyrenean basins, which separated the Iberian Peninsula from the Armorican massif.

In the Western Mediterranean, the redbed facies is similar in age, lithology, sedimentation history, diagenesis and orogenesis to individual Mesozoic deposits of the interior Apennines and Maghreb [*Perri et al.*, 2013]. They consist primarily of siliciclastic clastic materials, including sandstone, silt and clays, brought from areas of Paleozoic metasedimentary and metvolcanic rocks. Copper mineralization is represented by chrysocolla, azurite and malachite. The burial depth of the ores is at least 4–6 km with temperatures of 140–160 °C typical of the diagenetic stage.

The association of exhalation polymetallic deposits of the SEDEX and SSC types with paleorift structures may be associated with the processes of interaction of lower crustal and mantle fluid material due to delamination and mantle convection. Pyrite VMS deposits in volcanic rocks are determined by upper- and middle-crustal fluids, which, as a result of subduction and orogenesis, subsequent thickening of the crust, its delamination and metasomatism, are ultimately a product of the interaction of mantle-lower crustal and middle-upper crustal matter. All this does not contradict established ideas about the commonality of conditions and the mechanism of formation of ores of these types, as members of a continuous series [*Donets and Konkin*, 2017; *Ruchkin*, 1984].

4.4. Sedimentary cover and Pb-Zn deposits of MVT type

Mississippian and similar deposits, unlike VMS and SEDEX, were formed from sources with a very complex history. As spatial analysis shows, the formation of ores is not associated with the dynamic interaction of plates, and no patterns are observed in the placement of ores relative to the ratio of crustal layers. According to popular ideas [*Leach et al.*, 2005], the formation of these ores was determined by tectonic deformations and metasomatic changes in the ore-bearing strata of the subplatform cover. Deposits of this type are localized on the flanks of intra- and pericratonic basins formed in the extensional regime of the passive margin with terrigenous-carbonate sedimentation with hydrocarbon specialization and crustal sources of metals and sulfur [*Gorzhevsky and Makeeva*, 1982; *Leach et al.*, 2005; *Pavlov and Galyamov*, 1988; *Ruchkin and Donets*, 2002]. At the same time, the deposits gravitate towards deep sedimentary basins in the upper and middle layers of the sedimentary non-metamorphosed crust. There are many examples of this in Western Europe.

Consedimentation tectonic movements associated with rifting of deep Mesozoic basins in the Cantabrian region (with stratiform MVT deposits) caused facies variability of sediments, the presence of unconformities and paleokarst [*Velasco et al.*, 2003]. At the Reocín deposit, the productive ore stage appeared in the late stages of dolomitization, when ore was deposited in karst.

The circulation of metal-bearing fluids and the filling of karst occurred in post-Albian times. Carbon and oxygen isotopic signatures indicate that the metalliferous fluids were typical bottom brines [*Velasco et al.*, 2003]. The main source of metals was most likely siltstones and black carbonaceous shales. Metal chloride-rich brines were likely displaced from underlying sediments during burial compaction and diagenesis. The main reservoir of metals was most likely the underlying ones. Lead isotopy indicates its upper crustal origin [*Velasco et al.*, 2003].

In the Triassic deposits of the Eastern and Southern Alps, numerous lead-zinc occurrences of the Mississippian type are known. They are also found in the Central Alps and the adjacent European Plate of Austria. Economically important deposits are Bleiberg (Austria), Mesice and Topla (Slovenia) and the Italian Raibl and Salafossa in the south. All these Pb-Zn deposits were classified as the Alpine subtype [*Schroll*, 2005] and are located along the northern periphery of the Po oil and gas basin [*USGS*, 2012]. Ore-bearing Mesozoic carbonates overlie Permian and Early Triassic sandstones overlying the metamorphic basement. The origin of deposits of this subtype is associated with the development of the basin at the platform stage and subsequent tectonic events. In general, the characteristics of these deposits define the subclass of "low-temperature Pb-Zn objects in carbonate rocks," the ores of which were located in the bottom conditions of platform carbonate sedimentation, not exposed to thermal sulfate reduction [*Schroll*, 2005].

Stratiform deposits of the MVT type are also common in the North-East of Algeria, which represents the most important metallogenic zone of Pb-Zn-Fe-Ba (Cu, F, Sr) ore deposits. The mineral assemblage is represented by galena, sphalerite, barite, celestine, pyrite, chalcopyrite and marcasite in dolomite and limestone [*Ysbaa et al.*, 2021]. Stratiform lead-zinc deposits and occurrences of the MVT type (Ain Kahla, Chellala, Djebel Gustar, El Abed, etc.) are located in the section near the Hercynian basement, on the periphery of Mesozoic sedimentary basins. The formation of the deposits is associated with basin brines, the migration of which was caused by Atlas folding and, probably, Miocene tectonic activation.

In addition, general spatial analysis shows that the areas of MVT mineralization are located in areas with a reduced overall seismic thickness of the earth's crust (Figure 4), which can be explained by eclogitization of its lower horizons. In these environments, the process of crustal subsidence and the formation of oceanic basins with rifting intensifies. At the same time, the superimposed transformations of sedimentary rocks are limited by autometasomatosis, and mobile hydrocarbons were involved in the mechanism of migration and unloading of ore-bearing fluids during stratiform lead-zinc ore formation. Further superimposed transformations of ores and host rocks determined the epigenetic appearance of ores and metasomatic formations.

Thus, a comparison of the position of polymetallic deposits in different tectonic settings shows that there are two typical relationships of layers of the earth's crust (Table 1, Figure 5, Figure 6): 1) supra-subduction and back-arc riftogenic areas of local thickening of the middle "granite" and upper "metamorphic" left of the earth's crust (Balkan Dinarides, Taurids and Pontids in Turkey); 2) rift structures of the passive margin with the predominant development of the lower "mafic" layer of the crust (Central Europe, Iberian Zone, Turkish Taurides). Separately, the settings of pericratonic troughs with subplatform oil and gas complexes are highlighted (basins – Anglo-Danish, Po in Italy, Zagros in Turkey).

5. Conclusion

Spatial analysis of the distribution of Pb-Zn deposits in the folded frame of the Western and Eastern European platforms and the Mediterranian segment of the Tethys belt and comparison of the geodynamic settings of their formation indicates the following:

1. Sedimentary-exhalation polymetallic and silver-polymetallic deposits are confined to territories with the predominant development of the lower "mafic" layer of the earth's crust. SEDEX ores, as well as cuprous sandstones and shales (SSC), which were deposited closely simultaneously with the host rocks, are closely related to the rifting settings of mafic volcanism of the active and passive continental margin, with deep sources of fluids at the lower crustal and upper mantle levels.
2. VMS copper and lead-zinc deposits are located, more often, in supra-subduction island-arc and accretionary settings on consolidated crust with the predominant development of the middle "granite" layer. SEDEX-type mineralization also occurs in these settings, due to bottom fluid activation associated with island arc volcanism.

Table 1. Typical relationships of crustal layers and geodynamic regimes framing the Western European Platform and the Mediterranean segment of the Tethys belt.

Relationship between layers of the earth's crust	Thickened middle "granite" layer	Thickened lower "basaltic" layer	Platform frame
Geodynamic mode	Suprasubduction and accretion settings	Rifting on the passive margin and in the back arcs zone of active margins	Pericratonic platform basins with hydrocarbon specialization
Mechanism of mass transfer "mantle-crust"	Subduction and delamination transport crustal material into the mantle, building up continental crust	Mafic mantle magmatism transports mantle material upward and participates in the growth of new crust.	
Depth of metal sources	Middle and lower crust	Mantle – lower crust	Sedimentary and upper crust
Ore-formation type of deposits	Volcanogenic VMS deposits	SEDEX and SSC deposits	MVT Pb-Zn deposits in carbonate rocks

3. MVT-type stratabound lead-zinc ores are closely associated with pericratonic deep sedimentary petroleum basins on the shelf and continental slope. At the same time, their spatial connection with the stratification of the earth's crust is not obvious. The ores of this type were formed at the platforms frame in a carbonate host environment in sedimentary basins with hydrocarbon specialization for a long time, which determines the polychronism of their genesis and the epigenetic appearance of the ores. According to recent research results [*Zhou et al.*, 2022] in Chinese SEDEX- and MVT-type deposits, the source of sulfur in SEDEX ores was a sea water, and in MVT ores – a catagenetic elision fluids. The source of metals for SEDEX ores was mainly the deep basement rocks, and for MVT ore – the host sedimentary strata. Rifting determined the occurrence of synsedimentary SEDEX mineralization, and the formation of MVT ores at shallow levels of the earth's crust was determined by orogenesis.

At the same time, despite the numerous studies of hydrothermal ore-forming processes, an important objective still remains the identification of the mechanism of structural and matter interaction between the crust and the mantle and the evolution of fluids when moving from deep sources to the area of ore formation.

The results obtained can be used for regional forecasting and metallogeny, prospecting and assessment of new gold deposits.

Acknowledgments. The work was supported in terms of the State assignment of IGEM RAS.

References

Artemieva, I. M., and R. Meissner (2012), Crustal thickness controlled by plate tectonics: A review of crust–mantle interaction processes illustrated by European examples, *Tectonophysics*, *530–531*, 18–49, https://doi.org/10.1016/j.tecto.2011.12.037, EDN: PGPTQX.

Artemieva, I. M., and A. Shulgin (2019), Making and altering the crust: A global perspective on crustal structure and evolution, *Earth and Planetary Science Letters*, *512*, 8–16, https://doi.org/10.1016/j.epsl.2019.01.033, EDN: MKCXGQ.

Asch, K. (2003), *The 1 : 5 Million International Geological Map of Europe and Adjacent Areas. Development and Implementation of a GIS-enabled Concept*, Schweizerbartsche Verlagsbuchhandlung, E.

Balagansky, V. V., I. A. Gorbunov, and S. V. Mudruk (2016), Paleoproterozoic Lapland-Kola and Svecofennian orogens (Baltic Shield), *Herald of the Kola Science Center of RAS*, (3(26)) (in Russian).

Belousov, V. V., and N. I. Pavlenkova (1989), Types of the earth's crust in Europe and the North Atlantic, *Geotectonics*, (3), 3–14 (in Russian).

Blundell, D., N. Arndt, P. R. Cobbold, and C. Heinrich (2007), Geodynamics and Ore Deposit Evolution in Europe. Special Issue of Ore Geology Reviews, *Geological Magazine*, *144*(3), 604–604, https://doi.org/10.1017/S0016756806002743, EDN: HZKEHL.

Boni, M., and G. C. Amstutz (1982), The Permo-Triassic Paleokarst Ores of Southwest Sardinia (Iglesiente-Sulcis). An Attempt at a Reconstruction of Paleokarst Conditions, in *Ore Genesis*, pp. 73–82, Springer Berlin Heidelberg, https://doi.org/10.1007/978-3-642-68344-2_8.

Bortnikov, N. S., A. V. Volkov, A. L. Galyamov, I. V. Vikentyev, V. V. Aristov, A. V. Lalomov, and K. Y. Murashov (2016), Mineral resources of high-tech metals in Russia: state and development prospects, *Geology of ore deposits*, *58*(2), 97–119, https://doi.org/10.7868/S0016777016020027 (in Russian), EDN: VTOUMD.

Cammarano, F., and M. Guerri (2017), Global thermal models of the lithosphere, *Geophysical Journal International*, *210*(1), 56–72, https://doi.org/10.1093/gji/ggx144, EDN: YDPNNZ.

Dergachev, A. L., and N. I. Eremin (2008), The relationship between volcanic sulfide and stratiform lead-zinc mineralization in the history of the Earth, *Vestnik Moskovskogo Universiteta. Seriâ 4: Geologiâ*, (4), 26–34 (in Russian), EDN: JVAPUT.

Donets, A. I., and V. D. Konkin (2017), Geological and industrial types and regional geological features of stratiform lead-zinc deposits in carbonate strata, *Otechestvennaya Geologia*, (6), 31–39 (in Russian), EDN: ZWQMHR.

Fountain, D. M., R. Arculus, and R. W. Kay (Eds.) (1993), *Continental Lower Crust*, *Developments in Geotectonics*, Elsevier.

Galyamov, A. L., A. V. Volkov, and K. V. Lobanov (2021), Application of Models of the Earth's Crust-Depth Structure Based on GOCE Satellite Gravitational Data for Forecasting and Prospecting Pb–Zn Deposits in the Arctic Zone of Russia, *Izvestiya*, *Atmospheric and Oceanic Physics*, *57*(12), 1751–1761, https://doi.org/10.1134/S0001433821120082.

Galyamov, A. L., A. V. Volkov, and K. V. Lobanov (2022), Lithospheric Control of the Location of Polymetallic Deposits in the Folded Framework of the Siberian Platform, *Doklady Earth Sciences*, *506*(2), 756–760, https://doi.org/10.1134/S1028334X22600396.

Galyamov, A. L., A. V. Volkov, K. V. Lobanov, and K. Y. Murashov (2023), Structure of the Earth's crust according to gravity data from the GOCE satellite and the patterns of location of polymetallic deposits in the frame of the Siberian and East European platforms, *Issledovaniye Zemli iz kosmosa*, (1), 3–23, https://doi.org/10.31857/S0205961423010049 (in Russian), EDN: MLTXIF.

Gorzhevsky, D. I., and I. T. Makeeva (1982), *Stratiform deposits of non-ferrous metals: (Localization conditions and origin of stratiform deposits of lead, zinc and copper)*, VINITI, Moscow (in Russian).

Graciansky, P.-C. D., D. G. Roberts, and P. Tricart (2010), *Western Alps, from Rift to Passive Margin to Orogenic Belt. An Integrated Geoscience Overview*, Elsevier.

Groves, D. I., and F. P. Bierlein (2007), Geodynamic settings of mineral deposit systems, *Journal of the Geological Society*, *164*(1), 19–30, https://doi.org/10.1144/0016-76492006-065.

Hacker, B. R., P. B. Kelemen, and M. D. Behn (2015), Continental Lower Crust, *Annual Review of Earth and Planetary Sciences*, *43*(1), 167–205, https://doi.org/10.1146/annurev-earth-050212-124117.

Hasterok, D., J. A. Halpin, A. S. Collins, M. Hand, C. Kreemer, M. G. Gard, and S. Glorie (2022), New Maps of Global Geological Provinces and Tectonic Plates, *Earth-Science Reviews*, *231*, 104,069, https://doi.org/10.1016/j.earscirev.2022.104069.

Houseman, G. A., and P. Molnar (1997), Gravitational (Rayleigh-Taylor) instability of a layer with non-linear viscosity and convective thinning of continental lithosphere, *Geophysical Journal International*, *128*(1), 125–150, https://doi.org/10.1111/j.1365-246x.1997.tb04075.x.

Huismans, R. S., Y. Y. Podladchikov, and S. A. P. L. Cloetingh (2002), The Pannonian basin: Dynamic modelling of the transition from passive to active rifting, *Stephan Mueller Special Publication Series*, *3*, 41–63, https://doi.org/10.5194/SMSPS-3-41-2002.

Klyuykov, A. A. (2018), New era in the study of the Earth's gravitational field, *Naučnye trudy Instituta astronomii RAN*, (2(2)), 20–25, https://doi.org/10.26087/INASAN.2018.2.2.003 (in Russian), EDN: YRNSAX.

Laske, G., G. Masters, Z. Ma, and M. E. Pasyanos (2013), Update on CRUST1.0-A 1-degree global model of Earth's crust, *Geophysical Research Abstracts*, *15*.

Leach, D. L., D. F. Sangster, K. D. Kelley, R. R. Large, G. Garven, C. R. Allen, J. Gutzmer, and S. Walters (2005), Sediment-Hosted Lead-Zinc Deposits: A Global Perspective, in *One Hundredth Anniversary Volume*, pp. 561–607, Society of Economic Geologists, https://doi.org/10.5382/AV100.18.

Luchitskaya, M. V. (2014), *Granitoid magmatism and continental crust formation of the northern framework of Pacific Ocean in Mesozoic-Cenozoic*, 607, GEOS, Moscow (in Russian), EDN: XRALJB.

Makarov, V. I. (Ed.) (2005), *Recent geodynamics of areas of intracontinental collision mountain building (Central Asia)*, Scientific world, Moscow (in Russian).

Mazukabzov, A. M., E. V. Sklyarov, T. V. Donskaya, and D. V. Gladkochub (2011), Complexes of metamorphic cores of Central Asia and their nature, in *Geodynamic evolution of the lithosphere of the Central Asian mobile belt (from ocean to continent): Proceedings of the meeting*, vol. 9, pp. 134–139, Institute of the Earth's Crust SB RAS, Irkutsk (in Russian).

Mo, X., Z. Hou, Y. Niu, G. Dong, X. Qu, Z. Zhao, and Z. Yang (2007), Mantle contributions to crustal thickening during continental collision: Evidence from Cenozoic igneous rocks in southern Tibet, *Lithos*, *96*(1–2), 225–242, https://doi.org/10.1016/j.lithos.2006.10.005.

Pavlenkova, N. I., S. N. Kashubin, and G. A. Pavlenkova (2016), The Earth's crust of deep platform depressions of Northern Eurasia and the nature of their formation, *Physics of the Earth*, (5), 150–164, https://doi.org/10.7868/S0002333716050124 (in Russian), EDN: WHWCBF.

Pavlov, D. I., and A. L. Galyamov (1988), Geological relationships between stratiform lead-zinc mineralization and oil-producing strata (on the example of Southern Verkhoyansk), *Litologiâ i poleznye iskopaemye*, (3), 89–100 (in Russian).

Perri, F., S. Critelli, A. Martín-Algarra, M. Martín-Martín, V. Perrone, G. Mongelli, and M. Zattin (2013), Triassic redbeds in the Malaguide Complex (Betic Cordillera — Spain): Petrography, geochemistry and geodynamic implications, *Earth-Science Reviews*, *117*, 1–28, https://doi.org/10.1016/j.earscirev.2012.11.002.

Pirajno, F. (2009), *Hydrothermal Processes and Mineral Systems*, Springer Netherlands, EDN: SQMGED.

Plant, J., A. Whittaker, A. Demetriades, B. de Vivo, and J. Lexa (2005), The geological and tectonic framework of Europe, in *FOREGS Geochemical Atlas of Europe. Part 1: Background Information. Methodology and Maps*, pp. 23–42, Geological Survey of Finland ESPOO.

Reguzzoni, M., and D. Sampietro (2015), GEMMA: An Earth crustal model based on GOCE satellite data, *International Journal of Applied Earth Observation and Geoinformation*, *35*, 31–43, https://doi.org/10.1016/j.jag.2014.04.002.

Richards, J. P. (2015), Tectonic, magmatic, and metallogenic evolution of the Tethyan orogen: From subduction to collision, *Ore Geology Reviews*, *70*, 323–345, https://doi.org/10.1016/j.oregeorev.2014.11.009.

Robertson, A., S. Karamata, and K. Šarić (2009), Overview of ophiolites and related units in the Late Palaeozoic–Early Cenozoic magmatic and tectonic development of Tethys in the northern part of the Balkan region, *Lithos*, *108*(1–4), 1–36, https://doi.org/10.1016/J.LITHOS.2008.09.007.

Ruchkin, G. V. (1984), *Precambrian stratiform base metal deposits*, Nedra, Moscow (in Russian).

Ruchkin, G. V., and A. I. Donets (2002), *Stratiform lead-zinc deposits in carbonate strata*, 123 pp., TsNIGRI, Moscow (in Russian).

Schroll, E. (2005), Alpine type Pb-Zn-deposits (APT) hosted by Triassic carbonates, in *Mineral Deposit Research: Meeting the Global Challenge*, pp. 175–178, Springer Berlin Heidelberg, https://doi.org/10.1007/3-540-27946-6_46.

Tornos, F., C. Inverno, C. Casquet, A. Mateus, G. Ortiz, and V. Oliveira (2004), The metallogenic evolution of the Ossa-Morena zone, *Journal of Iberian Geology*, *30*, 143–180.

Trifonov, V. G. (2017), *Neotectonics of moving belts*, 614, GEOS, Moscow (in Russian), EDN: RTGVPV.

USGS (2012), Map of undiscovered conventional oil and gas resources of the world, https://certmapper.cr.usgs.gov/data/apps/world-energy/?resource=conventional, (date of access: 10.08.2023).

van Unen, M., L. Matenco, F. H. Nader, R. Darnault, O. Mandic, and V. Demir (2019), Kinematics of Foreland-Vergent Crustal Accretion: Inferences From the Dinarides Evolution, *Tectonics*, *38*(1), 49–76, https://doi.org/10.1029/2018TC005066.

Velasco, F., J. M. Herrero, I. Yusta, J. A. Alonso, I. Seebold, and D. Leach (2003), Geology and Geochemistry of the Reocin Zinc-Lead Deposit, Basque-Cantabrian Basin, Northern Spain, *Economic Geology*, *98*(7), 1371–1396, https://doi.org/10.2113/98.7.1371.

Volkov, A. V., A. L. Galyamov, P. E. Belousov, and A. A. Wolfson (2020), Application of space technologies in metallogenic analysis of the Russian Arctic territory, *Arctic: Ecology and Economy*, (2(38)), 77–85, https://doi.org/10.25283/2223-4594-2020-2-77-85 (in Russian), EDN: GFSZJJ.

Vos, W. D., M. J. Batista, A. Demetriades, M. Ďuriš, J. Lexa, J. Lis, K. Marsina, and P. O'Connor (2005), Metallogenic mineral provinces and world class ore deposits in Europe, in *FOREGS Geochemical Atlas of Europe. Part 1: Background Information. Methodology and Maps*, Geological Survey of Finland ESPOO.

Ysbaa, S., O. Haddouche, A. Boutaleb, L. Sami, and O. Kolli (2021), Mineralization and fluid inclusion characteristics of Pb-Zn-Fe-Ba (Cu, F, Sr) ore-deposits in northern east of Algeria, *Arabian Journal of Geosciences*, *14*(11), https://doi.org/10.1007/s12517-021-07281-2.

Zhang, H.-F. (2007), Temporal and spatial distribution of Mesozoic mafic magmatism in the North China Craton and implications for secular lithospheric evolution, *Geological Society, London, Special Publications*, *280*(1), 35–54, https://doi.org/10.1144/SP280.2.

Zhou, Z., H. Wen, J. de Fourestier, C. Qin, and L. Liu (2022), Sulphur and metal sources of polymetallic vein-type, sedimentary exhalative-type and Mississippi Valley-type Zn–Pb deposits along the southeast margin of the Yangtze Block, *Ore Geology Reviews*, *147*, 104,957, https://doi.org/10.1016/j.oregeorev.2022.104957.

RUSSIAN JOURNAL of EARTH SCIENCES

SPECIAL ISSUE: "25TH ANNIVERSARY OF THE RUSSIAN JOURNAL OF EARTH SCIENCES"

Structural Tectonic Scheme Creation Based on Seismic-Gravity Models and Isostasy Usage: Ural Case

P. S. Martyshko[*,1], **I. V. Ladovskii**[1], **D. D. Byzov**[*,1], **A. G. Tsidaev**[1]

[1] Bulashevich Institute of Geophysics, Ekaterinburg, Russia
* **Correspondence to:** Petr Martyshko, pmart3@mail.ru

Abstract: Process of Earth's density models creation leads to the solution of direct and inverse gravimetry problems. The inverse problem of gravimetry is a classic example of an ill-posed problem: in the common statement, its solution is not unique and unstably depends on input data. Therefore, it is necessary to determine solutions belonging substantial sets of correctness, choosing reasonable models of an initial approximation. In this paper the application of complex interpretation methods of seismic and gravitational data for the creation of three-dimensional models of crust and the upper mantle are presented. Original algorithms and programs were developed for implementation of these methods. They contain solution of non-linear (structural) inverse problem and the solution of the linear three-dimensional inverse problem taking note of the side sources. Coefficients of the "density-velocity" correlation formulas for a number of geo-traverses were defined. Also, we suggest a technique of tectonic maps construction, which is based on the lithostatic pressure calculation. Its idea can be applied to both two- and three-dimensional cases. In the 2D case we show the way to split the mantle to blocks with vertical boundaries. If lithostatic compensation hypothesis is adopted, the method also allows one to calculate density value for each block. Such separation of the mantle helps to diminish discrepancy between model and observed fields. In 3D case we suggest a method, which can be used to construct tectonic structure maps with information about approximate depth and height of each tectonic block.

Keywords: density crust models, geophysical data interpretation, inverse gravity problems.

Citation: Martyshko P. S., Ladovskii I. V., Byzov D. D., Tsidaev A. G. (2024), Structural Tectonic Scheme Creation Based on Seismic-Gravity Models and Isostasy Usage: Ural Case, *Russian Journal of Earth Sciences*, Vol. 24, ES1007, https://doi.org/10.2205/2024ES000896

RESEARCH ARTICLE

Received: 15 October 2023
Accepted: 15 January 2024
Published: 29 February 2024

1. Introduction

The results of complex interpretation of geophysical data are geological and geophysical models of structure of Earth's upper lithosphere (crust and upper mantle). One of main indicators of model correctness is a density [*Strakhov and Romanyuk*, 1984]. This is because density reflects petrophysical features of inhomogeneous structure and lithological consistency more than any of other physical parameters.

It is known that the most visible income to anomaly gravity field is generated by inhomogeneities that are located in upper part of geological cut (depth down to 10–15 km). However, seismic survey shows that seismic waves velocity is inhomogeneous not only in the crust, but also in the upper mantle. Therefore, we can build a compensated model where gravity anomaly from different inhomogeneous layers are partially (or fully) compensated. Such a model is a possible density analogue for the velocity model of the deep structures. The idea of the gravity and seismic methods combination is transparent. Seismic data allows one to build models of the lithosphere structure down to some specified depth. Gravity data can be used to connect model density with the observed gravity anomalies. This joint interpretation is performed under empirical constraints. Correlation between longitudinal waves velocities in inhomogeneous media and densities of different rocks defines desired result. Our goal is to select morphologically similar structures in anomaly fields of different nature. But the gravity field contains integral information about all the lithosphere features in the whole depths interval from the surface to the mantle. Thus, blocks selected by the gravity field could not be split by depth. Moreover, these blocks are usually invisible in horizontal maps of density distribution. So, even having the gravity field inverted, an attempt to separate lithosphere blocks by depth will most likely be unsuccessful. We propose a different approach. Assume that we have a density model, which can be obtained as a result of the gravity inversion or seismic velocity model conversion. Such a model is the input data for the calculation of the lithostatic pressure distribution. We calculate lithostatic pressure in a point by a mass of vertical rock column, which top is on the Earth surface and the lower end contains the point of calculation. Then, the mass is converted to the weight. But the lithostatic pressure itself is not representative parameter because pressure deviations inducted by density variations have much smaller value than pressure associated with absolute density values. Instead, we analyze lithostatic pressure anomaly, which is calculated as difference between the actual pressure value at the point and the mean pressure (hydrostatic) on this depth level. Similar approach was used by [*Jiménez-Munt et al.*, 2010]. Also the idea of usage of isostasy as an additional constrain in gravity inversion was studies in [*Geng et al.*, 2022; *Li and Yang*, 2020; *Satyakumar et al.*, 2023].

In this paper, we describe our method for both two- and three-dimensional cases. In the two-dimensional case, we also show how adoption of an idea of isostatic compensation helps one to reduce the error of density modelling (i.e., to minimize difference between the observed gravity field and one of the model). Isostatic compensation is the hypothesis that there are no more lateral changes in pressure starting from some depth level. For out study region (Ural Mountains in Russia and neighbouring areas), there is a theory of compensation on level of 80 km [*Druzhinin et al.*, 1990]. We performed our modelling under assumption that this theory is correct. However, we noticed that block structure can be traced even without actual performing of isostatic equalization of the model. In a three-dimensional case, we show that the block boundaries are visible just in the lithostatic model. Coordinate systems of lithostatic model and density model are equal, so, the block positions determined in the lithostatic model remain the same in the density model.

2. Data and Methods

Initial data is presented as gravity map of the region and deep seismic survey data along profiles. Figure 1 shows a fragment of the complete-Bouguer gravity anomaly map derived from the combined global gravity field model XGM2019e_2159_GA [*Zingerle et al.*, 2020] and converted to the Gauss-Krueger map projection coordinates. The positions of the regional seismic profiles are tied to the gravity map fragment; the structural schemes of tectonic zoning are used to verify the results of quantitative interpretation of gravity data. Study area is located inside trapezia 60°–68°N, 48°–72°E (Figure 1a). For territories in the boundaries of several 6-degree Gauss-Kruger zones it is permissible to use gravity model of flat layer. This is Near-Arctic zone of important Russian geological provinces junction: northeastern part of East-European platform, Timan-Pechora plate, northern part of Ural Folding System and northwestern sector of Western Siberia. Input data for initial 3D density model contains 3 parts: a) profile hodographs, time fields and appropriate 2d velocity models, b) empiric correlation between density and velocity and c) gravity field anomalies digital maps in Bougier reduction. The main stages of proposed methods are [*Martyshko et al.*, 2010, 2013, 2016] construction of velocity sections of the Earth's crust, refinement of the coefficients of the regression "velocity-density" dependence from the results of 2D gravitational modeling for the given region, construction of 3D model of the initial approximation, calculation of difference between observed and modelling field, extracting field from layers, density values calculating by method of local corrections with adaptive regularization in each layer. It is known that correlation between density and longitudinal wave velocity for Earth crust rocks can be represented as piece-wise linear regression dependence. Although the dependence coefficients are different for different regions, the trend is that density increases monotonically with increasing elastic waves speed. Density as well as velocity reflects petrochemical structure and physical mechanical state of rocks only partially. Linear regression does not regulate bijection "velocity-density", there can be fluctuation for both of values within the confidence interval. Any change is equiprobable. Modern views on Ural genesis and its platform structure were taken into account [*Druzhinin et al.*, 1990; *Sobolev et al.*, 1983] and form map of tectonic structures (Figure 1b). 2D velocity and corresponding density values along 10 seismic profiles form 3D carcass of initial model. Model itself is obtained after interpolation. We used gradient velocity cuts of region as the input data. Velocities were converted to density values using empirical formula *Martyshko et al.* [2017]. The following correlation between density and velocity was used for values recalculation. We had obtained this correlation as a result of inverse linear problem solution for 2D profiles [*Ladovskii et al.*, 2017]:

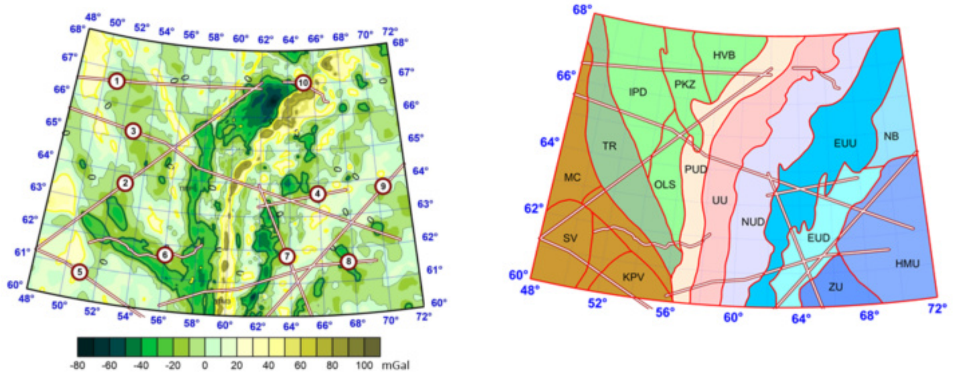

(a) **(b)**

Figure 1. a): gravity field and seismic profiles: 1) Agat-2; 2) Globus; 3) Quartz; 4) V. Nildino – Kazym; 5) Rubin-; 6) Syktyvkarsk; 7) N. Sosva – Yalutorovsk; 8) Krasnolelinsk; 9) Granit – Rubin-2; 10) Polar-Urals transsect. b): Tectonic scheme: Sysolsk vault (SV), Mezensk syneclise (MC), Komi-Perm vault (KPV), Timan ridge (TR), Izhma-Pechora depression (IPD), Omra-Luza saddle (OLS), PechoraKolvinsk zone (PKZ), Horeyversk basin (HVB), Pre-Urals deflection (PUD), Urals uplift (UU), Near-Urals deflection (NUD), East-Urals uplift (EUU), East-Urals deflection (EUD), Nadym block (NB), Zauralsk uplift (ZU), Hantymansiysk middle uplift (HMU).

$$\sigma(V) = \begin{cases} 0.113V + 2.034; 2.35 \leq V < 5, \\ 0.2V + 1.6; 5 \leq V < 7.75, \\ 0.25V + 1.3; 7.75 \leq V < 8.5. \end{cases}$$

Then we performed averaging filtration of density values and, thus, the initial model was obtained. Figure 2 presents one of the model cuts. All the models are constructed down to 80 km only, and we accepted the hypothesis of the existence of the isostatic compensation on this level.

Since the model is obtained as the result of seismic data interpretation, its calculated gravity field (Figure 2a, red curve) has significant discrepancy comparing with the observed one (Figure 2a, purple curve). Usage of isostasy hypothesis helps to reduce this difference [*Martyshko et al.*, 2017].

The lithostatic anomaly $\Delta P(x,z)$ is defined as difference between the lithostatic pressure $P(x,z)$ on a given level h and hydrostatic pressure calculated as mean pressure along the profile on the same depth

$$P(x,h) = g_a \int_h^0 \sigma(x,z)dz,$$
$$\overline{P}(h) = \frac{1}{L}\int_0^L P(x,h)dx = \frac{g_a}{L}\int_h^0 \int_0^L \sigma(x,z)dxdz = g_a \int_h^0 \overline{\sigma}(z)dz,$$
$$\Delta P(x,h) = P(x,h) - \overline{P}(h) = g_a \int_h^0 \Delta\sigma(x,z)dz.$$

Here, $g_a = 9.80665$ m/s^2 is the average value of gravity acceleration, $\sigma(x,z)$ is the density value at the point (x,z) of the cut, $\sigma(z)$ is the mean value of density on a depth z

$$\overline{\sigma}(z) = \frac{1}{L}\int_0^L \sigma(x,z)dx, \Delta\sigma(x,z) = \sigma(x,z) - \overline{\sigma}(z).$$

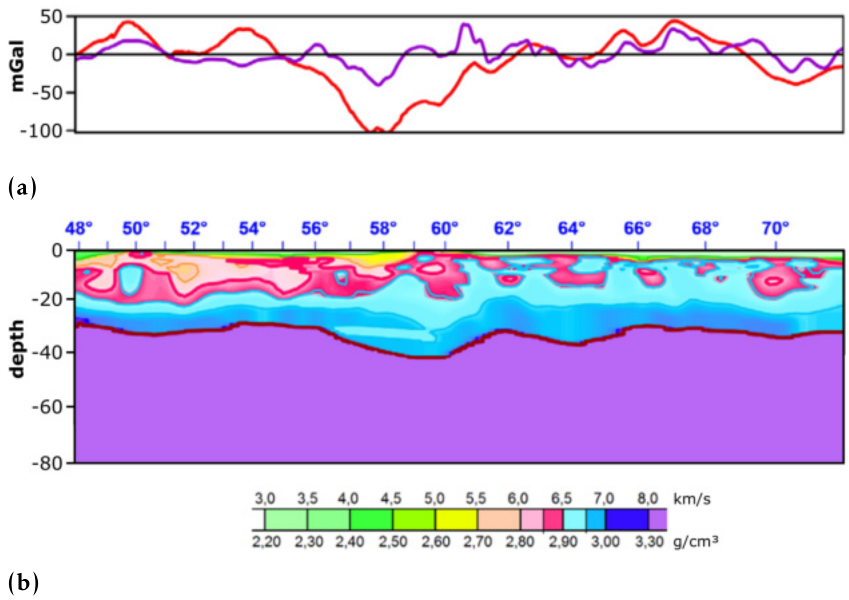

Figure 2. Density model with homogeneous mantle along the "Quartz" profile obtained from seismic data (b) and its gravity field (a, red curve) compared with the observed gravity field (a, purple curve).

Isostatically compensated model with the compensation level h_i should have no lateral pressure variations

$$\Delta P(x,h_i) = 0. \quad (1)$$

In our case, $h_i = -80$ km.

The lithostatic model for our density cut is presented in Figure 3. As it can be clearly seen, there is no constant value on $h_i = -80$ km.

To construct such a compensated model, we introduced compensation function $\rho(x)$. This compensator shows what density value should be subtracted from the mantle (in our case, this is the layer between the Mohorovicic discontinuity and the h_i level) to make condition (1) satisfied.

Let ΔP_{hom} and $\Delta\sigma_{\text{hom}}$ be the deviations of pressure and density from their mean values on given depth for the model with the homogeneous mantle. Lithostatic anomaly after addition of $\rho(x)$ is

$$\Delta P(x,h_i) = \Delta P_{\text{hom}}(x,h_i) - g_a(h_m(x) - h_i)\rho(x).$$

Here $z = h_M(x)$ is Mohorovicic discontinuity position.

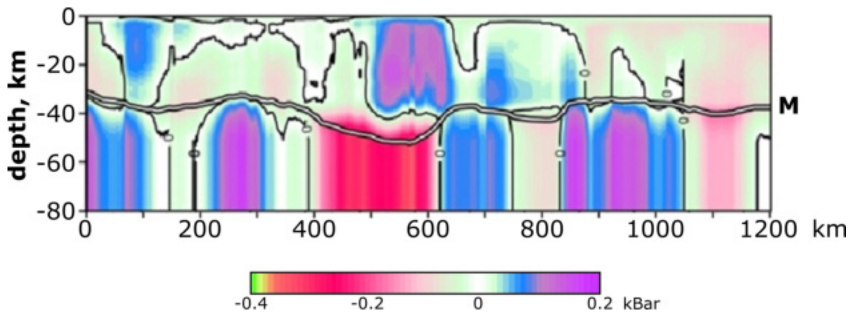

Figure 3. Lithostatic model for the "Quartz" density cut; the Mohorovicic discontinuity M is shown with the double line.

From condition (1), we have

$$\rho(x) = \frac{\Delta P_{\text{hom}}(x, h_i)}{g_a(h_m(x) - h_i)} = \frac{1}{h_m(x) - h_i} \int_{h_i}^{0} \Delta\sigma_{\text{hom}}(x, y)dy. \tag{2}$$

The compensator function for study cut is presented in Figure 4. As it could be easily predicted, it qualitatively repeats form of the Mohorovicic discontinuity. Zeros of compensator function were taken as boundaries of the mantle blocks. After, we distributed these excess densities in the upper mantle and performed density averaging inside blocks, and by this we obtained resulting density model (Figure 5).

As it can be seen from Figure 5a, the model field (red curve) now have a good match with the observed one (purple curve). Figure 6 presents the lithostatic model of resulting density distribution. There is isostatic compensation on $h_i = -80$ km now and the lithostatic anomaly on h_i is zero for almost all profile length. It is interesting to note that the same block boundaries could be selected without performing model compensation at all. Positions of blocks are clearly seen on the initial lithostatic model (Figure 3). Thus, for the case of relatively flat Mohorovicic discontinuity (when denominator of (2) is close to constant) blocks selection can be performed even for isostatically non-compensated model. We will use this approach in the three-dimensional case in the next section.

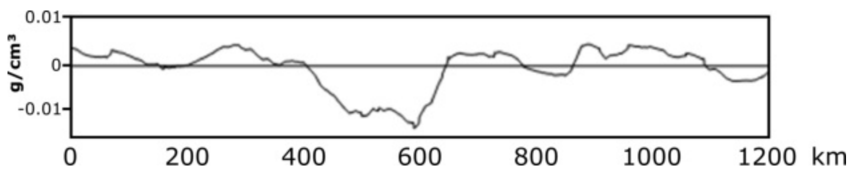

Figure 4. Compensating function for the "Quartz" density cut.

2D velocity cuts are digitized within the gravity field map limits and then are combined into 3D seismic carcass (Figure 7). This considers the mutual position of the seismic profiles (with curvature taken into account). Now we go to the 3D array of volume density model. The missing velocity data are filled with interpolated values. Interpolation was done in by slicing the model into 800 flat horizontal layers and performing triangulation and linear interpolation method for all of them. As the result the digital parallelepiped of 3D model is constructed [*Ladovskii et al.*, 2017].

2D-density models usage for 3D construction do not need high accuracy gravity field alignment along the profiles. It is enough to get qualitative agreement between model field and observed field projected to profile. There are 2 more important problems: correction for 3D density distribution near 2D profiles and removal of 3D model field edge attenuation outside the area under study.

Resulting 3D model contains 1336×969×800 discrete elements. Its anomaly gravity field is calculated using the background density, which is taken as a function of depth only. Such a density can be called "hydrostatical". It is used to calculate excessive density of anomaly masses on any depth.

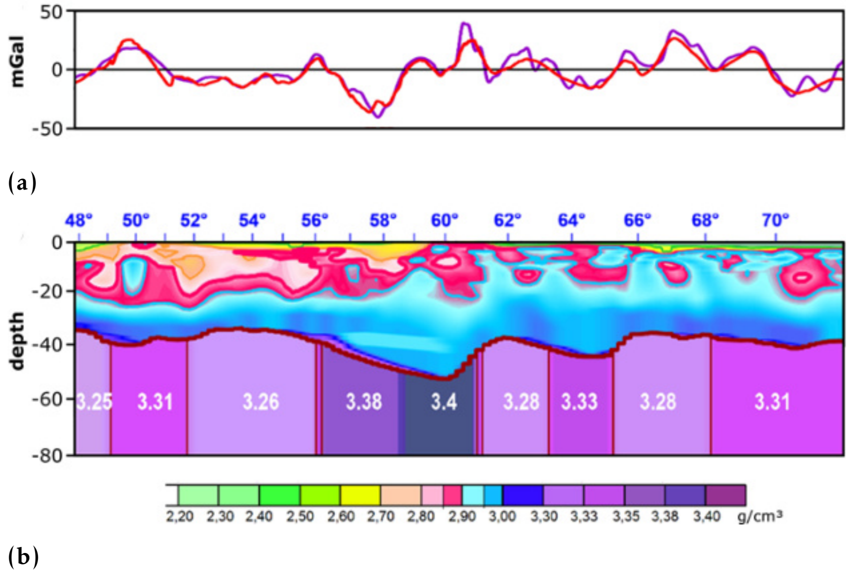

Figure 5. Resulting block density model for the “Quartz” density cut.

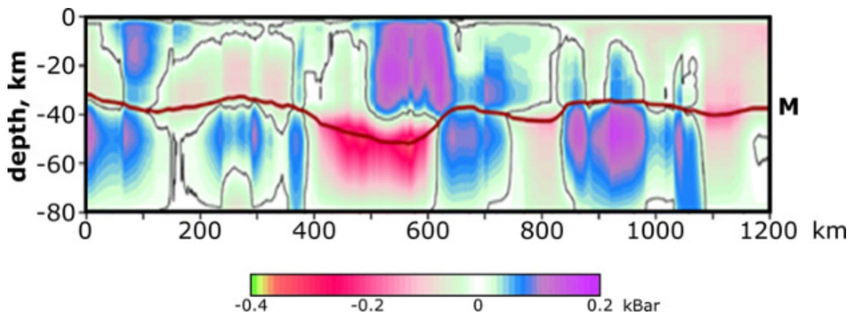

Figure 6. Compensated lithostatic model for the “Quartz” density cut.

The process of density models construction can be reduced to gravity inversion. One should search solution for the inverse gravity problem on practically meaningful sets of correctness by selecting reasonable initial models. Layered velocity distribution in a form of grid arrays fits initial model ideally. This provides stability of inverse gravity problem in a class of weak-unique solutions for models with inhomogeneous layers [*Martyshko et al.*, 2013]. The stable algorithm of layer-by-layer inversion use 2D corrective additions with zero average value [*Martyshko et al.*, 2016]. Iterative scheme of corrective additions calculations in horizontal layers provides uniqueness of inverse problem solution. In addition, it keeps the geological meaning of initial model (constructed by seismic data) in the resulting model (Figure 8).

3D models of upper lithosphere, which were constructed as a result of interpretation of geophysical fields complex, allows one to select a set of curvilinear layers. Boundaries of these layers are selected for specified interval of density values. Gravity anomalies on Earth’s surface level reflect information about density inhomogeneities from all sources below. Elements of tectonic schemes are not visible in layers of density models. We offer to calculate masses of columns with unit square from the Earth’s surface level down to some specified depth. These integral density parameter forms a block model of crystallic crust on different depth slices. The same is visible in maps of the lithostatic pressure anomalies. The lithostatic pressure values are proportional to the excess density. So, the 3D density model can be easily recalculated into a 3D model of the lithostatic pressure anomalies by summing values from density grids for all layers down to specified depth. The distribution of the lithostatic pressure on the horizontal slices have a good match with the tectonic scheme [*Ladovskii et al.*, 2017].

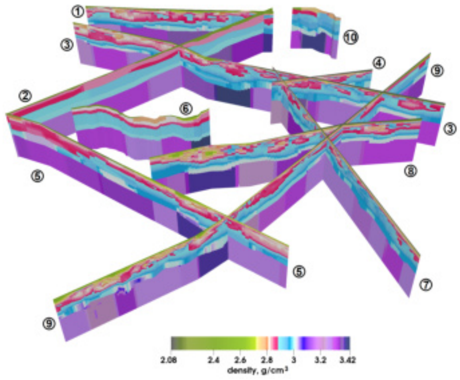

(a)

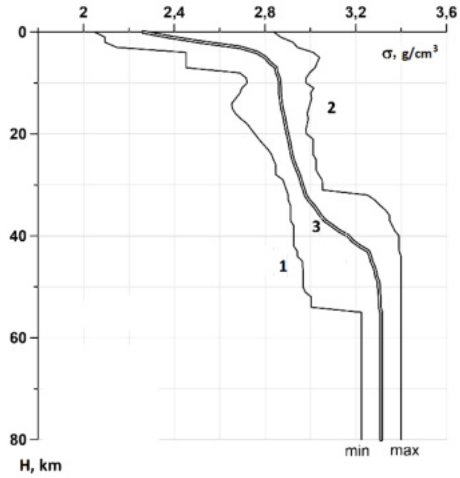

(b)

Figure 7. Density model of initial approximation. Left: spatial position of velocity sections within the study area (for profile designations, see Figure 1). Right: graph of changes in depth of one-dimensional density $\sigma_0(z)$ of the normal model (curve 3). Here are graphs of the minimum (curve 1) and maximum (curve 2) density values.

As a next step of the crust study, we select boundaries that are located inside the crust layer. These boundaries separate layers with constant densities. Such an approximation of a complex 3D model with a set of 2D boundaries is a possible way to lower number calculations and calculation time [*Martyshko et al.*, 2010].

Gravity field Δg of a boundary $z(x,y)$ with flat asymptota plane $z = h$ is calculated using formula

$$\Delta g\left(x',y',0\right) = \Delta\sigma\ f \int_{-\infty}^{\infty}\int_{-\infty}^{\infty}\left(\frac{1}{\sqrt{\left(x-x'\right)^2+\left(y-y'\right)^2+z^2(x,y)}} - \frac{1}{\sqrt{\left(x-x'\right)^2+\left(y-y'\right)^2+h^2}}\right)dxdy.$$

Here $\Delta\sigma$ is density jump on the boundary (density value below boundary minus upper density value), f – gravity constant.

Using technique of boundary selection in density interval, we selected three boundaries. They correspond to density values of 2.8 g/cm^3, 2.88 g/cm^3 and 2.95 g/cm^3 (Figure 9).

3. Isostasy three-dimensional case

Input data for the three-dimensional case are a tectonic structures map of the study region (Figure 1) and a set of two-dimensional profiles (constructed as described above). Profiles were included in a united 3D model (Figure 7). Then we interpolated this sparse model to fill density gaps between the profiles. Preferred interpolation methods are triangulation with linear interpolation method. As a result, the initial model was obtained in a form of the density prism.

The lithostatic anomaly in the three-dimensional case is defined similarly to 2D

$$\Delta P(x,y,h) = P(x,y,h) - \overline{P}(h) = g_a \int_h^0 \Delta\sigma(x,y,z)dz.$$

But for the blocks selection we used a different technique than for the 2D case. Firstly, we equalized the model field with the observed one. This was done by density inversion using local corrections method. The description of this procedure was presented in [*Martyshko et al.*, 2010, 2013], we omit it here. Resulting model has the gravity field equal to the observed one with error $E < 0.001$ mGal.

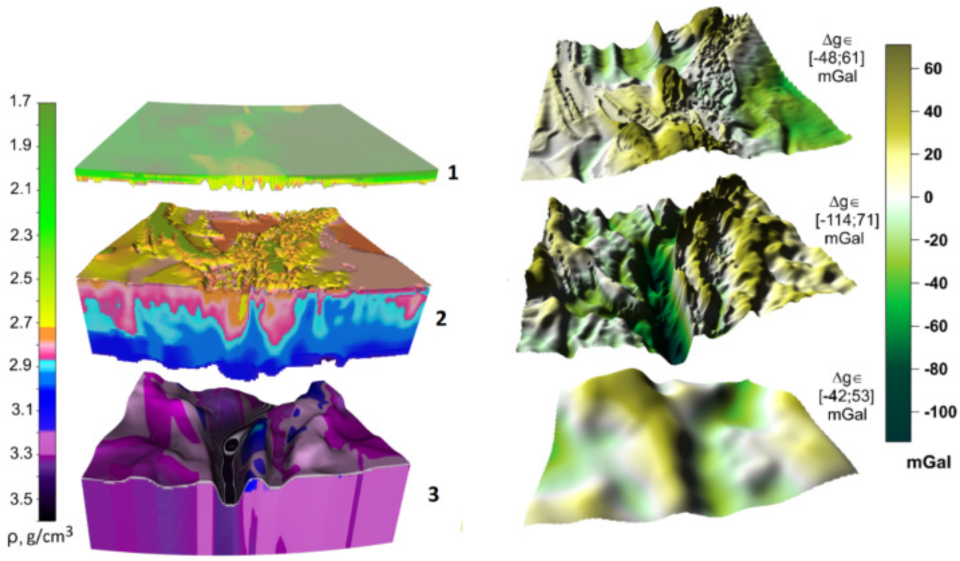

(a) **(b)**

Figure 8. Three-dimensional density model of the region (a), divided along the surface of the roof of the crystalline basement and the roof of the upper mantle: sedimentary cover (1); crystalline crust (2); upper mantle (3). On the right (b) are separated field anomalies calculated from densities that are excess of the normal model's one-dimensional "hydrostatic" density distribution.

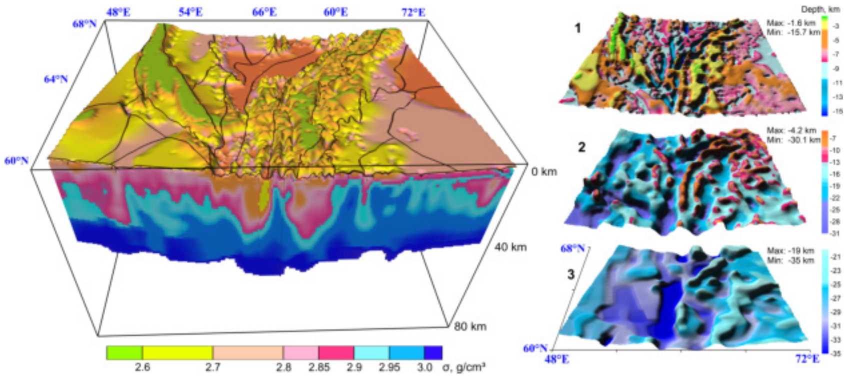

Figure 9. Resulting crust model: 3D layer (left); upper (1), middle (2) and lower (3) inner crust boundaries.

Then we calculated anomaly lithostatic pressure distribution for the resulting density model. Its horizontal cut is presented in Figure 10. Although we used isostatically compensated cuts, neither the initial nor the resulting models are isostatically compensated. This is related to the interpolation. Since we have no information of 3D positions of blocks, which were selected earlier on 2D cuts, we cannot perform correct continuation.

However, we are not obligated to compensate the model to detect blocks. As it was seen from the two-dimensional case, positions of block boundaries could be selected using the initial lithostatic model. We can perform matching of the map of the tectonic structures with the horizontal cuts of the lithostatic model (Figure 11).

4. Discussion

The sections were used to create new structural maps of the main boundaries of the upper lithosphere: between the sedimentary layer and the basement, as well as the Moho boundary – between the earth's crust and the upper mantle. The boundaries are identified by extreme values of the vertical gradient of longitudinal wave velocity. The basement map is in good agreement with previously constructed maps based on both seismic materials and drilling data (VSEGEI, GEON, etc.). A sharp subsidence of the foundation up to 6–8 km

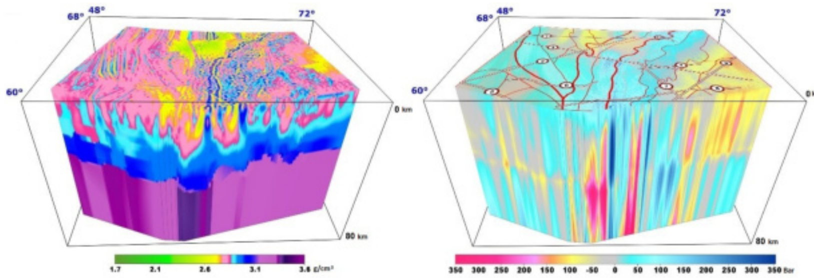

(a)

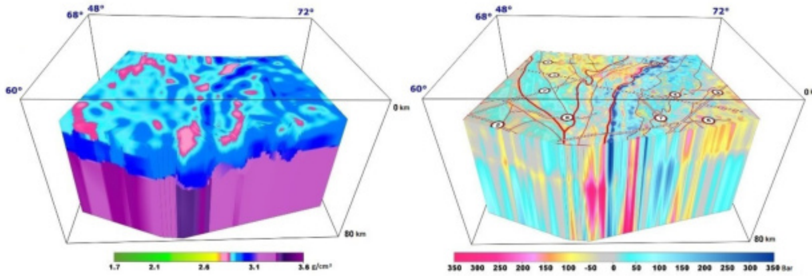

(b)

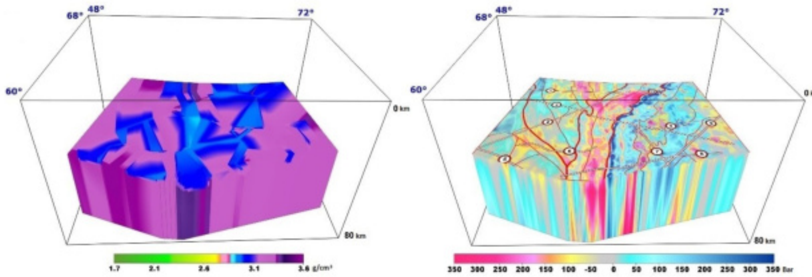

(c)

Figure 10. Horizontal section at a depth of 10 km (a), 20 km (b) and 40 km (c) of density model (left) and lithostatic model (right).

has been confirmed in the Pre-Ural foredeep and in the depressions of Western Siberia. The map of the Moho surface shows previously known features of the deep structure of the territory, published in the atlases of VNIIGeophysics, VSEGEI, GEON, CRUST1.0 and other works. However, the new map significantly clarifies and details the structure of this surface within the specified territory. The subsidence of the Moho boundary and an increase in crustal thickness to 50 km under the Urals have been confirmed, but the area of this subsidence is significantly reduced compared to all previous data. A sharp rise (from 48–50 to 36–38 km) of the Moho surface was revealed within the Tagil trough, in the immediate vicinity of the Main Ural Fault. A map of the surface of the basalt layer was constructed. When constructing, data for longitudinal wave speeds of 6.4–6.5 km/s were used. The average depth to the border is 18–20 km. Under the Ural Mountains and the Timan uplift, the surface of this layer has significant deflections, reaching 26–30 km.

5. Conclusion

We applied new methods for density models construction based on joint interpretation of seismic and gravity data for the structural tectonic schemes creation. These methods for interpretation of the potential geophysical fields are based on a stable algorithm for the solution of the inverse problem. Usage of the initial approximation density model and original fast algorithms for solution of the gravity problems on large grids make it possible to calculate large-scale geophysical models on a real-time basis.

The methods were tested by a practical example: Ural case study. On the first stage, seismic velocity data are recalculated into density values using known correlation between velocity and density. Then the interpolation is performed to fill space between profiles and initial 3D model is obtained. Now, analysing density distribution in the model, it is possible to select boundaries that correspond to known seismic-geological levels. Crust roof and the Mohorovicic discontinuity boundaries were selected using this method. These boundaries slice our model to sediments, crust and mantle. Finally, using the calculated lithostatic pressure distribution we created structural tectonic schemes of the region.

1: Basement $\sigma \in [2.7; 2.9]$ g/cm^3: ($V_p \in [5.6; 6.6]$ km/s)

Relief amplitude: $\Delta z = -(1.2; 6.4)$ km

2: Basement $\sigma = 2.8$ g/cm^3: ($V_p > 6$ km/s)

Relief amplitude: $\Delta z = -(1.6; 15.7)$ km

3: Basement $\sigma = 2.88$ g/cm^3: ($V_p > 6.4$ km/s)

Relief amplitude: $\Delta z = -(4.2; 30.8)$ km

4: Basement $\sigma = 2.95]$ g/cm^3: ($V_p > 6.75$ km/s)

Relief amplitude: $\Delta z = -(19; 35)$ km

5: Basement $\sigma \in [3.24; 3.42]$ g/cm^3: ($V_p \in [7.7; 8.4]$ km/s)

Relief amplitude: $\Delta z = -(32.5; 52.2)$ km

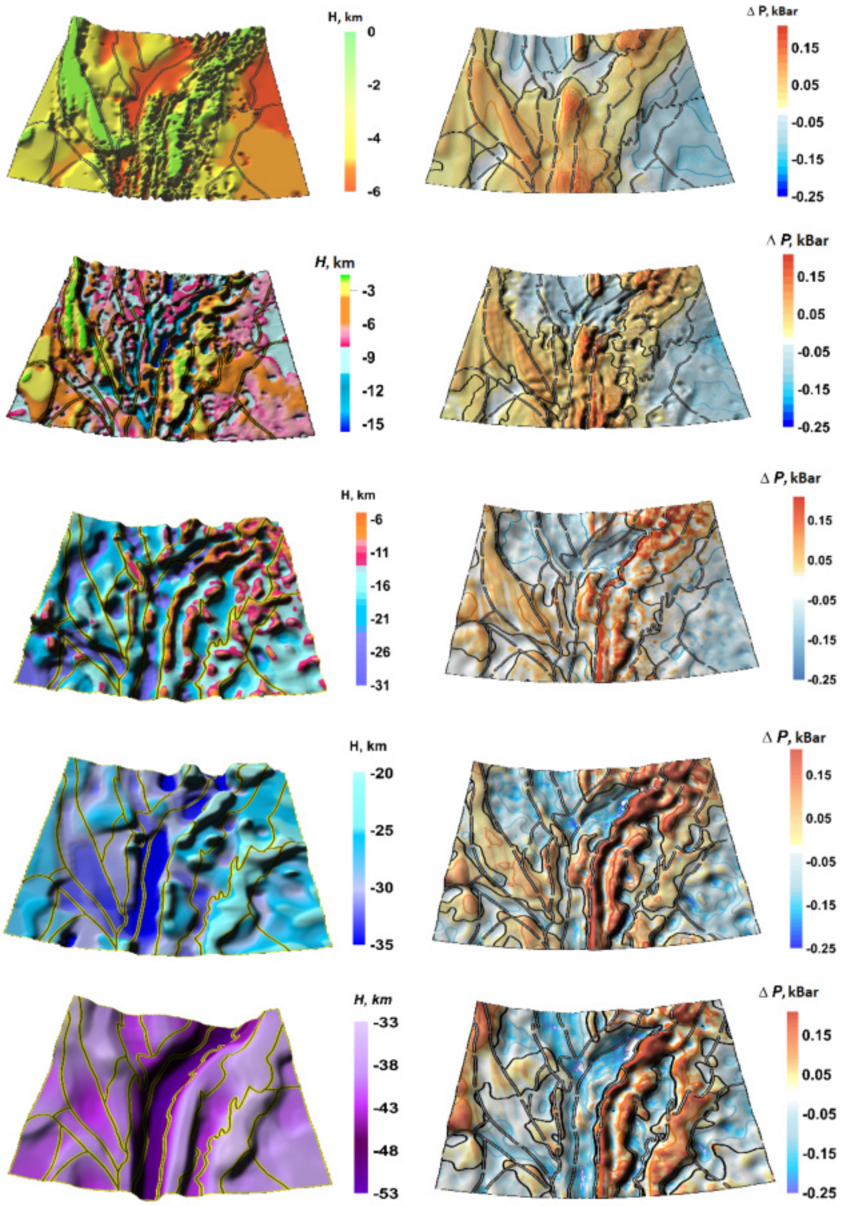

Figure 11. Boundaries of the main structural horizons, constructed using a density model (left) and lithostatic pressure anomalies on them. The contours of tectonic structures are also plotted (see Figure 1).

References

Druzhinin, V. S., A. V. Egorkin, and S. N. Kashubin (1990), New information on the plutonic structure of the Urals and adjoining areas, derived from deep seismic sounding data, *Doklady of the Academy of Sciences of the USSR. Earth Science Sections*, (315), 67–71.

Geng, M., M. Y. Ali, J. Derek Fairhead, S. Pilia, Y. Bouzidi, and B. Barkat (2022), Crustal structure of the United Arab Emirates and northern Oman Mountains from constrained 3D inversion of gravity and magnetic data: The Moho and basement surfaces, *Journal of Asian Earth Sciences*, *231*, https://doi.org/10.1016/j.jseaes.2022.105223.

Jiménez-Munt, I., M. Fernàndez, J. Vergés, J. C. Afonso, D. Garcia-Castellanos, and J. Fullea (2010), Lithospheric structure of the Gorringe Bank: Insights into its origin and tectonic evolution: GORRINGE BANK STRUCTURE AND EVOLUTION, *Tectonics*, *29*(5), 1–16, https://doi.org/10.1029/2009TC002458.

Ladovskii, I. V., P. S. Martyshko, D. D. Byzov, and V. V. Kolmogorova (2017), On selecting the excess density in gravity modeling of inhomogeneous media, *Izvestiya*, *Physics of the Solid Earth*, *53*(1), 130–139, https://doi.org/10.1134/S1069351316060057.

Li, Y., and Y. Yang (2020), Isostatic state and crustal structure of North China Craton derived from GOCE gravity data, *Tectonophysics*, *786*, https://doi.org/10.1016/j.tecto.2020.228475.

Martyshko, P. S., I. V. Ladovskii, and A. G. Tsidaev (2010), Construction of regional geophysical models based on the joint interpretation of gravitaty and seismic data, *Izvestiya*, *Physics of the Solid Earth*, *46*(11), 931–942, https://doi.org/10.1134/S1069351310110030.

Martyshko, P. S., I. V. Ladovskii, and D. D. Byzov (2013), Solution of the gravimetric inverse problem using multidimensional grids, *Doklady Earth Sciences*, *450*(2), 666–671, https://doi.org/10.1134/S1028334X13060172.

Martyshko, P. S., I. V. Ladovskiy, and D. D. Byzov (2016), Stable methods of interpretation of gravimetric data, *Doklady Earth Sciences*, *471*(2), 1319–1322, https://doi.org/10.1134/S1028334X16120199.

Martyshko, P. S., I. V. Ladovskii, D. D. Byzov, and A. G. Tsidaev (2017), Density block models creation based on isostasy usage, in *17th International Multidisciplinary Scientific Geoconference*, *SGEM 2017*, vol. 17, pp. 85–92, International Multidisciplinary Scientific Geoconference.

Satyakumar, A. V., S. Jin, V. M. Tiwari, and S. Xuan (2023), Crustal structure and isostatic compensation beneath the South China Sea using satellite gravity data and its implications for the rifting and magmatic activities, *Physics of the Earth and Planetary Interiors*, *344*, https://doi.org/10.1016/j.pepi.2023.107107.

Sobolev, I. D., S. V. Avtoneev, R. P. Belovskaya, T. Y. Petrova, and R. A. Syutkina (1983), Tectonic map of Urals in 1:1000000 scale: explanatory notes (in Russian).

Strakhov, V. N., and T. V. Romanyuk (1984), Reconstructing the crustal and upper mantle density from DSS and gravimetry data, *Izvestiya Akademii Nauk SSSR*, *Fizika Zemli*, (6), 44–63.

Zingerle, P., R. Pail, T. Gruber, and X. Oikonomidou (2020), The combined global gravity field model XGM2019e, *Journal of Geodesy*, *94*(7), https://doi.org/10.1007/s00190-020-01398-0.

Russian Journal of Earth Sciences

Special Issue: "25th anniversary of the Russian Journal of Earth Sciences"

A Global View on Internal Tides

E. G. Morozov[1,2]

[1]Shirshov Institute of Oceanology, Russian Academy of Sciences, Moscow, Russia
[2]Moscow Institute of Physics and Technology, Moscow, Russia
* **Correspondence to:** E. G. Morozov, egmorozov@mail.ru

Abstract: This is a review paper on generation of internal tides in the global ocean based on literature data and publications of the author. Energy fluxes of semidiurnal internal tide generation over submarine ridges were estimated based on modeling and measurements on moorings in many regions of the ocean. Data from 4000 moorings during a period of 50 years are considered. Regions of intense generation of internal tides are indicated. They are related to several underwater oceanic ridges. Energy fluxes from submarine ridges greatly exceed those from the continental slopes because generally the currents of the barotropic tide are parallel to the coastline. If the barotropic tide currents are normal to the ridge, they generate strong internal tides. They account approximately for one fourth of the energy losses of the barotropic tide. Decay of internal tide during propagation was estimated based on the data from lines of moorings located normal to the ridges. Model simulations and moored measurements result in a global map of semidiurnal internal tide amplitudes.

Keywords: Internal tides, bottom topography, overflows, submarine ridges, tidal energy dissipation.

Citation: Morozov E. G. (2024), A Global View on Internal Tides, *Russian Journal of Earth Sciences*, Vol. 24, ES1009, https://doi.org/10.2205/2024ES000898

1. Introduction

American scientist and politician Benjamin Franklin was the first to notice the existence of internal waves. In 1762, he described the waves at the interface between oil and water in a ship's lantern. More than 100 years passed since F. Nansen made observations of internal waves in the sea [*Nansen*, 1902] using water sampling bottles. Intense studies of internal waves began only in the 1960s [*LaFond*, 1961; *Lee and Cox*, 1966; *Summers and Emery*, 1963]. In this decade measurements on moorings revealed the existence of strong oscillations at tidal periods [*Cairns and LaFond*, 1966].

However, our knowledge of internal waves by the 1960s was quite poor, especially about the existence of internal tides. This was very briefly written in the book by W. Krauss [*Krauss*, 1966]. A paper by W. Munk [*Munk*, 1966] was published on the influence of tides on the entire dynamics of the ocean and especially on internal tides, but it was not yet deeply understood at that time. It is likely that the paper by Tareev [*Tareev*, 1966] was the only publication on internal waves in Russia, but it has not been associated yet with internal tides. The Garrett-Munk model describing the background state of the internal wave field appeared only in 1972 [*Garrett and Munk*, 1972]. The authors presented a model of dimensionless energy of internal waves, from which the observed spectra of temperature fluctuations and currents on moored buoys and the spectra measured by towed instruments were obtained. A brilliant American experiment in the technical sense to study internal waves (IWEX) was conducted in 1973 [*Briscoe*, 1975]. A pyramidal construction with one mutual buoyancy moored at three spatially separated locations was set in the Sargasso Sea where internal waves are very weak. However, at that time, the scientists did not know that internal tides in the Sargasso Sea are weak. In 1975, C. Wunsch published two review works summarizing the current knowledge about internal tides [*Wunsch*, 1975a,b].

Research Article

Received: 15 October 2023
Accepted: 15 January 2024
Published: 29 February 2024

The propagation of internal disturbances along inclined characteristic surfaces (which fall into the category of attractors, that is, the concentration of disturbances occurs around specific trajectories) was first described by Phillips [*Phillips*, 1977]. The finding of Phillips [*Phillips*, 1977] that unlike surface waves the motion of water particles in internal waves occurs along sloping lines was continued with the idea that generation of internal tides over sloping bottom occurs because when currents of the barotropic tide overflow topography the most intense generation of internal tides occurs over submarine slopes if their inclination is close to the inclination of internal wave characteristic curves $\frac{dz}{dx} = \frac{k_z}{k_x} = \sqrt{\frac{\omega^2 - f^2}{N^2 - \omega^2}}$ [*Baines*, 1982; *Holloway and Merrifield*, 2003; *Johnston et al.*, 2003; *Phillips*, 1977; *Torgrimson and Hickey*, 1979] (Figure 1). Usually this happens in the upper parts of the submarine ridges and in the regions of the shelf break where stratification is strong [*Hibiya*, 2004].

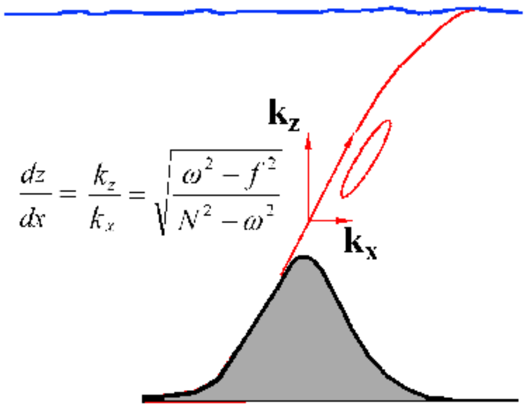

Figure 1. Scheme of internal wave beam. Excursion of water particles is shown by an elongated ellipse. Beam of internal perturbations is shown in red. Underwater topography is in gray. Formula describes the slope of internal wave beam.

Joint efforts of many scientists resulted in the idea that internal tides are generated by the barotropic tide currents flowing over sloping topography; thus, the vertical component of tidal currents periodically displaces isopycnals [*Baines*, 1982; *Morozov*, 1995, 2018; *Sjöberg and Stigebrandt*, 1992]. The frequency of these displacements is tidal. Internal waves are generated by periodical displacements of isopycnals and propagate from the sloping topography: continental slopes, submarine ridges, and seamounts. Numerous investigations show that tidal interactions and wind are the main sources of internal wave generation [*Garrett and Kunze*, 2007; *Munk*, 1966; *Munk and Wunsch*, 1998].

2. Energy fluxes of internal tides from bottom topography

Baines [*Baines*, 1982] used the following approach when studying generation of internal tides over continental slopes. After solving the equation system, he found an expression for mass force F that is responsible for internal wave generation; this force is nonzero over sloping topography:

$$\overrightarrow{F} = \frac{QN^2}{\omega} z \overrightarrow{z} \frac{\partial h}{\partial x} \frac{1}{h^2} \sin \omega t.$$

Here, Q is the water transport by the barotropic tide; $z = h(x)$ is the ocean bottom; ω is the tidal frequency; N is the Brunt-Väisälä frequency. This mass force is non-zero only in regions with variable depth due to the presence of the derivative of depth with respect to the horizontal coordinate in this formula: $h'(x)$.

Submarine ridges are important regions of internal tide generation [*Morozov*, 1995; *Sjöberg and Stigebrandt*, 1992]. The generation of internal tides over the slopes of ridges exceeds many times the generation over continental slopes. This result was reported by Morozov [*Morozov*, 1995]. After the first publication, the results and estimates were updated. This paper is a progressive report on internal tides in the global ocean and geographical distribution of semidiurnal internal tide, its amplitudes, and energy. The goal of this research is to apply observations and modeling to understand the distribution of internal tide energy and amplitudes over the global ocean.

As was previously written, P. Baines solved the equations, calculated the mass forces and energy of the internal tide over most of the continental slopes. Morozov [*Morozov*, 1988, 1995] continued this work and calculated the energy of the internal tide over most of the underwater ridges (more than 50 ridges). These modeling estimates were compared to the field observations on moorings. The results were repeatedly updated and published [*Morozov*, 1988, 1990, 1995, 2006, 2018]. This publication is an updated review of previous publications.

The estimated energies from all major ridges and island arcs in each ocean have been summed. Calculations from previous publications were updated to get more correct estimates of energy fluxes. The resulting sums of the energy of semidiurnal internal waves per time unit (power) in the three oceans (including the Southern Ocean as the southern parts of the three) are the following:

- 3.1×10^{11} W in the Atlantic;
- 2.8×10^{11} W in the Pacific;
- 2.2×10^{11} W in the Indian Ocean.

Thus, the sum for the entire World Ocean is 8.1×10^{11} W, which is approximately $\frac{1}{4}$ of the energy dissipation of the M_2 barotropic tide.

One of the first estimates of the total amount of the barotropic tide dissipation given by Cartwright [*Cartwright*, 1977] was 4.3×10^{12} W. Previously it was considered that tidal energy generally dissipates in the shallow seas. More recent astronomical estimates give a smaller value of tidal energy dissipation of the M_2 tide. The review papers by Munk and Wunsch [*Munk and Wunsch*, 1998] and Garrett [*Garrett*, 2003] emphasize the role of mid-oceanic ridges in the generation of internal tide. Egbert and Ray [*Egbert and Ray*, 2000, 2001] analyzed tidal elevation in the global ocean and estimated the total rate of the dissipation of tidal energy as 2.5 TW (1 TW = 10^{12} W) for the lunar semidiurnal tide M_2, 3.2 TW for all lunar tides. Much smaller energy (0.2 TW) dissipates in the atmosphere and solid Earth. Later estimates reported by Egbert and Ray [*Egbert and Ray*, 2003] indicate that the total dissipation of the M_2 tide is 2.435 TW, of which 1.649 TW dissipates in the shallow seas and 0.782 TW in the deep ocean. Kantha and Tierney [*Kantha and Tierney*, 1997] suggest on the basis of altimetric observations that the total energy of the M_2 baroclinic tide is 50 PJ, while the dissipation is 360 GW (3.6×10^{11} W).

Baines [*Baines*, 1982] estimated that less than 1% of semidiurnal tide energy (1.73×10^{10} W) is transferred to internal tides over continental slopes. Bell [*Bell*, 1975] estimated that about 10% of the tidal energy goes to internal tides over uneven abyssal topography in deep basins.

Let us consider the characteristic regions of very strong internal tides.

3. Regions of intense internal tides

3.1. Mascarene Ridge

The Mascarene Ridge is considered one of the regions, where internal tides of high energy are generated. The array of moorings was deployed in March 1987 assuming that the internal tide is generated by barotropic tidal currents in the underwater passage between the Saya de Malha and Nazareth banks [*Morozov and Vlasenko*, 1996]. The measurements confirmed the existence of large-amplitude internal tides. The mooring array of six moorings was extended in the direction to the southeast from the strait between the two banks. A scheme of location of moorings over bottom topography near the banks of the Mascarene Ridge is shown in Figure 2.

The vertical displacements caused by the internal tide were estimated from the temperature time series and vertical temperature gradient. Their mean amplitude at a depth of 1200 m was 0.2°C, which gives vertical displacements of the water particles equal to

120 m and correspondingly the amplitude of the displacement from the mean position as high as 60 m.

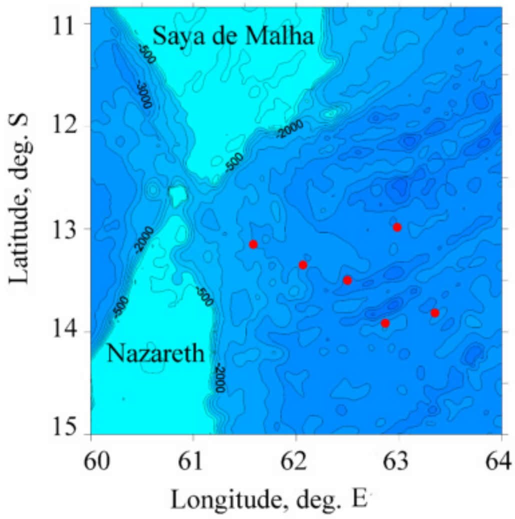

Figure 2. Bottom topography near the shallow banks of the Mascarene Ridge (m) and moorings east of the ridge. Depth contour lines are shown at depths of 500, 1000, 1500, 2000, 3000, 3500, and 4000 m. Locations of moorings are shown with red dots.

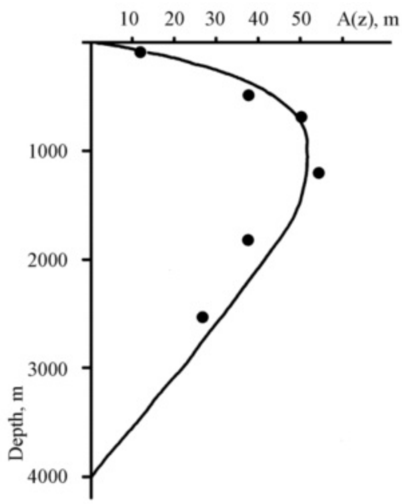

Figure 3. Amplitudes of semidiurnal internal waves near the Mascarene Ridge. The curve is the eigen function of the first mode (Equation 1). It was normalized by the maximum to fit the data of measured vertical displacements; the black dots show measured amplitudes of internal tide at the easternmost mooring.

Below we will analyze vertical distribution of semidiurnal internal tide amplitudes. A graph of the eigen function for the oscillations of the first mode is shown in Figure 3. It was calculated by the numerical integration of the equation for the vertical velocity (w) caused by internal waves at realistic stratification *N(z)* and zero boundary conditions for vertical velocity at the surface and bottom [*LeBlond and Mysak*, 1978]:

$$\frac{d^2w}{dz^2} + \frac{N^2(z)}{g}\frac{dw}{dz} + \frac{N^2(z) - \omega^2}{\omega^2 - f^2} wk^2 = 0, \tag{1}$$

where, $N^2(z)$ is the squared Brunt-Väisälä frequency based on the CTD data; ω is the semidiurnal frequency, f is the Coriolis parameter, and k is the horizontal wave number.

The theoretical wavelength of the first mode of internal tidal wave based on the integration of this equation was equal to 130 km, and the phase velocity was 2.9 m/s. The amplitudes of internal waves were also estimated from the spectra of time series at different depths on the easternmost mooring. Temperature fluctuations at semidiurnal frequency were divided by the vertical gradient of temperature; thus, vertical amplitudes of water particle displacements were estimated.

The wavelength and direction of propagation of internal tides were estimated based on the spatiotemporal spectra at the semidiurnal tidal frequency. They were calculated on the basis of measurements at six moorings (serving as an antenna for internal tides) at several levels using the method suggested by [*Barber*, 1963]. The wavelength of internal tide was 140–150 km, and its direction from the strait between the banks was 110°. Why are the amplitudes of internal tide so large over the Mascarene Ridge? Because the barotropic tide is strong, tidal currents are almost normal to the ridge, the tops of the ridges are shallow, while the surrounding waters are deep, and the stratification is strong.

3.2. Aleutian Ridge

Cummins et al. [*Cummins et al.*, 2001] used satellite altimetry to analyze internal tides radiated from the Aleutian Ridge. The authors reported coherent propagation of semidiurnal internal tides in the southern direction over a distance of at least 1100 km. The strongest energy fluxes occur in the vicinity of the Amutka Pass (52° N, 172° W).

The moorings were deployed during the GARS, FOCI, and NPBC experiments over the continental slopes of Alaska and the Aleutian Islands. The amplitude of internal tides at a depth of 1000 m was estimated at 70 m, while at a distance of 100 km from the slope the amplitude was 50 m. Locations of moorings are shown in Figure 4 [*Morozov*, 2018].

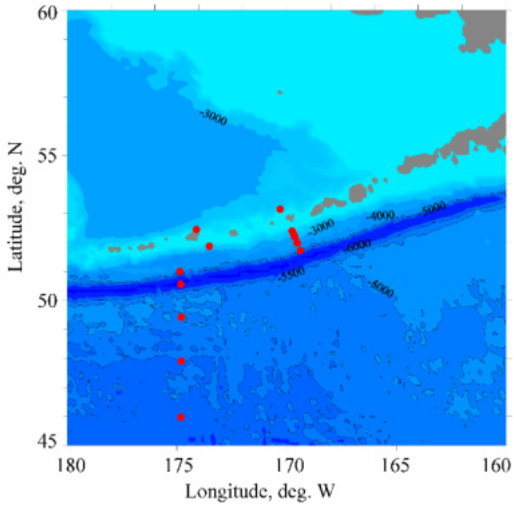

Figure 4. Bottom topography in the study site near the Aleutian Ridge and locations of moorings. Depth contour lines are shown at depths of 3000, 4000, 5000, 5500, and 6000 m. Land and islands are shown with gray color. Locations of moorings are shown with red dots.

A strong tidal flow propagates through the passes between the islands generating intense internal tides when overflowing the bottom slopes. A mooring at 52°24' N, 169°45' W deployed on the southern slope of the Aleutian Islands over a depth of 1050 m recorded the amplitudes of internal tides exceeding 150 m at a depth of 560 m. The records from another mooring over a depth of 2000 m showed amplitudes in the range 150–200 m. At a depth of 3000 m, the amplitudes decreased half of the initial amplitude (70–80 m) and after further spreading to a depth of 6000 m, they decreased to 25 m.

3.3. South China Sea

Several experiments were carried out in the South China Sea to study internal waves. The Luzon Strait is known as a strong generation region of internal tides due to the existence of two steep submarine ridges along the north-south direction. Internal tides generated over the pair of ridges propagate in both directions to the South China and Philippine seas. Many field studies with moored thermistor strings and ADCPs, satellite and radar observations, and model simulations were dedicated to this region of strong internal tides together with the theoretical research [*Fang et al.*, 2015; *Huan Lee et al.*, 2012; *Kerry et al.*, 2016; *Mercier et al.*, 2013; *Niwa and Hibiya*, 2004; *Orr and Mignerey*, 2003; *Ramp et al.*, 2004]. Internal tides generated over the slopes of these two submarine ridges propagate both sides. Internal tides propagating to the west of the Luzon Strait are very strong. Those internal tides propagating to the east are less intense. Analysis performed by Jan et al. [*Jan et al.*, 2008] revealed that strong internal tides are generated over the slopes of the eastern (70%) and western (30%) ridges. The results of experiments reported by Ramp et al. [*Ramp et al.*, 2004] report that the amplitudes of internal tides reached 50 m. Alford with coauthors [*Alford et al.*, 2015] report about the observations of internal tides at 20°30’ N, 119°00 E. The measurements reveal the existence of greater than 200-m high breaking internal waves in the region of generation. Many other publications report about amplitudes exceeding 100 m.

3.4. Gibraltar Strait

The flow in the Strait of Gibraltar (Figure 5) is characterized by a two-layer system of opposite currents that exists due to the difference in sea level and water density between the Atlantic Ocean and the Mediterranean Sea. Due to high water temperature evaporation of water in the Mediterranean is intense. Approximately 50 cm of water column evaporates during one year. This loss is compensated by the surface currents from the Atlantic Ocean. The velocities of this flow reach 40 cm/s. The flow changes its direction to the opposite at a depth of 100 m. A deep-water current of more saline Mediterranean Water flows into the ocean owing to the difference in water density. The velocities of this current in the lower layer reach 85 cm/s. The velocity maximum is close to the bottom. A barotropic tidal wave with mean velocities in the range 70-80 cm/s propagates through the strait. Strong internal tides are generated when the currents of the barotropic tide overflow transverse Camarinal Sill in the middle of the Strait of Gibraltar [*Bryden et al.*, 1994; *Farmer and Armi*, 1988; *Morozov et al.*, 2002].

The measurements over the Camarinal Sill reported by Boyce [*Boyce*, 1975] and Bockel [*Bockel*, 1962] indicate that the amplitudes of internal tides over the slopes of the sill are as high as 200 m.

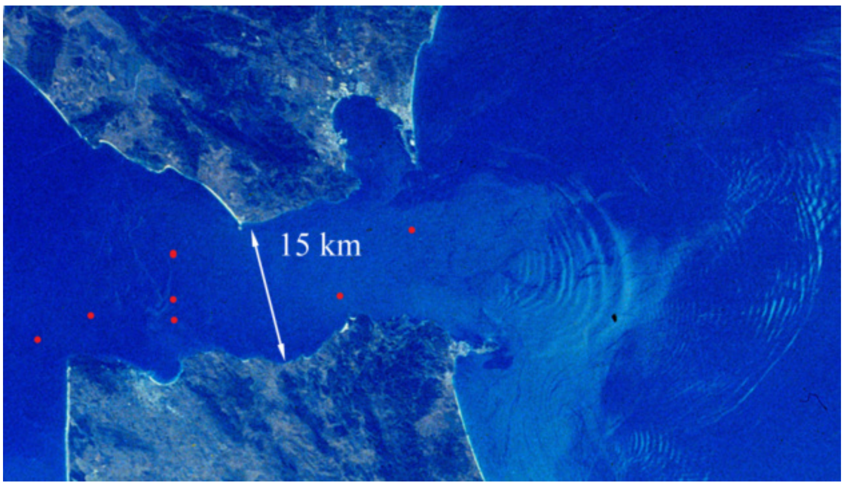

Figure 5. Satellite photo of the Strait of Gibraltar and surface manifestations of internal waves best seen in the eastern part. Red dots indicate locations of moorings in 1985–1986.

Analysis of moored temperature measurements shows that the displacement of the 13°C isotherm gives the best illustration pattern because this isotherm always remains within the depth interval of measurements. The vertical excursion of water particles (isotherm 13°C) ranges from 100 to 300 m depth. Superposition of the diurnal and semidiurnal tidal components based on the data from July 2 to July 31, 1986, is clearly seen in Figure 6.

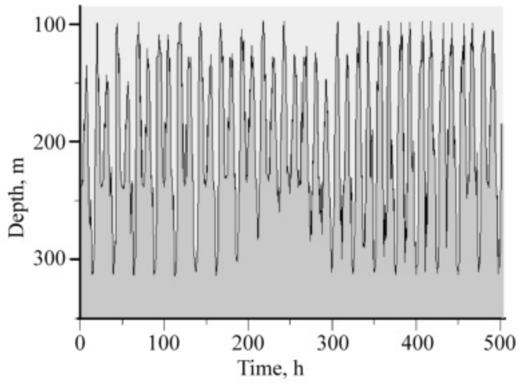

Figure 6. Depth variation of the 13°C isotherm over the Camarinal Sill from July 2 to July 31, 1986. Adopted from [*Morozov et al.*, 2002].

The internal tidal oscillations are observed over the sill exactly at the source of their generation; hence we conclude that these waves are forced internal oscillations, which transform into free propagating waves east and west of the sill. Internal tide waves lose their energy while propagating to the east and west from the Camarinal Sill. After propagating 50 km from the sill to the west, the amplitude of internal tides decreases three times.

However, strong internal tides here do not make any notable contribution to the internal wave energy balance in the ocean. The Strait of Gibraltar from the point of view of the global processes can be interpreted as a point source unlike quasi-linear sources of submarine ridges.

4. Decay of internal tides and global map of internal tide amplitudes

We have considered the estimates of energy fluxes of internal tides from most of the submarine ridges and estimated the amplitudes and energies of internal tides. The highest energies were revealed at those submarine ridges where the currents of the barotropic tide are normal to the ridge, and the geometry of the ridge intensifies generation of internal tides if the slopes of bathymetry are close to the characteristic curves of internal tide. This usually occurs near the crests if they are relatively close to the surface while the surrounding waters are deep. The energy of internal tides radiated from the submarine ridges is estimated as quarter of the barotropic tide dissipation. While propagating from the ridges internal tides lose their energy and their amplitude decreases. One of the goals of this study was to construct a global map of amplitudes of semidiurnal internal tides. In addition to the estimates of energy fluxes from submarine ridges as the sources areas we need estimates of energy decay in the course of propagation of internal tides. These estimates were evaluated from those moored measurements where long arrays of moorings were deployed in the normal direction to the ridge.

Spatial decay of the energy of semidiurnal internal tides in different regions was performed using the method described in [*Lozovatsky et al.*, 2003]. The density of the kinetic energy of the horizontal components of internal tide was determined as the sum of squared amplitudes of velocity. The total energy density of internal tide was calculated using the following formula [*Holloway and Merrifield*, 2003; *Torgrimson and Hickey*, 1979]:

$$E_{TW}(z) = 0.25\rho\left(\overline{u_{IT}^2(z)} + \overline{v_{IT}^2(z)} + N^2(z)\overline{\zeta_{IT}^2(z)}\right). \qquad (2)$$

Here, u_{IT}, v_{IT} are the amplitudes of the semidiurnal internal tide velocity components, ζ_{IT} are vertical displacements. Internal tide velocity components were calculated from the mooring data subtracting the barotropic tide velocities.

Horizontal velocities of the barotropic tide in the region were calculated using the OTIS tidal inversion software based on satellite data assimilation [*Egbert and Erofeeva*, 2002]. The barotropic tide velocities over the slopes of the ridge sometimes exceed 40 cm/s, while far away from the ridge they decrease to 1–2 cm/s.

We normalized the distances by the scale equal to the wavelength of the first mode $\lambda = 145$ km. Over a distance of 1000–1500 km the energy density of the internal tide in the main thermocline (1000–1200 m) decreases by a factor of 10 approximately from 1 J/m^3 to 0.1 J/m^3. This is approximately 15% loss of energy over one wavelength; hence, a 10-fold energy decrease occurs over a distance of 12 wavelengths.

We compared the energy decay of the internal tide in the Mascarene region with some other regions. The graphs of energy decay in the Kuroshio, Aleutian, Kermadec, and Mozambique regions, are shown in Figure 7. The energy level in each of the regions is different but the rate of energy decay is very similar to the one analyzed near the Mascarene Ridge. The graphs in Figure 7 show that the energy decay with distance is similar in different regions of the oceans.

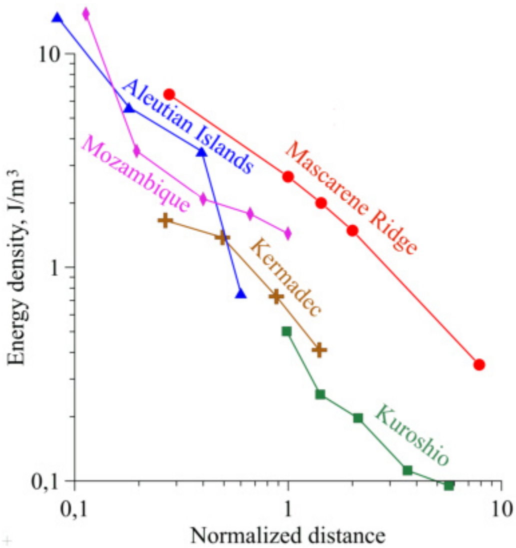

Figure 7. Combined graph of the semidiurnal internal tide energy decay with the distance from the source. The graph shows total energy density $E_{TW} + E_H + E_\zeta$ (see Equation 2) of the semidiurnal internal tide versus distance from the ridge. The distance from the ridge is normalized by the wavelength of the first mode $\lambda = 145$ km. The measurement depth is in the interval 1000–1200 m. Energy decay from the Mascarene Ridge is shown with circles of red color; from the Aleutian Islands with blue triangles; from the Mozambique slope with magenta diamonds; from the east Japan coast (Kuroshio) with green squares, and from the Kermadec Ridge (South Pacific) with brown crosses.

Decay of the semidiurnal internal tide amplitudes with distance in the regions of the Mascarene ridge and Aleutian Islands is shown in Figure 8. Decay is stronger near the source of internal tide generation. At greater distances from the ridge the amplitudes decrease slower, and eventually become close to 20 m, which is the background level of amplitudes worldwide.

The estimates of energy and amplitude decay made it possible to conclude that approximately 10% of internal tide energy and 5% of the amplitude are lost over a distance of one wavelength (~145 km). In deep basins far from the sources the energies of semidiurnal internal tide approach the natural background level [*Garrett and Munk*, 1972], 1972]. Thus, the waves propagate over 12–15 wavelengths. After evaluating the estimates of internal tide energy flux and decay of internal tides over distance it was possible to construct a map

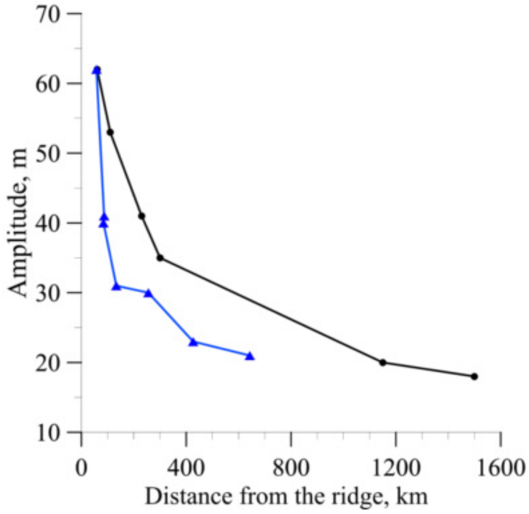

Figure 8. Combined graph of the semidiurnal internal tide amplitude decay with the distance from the Mascarene Ridge (black line and circles) and Aleutian Islands (blue line and triangles) based on the data of moorings.

of internal tide amplitudes in the ocean (Figure 9). The map is based on modeling and measurements. The largest amplitudes were found near submarine ridges. Several ridges in the ocean make the greatest contribution to the global energy balance of internal tide and dissipation of the barotropic tide. These ridges include the Mascarene Ridge, Aleutian Islands, Hawaii Islands, Kusu Palau Ridge, Mid-Atlantic Ridge in the South Atlantic, great Meteor Banks, and ridges in the Luzon Strait. The map is very general because it shows only the outline of the amplitude distribution. The amplitudes should be considered as "vertically averaged" and also "time averaged" over a half-month (spring-neap) time scale.

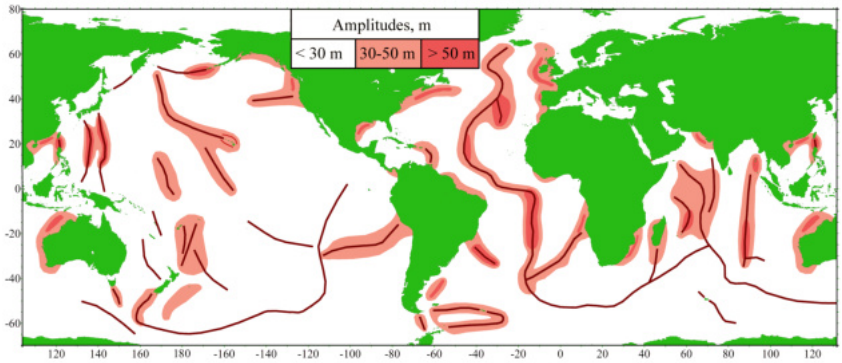

Figure 9. World map of the amplitudes of semidiurnal internal tides (meters). Submarine ridges are shown with heavy brown lines. The regions of the semidiurnal internal tide amplitudes exceeding 50 and 30 m (peak-to-peak) are shown in dark and light brown colors, respectively.

5. Conclusions

The major generation of internal tides occurs near submarine ridges. The highest energies were revealed at those submarine ridges where the currents of the barotropic tide are normal to the ridge, and the geometry of the ridge intensifies generation of internal tides if the slopes of bathymetry are close to the characteristic curves of internal tide. This usually occurs near the crests if they are relatively close to the surface while the surrounding waters are deep. The energy of internal tides radiated from the submarine ridges is estimated as quarter of the barotropic tide dissipation. The balance of tide dissipation energy has been closed. A quarter of the tide dissipation energy is transferred to internal tides. Previously it was considered that the major part of the barotropic tide dissipates in shallow seas, but the balance was not closed. A map of the amplitudes of tidal internal waves in the ocean has been constructed.

Acknowledgments. The study was carried out within the framework of State Assignment FMWE-2024-0016 (ship measurements) and supported by the Russian Science Foundation grant no. 21-77-20004 (field data analysis and interpretation).

References

Alford, M. H., T. Peacock, J. A. MacKinnon, J. D. Nash, M. C. Buijsman, L. R. Centurioni, S.-Y. Chao, M.-H. Chang, D. M. Farmer, O. B. Fringer, K.-H. Fu, P. C. Gallacher, H. C. Graber, K. R. Helfrich, S. M. Jachec, C. R. Jackson, J. M. Klymak, D. S. Ko, S. Jan, T. M. S. Johnston, S. Legg, I.-H. Lee, R.-C. Lien, M. J. Mercier, J. N. Moum, R. Musgrave, J.-H. Park, A. I. Pickering, R. Pinkel, L. Rainville, S. R. Ramp, D. L. Rudnick, S. Sarkar, A. Scotti, H. L. Simmons, L. C. St. Laurent, S. K. Venayagamoorthy, Y.-H. Wang, J. Wang, Y. J. Yang, T. Paluszkiewicz, and T.-Y. (David) Tang (2015), The formation and fate of internal waves in the South China Sea, *Nature*, *521*(7550), 65–69, https://doi.org/10.1038/nature14399.

Baines, P. G. (1982), On internal tide generation models, *Deep Sea Research Part A. Oceanographic Research Papers*, *29*(3), 307–338, https://doi.org/10.1016/0198-0149(82)90098-X.

Barber, N. F. (1963), The directional resolving power of an array of wave detectors, in *Ocean Wave Spectra*, pp. 137–150, Prentice Hall, NY, Engelwood Cliffs.

Bell, T. H. (1975), Topographically generated internal waves in the open ocean, *Journal of Geophysical Research*, *80*(3), 320–327, https://doi.org/10.1029/JC080i003p00320.

Bockel, M. (1962), Travaux oceanographiques de l'"Origny" a Gibralter, in *Campagne Intemationale 15 Mai - 15 Juin 1961. I. Partie: Hydrologic dans le deroit*, pp. 325–329, Cahiers Oceanographie.

Boyce, F. M. (1975), Internal waves in the Straits of Gibraltar, *Deep Sea Research and Oceanographic Abstracts*, *22*(9), 597–610, https://doi.org/10.1016/0011-7471(75)90047-9.

Briscoe, M. G. (1975), Preliminary results from the trimoored internal wave experiment (IWEX), *Journal of Geophysical Research*, *80*(27), 3872–3884, https://doi.org/10.1029/JC080i027p03872.

Bryden, H. L., J. Candela, and T. H. Kinder (1994), Exchange through the Strait of Gibraltar, *Progress in Oceanography*, *33*(3), 201–248, https://doi.org/10.1016/0079-6611(94)90028-0.

Cairns, J. L., and E. C. LaFond (1966), Periodic motions of the seasonal thermocline along the southern California coast, *Journal of Geophysical Research*, *71*(16), 3903–3915, https://doi.org/10.1029/JZ071i016p03903.

Cartwright, D. E. (1977), Oceanic tides, *Reports on Progress in Physics*, *40*(6), 665–708, https://doi.org/10.1088/0034-4885/40/6/002.

Cummins, P. F., J. Y. Cherniawsky, and M. G. G. Foreman (2001), North Pacific internal tides from the Aleutian Ridge: Altimeter observations and modeling, *Journal of Marine Research*, *59*(2), 167–191, https://doi.org/10.1357/002224001762882628.

Egbert, G. D., and S. Y. Erofeeva (2002), Efficient Inverse Modeling of Barotropic Ocean Tides, *Journal of Atmospheric and Oceanic Technology*, *19*(2), 183–204, https://doi.org/10.1175/1520-0426(2002)019<0183:EIMOBO>2.0.CO;2.

Egbert, G. D., and R. D. Ray (2000), Significant dissipation of tidal energy in the deep ocean inferred from satellite altimeter data, *Nature*, *405*(6788), 775–778, https://doi.org/10.1038/35015531.

Egbert, G. D., and R. D. Ray (2001), Estimates of M2 tidal energy dissipation from TOPEX/Poseidon altimeter data, *Journal of Geophysical Research: Oceans*, *106*(C10), 22,475–22,502, https://doi.org/10.1029/2000JC000699.

Egbert, G. D., and R. D. Ray (2003), Semi-diurnal and diurnal tidal dissipation from TOPEX/Poseidon altimetry, *Geophysical Research Letters*, *30*(17), https://doi.org/10.1029/2003GL017676.

Fang, Y., Y. Hou, and Z. Jing (2015), Seasonal characteristics of internal tides and their responses to background currents in the Luzon Strait, *Acta Oceanologica Sinica*, *34*(11), 46–54, https://doi.org/10.1007/s13131-015-0747-z.

Farmer, D. M., and L. Armi (1988), The flow of Atlantic water through the Strait of Gibraltar, *Progress in Oceanography*, *21*(1), 1–103, https://doi.org/10.1016/0079-6611(88)90055-9.

Garrett, C. (2003), Internal Tides and Ocean Mixing, *Science*, *301*(5641), 1858–1859, https://doi.org/10.1126/science.1090002.

Garrett, C., and E. Kunze (2007), Internal Tide Generation in the Deep Ocean, *Annual Review of Fluid Mechanics*, *39*(1), 57–87, https://doi.org/10.1146/annurev.fluid.39.050905.110227.

Garrett, C., and W. Munk (1972), Space-Time scales of internal waves, *Geophysical Fluid Dynamics*, *3*(3), 225–264, https://doi.org/10.1080/03091927208236082.

Hibiya, T. (2004), Internal Wave Generation by Tidal Flow over a Continental Shelf Slope, *Journal of Oceanography*, *60*(3), 637–643, https://doi.org/10.1023/B:JOCE.0000038356.45342.6c.

Holloway, P. E., and M. A. Merrifield (2003), On the spring-neap variability and age of the internal tide at the Hawaiian Ridge, *Journal of Geophysical Research: Oceans*, *108*(C4), https://doi.org/10.1029/2002JC001486.

Huan Lee, I., Y. Wang, Y. Yang, and D. Wang (2012), Temporal variability of internal tides in the northeast South China Sea, *Journal of Geophysical Research: Oceans*, *117*(C2), https://doi.org/10.1029/2011JC007518.

Jan, S., R.-C. Lien, and C.-H. Ting (2008), Numerical study of baroclinic tides in Luzon Strait, *Journal of Oceanography*, *64*(5), 789–802, https://doi.org/10.1007/s10872-008-0066-5.

Johnston, T. M. S., M. A. Merrifield, and P. E. Holloway (2003), Internal tide scattering at the Line Islands Ridge, *Journal of Geophysical Research: Oceans*, *108*(C11), https://doi.org/10.1029/2003JC001844.

Kantha, L. H., and C. C. Tierney (1997), Global baroclinic tides, *Progress in Oceanography*, *40*(1–4), 163–178, https://doi.org/10.1016/S0079-6611(97)00028-1.

Kerry, C. G., B. S. Powell, and G. S. Carter (2016), Quantifying the Incoherent M2 Internal Tide in the Philippine Sea, *Journal of Physical Oceanography*, *46*(8), 2483–2491, https://doi.org/10.1175/JPO-D-16-0023.1.

Krauss, W. (1966), *Interne Wellen*, Gebrüder Borntraeger.

LaFond, E. C. (1961), The isotherm follower, *Journal of Marine Research*, *19*(1), 33–39.

LeBlond, P. H., and L. A. Mysak (Eds.) (1978), *Waves in the Ocean*, Elsevier.

Lee, W. H. K., and C. S. Cox (1966), Time variation of ocean temperatures and its relation to internal waves and oceanic heat flow measurements, *Journal of Geophysical Research*, *71*(8), 2101–2111, https://doi.org/10.1029/JZ071i008p02101.

Lozovatsky, I. D., E. G. Morozov, and H. J. S. Fernando (2003), Spatial decay of energy density of tidal internal waves, *Journal of Geophysical Research: Oceans*, *108*(C6), https://doi.org/10.1029/2001JC001169.

Mercier, M. J., L. Gostiaux, K. Helfrich, J. Sommeria, S. Viboud, H. Didelle, S. J. Ghaemsaidi, T. Dauxois, and T. Peacock (2013), Large-scale, realistic laboratory modeling of M2 internal tide generation at the Luzon Strait, *Geophysical Research Letters*, *40*(21), 5704–5709, https://doi.org/10.1002/2013GL058064.

Morozov, E. G. (1988), Generation of internal tides over submarine ridges, *Oceanological Researches*, *41*, 55–67 (in Russian).

Morozov, E. G. (1990), Geographical variability of internal waves, *Oceanological Researches*, *43*, 48–68 (in Russian).

Morozov, E. G. (1995), Semidiurnal internal wave global field, *Deep Sea Research*, *42*(1), 135–148.

Morozov, E. G. (2006), Internal Tides. Global field of internal tides and mixing caused by internal tides, in *Waves in Geophysical Fluids*, pp. 271–332, Springer, Wein, New York.

Morozov, E. G. (2018), *Oceanic Internal Tides: Observations, Analysis and Modeling*, Springer International Publishing, https://doi.org/10.1007/978-3-319-73159-9.

Morozov, E. G., and V. I. Vlasenko (1996), Extreme tidal internal waves near the Mascarene ridge, *Journal of Marine Systems*, *9*(3–4), 203–210, https://doi.org/10.1016/S0924-7963(95)00042-9.

Morozov, E. G., K. Trulsen, M. G. Velarde, and V. I. Vlasenko (2002), Internal Tides in the Strait of Gibraltar, *Journal of Physical Oceanography*, *32*(11), 3193–3206, https://doi.org/10.1175/1520-0485(2002)032<3193:ITITSO>2.0.CO;2.

Munk, W. H. (1966), Abyssal recipes, *Deep Sea Research and Oceanographic Abstracts*, *13*(4), 707–730, https://doi.org/10.1016/0011-7471(66)90602-4.

Munk, W. H., and C. Wunsch (1998), Abyssal recipes II: energetics of tidal and wind mixing, *Deep Sea Research Part I: Oceanographic Research Papers*, *45*(12), 1977–2010, https://doi.org/10.1016/S0967-0637(98)00070-3.

Nansen, F. (1902), *The Oceanography of the North Polar BasinNorwegian North Polar Expedition 1893 - 1896 : scientific results*, vol. 9, Longmans and Green.

Niwa, Y., and T. Hibiya (2004), Three-dimensional numerical simulation of M2 internal tides in the East China Sea, *Journal of Geophysical Research: Oceans*, *109*(C4), https://doi.org/10.1029/2003JC001923.

Orr, M. H., and P. C. Mignerey (2003), Nonlinear internal waves in the South China Sea: Observation of the conversion of depression internal waves to elevation internal waves, *Journal of Geophysical Research: Oceans*, *108*(C3), https://doi.org/10.1029/2001JC001163.

Phillips, O. M. (1977), *The Dynamics of the Upper Ocean*, ii ed., Syndics of the Cambridge University Press, England.

Ramp, S. R., T. Y. Tang, T. F. Duda, J. F. Lynch, A. K. Liu, C.-S. Chiu, F. L. Bahr, H.-R. Kim, and Y.-J. Yang (2004), Internal Solitons in the Northeastern South China Sea Part I: Sources and Deep Water Propagation, *IEEE Journal of Oceanic Engineering*, *29*(4), 1157–1181, https://doi.org/10.1109/JOE.2004.840839.

Sjöberg, B., and A. Stigebrandt (1992), Computations of the geographical distribution of the energy flux to mixing processes via internal tides and the associated vertical circulation in the ocean, *Deep Sea Research Part A. Oceanographic Research Papers*, *39*(2), 269–291, https://doi.org/10.1016/0198-0149(92)90109-7.

Summers, H. J., and K. O. Emery (1963), Internal waves of tidal period off Southern California, *Journal of Geophysical Research*, *68*(3), 827–839, https://doi.org/10.1029/JZ068i003p00827.

Tareev, B. A. (1966), Dynamics of internal gravity waves in a continuously stratified ocean, *Izvestiya, Academy of Sciences, USSR. Atmospheric and Oceanic Physics*, *2*(10), 1064–1075.

Torgrimson, G. M., and B. M. Hickey (1979), Barotropic and Baroclinic Tides over the Continental Slope and Shelf off Oregon, *Journal of Physical Oceanography*, *9*(5), 945–961, https://doi.org/10.1175/1520-0485(1979)009<0945:BABTOT>2.0.CO;2.

Wunsch, C. (1975a), Deep ocean internal waves: What do we really know?, *Journal of Geophysical Research*, *80*(3), 339–343, https://doi.org/10.1029/JC080i003p00339.

Wunsch, C. (1975b), Internal tides in the ocean, *Reviews of Geophysics*, *13*(1), 167–182, https://doi.org/10.1029/RG013i001p00167.

Russian Journal of Earth Sciences

Special Issue: "25th anniversary of the Russian Journal of Earth Sciences"

Роль россыпных месторождений в обеспечении воспроизводства минерально-сырьевой базы дефицитных видов стратегического минерального сырья России на современном этапе

Н. С. Бортников[1], А. В. Волков[1], А. В. Лаломов[1], А. А. Бочнева[1], Ю. Н. Иванова[1,2], Д. А. Лаломов[3]

[1]Институт геологии рудных месторождений, петрографии, минералогии и геохимии РАН, г. Москва, Россия
[2]Российский университет дружбы народов, г. Москва, Россия
[3]ООО «Геодевайс технолоджис», г. Санкт-Петербург, Россия
* **Контакт:** Александр Валерианович Лаломов, lalomov@mail.ru

Россыпные месторождения играли (а по ряду компонентов и сейчас играют) важную роль в обеспечении стратегических видов минерально-сырьевой базы как России, так и мира в целом. Россыпи обладают рядом преимуществ, которые делают их востребованными горнодобывающей промышленностью: относительно неглубокое (часто – доступное для открытой добычи) залегание, дезинтегрированное состояние продуктивных отложений, простота процессов обогащения (преимущественно — гравитационные системы), а также возможность быстрого вовлечения в эксплуатацию, что значительно сокращает сроки окупаемости вложенных средств. Все это еще более актуально для современной России, когда в кратчайшие сроки в условиях дефицита кредитных ресурсов требуется осуществить программу импортозамещения и обеспечения страны дефицитными видами стратегического минерального сырья, такого как золото, платиноиды, олово, редкие металлы, титан, хром, алмазы.

Ключевые слова: стратегические металлы, россыпи, золото, олово, редкие металлы, алмазы.

Цитирование: Бортников Н. С., Волков А. В., Лаломов А. В., Бочнева А. А., Иванова Ю. Н., Лаломов Д. А. Роль россыпных месторождений в обеспечении воспроизводства минерально-сырьевой базы дефицитных видов стратегического минерального сырья России на современном этапе // Russian Journal of Earth Sciences. — 2024. — Т. 24. — ES1012. — DOI: 10.2205/2024es000897

Введение

Россыпи, по определению из нормативных документов ГКЗ, это «скопления рыхлого или сцементированного обломочного материала, содержащего в виде зерен, их обломков или агрегатов ценные минералы» [*МПР России*, 2000]. Наибольшее промышленное значение имеют россыпи золота, платины, касситерита, титана, редких металлов, алмазов, янтаря, хотя разрабатываются и более экзотические типы (магнезита, гранатов, хромита, драгоценных камней и т. д.).

Россыпные месторождения являются, по-видимому, древнейшим типом полезных ископаемых, эксплуатируемых человеком. Желваки кремня (основного материала для производства орудий труда каменного века) могли добываться и из коренных проявлений, но в россыпях они более доступны и широко распространены; этот тип россыпей относится к классу «валунных» наряду с россыпями хромита, нефрита-жадеита, оптического кварца и мамонтового бивня. Также россыпное золото относится к наиболее древнему полезному ископаемому, дошедшему до нас в письменных источниках: упоминаемое в Библии «хорошее золото земли Хавила», приуроченное к р. Фисон, также,

Получено: 15 октября 2024 г.
Принято: 15 января 2024 г.
Опубликовано: 29 февраля 2024 г.

скорее всего, являлось россыпным. Достоверно известно о добыче россыпного золота в древности и в средние века в Восточной Африке, Испании, Южной Америке и т. д.

Хотя в России коренные месторождения золота стали эксплуатироваться раньше россыпных, но с открытием в 1814 г. Л. И. Брусницыным на Урале россыпей золота и разработкой методов его промышленного извлечения, они вплоть до начала XXI-го века занимали ведущее место в золотодобыче. Россыпи других минерально-сырьевых типов также имеют значительное (а иногда и ведущее) место в мировой ресурсной базе (табл. 1).

Таблица 1. Доля россыпей различных типов в структуре запасов и добычи [*Лаломов и др.*, 2022a; *Павловский*, 2014; *U.S. Geological Survey*, 2020]

Вид сырья	Доля запасов категорий $A+B+C_1$ (≈ measured resources) россыпей, %	Доля россыпей в общей добыче, %
Золото (Россия) в 2021 г.	10,2	19,9
Платиноиды (Россия)	0,3	4,5
Алмазы (Россия, карат)	6,8	11
Олово (СССР, 1989 г.)	12,4	25
Олово (мир)	46,6	65
Титан (мир)	33	70
Цирконий (мир)	80	95
Ниобий (мир, с корами выветривания)	20	70
Тантал (мир, с корами выветривания)	4	>10
Вольфрам (с ТМО)*	0,73	3,2
Хром (Россия)	0,56	1,14

* ТМО — техногенно-минеральные образования.

В перспективе до 2035 года в мире прогнозируется кратное (в 2–6 раз) увеличение потребления для подавляющего числа видов высокотехнологичных металлов [*Бортников и др.*, 2022], существенная часть которых добывается из россыпных месторождений. Хотя в последние десятилетия основное внимание горнодобывающей промышленности как России, так и мира в целом, сосредоточено на крупных коренных объектах, пусть даже с низкими содержаниями, но большими запасами полезных компонентов, сложившаяся в настоящее время в России ситуация требует разработки новых подходов к воспроизводству минерально-сырьевой базы (МСБ) дефицитных видов стратегического минерального сырья России (рис. 1).

1. Золото

Несмотря на ведущую роль коренных месторождений, россыпи продолжают играть важную роль в добыче золота, что отличает Россию от других производителей золота в мире. На протяжении XX века основная часть золота добывалась из россыпных месторождений, и только в начале нашего века коренные месторождения стали преобладать, преимущественно за счет открытия и освоения новых крупных коренных источников. Россыпная добыча заметно падала с 120 т в 1990 г. до 55 т в 2009 г., (46 % от 1990 г), но потом стала возрастать, и к концу 2021 г. достигла 87,1 т (73 % от 1990 г.), что составляет 19,9 % от общей добычи (рис. 2). Роль россыпей для разных регионов неодинакова. По итогам 2021 г. в Пермском крае, ХМАО, Новосибирской, Кемеровской областях и Еврейской АО золото добывалось только из россыпей. Более 30 % россыпной добычи отмечается в Респ. Алтай (74 %), Хакассии (45 %), Приморском крае (37,5 %), Иркутской обл. (34,5 %), Бурятии (31,1 %) и Магаданской обл. (30,2 %).

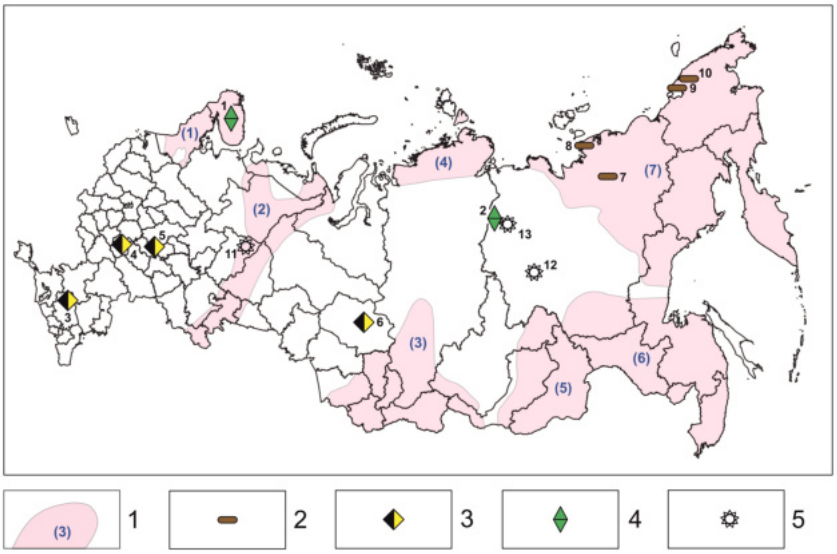

Рис. 1. Перспективные объекты для обеспечения России дефицитными видами стратегического минерального сырья. 1 — основные золотоносные провинции России: (1) Карело-Кольская, (2) Уральская, (3) Южно-Сибирская, (4) Таймыро-Североземельская, (5) Забайкальская, (6) Дальневосточная, (7) Северо-Восточная; 2 — олово, 3 — титан, цирконий, 4 — редкоземельные металлы (РЗМ), 5 — алмазы. Месторождения. РЗМ: 1 — Ловозерское, 2 — Томторское; титан и циркон: 3 — Бешпагирское, 4 — Центальное, 5 — Лукояновское, 6 — Туганское; олово: 7 — Тирехтях, 8 — Чокурдах, 9 — Валькумй, 10 — Пыркакай; алмазы: 11 — Сюзевская (Сев. Урал), 12 — Нюрбинская, 13 — Эбеляхская.

В целом, по результатам 2021 г., из стоящих на балансе на начало года 1122,01 т было добыто 87,1 т россыпного золота, при этом уменьшение балансовых запасов составило 9,8 т (0,9 % от запасов или 11,3 % от добычи) — добытое в 2021 г. россыпное золото было на 88,7 % компенсировано результатами, в первую очередь, разведки, а также переоценки и постановки на учет новых запасов.

В Государственном докладе «О состоянии и использовании минерально-сырьевых ресурсов Российской Федерации в 2021 году» [*ВИМС-ЦНИГРИ*, 2022] указывается, что сроки исчерпания балансовых запасов разрабатываемых россыпных месторождений составляют менее 7 лет. Примерно про такие же сроки исчерпания россыпных месторождений один из авторов статьи слышал в 1982 г. в Магадане в объединении «Севвостгеология», а старожилы утверждали, что подобная фраза звучала и за 20 лет до этого. Источником такого пессимистического прогноза служит простое деление распределенных запасов россыпного золота на объем ежегодной добычи. Учитывая, что разведка и постановка на баланс новых запасов в значительной мере (на 88,7 % от добытого металла или на 99,1 % от стоящего на балансе, по данным 2021 г.) компенсируют его добычу, имеющуюся оценку сроков исчерпания россыпных запасов можно увеличить на порядок.

При существующих уже на протяжении многих десятков лет темпах воспроизводства МСБ россыпного золота, можно утверждать возможность эксплуатации промышленных россыпных месторождений на протяжении десятков лет, и это не считая большого потенциала ТМО, а также новых типов россыпей (золото в песчано-гравийных смесях (ПГС), золотоносные конгломераты [*Волков и др.*, 2021], попутное золото в редкометалльно-титановых россыпях [*Левченко и Григорьева*, 2021] и т. д.). В ряде случаев (ТМО и ПГС) основные проблемы вовлечения этих месторождений в эксплуатацию носят не экономический или технологический, а юридический характер, что вполне преодолимо путем принятия соответствующих законодательных решений.

Рис. 2. Структура добычи золота в России [*Лаломов и др.*, 2022a].

Таким образом, продолжающаяся эксплуатация россыпных месторождений золота при минимальном вложении средств и решении правовых вопросов может на протяжении длительного времени обеспечивать от 15 до 20 % золотодобычи России.

2. Олово

По общему количеству разведанных запасов олова Россия занимает первое место в мире — по категориям $A+B+C_1+C_2$ на государственном балансе числится 2110,3 тыс. т, и наряду с Бразилией (2000 тыс. т) и Китаем (1800 тыс. т) входит в тройку мировых лидеров. Запасы олова в россыпях по категориям $A+B+C_1+C_2$ составляют 223,5 тыс. т (10,6 % общероссийских запасов) [*Росгеолфонд*, 2022].

Сырьевая база россыпного олова России характеризуется высокой степенью концентрации: 99,3 % запасов и 97,9 % прогнозных ресурсов сосредоточены в восточном секторе Арктической зоны. При этом 71,5 % разведанных запасов россыпного олова высоких категорий сконцентрировано в 4 крупных месторождениях: континентальных Тирехтях, Одинокая, и гетерогенных прибрежно-морских Чокурдах и Валькумей.

В мире доля россыпных месторождений в общем объеме добычи составляет 53,4 % (в Азии — 80,5 %), в России (на конец 1990-х гг.) из россыпей добывалось 25 % [*Быховский и Спорыхина*, 2013; *Смирнов и др.*, 2008; *Kamilli et al.*, 2017]. Еще во времена Советского Союза добыча олова на Северо-Востоке была нерентабельна на фоне мировых цен в силу высоких сопутствующих накладных расходов и дотировалась из государственного бюджета как стратегическое сырье. После открытия рынка и падения мировых цен на олово в начале 90-х добыча олова на Северо-Востоке как на россыпных, так и на коренных объектах была свернута.

Значительный рост цены на рафинированное олово (до 40 тыс. долл./т в первой половине 2022 г.) сделал возможным возобновление рентабельной добычи на российских месторождениях.

Наиболее крупным из подготавливаемых к эксплуатации объектов является группа Пыркакайских штокверков на Чукотке, запасы которых по категориям $A+B+C_1+C_2$ составляют 238.4 тыс. т олова при содержании 0,25 %. В 2020 г. ПАО «Русолово» (оловянный дивизион ПАО «Селигдар») по результатам аукциона получило право на геологическое изучение, разведку и добычу олова месторождений Пыркакайского рудного узла. Разработка месторождений возможна открытым способом; срок отработки, по предварительным оценкам, около 30 лет. Согласно лицензионному соглашению, не позднее августа 2031 г. должна начаться эксплуатация [*ВИМС-ЦНИГРИ*, 2021]. Вложения, необходимые для строительства ГОКа, на сегодняшний день оцениваются в 300 млн $ US. При этом содержания олова в рудах существенно уступают месторождениям, разрабатываемым за рубежом: содержания олова в рудах основных эксплуатируемых зарубежных месторождений варьируют в интервале 0,27–1,68 % [*Kamilli et al.*, 2017]. Учитывая удаленность и сложные природные условия отработки руд Пыркакайского месторождения, его конкурентоспособность на мировом рынке олова вызывает ряд вопросов.

Что касается россыпных месторождений, компания АО «Янолово» летом 2021 г. возобновила разработку Тирехтяхской россыпи, по которой на государственном балансе находится 68,2 тыс. т олова с содержанием 960 г/м^3. Россыпь относится к аллювиально-делювиальному и аллювиальному типам. Ее запасы доступны для открытой отработки (рис. 3). Уже в первый год после возобновления эксплуатации на месторождении было добыто 452 т олова.

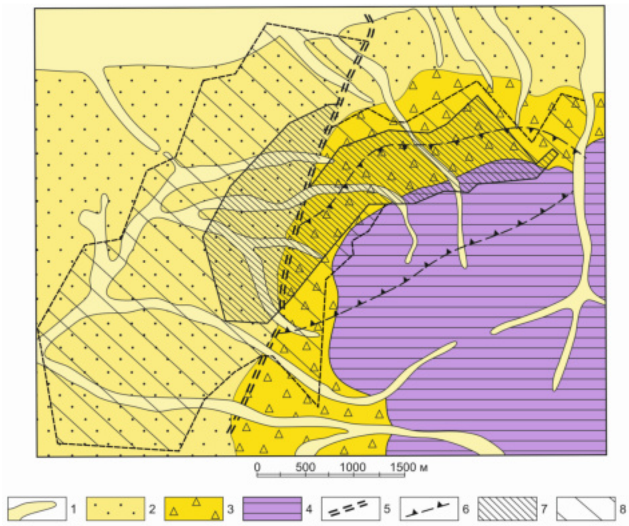

Рис. 3. Схема строения Тирехтяхского месторождения россыпного олова с использованием данных [*Спорыхина и Патык-Кара*, 1997]: 1 — современные аллювиальные отложения, 2 — отложения плейстоценовой аккумулятивной равнины, 3 — склоново-пролювиальные шлейфы (верхний плейстоцен–голоцен), 4 — терригенно-осадочные породы верхнего триаса, 5 — тектонические нарушения, выраженные в рельефе коренных пород, 6 — граница рудного поля месторождения Дружба, 7, 8 – контур россыпи (7 — с балансовыми запасами, 8 — с забалансовыми запасами).

Согласно проекту (2020 г.), предприятие выйдет на проектную производительность в 3 млн м^3 песков (2,8 тыс. т олова) в год в 2025 г., что полностью покроет текущие потребности России. Ожидаемый срок отработки запасов — 2051 г. Обогащение песков будет вестись по гравитационной схеме (извлечение Sn $>$ 85 %) с получением оловянного концентрата марки КО-1 (содержание Sn $\geqslant$ 60 %).

К россыпным месторождениям олова, отработка которых может быть начата в кратчайшие сроки, относятся прибрежно-морские россыпи Валькумейская на Чукотке (15,7 тыс. т при содержании 1260 г/м^3), Чокурдах в Якутии (18,2 тыс. т при содержании 493 г/м^3) и Одинокая в Якутии (51,9 тыс. т при содержании 829 г/м^3). Кроме того, за пределами гос. баланса остались россыпи Ляховского оловоносного узла, поисково-разведочные работы в котором были свернуты по экологическим соображениям в 1992 г., где по категории C_2 были оценены россыпи с общими запасами 109,9 тыс. т при средних содержаниях 800–1670 г/м^3.

Таким образом, в обеспечении страны оловом преимущества россыпей, которые требуют гораздо меньших вложений, а отдачу дают в течение уже первого года эксплуатации, по сравнению с коренными объектами, являются неоспоримыми. Понимание этих аспектов находит отклик у руководства российской горнодобывающей отраслью: еще несколько лет назад влияние россыпей на оловодобычу оценивалось как «незначительное» («Основой российской сырьевой базы олова являются разномасштабные коренные месторождения оловянных руд... На долю россыпей приходится менее 11 % российских запасов олова; среди них в количественном отношении преобладают мелкие объекты с запасами менее 1 тыс. т олова» [*ВИМС–Минерал-Инфо*, 2018, с. 178—179]).

В настоящее время основным перспективным объектом России по олову считается россыпное месторождение Тирехтях [*ВИМС-ЦНИГРИ*, 2022, с. 279]. Учитывая, что видимое внутреннее потребление металлического олова в России составляет 2–2,6 тыс. т в год [*ВИМС-ЦНИГРИ*, 2022], только стоящие на балансе россыпные запасы олова (233,5 тыс. т) могут обеспечить текущие потребности страны приблизительно на 100 лет.

3. Титан

Согласно Стратегии развития минерально-сырьевой базы до 2035 года, утвержденной распоряжением Правительства РФ от 22.12.2018 № 2914-р, титан относится к группе дефицитных полезных ископаемых, внутреннее потребление которых в значительной степени обеспечивается вынужденным импортом. Кроме того, титан входит в перечень основных видов стратегического минерального сырья, утвержденный распоряжением Правительства РФ от 30.018.2022 № 2473-р.

Россия располагает одной из крупнейших в мире сырьевых баз титана — на ее долю приходится 15 % запасов мира. При этом вклад страны в мировое производство концентратов титана составляет всего 0,03 %.

Россия является одним из ведущих в мире продуцентов губчатого титана и титановых изделий, но практически все российские предприятия, использующие титановое сырье, импортируют его. Главным производителем губчатого титана, обеспечивающим России статус лидера мирового рынка, является ПАО «Корпорация ВСМПО-АВИСМА», выпускающая его на титаномагниевом комбинате «АВИСМА» в г. Березники (Пермский край). Главным производителем пигментного диоксида титана, используемого в лакокрасочной промышленности, является завод «Крымский титан» (Республика Крым).

Основной (еще с советских времен) поставщик титановых концентратов на заводы Урала — Украина — с марта 2022 г. полностью прекратила поставки. В настоящее время российские заводы испытывают большой дефицит титанового сырья, который покрывается за счет складских запасов и поставок из Вьетнама, Мозамбика и Казахстана. Завод «Крымский титан» из-за дефицита сырья работает только на 25 % от возможного объема переработки 80 тыс. т/год ильменитового концентрата. Поэтому обеспечение российской титановой промышленности собственным сырьем является крайне насущной проблемой.

Российская сырьевая база титана на 97 % состоит из месторождений магматогенного генезиса в габброидных и щелочных породах и литифицированных погребенных россыпей (крупные Пижемское и Ярегское месторождения), относимых по условиям эксплуатации к коренным рудам. В мире 60–70 % титановых концентратов производится из комплексных россыпных месторождений [*Suiekpayev et al.*, 2021; *U.S. Geological Survey*, 2020]. Эксплуатируемые в мире коренные объекты отличаются от стоящих на балансе российских повышенными содержаниями титана: так, содержание титана в рудах месторождения Лак-Тио в Канаде составляет 32–38 % [*Charlier et al.*, 2010], в рудах месторождения Теллнес в Норвегии — 16–20 % [*Charlier et al.*, 2006], месторождения Дамиао (Damiao) в Китае — 8–10 % [*Charlier et al.*, 2015]. Содержание титана в рудах российских коренных месторождений не превышает 7–8,5 %. К тому же российские месторождения испытывают большие проблемы с технологией обогащения и переработки руд [*ВИМС-ЦНИГРИ*, 2022, с. 319, 322]. Ряд месторождений расположены в удаленных слабо освоенных районах. В незначительных количествах (3 тыс. т TiO_2 в 2021 г.) титановый концентрат получают только из лопаритовых руд Ловозерского месторождения.

Россыпные месторождения представлены погребенными древними (от юрских до плиоценовых) прибрежно-морскими россыпями, расположенными в пределах Восточно-Европейской и Западно-Сибирской платформ (табл. 2). Россыпи имеют комплексный характер — помимо титановых минералов (ильменита и рутила) и минерального агрегата лейкоксена они содержат в промышленных количествах циркон, устойчивые алюмосиликаты (дистен, ставролит, силлиманит), в отдельных случаях монацит, глауконит, фосфориты, мелкое и тонкое золото.

В декабре 2021 г. АО «Туганский ГОК „Ильменит“» ввело в эксплуатацию первую очередь ГОКа на россыпном циркон-рутил-ильменитовом Туганском месторождении в Томской области, что позволяет выпускать 11,4 тыс. т/год ильменитового и 0,8 тыс. т рутил-лейкоксенового, а к 2029 г., работая на полную мощность, ГОК сможет ежегодно выпускать 136,6 тыс. т/год ильменитового и 9,4 тыс. т рутил-лейкоксенового концентратов. Учитывая видимое потребление концентратов титана на 2021 г. 226,8 тыс. т [*ВИМС-ЦНИГРИ*, 2022], при выходе на полную мощность комбинат сможет покрыть текущие потребности России на 64 %. Срок отработки всех запасов месторождения оценивается в 43–45 лет.

Таблица 2. Параметры основных комплексных редкометалльно-титановых россыпей России

Месторождение	TiO_2		ZrO_2		Расположение
	Запасы, тыс. т	Среднее содержание, кг/м^3	Запасы, тыс. т	Среднее содержание, кг/м^3	
Восточно-Европейская мегапровинция					
Бешпагирское	2630	20,9	620,6	5,1	Ставропольский край
Центральное	6396	54,1	830,3	3,1	Тамбовская область
Лукояновское	166	5,5	346,4	13	Нижегородская область
Новозыбковское	237	8,1	27,6	1,7	Брянская область
Западно-Сибирская мегапровинция					
Тарское	1001	32,2	181,4	6,4	Омская область
Самсоновское	1674	34,2	266,6	5,2	Омская область
Туганское	2502	19,7	1007,3	7,7	Томская область
Георгиевское	1568	17,6	408,8	4,9	Томская область
Ордынское	56	14,4	15,3	3,9	Новосибирская область
Буткинское	133	16,8	12,3	1,8	Свердловская область
Правобережное	270	20	30,7	2,6	ХМАО

Среди месторождений нераспределенного фонда недр наиболее перспективными для освоения являются погребенные прибрежно-морские россыпи Ставропольского края: Бешпагирское месторождение, Константиновский и Камбулатский участки. Их совокупные запасы, качественные показатели потенциальной продукции и инфраструктурная освоенность региона позволяют создать на их базе крупное горно-обогатительное производство. Получаемый из них ильменитовый концентрат (62,2 % TiO_2) подходит для производства губчатого титана и пигментного диоксида титана. Технико-экономические показатели отработки запасов открытым способом определены для 15-летнего расчетного периода со среднегодовым производством товарных концентратов: рутилового — 10 тыс. т, ильменитового — 28 тыс. т [*Быховский и др.*, 2010a], что покроет еще 17 % потребностей России.

Таким образом, ввод в эксплуатацию россыпных редкометалльно-титановых месторождений России может в кратчайшие сроки обеспечить основную часть потребностей в титановом сырье и снизить зависимость отечественной промышленности от импорта. Россыпные месторождения титана, запасы которых оцениваются в 17,8 млн т, могут обеспечить текущие потребности страны на срок до 80 лет.

4. Редкие и редкоземельные металлы

Редкие металлы (к которым относятся и редкоземельные) мало распространены в природе, встречаются в собственных минеральных формах или в качестве примесей в других минералах. Из россыпных месторождений добывают цирконий, ниобий, тантал, группу редкоземельных металлов (РЗМ), в незначительных количествах вольфрам, в качестве примесей в россыпных минералах присутствуют гафний (в цирконе), индий (в касситерите). К группе РЗМ относятся лантан (La), церий (Ce), празеодим (Pr), неодим (Nd), самарий (Sm), европий (Eu), гадолиний (Gd), тербий (Tb), диспрозий (Dy), гольмий (Ho), эрбий (Er), тулий (Tm), иттербий (Ib), лютеций (Lu), иттрий (Y) и скандий (Sc).

Цирконий. Россия располагает крупной МСБ циркония, достаточной для обеспечения внутренних потребностей страны: на 01.01.2022 на государственном балансе находились 12,4 млн т ZrO_2. МСБ циркония России структурно и качественно отличается от зарубежной. На долю циркон-рутил-ильменитовых россыпных месторождений, с которыми за рубежом связано 80 % запасов и 95 % добычи, в России приходится 33 % запасов, заключенных в 10 месторождениях, но промышленностью они практически не освоены.

В то же время по выпуску циркониевого проката Россия — один из мировых лидеров, обеспечивающий около пятой части поставок на рынок. Для производства металлического циркония (в том числе ядерной чистоты), его сплавов и изделий из них отечественные предприятия импортируют циркониевый концентрат.

Основная часть российских запасов циркония (8,6 млн т ZrO_2, 68,9 %) сосредоточена в 4 коренных месторождениях: 3 редкометалльного щелочно-гранитного типа (Улуг-Танзекское, Катугинское и Зашихинское месторождения) и одного карбонатитового (Ковдорское). Остальные запасы содержатся в погребенных прибрежно-морских россыпях (3,9 млн т ZrO_2).

За рубежом на коренные месторождения приходится всего 2 % запасов, и они не рассматриваются в качестве перспективных источников циркония. Кроме того, Улуг-Танзекское месторождение находится в труднодоступном районе (юго-восточная Тува). Комплексные руды (Ta, Nb, Zr, U, Ti, Fe, РЗМ) Катугинского и Улуг-Танзекского месторождений относятся к труднообогатимым [*ВИМС-ЦНИГРИ*, 2021].

В Мурманской области также учтены забалансовые запасы циркония в эвдиалитовых рудах участка Аллуайв Ловозерского месторождения. Хотя в лабораторных условиях были разработаны различные варианты технологических схем их переработки, промышленная технология обогащения и передела такого сырья пока отсутствует [*ВИМС-ЦНИГРИ*, 2022].

В качестве первоочередных к освоению россыпных объектов на территории России можно выделить следующие: Туганское, Томская область, Лукояновское, Нижегородская область и Бешпагирское, Ставропольский край.

Запасы ***Туганского месторождения*** составляют около 1 млн т ZrO_2. Уже в настоящее время комбинат производит 3,7 тыс. т циркониевого концентрата, а после вывода ГОКа на полную мощность к 2029 г. он сможет ежегодно выпускать 44,2 тыс. т. Учитывая, что видимое потребление циркониевого концентрата в России составляет 9,9–11,6 тыс. т/год, это позволит полностью обеспечить потребности страны и возможность экспорта как концентратов, так и изделий из циркония на протяжении более чем 20 лет.

Лукояновское месторождение — богатейшее по содержанию диоксида циркония в России (13 кг/м^3) и второе в мире (после австралийской россыпи Атлас-буна Нарринг с содержанием 17,4 кг/м^3), представляет собой пространственно и структурно разобщенные залежи, из которых только Итмановская россыпь детально разведана: запасы по категории $C_1 + C_2$ составляют 388,9 тыс. т при содержании диоксида циркония 13 кг/м^3 [*ВИМС-ЦНИГРИ*, 2022]. Запасы диоксида гафния, содержащегося в цирконе, оценены в 6,3 тыс. т при содержании 0,2 кг/м^3. Также в составе россыпи присутствуют титановые минералы (ильменит, лейкоксен и рутил), запасы диоксида титана оценены в 166,7 тыс. т при содержании 5,5 кг/м^3. Отличительная черта Итмановской россыпи – повышенное содержание хромита (9,9 кг/м^3), запасы которого составляют 296,9 тыс. т. Глубина залегания рудного пласта изменяется от 0 до 20 м, при этом 40 % россыпи может быть отработана карьером, остальные запасы — с использованием метода скважинной гидродобычи (СГД) (рис. 4).

Вокруг Итмановской залежи на расстоянии от 15 до 40 км расположены другие россыпи Лукояновского месторождения, поисково-оценочные работы на которых позволили локализовать прогнозные ресурсы категории P_1, которые при мощности промышленного пласта более 2 м составляют 678 тыс. т диоксида циркония [*Быховский и др.*, 2010b], что существенно увеличивает срок жизнедеятельности возможного добывающего предприятия.

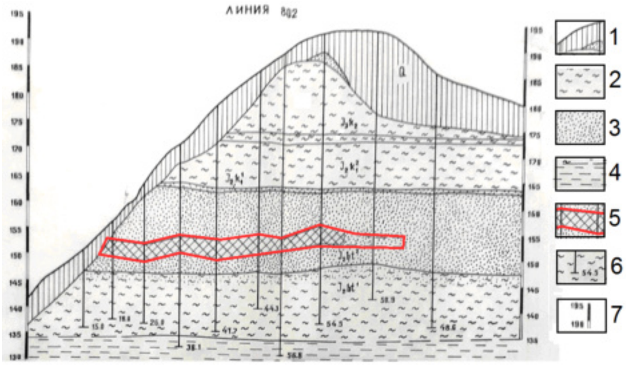

Рис. 4. Геологический разрез Итмановской россыпи Лукояновского титано-циркониевого месторождения [*Осипов*, 1985]. 1 — почвенно-растительный слой; 2 — глины; 3 — пески; 4 — алевриты; 5 – промышленный пласт; 6 — скважины (глубина, м); 7 — высотные отметки. Среднеюрские отложения: J_2bt — батский ярус; J_2k — келловейский ярус.

Перспективы обеспечения России циркониевым сырьем связаны также с запасами около 620 тыс. т ZrO_2 ***Бешпагирского месторождения***, цирконовый концентрат которого (64,5 % ZrO_2) удовлетворяет требованиям для производства циркония, в том числе ядерной чистоты. Среднегодовое производство концентрата проектируется на уровне 15 тыс. т/год.

Таким образом, внутренние потребности России и экспортный потенциал по цирконию могут быть обеспечены в кратчайшие сроки и с минимальными затратами за счет россыпных месторождений.

РЗМ. Сырьевая база РЗМ России характеризуется высокой концентрацией: 46,3 % сосредоточено в девяти объектах Мурманской области. Из них около 24,9 % — в Ловозерском месторождении комплексных лопаритовых руд — единственном в России объекте, разрабатываемом на РЗМ. Остальные запасы региона заключены в апатит-нефелиновых рудах восьми месторождений Хибинской группы, основным компонентом которых является фосфор. РЗМ характеризуются низким содержанием (в среднем 0,34 % $\sum TR_2O_3$), в настоящее время не извлекаются и накапливаются в продуктах отвального комплекса.

В объектах Сибири и Дальнего Востока содержится 44,2 % запасов РЗМ страны, из которых основные запасы связаны с крупными месторождениями комплексных руд, в карбонатитах и развитых по ним корам выветривания (Томторском в Республике Саха-Якутия, Чуктуконском в Красноярском крае и Белозиминском в Иркутской области). Остальные запасы заключены в Селигдарском месторождении апатит-карбонатных метасоматитов, в комплексных редкометалльных метасоматических месторождениях по щелочным гранитам (Улуг-Танзекском в Республике Тыва и Зашихинском в Иркутской области; 3,9 %) и метаморфогенным породам зон тектонических нарушений (Катугинском в Забайкальском крае; 5,8 %), в рудах которых отмечаются высокие содержания иттрия и лантаноидов иттриевой группы. Еще 3,6 % запасов России связаны с нефтеносными лейкоксеновыми песчаниками Ярегского месторождения в Республике

Коми. Среднее содержание РЗМ в них составляет 0,04 %, промышленная технология их извлечения отсутствует [*ВИМС-ЦНИГРИ*, 2022]. Значительная часть месторождений находится в удаленных труднодоступных районах.

Из подготавливаемых к освоению месторождений извлечение РЗМ в товарную продукцию предусмотрено только для Томторского и Зашихинского месторождений. Особенность Томторского месторождения в том, что его руда является природным концентратом, не требующим предварительного обогащения. Для него характерно совместное присутствие нескольких полезных минералов, нередко имеющих разные формы выделения, тесные срастания полезных минералов между собой и с породообразующими фазами. Этим определяется сложность технологии извлечения из руды всех ценных компонентов с получением продукции требуемого промышленностью качества. Проект требует весьма крупных капиталовложений. Сложные логистические решения, сложные технологические процессы, а также крайне неблагоприятное расположение объекта сильно повышают себестоимость конечной продукции. Негативным фактором также является радиоактивность руд, связанная с повышенным содержанием тория.

В настоящее время единственным действующим источником редкоземельных металлов (и значительной части редких) в России является Ловозерский горно-обогатительный комбинат, разрабатывающий месторождение лопарита Ловозерского массива — источника ниобия, тантала, редких земель и титана. В 2021 г. на фабрике было получено 7747 т лопаритового концентрата, содержащего в среднем 28–30 % оксидов РЗМ, 35–38 % TiO_2, 7,5–8,0 % Nb_2O_5, 0,5–0,8 % Ta_2O_5 [*ВИМС-ЦНИГРИ*, 2022]. В настоящее время добыча ведется в сложных горно-геологических условиях при низкой рентабельности существующих разрезов. Горнотехническая авария и закрытие Умбозерского рудника существенно сократили потенциал развития месторождения.

Дополнительным источником редкоземельного сырья комбината могут служить разведанные россыпи лопарита, расположенные на северном обрамлении Ловозерского массива, а также техногенные отвалы — хвосты обогатительной фабрики Карнасурт.

Россыпные месторождения тесно связаны с гляциальными и флювиогляциальными отложениями местного горного оледенения. Содержание лопарита в них достигает в отдельных случаях 36 кг/м^3, составляя в среднем по разным участкам 2,8–3,9 кг/м^3. Мощность продуктивного пласта составляет в среднем 20,7 м; залегание пласта приповерхностное — коэффициент вскрыши (отношение мощности перекрывающих «торфов» к мощности пласта) равен 0,5 [*Лаломов и др.*, 2019].

Наиболее перспективным по совокупности параметров является Сергеваньский участок Ревдинской (Северной) россыпи. Он расположен в непосредственной близости вниз по долине от хвостохранилища ГОКа (рис. 5).

Рис. 5. Обзорная схема района обогатительной фабрики Ловозерского ГОКа и хвостохранилищ (на основе космоснимка, полученного из открытых источников — программа «Google Earth»).

Продуктивный пласт представлен песчано-гравийно-галечными отложениями с незначительным содержанием глинистых классов, что обуславливает хорошую промывистость отложений. Лопарит сосредоточен в классах 0,14–0,56 мм (64,3 % от общего содержания) [*Лаломов и др.*, 2022b]. Проведенные минералого-технологические исследования показали, что руды Сергеваньского участка могут обогащаться по гравитационно-магнитной схеме, что позволит получить промышленный лопаритовый концентрат для редкометалльной промышленности [*Левченко и др.*, 2023].

Учитывая текущую годовую производительность Ловозерского ГОКа по производству лопаритового концентрата, отработка только одного Сергеваньского участка способна обеспечить поставки лопаритового концентрата на протяжении 68 лет. При этом отработка россыпи не потребует значительных и долговременных финансовых вложений, концентрат может быть получен уже к концу первого года после начала отработки, а технологическая схема не потребует дорогостоящей и энергозатратной операции дробления.

Вторым альтернативным источником обеспечения сырьевой базы Ловозерского ГОКа могут служить накопленные хвосты обогатительной фабрики Карнасурт. Хвосты обогащения руд вызывают в последнее время значительный интерес горнодобывающих компаний. Так, по оценке специалистов ЮАР, переработка хвостов на 90 % более энергоэффективна и на 90 % менее капиталоемка, чем запуск основного рудника, не говоря уже о более коротком цикле получения разрешений [*Золотодобыча*, 2023].

Содержание лопарита в хвостах фабрики (Карнасурт-1 и Карнасурт-2) оценено как на основе расчета по содержанию лопарита в перерабатываемых рудах и потерях при обогащении, так и по данным точечного опробования (пробы К-1 и К-2). Эти методы дали хорошую сходимость результатов на уровне 0,58–0,77 %. Минералого-технологическое исследование малых технологических проб показало, что лопарит в хвостах обогащения присутствует в виде как обломков крупных зерен, так и мелких идиоморфных кристаллов. Основная масса лопарита находится в гравитационно обогатимых классах. Структура хвостохранилища неоднородная, она определяется перераспределением тяжелой фракции за счет природно-техногенных процессов и имеет преимущественно концентрическую форму, что должно учитываться при постановке оценочных работ.

Учитывая содержание полезных компонентов в отрабатываемых рудах и извлечение лопарита в концентрат, можно предположить валовое содержание в образованных отвалах. Эта расчетная оценка валового содержания близка к результатам минералого-технологического опробования (табл. 3). Запасы лопарита в хвостах обогащения ГОКа сопоставимы с производительностью комбината за период 15–20 лет.

Таким образом, лопаритовые россыпи Ловозерского массива и хвосты обогатительной фабрики ГОКа могут служить альтернативным или дополнительным источником редкометального сырья, способного обеспечить потребности нашей страны на протяжении десятков лет. Они могут быть вовлечены в эксплуатацию в кратчайшие сроки и с минимальными затратами, что дает им преимущества по сравнению с коренными объектами.

Таблица 3. Содержание лопарита и основных компонентов в отложениях хвостохранилищ по данным расчета и точечного опробования (в % от исходной пробы)

	Лопарит	Nb_2O_5,	Ta_2O_5	$\sum TR_2O_3$
Карнасурт-1 (расчётное)	0,77	0,07	0,005	0,25
Карнасурт-2 (расчётное)	0,64	0,058	0,004	0,21
К-1 МТП РФА*	0,58	0,079	0,005	0,33
К-2 МТП РФА*	0,77	0,081	0,005	0,34

* Минералого-технологическая проба, проанализированная РФА.

5. Алмазы

По состоянию на 01.01.2022 балансовые запасы алмазов России составляют 1 018,9 млн карат, которые заключены в 65 месторождениях (20 коренных и 45 россыпных). Основу отечественной сырьевой базы алмазов составляют коренные кимберлитовые месторождения, заключающие 93,2 % запасов страны и обеспечивающие 89 % добычи. Соответственно, россыпные объекты вмещают 6,8 % запасов алмазов и обеспечивают 11 % добычи в объемном выражении. Здесь надо учитывать, что россыпные алмазы обладают более высоким качеством, чем коренные в силу разрушения некачественных (немонолитных) зерен при выветривании. Следствие этого — их более высокая рыночная цена. Так, средняя цена российских алмазов (преимущественно, коренных) — 67,6 долл./кар., а алмазов в прибрежно-морских россыпях Намибии — 466,6 долл./кар. [*ВИМС-ЦНИГРИ*, 2022]. Средняя цена россыпных алмазов Урала в месторождениях Вишерского района составляет 450–500 $ US/карат [*Чуйко и др.*, 2023]. Таким образом, значение россыпных алмазов в стоимостном отношении (особенно, в классе ювелирных камней) значительно выше, чем в объемном.

Россыпи алмазов расположены, преимущественно, на территории Республики Саха (Якутия), наиболее крупные — Нюрбинская и р. Эбелях являются уникальными по запасам и содержанию алмазов.

Добыча алмазов из россыпей Урала, продолжавшаяся почти два столетия, была приостановлена в 2005 г. из-за истощения имеющихся россыпей. С открытием на Западном Урале (Пермский край) и постановкой на баланс Сюзевской глубокозалегающей россыпи, относящейся к типу россыпей погребенных грабен-долин, открываются перспективы возобновления россыпной добычи на Урале. Более 90 % алмазов россыпи имеют ювелирное качество, средняя стоимость алмазов россыпи 361,59 $ US/карат [*Чуйко и др.*, 2023].

6. Заключение

Выполненный анализ (табл. 1) показал, что практически по всем компонентам доля россыпей в балансе добычи превышает их долю в балансе запасов. Из этого следует, что, несмотря на валовое преобладание в балансе запасов коренных месторождений, востребованность россыпей в горнодобывающей промышленности — весьма высокая. Это объясняется следующими факторами:

- относительно неглубокое залегание промышленного пласта (десятки метров), позволяющее проводить отработку открытым карьером; для глубокозалегающих россыпей возможно применение метода СГД, который по эффективности сопоставим с открытой отработкой;
- технологическая простота процессов обогащения, не требующая сложных технологий (преимущественно гравитационное обогащение);
- энергетическая эффективность процессов обогащения, исключающая дробление материала, на которое уходит 50 % энергетических затрат при разработке коренных месторождений;
- быстрое (часто в течение одного сезона) начало отдачи средств, вложенных в добычу россыпей.

Отработка россыпных месторождений не просто экономически выгодна, в ряде случаев она дает возможность в кратчайшие сроки и с минимальными затратами решить для нашей страны проблему импортозамещения и обеспечения воспроизводства МСБ дефицитных видов стратегического минерального сырья. Это особенно актуально в настоящее время, когда России трудно рассчитывать на международное кредитование горнодобывающей промышленности, а импорт сырья имеет высокие логистические риски.

Как показывает многолетний опыт СССР по вводу в строй и эксплуатацию россыпных месторождений золота и олова, а также рассмотренные выше примеры Тирехтяхского прииска и Туганского ГОКа, быстрыми темпами самообеспечение по ряду импортозависимых видов стратегического минерального сырья (Sn, Ti, Zr, Nb, Ta, REE) может быть достигнуто за счет освоения россыпных месторождений.

Выполненный в статье анализ (в плане импортозамещения) для первоочередного освоения позволяет рекомендовать следующие объекты: Sn — Тирехтяхская, Чокурдахская и Валькумейская россыпи (Якутия и Чукотка); Nb, Ta, Ti, REE — лопаритовые россыпи Ревдинской группы и техногенные отложения в хвостохранилищах Ловозерского ГОКа (Кольский полуосров); Ti и Zr — Туганское и Бешпагирское месторождения, Итмановский участок Лукояновского россыпного месторождения (Zr).

Благодарность. Исследования выполнены при финансовой поддержке Гос. задания ИГЕМ РАН.

Список литературы

Бортников Н. С., Волков А. В., Галямов А. Л. *и др.* Фундаментальные проблемы развития минерально-сырьевой базы высокотехнологичной промышленности и энергетики России // Геология рудных месторождений. — 2022. — Т. 64, № 6. — С. 617—633. — DOI: 10.31857/S0016777022060028.

Быховский Л. З., Васильев А. Т., Забирко А. Г. О проекте освоения Бешпагирского комплексного россыпного редкометалльно-титанового месторождения // Минеральные ресурсы России. Экономика и управление. — 2010a. — № 1. — С. 68—75. — EDN: LBDHEN.

Быховский Л. З., Спорыхина Л. В. Россыпные месторождения в сырьевой базе и добыче полезных ископаемых // Минеральные ресурсы России. Экономика и управление. — 2013. — № 6. — С. 6—17. — EDN: RMXKHF.

Быховский Л. З., Тигунов Л. П., Емельянов С. А. Разработка технико-экономического обоснования постоянных кондиций, подсчет запасов титано-циркониевых песков Итмановской россыпи Лукояновского м-ния в Нижегородской области (по состоянию на 01.06.2010 г.) — 2010b. — URL: https://www.rfgf.ru/catalog/docview.php?did=38901377e029066333bc9b71d1aaa71a.

ВИМС-ЦНИГРИ. Государственный доклад «О состоянии и использовании минерально-сырьевых ресурсов Российской Федерации в 2020 году». — 2021.

ВИМС-ЦНИГРИ. Государственный доклад «О состоянии и использовании минерально-сырьевых ресурсов Российской Федерации в 2021 году». — 2022.

ВИМС–Минерал-Инфо. Государственный доклад «О состоянии и использовании минерально-сырьевых ресурсов Российской Федерации в 2016 и 2017 годах». — 2018.

Волков А. В., Галямов А. Л., Лаломов А. В. *и др.* Металлоносные конгломераты - потенциальные источники россыпей в арктической зоне России // Арктика: экология и экономика. — 2021. — Т. 11, № 2. — С. 232—243. — DOI: 10.25283/2223-4594-2021-2-232-243.

Золотодобыча. Из хвостохранилищ золотодобывающих предприятий в ЮАР можно извлечь почти 1000 тонн золота. — 2023. — URL: https://zolotodb.ru/article/13040 (дата обр. 03.10.2023).

Лаломов А. В., Владимирцева О. В., Бочнева А. А. Роль россыпных месторождений в золотодобывающей промышленности России // Золото и технологии. — 2022a. — № 4 (58). — С. 36—44.

Лаломов А. В., Григорьева А. В., Бочнева А. А. *и др.* Редкометалльные россыпи Ловозерского массива // Разведка и охрана недр. — 2019. — № 1. — С. 51—56. — EDN: YZANOP.

Лаломов А. В., Григорьева А. В., Зайцев В. А. Минеральный состав редкометалльных россыпей Ловозерского массива // Геология рудных месторождений. — 2022b. — № 5. — С. 485—497. — DOI: 10.31857/S0016777022050069.

Левченко Е. Н., Григорьева А. В. Типоморфные и технологические особенности попутного золота в комплексных россыпных месторождениях // Обогащение руд. — 2021. — № 3. — С. 24—32. — DOI: 10.17580/or.2021.03.05.

Левченко Е. Н., Лаломов А. В., Григорьева А. В. *и др.* Минералого-технологическое исследование Лопаритовых россыпей Ловозерского массива // Обогащение руд. — 2023. — № 1. — С. 29—37. — DOI: 10.17580/or.2023.01.05.

МПР России. Методические рекомендации по применению классификации запасов твердых полезных ископаемых к россыпным месторождениям (введены в действие Приказом МПР России от 04.07.2000 № 169). — 2000. — URL: http://www.gkz-rf.ru/sites/default/files/docs/tpi_rossypnye_mestorozhdeniya.doc.

Осипов А. П. Отчет о поисково-оценочных работах в пределах центральной части Лукояновского титано-циркониевого м-ния (Итмановская залежь) в Лукояновском р-не Горьковской обл., выполненных Лукояновской ГПП в 1982–85 гг. — Горький, 1985. — URL: https://www.rfgf.ru/catalog/docview.php?did=1c7e4795ef9e883d4fc8da6c8770cbee.

Павловский А. Б. Оловянные руды // Большая Российская энциклопедия. — 2014. — Т. 24.

Росгеолфонд. Государственный баланс запасов полезных ископаемых Российской Федерации на 1 января 2022 года. Выпуск 14. Олово. — 2022.

Смирнов А. Н., Ушаков В. И., Крюков В. Д. Резерв минерально-сырьевой базы олова на шельфах арктических морей России // Минеральные ресурсы России. Экономика и управление. — 2008. — № 6. — С. 15—21. — EDN: JWIPPF .

Спорыхина Л. В., Патык-Кара Н. Г. Россыпи олова // Россыпные месторождения России и других стран СНГ. — Москва : Научный мир, 1997. — С. 165—206.

Чуйко В. А., Синкин В. А., Наумов В. А. *и др.* Сюзёвское месторождение россыпных алмазов: новый этап изучения алмазоносности Западного Урала // Литосфера. — 2023. — Т. 23, № 4. — С. 701—713. — DOI: 10.24930/1681-9004-2023-23-4-701-713.

Charlier B., Duchesne J.-C., Vander Auwera J. Magma chamber processes in the Tellnes ilmenite deposit (Rogaland Anorthosite Province, SW Norway) and the formation of Fe–Ti ores in massif-type anorthosites // Chemical Geology. — 2006. — Vol. 234, no. 3/4. — P. 264–290. — DOI: 10.1016/j.chemgeo.2006.05.007.

Charlier B., Namur O., Bolle O., *et al.* Fe–Ti–V–P ore deposits associated with Proterozoic massif-type anorthosites and related rocks // Earth-Science Reviews. — 2015. — Vol. 141. — P. 56–81. — DOI: 10.1016/j.earscirev.2014.11.005.

Charlier B., Namur O., Malpas S., *et al.* Origin of the giant Allard Lake ilmenite ore deposit (Canada) by fractional crystallization, multiple magma pulses and mixing // Lithos. — 2010. — Vol. 117, no. 1–4. — P. 119–134. — DOI: 10.1016/j.lithos.2010.02.009.

Kamilli R. J., Kimball B. E., Carlin J. F. Critical mineral resources of the United States—Economic and environmental geology and prospects for future supply / ed. by K. J. Schulz, J. H. DeYoung, R. R. Seal, *et al.* — US Geological Survey Professional Paper, 2017. — DOI: 10.3133/pp1802S.

Suiekpayev Y. S., Sapargaliyev Y. M., Dolgopolova A. V., *et al.* Mineralogy, geochemistry and U-Pb zircon age of the Karaotkel Ti-Zr placer deposit, Eastern Kazakhstan and its genetic link to the Karaotkel-Preobrazhenka intrusion // Ore Geology Reviews. — 2021. — Vol. 131. — P. 104015. — DOI: 10.1016/j.oregeorev.2021.104015.

U.S. Geological Survey. Mineral commodity summaries 2020. — 2020. — DOI: 10.3133/mcs2020.

Russian Journal *of* Earth Sciences

The Role of Placer Deposits in Ensuring the Reproduction of the Mineral Resource Base of Scarce Types of Strategic Mineral Raw Materials in Russia at the Present Stage

N. S. Bortnikov[1], A. V. Volkov[1], A. V. Lalomov[1], A. A. Bochneva[1], Y. N. Ivanova[1,2], D. A. Lalomov[3]

[1]Institute of Geology of Ore Deposits, Petrography, Mineralogy and Geochemistry of Russian Academy of Science, Moscow, Russia
[2]RUDN University, Moscow, Russia
[3]Geodevice Technologies Ltd., St.Petersburg, Russia

****Correspondence to:** Alexander Lalomov, lalomov@mail.ru

Received: 15 October 2023
Accepted: 15 January 2024
Published: 29 February 2024

Placer deposits had (and for a number of components still have) an important role in providing strategic types of mineral resource base for both Russia and the world as a whole. Placers have a number of advantages that make them in demand by the mining industry: relatively shallow (often accessible for open-pit mining) occurrence, disintegrated state of productive deposits, simplicity of enrichment processes (mainly gravitational systems), as well as the possibility of rapid involvement in exploitation, which significantly reduces payback period for investments. All this is even more relevant for modern Russia, when, in the shortest possible time, in conditions of a shortage of credit resources, it is necessary to implement a program of import substitution and provide the country with scarce types of strategic mineral raw materials, such as gold, platinum group metals, tin, rare metals, titanium, chromium, diamonds.

Keywords: strategic metals, placer deposits, gold, tin, titanium, rare metals, diamonds.

Citation: Bortnikov N. S., Volkov A. V., Lalomov A. V., Bochneva A. A., Ivanova Y. N., Lalomov D. A. (2024), The Role of Placer Deposits in Ensuring the Reproduction of the Mineral Resource Base of Scarce Types of Strategic Mineral Raw Materials in Russia at the Present Stage, *Russian Journal of Earth Sciences*, 24, ES1012, https://doi.org/10.2205/2024es000897

References

Bortnikov N. S., Volkov A. V., Galyamov A. L., *et al.* Fundamental problems of development of the mineral resource base of high-tech industry and energy in Russia // Geology of ore deposits. — 2022. — Vol. 64, no. 6. — P. 617–633. — DOI: 10.31857/S0016777022060028.

Bykhovsky L. Z., Sporykhina L. V. Placer deposits in the resource base and mineral mining // Mineral resources of Russia. Economics and Management. — 2013. — No. 6. — P. 6–17. — EDN: RMXKHF.

Bykhovsky L. Z., Tigunov L. P., Emelyanov S. A. Development of a feasibility study of permanent conditions, calculation of reserves of titanium-zirconium sands of the Itmanovskaya placer of the Lukoyanovsky deposit in the Nizhny Novgorod region (as of 06/01/2010). — 2010a. — URL: https://www.rfgf.ru/catalog/docview.php?did=38901377e029066333bc9b71d1aaa71a.

Bykhovsky L. Z., Vasilyev A. T., Zabirko A. G. On the development project for the Beshpagirskoye complex rare metal-titanium placer deposit // Mineral resources of Russia. Economics and Management. — 2010b. — No. 1. — P. 68–75. — EDN: LBDHEN.

Charlier B., Duchesne J.-C., Vander Auwera J. Magma chamber processes in the Tellnes ilmenite deposit (Rogaland Anorthosite Province, SW Norway) and the formation of Fe–Ti ores in massif-type anorthosites // Chemical Geology. — 2006. — Vol. 234, no. 3/4. — P. 264–290. — DOI: 10.1016/j.chemgeo.2006.05.007.

Charlier B., Namur O., Bolle O., *et al.* Fe–Ti–V–P ore deposits associated with Proterozoic massif-type anorthosites and related rocks // Earth-Science Reviews. — 2015. — Vol. 141. — P. 56–81. — DOI: 10.1016/j.earscirev.2014.11.005.

Charlier B., Namur O., Malpas S., *et al.* Origin of the giant Allard Lake ilmenite ore deposit (Canada) by fractional crystallization, multiple magma pulses and mixing // Lithos. — 2010. — Vol. 117, no. 1–4. — P. 119–134. — DOI: 10.1016/j.lithos.2010.02.009.

Chuiko V. A., Sinkin V. A., Naumov V. A., *et al.* Syuzevskoye diamond placer: A new stage in studying the diamond potential of Western Urals // Lithosphere. — 2023. — Vol. 23, no. 4. — P. 701–713. — DOI: 10.24930/1681-9004-2023-23-4-701-713.

Kamilli R. J., Kimball B. E., Carlin J. F. Critical mineral resources of the United States – Economic and environmental geology and prospects for future supply / ed. by K. J. Schulz, J. H. DeYoung, R. R. Seal, *et al.* — US Geological Survey Professional Paper, 2017. — DOI: 10.3133/pp1802S.

Lalomov A. V., Grigoreva A. V., Bochneva A. A., *et al.* Rare metal placer deposits of the Lovozero massif // Exploration and protection of subsoil. — 2019. — No. 1. — P. 51–56. — EDN: YZANOP.

Lalomov A. V., Grigoreva A. V., Zajczev V. A. Mineral composition of rare metal placers of the Lovozero massif // Geology of ore deposits. — 2022a. — No. 5. — P. 485–497. — DOI: 10.31857/S0016777022050069.

Lalomov A. V., Vladimirczeva O. V., Bochneva A. A. The role of alluvial deposits in the Russian gold mining industry // Gold and technology. — 2022b. — 4 (58). — P. 36–44.

Levchenko E. N., Grigoreva A. V. Typomorphic and processrelated features of associated gold in complex placer deposits // Ore beneficiation. — 2021. — No. 3. — P. 24–32. — DOI: 10.17580/or.2021.03.05.

Levchenko E. N., Lalomov A. V., Grigor'eva A. V., *et al.* Mineralogical and processing study of loparite placers of the Lovozero massif // Ore beneficiation. — 2023. — No. 1. — P. 29–37. — DOI: 10.17580/or.2023.01.05.

MPR Rossii. Methodological recommendations for applying the classification of reserves of solid minerals to alluvial deposits (put into effect by Order of the Ministry of Natural Resources of Russia dated July 4, 2000 No. 169). — 2000. — URL: http://www.gkz-rf.ru/sites/default/files/docs/tpi_rossypnye_mestorozhdeniya.doc.

Osipov A. P. Report on prospecting and assessment work within the central part of the Lukoyanovsky titanium-zirconium deposit (Itmanovskaya deposit) in the Lukoyanovsky district of the Gorky region, carried out by the Lukoyanovsky State Enterprise in 1982-85. — Gorkii, 1985. — URL: https://www.rfgf.ru/catalog/docview.php?did=1c7e4795ef9e883d4fc8da6c8770cbee.

Pavlovskii A. B. Tin ores // Great Russian Encyclopedia. — 2014. — Vol. 24.

Rosgeolfond. State balance of mineral reserves of the Russian Federation as of January 1, 2022. Issue 14. Tin. — 2022.

Smirnov A. N., Ushakov V. I., Kryukov V. D. A reserve of the tin resource base in the shelf areas of the Russian Arctic seas // Mineral resources of Russia. Economics and Management. — 2008. — No. 6. — P. 15–21. — EDN: JWIPPF .

Sporykhina L. V., Patyk-Kara N. G. Placers of tin // Placer deposits in Russia and other CIS countries. — Moscow : Nauchnyi mir, 1997. — P. 165–206.

Suiekpayev Y. S., Sapargaliyev Y. M., Dolgopolova A. V., *et al.* Mineralogy, geochemistry and U-Pb zircon age of the Karaotkel Ti-Zr placer deposit, Eastern Kazakhstan and its genetic link to the Karaotkel-Preobrazhenka intrusion // Ore Geology Reviews. — 2021. — Vol. 131. — P. 104015. — DOI: 10.1016/j.oregeorev.2021.104015.

U.S. Geological Survey. Mineral commodity summaries 2020. — 2020. — DOI: 10.3133/mcs2020.

VIMS-CZNIGRI. State report "On the state and use of mineral resources of the Russian Federation in 2020". — 2021.

VIMS-CZNIGRI. State report "On the state and use of mineral resources of the Russian Federation in 2021". — 2022.

VIMS–Mineral-Info. State report "On the state and use of mineral resources of the Russian Federation in 2016 and 2017". — 2018.

Volkov A. V., Galyamov A. L., Lalomov A. V., *et al.* Metalliferous conglomerates — potential sources of placers in the Arctic zone of Russia // Arctic: ecology and economics. — 2021. — Vol. 11, no. 2. — P. 232–243. — DOI: 10.25283/2223-4594-2021-2-232-243.

Zolotodobycha. Nearly 1000 tonnes of gold could be recovered from gold mining tailings in South Africa. — 2023. — URL: https://zolotodb.ru/article/13040 (visited on 10/03/2023).

Russian Journal of Earth Sciences

Special Issue: "25th anniversary of the Russian Journal of Earth Sciences"

A Closer Cooperation between Space and Seismology Communities – a Way to Avoid Errors in Hunting for Earthquake Precursors

V. A. Pilipenko[1,2], **K. Shiokawa**[3]

[1]Schmidt Institute of Physics of the Earth, RAS, Moscow
[2]Geophysical Center of RAS, Moscow
[3]Nagoya University, Japan
* **Correspondence to:** V. A. Pilipenko, pilipenko_va@mail.ru

Abstract: The space physicists and the earthquake (EQ) prediction community exploit the same instruments – magnetometers, but for different tasks: space physicists try to comprehend the global electrodynamics of near-Earth space on various time scales, whereas the seismic community develops electromagnetic methods of short-term EQ prediction. The lack of deep collaboration between those communities may result sometimes in erroneous conclusions. In this critical review, we demonstrate some incorrect results caused by a neglect of specifics of geomagnetic field evolution during space weather activation. The considered examples comprise: Magnetic storms as a trigger of EQs; ULF waves as a global EQ precursor; Geomagnetic impulses before seismic shocks; Long-period geomagnetic disturbances generated by strong EQs; Discrimination of underground ULF sources by amplitude-phase gradients; Depression of ULF power as a short-term EQ precursor; and Detection of seimogenic emissions by satellites. To verify the reliability of the above widely disseminated results data from available arrays of fluxgate and search-coil magnetometers have been re-analyzed. In all considered events, the "anomalous" geomagnetic field behavior can be explained by global geomagnetic activity, and it is apparently not associated with seismic activity. This critical review does not claim that ULF electromagnetic field cannot be used as a sensitive indicator of the EQ preparation processes, but we suggest that both communities must cooperate their studies more tightly using data exchange, combined usage of magnetometer networks, organization of CDAW for unique events, etc.

Keywords: seismo-electromagnetic phenomena, earthquake prediction, geomagnetic pulsations.

Citation: Pilipenko V. A., Shiokawa K. (2024), A Closer Cooperation between Space and Seismology Communities – a Way to Avoid Errors in Hunting for Earthquake Precursors, *Russian Journal of Earth Sciences*, Vol. 24, ES1001, https://doi.org/10.2205/2024ES000899

Research Article

Received: 15 October 2023
Accepted: 15 January 2024
Published: 29 February 2024

1. Introduction: seismo-electromagnetic ULF phenomena

Monitoring of the near-Earth electromagnetic environment in various frequency bands by ground and satellite sensors is the main research tool for the space physics community and the seismic community, though it is used for different tasks. Space physicists are interested to know how electromagnetic disturbances and emissions convey information about dynamic processes in the near-Earth plasma. The seismic community attempts to develop the detection methods of the electromagnetic signatures of the ongoing crust destruction. A useful signal for one community is an interference for the other, whereas industrial and lightning sources obscure all desired signals. A zoo of natural electromagnetic emissions, noise, impulses, and waves is enormous, so any progress in the hunt for seismic-associated disturbances is possible only with the close collaboration of both communities. However, such collaboration is still insufficient, and in this critical review, we demonstrate how seemingly amazing discoveries have turned out to be errors or misinterpretations.

A search and recognition of electromagnetic precursors of EQs remain one of the hot topics in geophysics. The observational results indicated that it is promising to study such phenomena in the ultra-low-frequency (ULF) range (10 mHz–10 Hz) [*Petraki et al.*, 2015]. The signatures of anomalous electromagnetic ULF activity near the epicenter hours – days before EQs were reported (see numerous articles in monographs [*Hayakawa*, 2009, 2013; *Hayakawa and Molchanov*, 2002]). Several types of ULF geomagnetic anomalies were noticed: the appearance of broadband electromagnetic noise [*Molchanov et al.*, 1992]; a change in the spectral composition [*Hayakawa et al.*, 1999]; changes in the polarization structure [*Hayakawa et al.*, 1996]. Enhancements of broad-band electromagnetic noise recorded during periods preceding EQ were suggested to be associated with the irregular flow of the crust fluid [*Fedorov et al.*, 2001; *Fenoglio et al.*, 1995], micro-cracking of the rock medium [*Molchanov and Hayakawa*, 1995], acoustic impulsive background [*Surkov and Hayakawa*, 2006]. These effects were observed only for strong EQs in the immediate vicinity (up to several hundred kilometers) from the epicenter [*Hattori*, 2004].

A surprisingly large number of electromagnetic phenomena can occur within a few minutes in the temporal vicinity of a seismic shock. A seismic wave propagating from the quake hypocenter excites a transient burst of the electromagnetic field due to induction or electrokinetic effects [*Surkov et al.*, 2018]. A few seconds before the arrival of a seismic wave at the registration point, its electromagnetic "forerunner" may begin to grow, excited by currents at the wavefront [*Surkov and Pilipenko*, 1997]. Such a preliminary growth of the magnetic disturbance immediately ahead of the seismic wavefront was observed by Iyemori et al. [*Iyemori et al.*, 1996]. In addition, a rapid movement of crustal blocks at the time of an EQ can cause the appearance of isolated electromagnetic pulse that are several seconds ahead of the front of a seismic wave [*Guglielmi and Levshenko*, 1996]. If this pulse is strong enough, then it will presumably cause a burst of the vertical electric field and light flash in the near-surface atmosphere (EQ light) [*Lockner et al.*, 1983].

Yet, the situation with ULF electromagnetic precursors remains ambiguous. The results of disparate observations cannot be considered strictly substantiated, and some of them are disputed [*Masci and Thomas*, 2015; *Thomas et al.*, 2009a,b]. Various manifestations of electromagnetic effects in different events, poor repeatability of the results, and the absence of a confirmed generation mechanism raise doubts about the reliability of the relationship between the detected geomagnetic phenomena and EQs.

In this review, we re-analyze some observational results and suggested hypotheses, published by leading experts in top-level geophysical journals. We consider the following specific examples: Magnetic storms as a trigger of EQs; Global ULF waves before strong EQs; Global geomagnetic impulses preceding quakes; Long-period geomagnetic disturbances generated by strong EQs; Discrimination of underground ULF sources by amplitude-phase gradients; Depression of ULF power as a short-term EQ precursor, and Feasibility of ULF precursor detection by satellites. To verify the reliability of the above phenomena, we have used available data from the existing fluxgate and search-coil magnetometer databases: INTERMAGNET [*Love and Chulliat*, 2013], IMAGE [*Tanskanen*, 2009], PWING [*Shiokawa et al.*, 2017], and Russian Arctic stations [*Kozyreva et al.*, 2022].

2. Magnetic storms as a trigger of EQs

The possibility of a triggering effect of solar activity and associated space weather disturbances (magnetic storms) on the Earth's seismicity is actively discussed. When the accumulated stress along the fault is close to the critical level, even a weak external impact can provoke instability of lithospheric blocks and serve as an EQ trigger. This concept is based on the assumed excitation during magnetic storms of telluric fields and currents flowing along faults, affecting the dynamics of the pore fluid. It was reported that after magnetic storms with sudden commencement (SC), the number of weak EQs in Tajikistan and Kyrgyzstan increased by 3–4 per day in an area with a size of about a hundred km [*Sobolev et al.*, 2001; *Zakrzhevskaya and Sobolev*, 2002, 2004]. An increase in the daily number of local EQs in Kyrgyzstan and Carpathians on the 2nd day after the solar flare was found [*Kuznetsova et al.*, 2005]. A high correlation was found between the diurnal variation of weak seismicity and the geomagnetic Sq variation [*Duma and Ruzhin*, 2003].

To substantiate the idea of a triggered release of energy accumulated in the crust in the form of weak EQs, experiments were carried out in Tajikistan and Kyrgyzstan with the magnetohydrodynamic (MHD) generator. Powerful electromagnetic pulses from an MHD generator were found to cause a noticeable activation of seismicity, which was most pronounced in its upper 5-km layer [*Tarasov*, 1997]. The intensity of the EQ flux increased sharply 5–6 days after the impact, and the release of the seismic energy turned out to be 5 orders of magnitude greater than the pulse energy. These results were confirmed in the Northern Tien Shan, where similar changes in the seismic regime after the MHD impact were revealed [*Tarasov et al.*, 1999]. Later, instead of an MHD generator, a capacitor-thyristor source was used, but, as in previous works, a noticeable activation of seismicity after impact was revealed [*Smirnov and Zavyalov*, 2012; *Tarasov et al.*, 2001]. The fundamental possibility of the initiating effect of electrical impulses on microcracking processes and the level of acoustic emission was confirmed in laboratory experiments with rock samples under load [*Zeigarnik et al.*, 2022].

Often the literature presents the observations of possible triggered phenomena related to a selected event [*Straser et al.*, 2015]. Despite the importance of case studies, this approach does not provide reliable evidence in favor of the trigger effect reality and should be supplemented by statistical analysis. Kozyreva and Pilipenko [*Kozyreva and Pilipenko*, 2020] tested the idea of a magnetic storm as an EQ trigger for a region of Alaska with high seismicity, and where magnetic activity is much stronger than at low latitudes. They used the super-posed epoch (SPE) method for the College magnetometer data, whereas the moment of a quake was chosen as a reference zero point. To characterize the central trend in the sample, the median value was used, which (unlike the mean value) is resistant to outliers, and only for a normal distribution coincides with the mean value. If the magnetic field variations are in no way associated with seismic activity, the dynamics of the magnetic variation intensity on the SPE plot before and after an EQ will be the same. If strong field variations are an EQ trigger, then the dynamics in the previous 10 days should show a systematic increase in the disturbance and variability of the geomagnetic field. The SPE graphs of the magnetic activity parameters (hourly Dst-index, $|\Delta X|$, and $|dX/dt|$), before "strong" ($M > 5$) EQs did not show any statistically significant enhancement before the seismic shock that goes beyond the dispersion. Similar negative results were obtained for weak (3<M<5) near-surface (H<5 km) EQs, weak small-depth (H=5-10 km) EQs, and weak shallow (H = 10-30 km) EQs. The obtained negative result casts doubt on the hypothesis of a magnetic storm as a possible EQ trigger.

The question under consideration is part of the fundamental problem of the impact of solar activity on geophysical processes. Analysis of long-term archives of solar and geophysical data led to completely different conclusions. On long time scales (tens to hundreds of years), global seismicity was found to be higher either during periods of solar maxima [*Han et al.*, 2004; *Odintsov et al.*, 2006], or minima [*Simpson*, 1967]. On smaller time scales (monthly and annual variations), it was argued that global seismicity correlates with geomagnetic variations [*Duma and Vilardo*, 1998; *Rabeh et al.*, 2009]. At the micro level, high-frequency seismic noise was claimed to be sensitive to magnetic storms [*Adushkin et al.*, 2012; *Sycheva et al.*, 2011], but the connection between background seismicity and geomagnetic variations was denied in [*Desherevskii and Sidorin*, 2016]. At the same time, the statistical relationships between seismicity and solar activity were refuted in [*Love and Thomas*, 2013; *Stothers*, 1990].

Nonetheless, attempts to reveal a hypothetical relationship between the solar activity and seismic process still go on. [*Doda et al.*, 2013] developed the forecasting scheme based on the empirical fact that a strong EQ happens on 14-th day after the solar ejecta (flare or coronal mass ejection) in the region of intersection of lithospheric fault with the meridian with most intense geomagnetic disturbance. Dedicated experiments indicated that "laboratory EQs" (disruption of samples under load) can be triggered by electromagnetic impulses [*Sorokin et al.*, 2019]. Authors supposed that similar electromagnetic triggering of EQs by solar flare or sudden impulses preceding the magnetic storm onset may operate in the terrestrial lithosphere as well. Thus, a large work is still ahead to validate the reported solar-seismic relationships an comprehend their mechanisms (if any).

3. Global ULF wave precursors of strong EQs

The possibility of sporadic quasi-monochromatic signals before an EQ deserves special consideration. There were a number of reports on the observation of "precursory" ULF signals. At low-latitude station Dusheti before several strong (M>6) EQs in the world, [*Gogatishvili*, 1984] observed specific geomagnetic pulsations with a duration from several minutes to several hours with an amplitude of ~10–15 nT and periods of 1–20 s (range of Pc1-2) several tens of minutes or several hours before the quake. [*Bortnik et al.*, 2008] examined the association between EQs and Pc1 pulsations observed for 7.5 years at a low-latitude station in California. They found a statistically significant enhanced occurrence probability of dayside Pc1 pulsations 5–15 days in advance of EQ (M>3) within 200 km around the magnetometer. However, [*Guglielmi and Zotov*, 2010] from the catalogues of Pc1 and earthquakes, revealed that diurnal Pc1 activity in the middle latitudes is statistically higher when the global seismic activity is lower. Before the strongest EQ off the coast of Antarctica on March 25, 1998 (H = 10 km, M = 8.8) at station Vernadsky, a series of intense pulsations with periods of several tens of seconds (Pc3-4 range) was recorded [*Bakhmutov et al.*, 2003]. A possible mechanism of "anomalous" ULF signal generation has not been even suggested.

The most active searches for "precursory" ULF signals have been carried out at the Caucasian Geophysical Observatory (CGO), located at a depth of 3.5 km. In a series of publications [*Sobisevich et al.*, 2009a,b, 2010a, 2012, 2013] the detection of quasi-periodic short-term signals with periods of 50–150 s before large EQs ($M > 5.5$) in the world a few hours before the shock was reported. However, in [*Kosterin et al.*, 2015] the registered "precursory" signals were compared with the data of other magnetic stations. The set of morphological properties of the observed global "precursory" signals – impulsive waveform, characteristic frequencies, decrease in amplitude with decreasing latitude, confinement to the night sector – was in good agreement with the characteristic features of magnetospheric Pi2 pulsations. In a similar way, the reported by [*Sobisevich et al.*, 2017; *Sobisevich*, 2020; *Sobisevich et al.*, 2010b] daytime long-term quasi-monochromatic "precursory" signals turned out to be Pc3-4 pulsations of the magnetospheric origin. Thus, it can almost certainly be asserted that the recorded signals are magnetospheric ULF pulsations and are not related to seismic activity.

4. Geomagnetic impulses before quakes

Anomalous ULF disturbances during the activation of seismic activity may have an impulsive character [*Bleier et al.*, 2009; *Naumov*, 1999]. An amazing phenomenon was described in a series of papers [*Dovbnya*, 2011, 2014, 2021; *Dovbnya et al.*, 2006, 2008, 2019] – the appearance of global magnetic impulses a few minutes before the seismic shock (see example in Figure 1). The effect was found from the data of induction magnetometers at stations Borok and College, separated by 12 h in longitude and 10° in latitude. Precursory pulses with an amplitude not exceeding 20 pT in the frequency range from 0 to 5 Hz appeared at both stations almost simultaneously at significant distances from the epicenter (up to 10^4 km). This intriguing hypothesis may be a truly major discovery in geophysics, so its critical consideration should be taken carefully.

In [*Martinez-Bedenko et al.*, 2023] the hypothesis about the appearance of a pulsed magnetic precursor was suggested to test using the network of induction magnetometers PWING at Far East. Indeed, the appearance of impulse disturbances synchronously at several stations was detected. However, the waveforms of the pulses indicate that they can be associated with the excitation of the Schumann Resonance (Figure 2). This resonant electromagnetic structure with a fundamental frequency of 7.8 Hz is formed by the Earth's

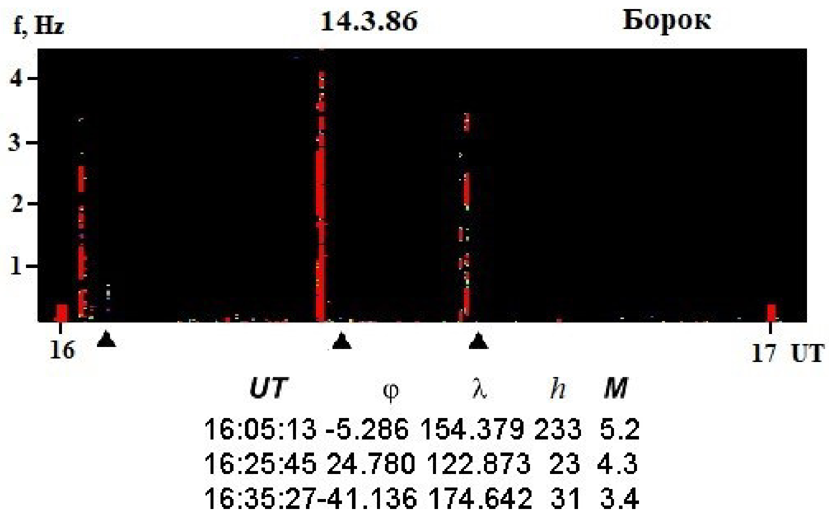

Figure 1. The appearance of global magnetic impulses few minutes before the seismic shocks in dynamic spectra from Borok observatory (from [*Dovbnya*, 2021]).

surface and conductive layers of the upper atmosphere (~80 km) and is effectively excited by lightning discharges. Comparison with the world-wide lightning monitoring system WWLLN shows that at least a part of the pulses is a response to a lightning discharge (Figure 3). Statistics based on automatic calculation of the number of impulses before and after a seismic shock in a 5-min interval has not shown any predominance of impulse disturbances before local EQs.

Although the detailed analysis did not confirm the hypothesis of ultra-short ULF pulses as a precursor of EQs, their physical nature was established – they are caused by atmospheric electric discharges [*Marchuk et al.*, 2022]. In principle, it can be suggested that the appearance of a lightning discharge before an EQ is not just a coincidence, since a seismic process can cause changes in the electrochemical properties of the lower atmosphere due to the release of radioactive emanations [*Harrison et al.*, 2010; *Pulinets and Davidenko*, 2014]. Additional ionization of the lower atmosphere by aerosols and Rn emanations can trigger lightning discharges under favorable conditions [*Yagova et al.*, 2019]. In general, the question of the connection between the process of EQ preparation and atmospheric electricity remains poorly studied, and any reasonable assumptions in this area are hard to make. The WWLLN data on global lightning activity may be used to construct the index characterizing a possible contribution of ULF noise at a particular site produced by distant atmospheric discharges. This new index may help to avoid confusion about magnetospheric, atmospheric, and lithospheric sources.

5. Long-period geomagnetic disturbances generated by strong EQs

The study of the Earth's magnetic field variations accompanying seismic phenomena is important for understanding the mechanisms of inter-geosphere interactions. Besides the co-seismic magnetic effect, long-period geomagnetic disturbances (time scale of a few tens of minutes) around the main shock were noticed [*Adushkin and Spivak*, 2021]. It was suggested that the probable mechanism of this effect is the excitation of the ionosphere in the epicentral region by acoustic-gravity waves (AGWs) resulting from movements of the earth's crust [*Adushkin and Spivak*, 2021; *Chernogor*, 2019]. Based on observations at mid-latitude station Mikhnevo (MKH) [*Spivak and Ryabova*, 2019] claimed that strong EQs are accompanied at far-distant stations by geomagnetic long-period disturbances (period ~5–20 min) with amplitude 2–4 nT (see example in Figure 4, where the reported mid-latitude long-period disturbance is marked by the rounded red box). The authors suggested that these disturbances of the magnetic field are caused either by underground dynamic processes or disturbances in the Earth's ionosphere over the epicenter. This interesting

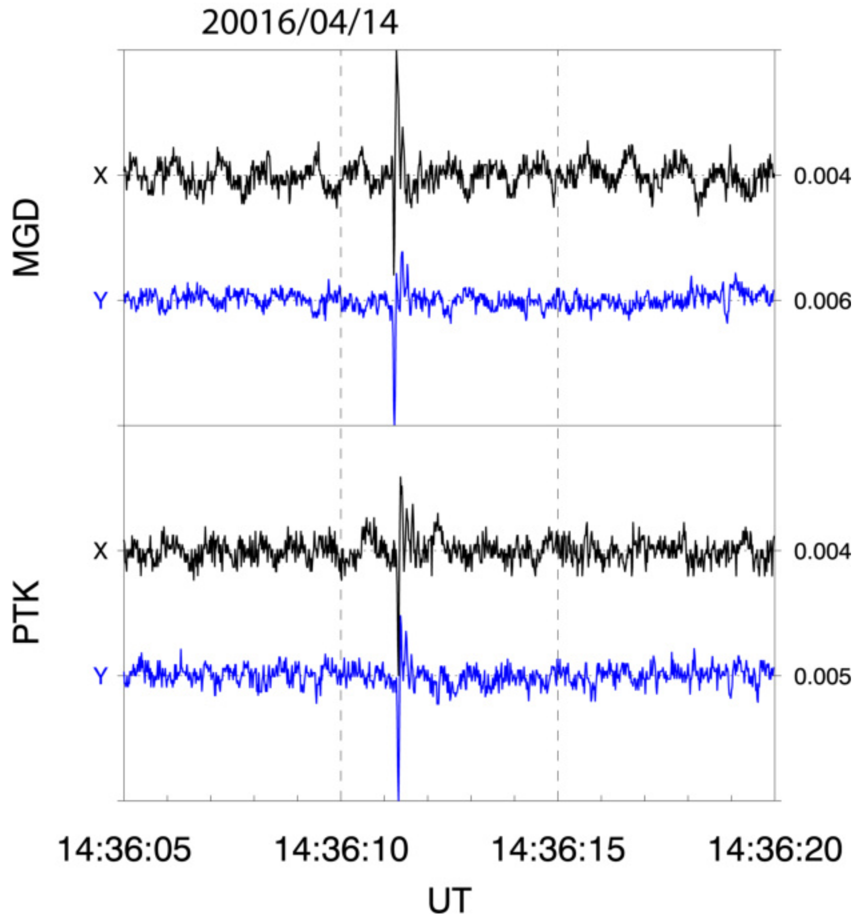

Figure 2. The example of impulse disturbances synchronously recorded at stations MGD and PTK (X and Y components).

hypothesis certainly requires a detailed discussion from various points of view [*Nosikova et al.*, 2023].

All the results presented in those studies were obtained at low- and mid-latitude stations. We have performed an extended analysis of published events, using additional data from stations at auroral latitudes in the same longitudinal sector, where anomalous disturbances were detected. The consideration of magnetograms from a latitudinal profile of stations from low-latitude up to auroral latitudes evidence that the reported "seismogenic" disturbance is just a weak low-latitude response to an intense disturbance at higher latitudes (Figure 4). Thus, the long-period "seismic-associated" geomagnetic disturbances are just accidentally coincided with EQs.

Moreover, there are no physical grounds to expect the appearance of harmonic ULF signals before an EQ, which propagates over the entire globe. Excitation of geomagnetic Pc5 pulsations in the ionosphere above the epicenter by acoustic waves generated by oscillations of the earth's surface was indeed observed after some intense EQs [*Iyemori et al.*, 2005], but distant propagation of such a disturbance along the ionosphere over vast distances is hardly possible. An MHD waveguide in the upper ionosphere capable of propagating ULF waves over distances of up to several thousand km has a critical frequency of ~0.5 Hz, which is much higher than the considered frequency range. Although AGWs can reach the conducting E-layer (~120 km) and induce periodic currents, thereby creating magnetic disturbances [*Zettergren and Snively*, 2015], the propagation of AGWs along the earth's surface occurs at low speeds ~100 m/s, and their magnetic signatures can be revealed after intense quakes or volcano eruptions on a regional scale only [*Gavrilov et al.*, 2022].

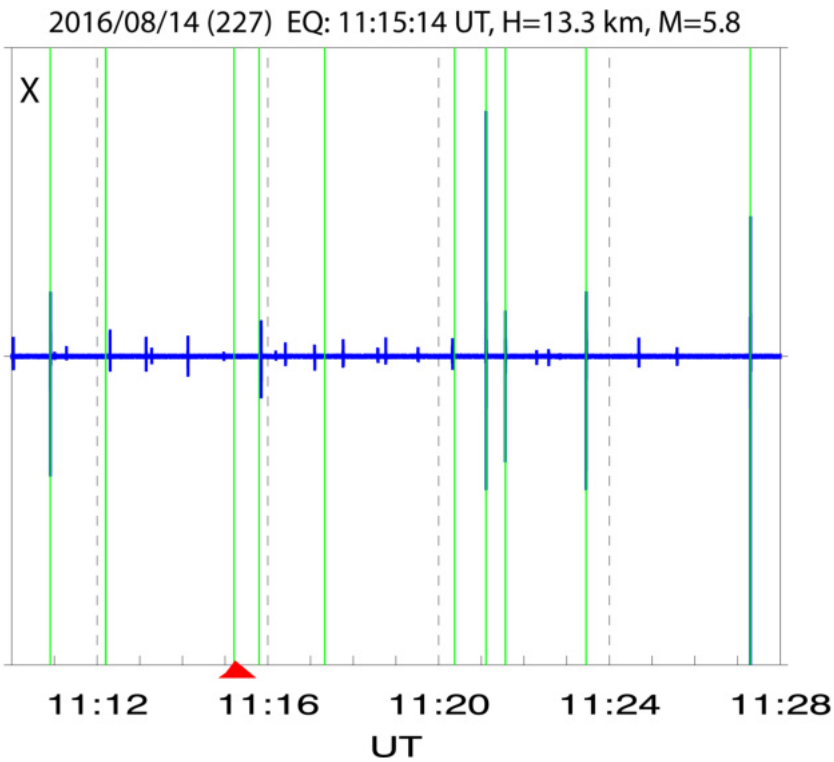

Figure 3. Comparison of discharge moments from the WWLLN database (green vertical lines) and geomagnetic impulses (blue) around EQ (marked by red triangle).

6. Discrimination of underground ULF sources by amplitude-phase gradients

The situation with ULF electromagnetic precursors remains ambiguous to date, as the amplitude of possible electromagnetic noise caused by seismic activity is apparently small. Therefore, for confident discrimination of seismogenic disturbances, the development of special methods for recording and analyzing data is required. There were proposals to use gradient measurements with a small baseline (no more than a few km), which would suppress the contribution of large-scale disturbances of ionospheric origin [*Ismaguilov et al.*, 2003].

The approach used in [*Ismaguilov et al.*, 2003, 2006; *Kopytenko et al.*, 2006] is based on the premise that an electromagnetic field propagates in the conductive Earth in a wave manner with strong attenuation. The amplitude-phase gradient method assumes that ULF wave horizontal propagation velocity is determined by crust conductivity as follows $U = \lambda/T = \sqrt{10\rho/T}$, where the relation of the wavelength with resistivity was used $\lambda = \sqrt{10\rho T}$. The gradient method enabled to seemingly successfully retrieve seismogenic signals several months before nearby EQs with $M = 5$–6 in Japan at a distance <100 km [*Kopytenko et al.*, 2012]. The measured amplitude gradient in the band 0.03–0.1 Hz (Pc2-3 band) was typically around G ≈ 0.1–1 pT/km, and phase velocity U ≈ 20–100 km/s.

However, amplitude/phase gradients of ULF field can be created by the magnetospheric wave conversion process in the resonant region, where the period of source T tends to Alfven period T_A of local field line oscillations. The latitudinal structure of ULF wave amplitude and phase in the resonant region has been modeled using the numerical solution of the equations for coupled MHD modes [*Pilipenko et al.*, 2016]. The modeling results in Figure 5 demonstrate that the resonant component By (corresponding to the ground H-component) in the meridional direction has a strong gradient of amplitude ∇B and phase difference $\Delta\phi$ up to 180°. The spatial-frequency ULF wave structure in a vicinity

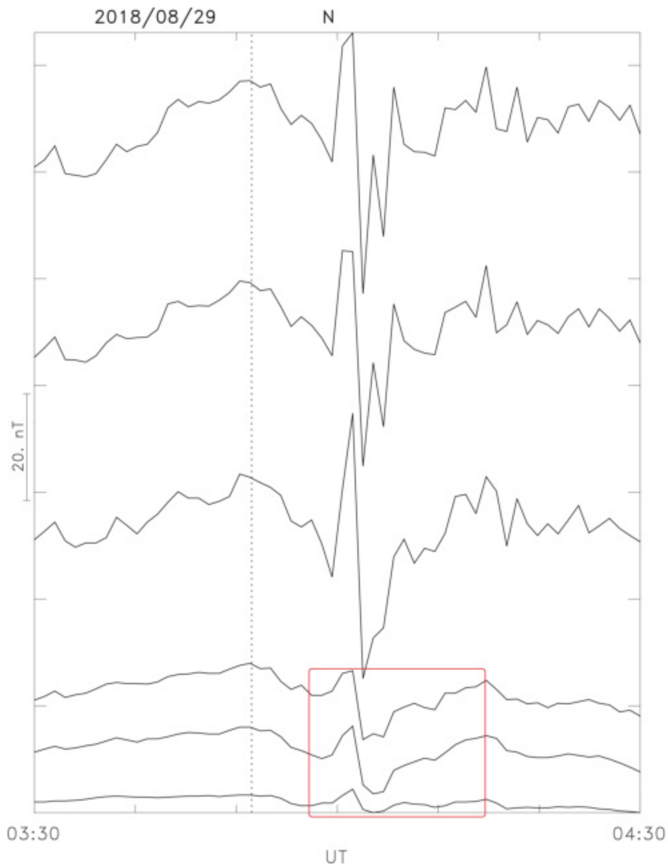

Figure 4. The long-period geomagnetic disturbance detected at mid-latitudes (marked by a red empty box) that was claimed in [*Spivak and Ryabova*, 2019] to be associated with strong EQ (marked by a vertical dashed line). The geomagnetic latitude and longitude are indicated near the station codes at left-hand vertical axis.

of the Alfven resonance is described analytically by asymptotic decomposition [*Best et al.*, 1986]. The phase gradient reaches an extreme value at $x \to x_A(f)$ as follows

$$\frac{\partial \phi}{\partial x} = (a\Gamma)^{-1}, \tag{1}$$

where $a^{-1} = \partial \ln V_A/\partial x$ is the latitudinal scale of the Alfven velocity inhomogeneity, and Γ is the normalized wave dissipation coefficient. The relationship (1) can be used to estimate the phase gradient from the data from stations separated by distance $\Delta x, \Delta\phi(\text{rad}) = \Delta x/a\Gamma$. The sign of phase shift corresponds to an apparent poleward propagation. The phase shift $\Delta\phi$ corresponds to an apparent phase velocity $U = \omega(\partial\phi/\partial x)^{-1}$. The measurements in [*Ismaguilov et al.*, 2003; *Kopytenko et al.*, 2002] were made for Pc3 frequency band (0.05 Hz). For the reasonable values $\Gamma \sim 0.1$, $a \sim 10^3$ km, the apparent phase velocity in the resonant region is to be U~25 km/s. This estimate is close to the observational results, presented in Figure 6.

The latitudinal structure of magnetospheric ULF waves with significant amplitude/phase gradients is formed in the resonance region, therefore, the gradient method of the seismogenic pulsations detection must be applied only in the frequency band far from the magnetospheric field-line resonator frequency. To choose a proper frequency range not contaminated by the resonant effect, the theoretically calculated latitudinal profile of fundamental Alfven period $T_A(\Phi)$ can be used [*Menk and Waters*, 2013]. Notice, the results presented in [*Ismaguilov et al.*, 2003; *Kopytenko et al.*, 2012] were obtained at low latitudes for geomagnetic signals with periods around the resonant periods. Thus, the gradient method of seismic-related signal detection must be supported by the examination of reso-

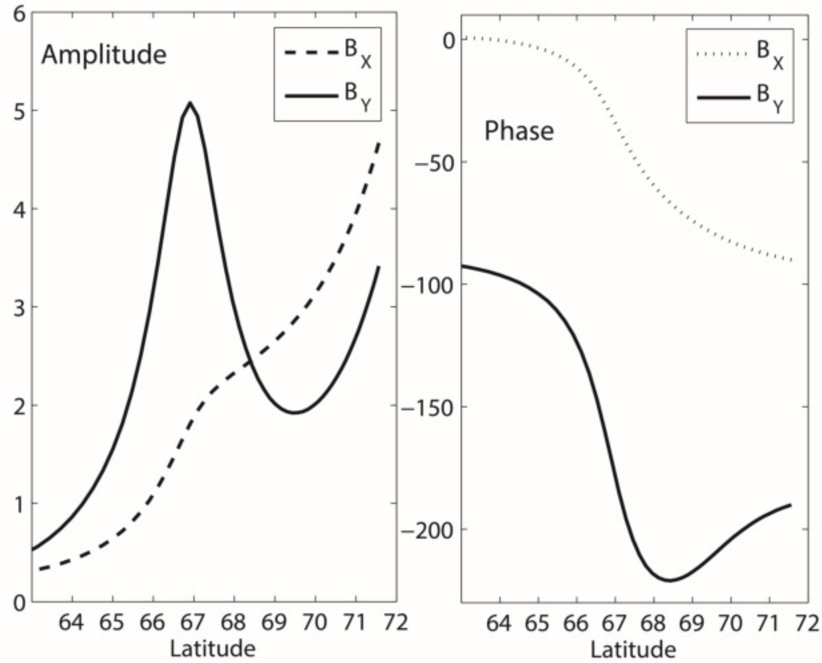

Figure 5. The numerically modeled resonant structure of ULF waves in the magnetosphere: the left-hand panel shows the latitudinal profile of amplitudes, and the right-hand panel shows the phase profile. The magnetospheric $B_Y(B_X)$ components correspond to the components $H(D)$ on the ground.

nant effects, and can be performed only in a frequency-space domain far from the resonant region.

The ground magnetic effect of an underground source (e.g. current along a fault) is a mixture of the source current produced mechano-electrical transformations and the spreading conductive currents. Moreover, for ULF range the propagation inside the crust has a diffusive character. Therefore, the reliable gradient method must be augmented by a numerical model of ULF emission from an underground horizontal current of a finite length.

7. Depression of ULF power as a short-term EQ precursor

Most of the research on the search for electromagnetic precursors was aimed at detecting radiation caused by mechano-electromagnetic converters in the earth's crust. At the same time, the opposite phenomenon was unexpectedly discovered - depression of ULF noise intensity of the geomagnetic field in the frequency band 0.01–0.1 Hz a few days before EQs [*Hayakawa*, 2013; *Li et al.*, 2015; *Molchanov et al.*, 2004; *Schekotov and Hayakawa*, 2017; *Schekotov et al.*, 2006, 2008]. This interesting new phenomenon could be applied to short-term EQ prediction [*Hayakawa et al.*, 2015; *Schekotov et al.*, 2013]. The ULF depression may be caused by an enhancement of ionospheric turbulence before an EQ, which leads to additional absorption of magnetospheric noise upon passing through the ionosphere [*Sorokin et al.*, 2004]. Additional turbulence of the ionosphere can be caused by the action of AGWs excited by seismic activity.

If the effect of geomagnetic depression is really associated with the processes of preparation of a seismic event, then the same effect should be absent at observatories remote from the epicenter. To test this assumption, we have used data from the entire PWING network of induction magnetometers for the EQ event on April 14, 2016 ($M = 6.2, H = 32$ km) in Kamchatka, previously described in [*Schekotov et al.*, 2020]. In the latter study, in the period from April 06 to April 14, 2016, anomalies in the behavior of ULF noise were detected – the depression of the noise intensity several days before the EQ. To identify anomalies, the parameter ΔS was used, which is the reciprocal value of the

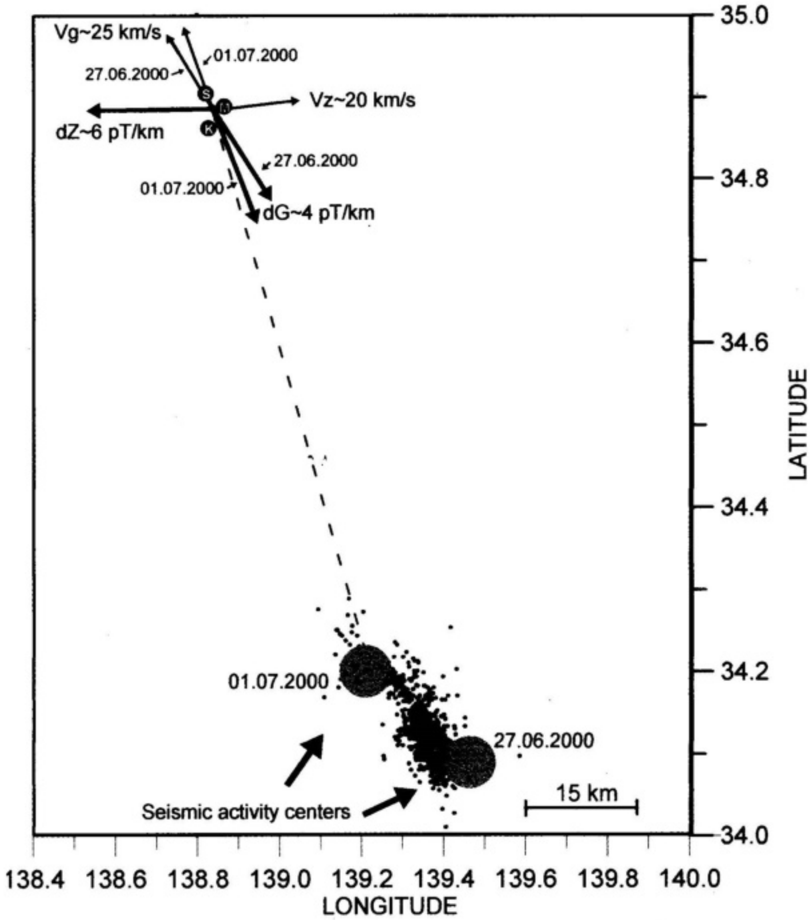

Figure 6. The gradients and phase velocities of anomalous ULF signals in Pc3 frequency band (0.05 Hz) detected before EQ by gradient method in [*Ismaguilov et al.*, 2003; *Kopytenko et al.*, 2002].

band-integrated spectral density W of the horizontal component, calculated over 3-hour nighttime intervals. Comparison of the ΔS parameter with the seismicity index showed that the largest depression value preceded the moment of the EQ by 4 days (Figure 5). Using a similar scheme, we have calculated the variations in the spectral power W(t) in the band 0.01–0.8 Hz for the horizontal Y component at night hours for all PWING stations (Figure 7). Since the equipment at each station has its own sensitivity, the time series of W(t) at each station has been normalized separately to the maximum value during the entire interval. At two nearby stations KRM and PTK, located not far from the epicenter, the depression was most clearly observed on the nights of April 8–9 and April 10–11. This behavior of $W(t)$ coincides with the results from [*Schekotov et al.*, 2020]. But if the effect of geomagnetic depression is really associated with pre-EQ processes, then the same effect should be absent at observatories far from the epicenter. Therefore, the same method was used to analyze the data from the distant MSR and MGD stations located 1514 km and 915 km away from the epicenter. Comparison of W(t) variations at different stations shows that noise intensity depression is observed synchronously both at nearby to the epicenter and at remote (farther than ~1000 km) stations. Thus, depression turns out to be a general magnetospheric process, apparently unrelated to seismic activity.

The reason for the global depression of ULF noise is clearly seen in Figure 8, which shows the planetary geomagnetic index AE, characterizing the disturbance of the geomagnetic field at auroral latitudes. During the periods of April 8–9 and April 10–11, the planetary magnetic situation was exceptionally calm, so even at auroral latitudes the AE index dropped to about several tens of nT. Only after April 11 the geomagnetic activity begins to increase, which can be seen from the behavior of the AE index.

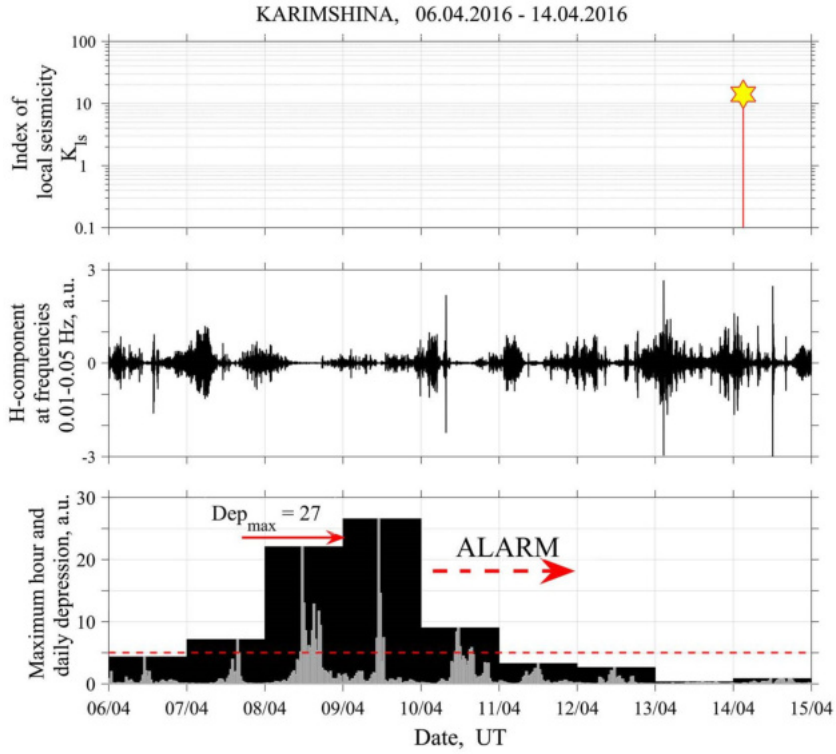

Figure 7. Comparison of the ΔS parameter (bottom panel), characterizing the depression of the ULF noise intensity at night, with the seismicity index (top panel) before the EQ on April 14, 2016 with $M = 6.2 and H = 32$ km in Kamchatka from [*Schekotov et al.*, 2020].

8. Feasibility of the seismogenic ULF disturbance detection by satellites

Attempts are being made to detect seismogenic ULF disturbances on low-Earth-orbit (LEO) satellites [*Kodama et al.*, 2000; *Picozza et al.*, 2021]. The number of reports of "anomalous" electromagnetic disturbances in the ULF range, detected by satellites in the upper ionosphere, is constantly growing [*Bilichenko et al.*, 1990; *De Santis et al.*, 2015; *Huang et al.*, 2020; *Zhu et al.*, 2021]. The most cited pioneering results of EQ precursors detection in the upper ionosphere were obtained on the OREOL-3 and IKB-1300 satellites [*Chmyrev et al.*, 1986, 1989]. During the nighttime flight of IKB-1300 (altitude 800 km) above the EQ source, 15 minutes before the main shock variations were recorded in the range of 0.1–8 Hz in the horizontal magnetic components with typical amplitude about several nT and in the electric field component with amplitude about few mV/m. [*Gousheva et al.*, 2008] revealed the enhancement up to ~5–15 mV/m of the quasi-DC electric field in the upper ionosphere at ICB-1300 over epicenters during seismic activity over various regions. In many studies bursts of electromagnetic noise in the ionosphere in the ELF and VLF frequency bands were noticed in the vicinity of epicenter before the seismic shock.

These encouraging results have stimulated the development of specialized satellite missions for detecting seismo-electromagnetic emissions – DEMETER (orbit altitude ~660 km) [*Parrot and Lil*, 2015], CSES (orbit altitude ~500 km) [*Zhima et al.*, 2022], ESPERIA [*Sgrigna et al.*, 2008], QUAKESAT [*Warden et al.*, 2020]. Besides, data from the multi-probe mission SWARM were used for the search of seismogenic ULF disturbances [*De Santis et al.*, 2019]. In the specialized satellite project DEMETER the sensitivity of the electromagnetic complex was so high that at auroral latitudes the sensors went into saturation. Before an EQ with $M = 7.9 and H = 10$ km, an increase in the electrical component of the noise was found in the vicinity of 5.8 Hz [*Walker et al.*, 2013]. [*Zhang et al.*, 2014] introduced a new parameter for the ULF/ELF electric field perturbations, which includes not only the intensity, but also its attenuation character. After processing the local nighttime DEMETER data during 5 days around 25 seismic events with $M > 6.0$

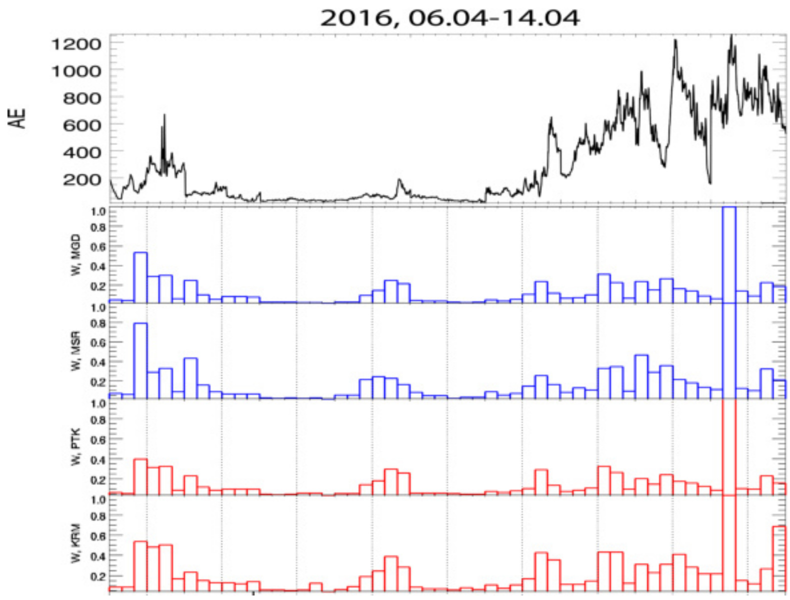

Figure 8. Variations in the spectral power W in the band 0.01–0.8 Hz for the horizontal Y component at night hours for PWING stations. The red color corresponds to nearby stations, blue color denotes distant stations. The upper panel shows the planetary geomagnetic index AE, characterizing the disturbance of the geomagnetic field at auroral latitudes.

in Chile they found precursory anomalies before 2/3 of EQs. Clear temporal and spatial statistical correlations between ULF wave activity in the nighttime ionosphere and EQs ($M \geq 5.0, H \leq 70$ km) were found in the electric field data from DEMETER [*Ouyang et al.*, 2020]. The enhanced ULF wave occurrence rate happened ~1 day and ~1 week before the EQs at distance <200 km from the epicenters. [*Zhang et al.*, 2014] presented ULF electric field (DC-15 Hz) observations during local nighttime by DEMETER satellite around seismic regions of Indonesia and Chile. Anomalous ULF electric field perturbations were revealed with amplitudes ≤ 10 mV/m before some large EQs. [*Akhoondzadeh*, 2013] observed anomalies in the ULF magnetic and electric components a few days prior to the strong earthquake. Electromagnetic measurements on the CSES satellite in the band 75–90 Hz revealed an increase in noise power in the nighttime ionosphere by 10–30% a few days before EQs with $M = 6.4$ and $M = 7.4$ [*Wang et al.*, 2021]. Zhima et al. [2022] suggested that the possible abnormal emissions in the ULF band recorded by CSES satellite were emitted during the EQs.

It is implicitly assumed that the emission from an underground ULF/ELF source directly reaches a LEO satellite upon propagation through the ionosphere as illustrated in Figure 9. To estimate the necessary intensity of a seismic source of anomalous radiation that can be detected at LEO, one has to model the response of the ionosphere to a large-scale underground emitter. The obtained estimate can be compared with the observational results, so a conclusion about the prospects of satellite observations for the search for seismo-electromagnetic emissions may be given. The problem cannot be reduced to the classical problems of electromagnetic radiation from a dipole buried in a conducting half-space. In the situation under consideration, the system of oscillating currents in the earth's crust has a length comparable to the height of the ionosphere, so its finite scale must be taken into account. Such numerical calculations of the penetration of ULF fields from an underground source into the ionosphere were performed in [*Molchanov et al.*, 1995; *Wang et al.*, 2021], but these models have certain significant limitations and cannot provide a comprehensive solution to the problem.

The advanced numerical model that makes it possible to estimate the ULF fields generated by an underground horizontal current of finite length both on the earth's surface and in the upper ionosphere was elaborated in [*Fedorov et al.*, 2023; *Mazur et al.*, 2024].

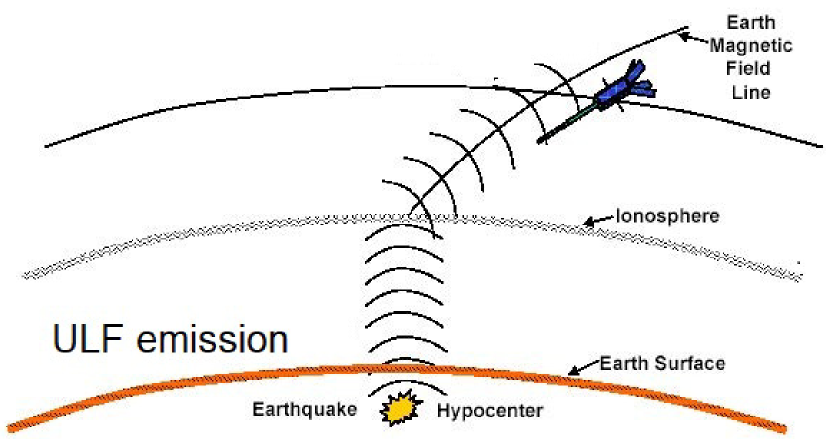

Figure 9. A schematic illustration of the satellite experiments to detect ULF electromagnetic emission from the EQ hypocenter.

This model includes the atmospheric conductivity profile and realistic vertical structure of the ionospheric parameters derived from the IRI model. With the use of this model, the spatial structure of the amplitude of the 0.1-Hz radiation field is calculated simultaneously for the upper ionosphere ($z = 500$ km) and on the ground (Figure 10). The underground current with intensity 1-A, length 20 km, at depth 20 km in the crust with conductivity 10^{-3} S/m, was taken. The maximum disturbance of transverse electric components directly above the source current ($y = 0$) reaches $|E| \sim 2 \times 10^{-3}$ μV/m. The underground current that is capable to produce the observed in early satellite mission E-field disturbance > 1 mV/m in the upper ionosphere is to be $>10^6$ A. However, according to the numerical model, in this case, a perturbation of the geomagnetic field B~10^3 nT arises on the earth's surface (see the bottom panel in Figure 10). Such geomagnetic disturbances, comparable to disturbances during strong substorms, would be detected by the existing network of magnetometers. Therefore, ULF disturbances before EQs recorded onboard early satellites can hardly be associated with direct radiation from underground sources of a seismic nature. Only modern observations with sensitivity better than 1 μV/m may produce trustworthy observations because the associated ground signature is to be around 1 nT.

9. Prospects of future research

The most decidedly adverse perspective in EQ studies, mainly from the seismology and geodesy point of view, is that such complex system as EQ is inherently unpredictable because of the highly sensitive nonlinear dependence on initial conditions. The situation is similar to the following example. Having a dense array of all necessary meteodata one can reliably predict an occurrence of severe weather. However, even with most complete set of data it would be hardly possible to predict exactly the place and time where lighting strike. Hopefully, overturning the situation with seismic process is possible through multidisciplinary science. We believe that a critical analysis of all published results is as important as a search for new seismo-electromagnetic effects. This may help to shut down unpromising and misleading directions and thus save time and resources.

The elusive seismogenic ULF emissions are weak, so a simple monitoring of the ULF power is not sufficient to reveal them from other sources. Advanced methods of time series analysis may be helpful to resolve this issue. Some encouraging attempts have been undertaken. [*Serita et al.*, 2005] applied the principal component analysis (PCA) to ground measurements of magnetic field in order to point out earthquake related anomalies. The authors extracted the first two principal components related to geomagnetic variation and anthropogenic sources, while the third component pointed out the possible seismo-associated disturbances. By applying PCA to magnetic data from six observato-

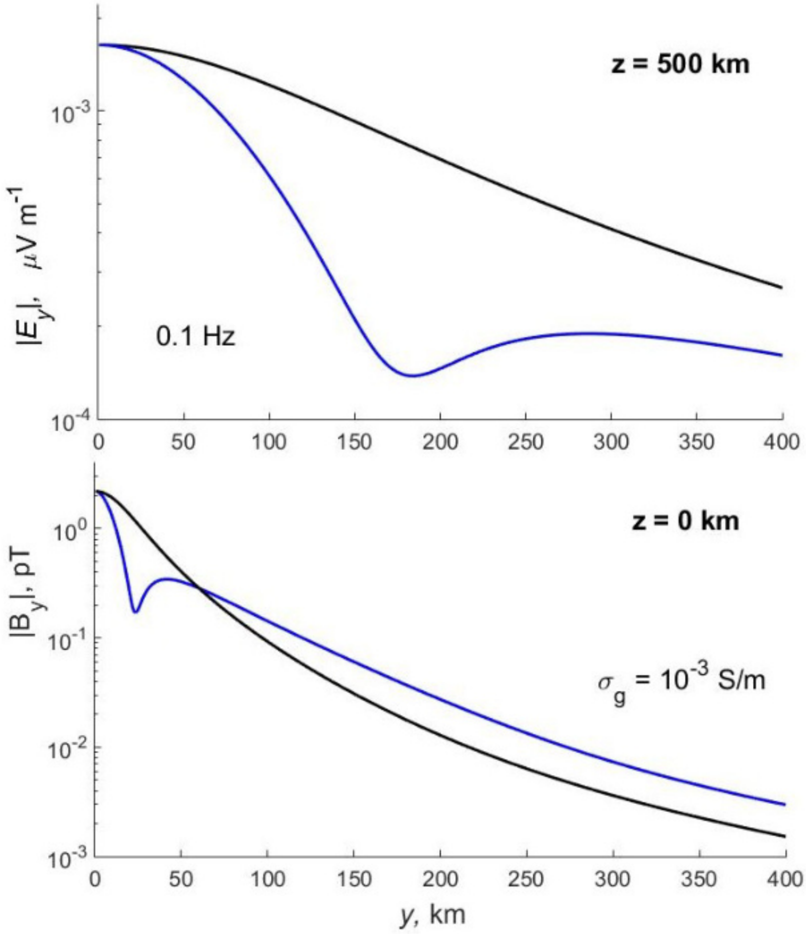

Figure 10. The spatial structure of the amplitude of the 0.1-Hz radiation field calculated for the upper ionosphere (z = 500 km) (electric field components), and on the ground (magnetic field components).

ries [*Kappler et al.*, 2017] were able to identify and distinguish global geomagnetic signals and anthropogenic signals. The application of machine learning methods for automatically classifying and recognizing earthquake precursors on ground and in space have been explored [*Rouet-Leduc et al.*, 2017].

Though the reported results on the effect of magnetic storms on seismicity seem questionable, we do not completely deny the possibility of a relationship between solar activity, the geomagnetic field, and seismicity, and do not deny in principle the possibility of triggered effects in geophysical processes. It is possible that a trigger effect can manifest itself only under a unique combination of favorable factors that are extremely rare and do not appear in general statistics.

Though our analysis has not confirmed the occurrence of impulsive disturbances few minutes before EQs, the study of the generation of electromagnetic pulses at the stage of rock destruction seems to be very promising [*Bleier et al.*, 2010; *Freund et al.*, 2021; *Tsutsui*, 2005]. To isolate unipolar magnetic pulses, presumably associated with an increase in tectonic load on the rock, specialized time series analysis algorithms are to be developed [*Kappler et al.*, 2019].

A comparison of the variations in the integrated spectral power of magnetic noise at array of stations showed that the depression of nighttime magnetic noise, which was previously considered an operative precursor, occurred simultaneously at all nearby and distant stations. Thus, at least for the re-examined event, noise depression cannot be considered as a local short-term precursor. Thus, an additional analysis of all the reported events is required using an extended regional network of magnetometers to validate this effect.

The evident weak point of seismo-electromagnetic studies is the lack of quantitative physical models. Many studies are still based on qualitative concepts, without any estimate of expected effect even with simplified theoretical models. Theoretical modeling would make it possible to discard unrealistic physical mechanisms, otherwise, random coincidences can be perceived as reliable experimental evidence. In particular, a new theoretical formalism is needed for calculating electromagnetic fields in the Earth-atmosphere-ionosphere system, created by an underground current source. This numerical model can be used to indicate characteristic features of such an underground source field that can be used to discriminate disturbances from seismogenic sources. The first application of such model to estimate the self-consistently expected amplitude of ULF emission in the topside ionosphere and on the ground has shown that early "classical" results of satellite observations cannot be interpreted as a result of direct ULF emission from a hypothetical seismogenic source.

In all presented events, the geomagnetic field "anomalies" can be explained by global geomagnetic activity and are apparently not associated with seismic processes. The considered issues are a clear illustration of the fact that the analysis of anomalous disturbances should be carried out jointly by specialists in EQ physics and space weather. We suggest that both communities must cooperate their studies more tightly and perform data exchange. A very effective tool for the in-depth study of geophysical phenomena and the unification of the researcher's expertise is the common data analysis workshop (CDAW). During the CDAW, all participants combine their observational data and modeling efforts for a selected event to achieve the most comprehensive understanding of a phenomena under study.

Acknowledgments. This work was supported by the Russian Science Foundation grant 22-17-00125 and presented at the 7th International Workshop on EQ Preparation Process, Observation, Validation, Modeling, Forecasting (IWEP7) in Chiba.

References

Adushkin, V. V., and A. A. Spivak (2021), Impact of Natural Extreme Events on Geophysical Fields in the Environment, *Izvestiya, Physics of the Solid Earth*, *57*(5), 583–592, https://doi.org/10.1134/s1069351321050037.

Adushkin, V. V., S. A. Ryabova, A. A. Spivak, and V. A. Kharlamov (2012), Response of the seismic background to geomagnetic variations, *Doklady Earth Sciences*, *444*(1), 642–646, https://doi.org/10.1134/s1028334x12050157.

Akhoondzadeh, M. (2013), Novelty detection in time series of ULF magnetic and electric components obtained from DEMETER satellite experiments above Samoa (29 September 2009) earthquake region, *Natural Hazards and Earth System Sciences*, *13*(1), 15–25, https://doi.org/10.5194/nhess-13-15-2013.

Bakhmutov, V. G., F. I. Sedova, and T. A. Mozgova (2003), Morphological analysis of geomagnetic variations in preparation period of the strongest earthquake of 25 March 1998, *Ukrainian Antarctic Journal*, (1), 54–60, https://doi.org/10.33275/1727-7485.1.2003.624 (in Ukranian).

Best, A., S. M. Krylov, I. P. Kurchashov, I. S. Nikomarov, and V. A. Pilipenko (1986), Gradient-time analysis of Pc3 pulsations, *Geomagnetism and Aeronomy*, *26*(6), 980–984 (in Russian).

Bilichenko, S. V., A. S. Inchin, E. F. Kim, O. A. Pokhotelov, P. P. Puschaev, G. G. Stanev, A. V. Streltsov, and V. M. Chmyrev (1990), ULF response of the ionosphere to earthquake preparation processes, *Doklady Akademii Nauk*, *311*(5), 1077–1081 (in Russian).

Bleier, T., C. Dunson, M. Maniscalco, N. Bryant, R. Bambery, and F. Freund (2009), Investigation of ULF magnetic pulsations, air conductivity changes, and infra red signatures associated with the 30 October Alum Rock M5.4 earthquake, *Natural Hazards and Earth System Sciences*, *9*(2), 585–603, https://doi.org/10.5194/nhess-9-585-2009.

Bleier, T., C. Dunson, C. Alvarez, F. Freund, and R. Dahlgren (2010), Correlation of pre-earthquake electromagnetic signals with laboratory and field rock experiments, *Natural Hazards and Earth System Sciences*, *10*(9), 1965–1975, https://doi.org/10.5194/nhess-10-1965-2010.

Bortnik, J., J. W. Cutler, C. Dunson, and T. E. Bleier (2008), The possible statistical relation of Pc1 pulsations to Earthquake occurrence at low latitudes, *Annales Geophysicae*, *26*(9), 2825–2836, https://doi.org/10.5194/angeo-26-2825-2008.

Chernogor, L. F. (2019), Geomagnetic Disturbances Accompanying the Great Japanese Earthquake of March 11, 2011, *Geomagnetism and Aeronomy*, *59*(1), 62–75, https://doi.org/10.1134/S0016793219010043.

Chmyrev, V. M., N. V. Isaev, S. V. Bilichenko, and G. Stanev (1986), Electric fields and hydromagnetic waves in the ionosphere above the earthquake source, *Geomagnetism and Aeronomy*, *26*(6), 1020–1022 (in Russian).

Chmyrev, V. M., N. V. Isaev, S. V. Bilichenko, and G. Stanev (1989), Observation by space-borne detectors of electric fields and hydromagnetic waves in the ionosphere over an earthquake centre, *Physics of the Earth and Planetary Interiors*, *57*(1–2), 110–114, https://doi.org/10.1016/0031-9201(89)90220-3.

De Santis, A., G. De Franceschi, L. Spogli, L. Perrone, L. Alfonsi, and other (2015), Geospace perturbations induced by the Earth: The state of the art and future trends, *Physics and Chemistry of the Earth, Parts A/B/C*, *85–86*, 17–33, https://doi.org/10.1016/j.pce.2015.05.004.

De Santis, A., D. Marchetti, F. J. Pavón-Carrasco, G. Cianchini, L. Perrone, and other (2019), Precursory worldwide signatures of earthquake occurrences on Swarm satellite data, *Scientific Reports*, *9*(1), https://doi.org/10.1038/s41598-019-56599-1.

Desherevskii, A. V., and A. Y. Sidorin (2016), Comparative morphological analysis of the diurnal rhythms in geomagnetic and seismic activity, *Izvestiya, Atmospheric and Oceanic Physics*, *52*(8), 853–861, https://doi.org/10.1134/s0001433816080041.

Doda, L. N., V. L. Natyaganov, and I. V. Stepanov (2013), An empirical scheme of short-term earthquake prediction, *Doklady Earth Sciences*, *453*(2), 1257–1263, https://doi.org/10.1134/S1028334X1312009X.

Dovbnya, B. V. (2011), On the effects of earthquakes in geomagnetic pulsations and their possible nature, *Geophysical Journal*, *33*(1), 72–79 (in Russian).

Dovbnya, B. V. (2014), Electromagnetic precursors of earthquakes and their frequency, *Geophysical Journal*, *36*(3), 160–165 (in Russian).

Dovbnya, B. V. (2021), On the results of remote observation of pulsed ultra-low-frequency electromagnetic signals detected minutes before an earthquake, *Life of the Earth*, *43*(3), 304–313, https://doi.org/10.29003/m2435.0514-7468.2020_43_3/304-313 (in Russian).

Dovbnya, B. V., O. D. Zotov, A. O. Mostryukov, and R. V. Shchepetnov (2006), Electromagnetic signals close in time to earthquakes, *Izvestiya, Physics of the Solid Earth*, *42*(8), 684–689, https://doi.org/10.1134/s1069351306080052.

Dovbnya, B. V., O. D. Zotov, and R. V. Shchepetnov (2008), Connection of ULF electromagnetic waves with earthquakes and anthropogenic impacts, *Izvestiya, Physics of the Solid Earth*, *9*, 3–23 (in Russian).

Dovbnya, B. V., A. Y. Pashinin, and R. A. Rakhmatulin (2019), Short-term electromagnetic precursors of earthquakes, *Geodynamics & Tectonophysics*, *10*(3), 731–740, https://doi.org/10.5800/GT-2019-10-3-0438.

Duma, G., and Y. Ruzhin (2003), Diurnal changes of earthquake activity and geomagnetic Sq-variations, *Natural Hazards and Earth System Sciences*, *3*(3/4), 171–177, https://doi.org/10.5194/nhess-3-171-2003.

Duma, G., and G. Vilardo (1998), Seismicity cycles in the Mt. Vesuvius area and their relation to solar flux and the variations of the Earth's magnetic field, *Physics and Chemistry of the Earth*, *23*(9–10), 927–931, https://doi.org/10.1016/s0079-1946(98)00121-9.

Fedorov, E., V. Pilipenko, and S. Uyeda (2001), Electric and magnetic fields generated by electrokinetic processes in a conductive crust, *Physics and Chemistry of the Earth, Part C: Solar, Terrestrial & Planetary Science*, *26*(10–12), 793–799, https://doi.org/10.1016/S1464-1917(01)95027-5.

Fedorov, E. N., N. G. Mazur, V. A. Pilipenko, and V. V. Vakhnina (2023), Generation of Artificial ULF/ELF Electromagnetic Emission in the Ionosphere by Horizontal Ground-Based Current System, *Journal of Geophysical Research: Space Physics*, *128*(12), https://doi.org/10.1029/2023ja031590.

Fenoglio, M. A., M. J. S. Johnston, and J. D. Byerlee (1995), Magnetic and electric fields associated with changes in high pore pressure in fault zones: Application to the Loma Prieta ULF emissions, *Journal of Geophysical Research: Solid Earth*, *100*(B7), 12,951–12,958, https://doi.org/10.1029/95JB00076.

Freund, F. T., J. A. Heraud, V. A. Centa, and J. Scoville (2021), Mechanism of unipolar electromagnetic pulses emitted from the hypocenters of impending earthquakes, *The European Physical Journal Special Topics*, *230*(1), 47–65, https://doi.org/10.1140/epjst/e2020-000244-4.

Gavrilov, B. G., Y. V. Poklad, I. A. Ryakhovsky, V. M. Ermak, N. S. Achkasov, and E. N. Kozakova (2022), Global Electromagnetic Disturbances Caused by the Eruption of the Tonga Volcano on 15 January 2022, *Journal of Geophysical Research: Atmospheres*, *127*(23), https://doi.org/10.1029/2022jd037411.

Gogatishvili, I. M. (1984), Geomagnetic precursors of intense earthquakes in the spectrum of geomagnetic pulsations with frequencies of 1-0.02 Hz, *Geomagnetism and Aeronomy*, *24*, 697–700 (in Russian).

Gousheva, M., D. Danov, P. Hristov, and M. Matova (2008), Quasi-static electric fields phenomena in the ionosphere associated with pre- and post earthquake effects, *Natural Hazards and Earth System Sciences*, *8*(1), 101–107, https://doi.org/10.5194/nhess-8-101-2008.

Guglielmi, A. V., and V. T. Levshenko (1996), Electromagnetic impulse from the source of an earthquake, *Doklady Akademii Nauk*, *349*(5), 676–678 (in Russian).

Guglielmi, A. V., and O. D. Zotov (2010), Correlation between Pc1 electromagnetic activity and earthquakes, *Izvestiya, Physics of the Solid Earth*, *46*(6), 486–492, https://doi.org/10.1134/S1069351310060030.

Han, Y., Z. Guo, J. Wu, and L. Ma (2004), Possible triggering of solar activity to big earthquakes ($Ms \geq 8$) in faults with near west-east strike in China, *Science in China Series G*, *47*(2), 173, https://doi.org/10.1360/03yw0103.

Harrison, R. G., K. L. Aplin, and M. J. Rycroft (2010), Atmospheric electricity coupling between earthquake regions and the ionosphere, *Journal of Atmospheric and Solar-Terrestrial Physics*, *72*(5–6), 376–381, https://doi.org/10.1016/j.jastp.2009.12.004.

Hattori, K. (2004), ULF Geomagnetic Changes Associated with Large Earthquakes, *Terrestrial, Atmospheric and Oceanic Sciences*, *15*(3), 329, https://doi.org/10.3319/TAO.2004.15.3.329(EP).

Hayakawa, M. (Ed.) (2009), *Electromagnetic phenomena associated with earthquakes*, Transworld Research Network, Trivandrum (India).

Hayakawa, M. (Ed.) (2013), *Earthquake Prediction Studies: Seismo Electromagnetics*, TERRAPUB, Tokyo.

Hayakawa, M., and O. A. Molchanov (Eds.) (2002), *Seismo Electromagnetics: Lithosphere-Atmosphere-Ionosphere Coupling*, TERRAPUB, Tokyo.

Hayakawa, M., R. Kawate, O. A. Molchanov, and K. Yumoto (1996), Results of ultra-low-frequency magnetic field measurements during the Guam Earthquake of 8 August 1993, *Geophysical Research Letters*, *23*(3), 241–244, https://doi.org/10.1029/95GL02863.

Hayakawa, M., T. Ito, and N. Smirnova (1999), Fractal analysis of ULF geomagnetic data associated with the Guam Earthquake on August 8, 1993, *Geophysical Research Letters*, *26*(18), 2797–2800, https://doi.org/10.1029/1999GL005367.

Hayakawa, M., A. Schekotov, S. Potirakis, and K. Eftaxias (2015), Criticality features in ULF magnetic fields prior to the 2011 Tohoku earthquake, *Proceedings of the Japan Academy, Series B*, *91*(1), 25–30, https://doi.org/10.2183/pjab.91.25.

Huang, Q., P. Han, K. Hattori, and H. Ren (2020), Electromagnetic Signals Associated With Earthquakes: A Review of Observations, Data Processing, and Mechanisms in China, https://doi.org/10.1002/9781119127383.ch26.

Ismaguilov, V. S., Y. A. Kopytenko, K. Hattori, and M. Hayakawa (2003), Variations of phase velocity and gradient values of ULF geomagnetic disturbances connected with the Izu strong earthquakes, *Natural Hazards and Earth System Sciences*, *3*(3/4), 211–215, https://doi.org/10.5194/nhess-3-211-2003.

Ismaguilov, V. S., Y. A. Kopytenko, K. Hattori, and M. Hayakawa (2006), Gradients and phase velocities of ULF geomagnetic disturbances used to determine the source of an impending strong earthquake, *Geomagnetism and Aeronomy*, *46*(3), 403–410, https://doi.org/10.1134/S0016793206030157.

Iyemori, T., T. Kamei, Y. Tanaka, M. Takeda, T. Hashimoto, T. Araki, T. Okamoto, K. Watanabe, N. Sumitomo, and N. Oshiman (1996), Co-Seismic Geomagnetic Variations Observed at the 1995 Hyogoken-Nanbu Earthquake, *Journal of geomagnetism and geoelectricity*, *48*(8), 1059–1070, https://doi.org/10.5636/jgg.48.1059.

Iyemori, T., M. Nose, D. Han, Y. Gao, M. Hashizume, and other (2005), Geomagnetic pulsations caused by the Sumatra earthquake on December 26, 2004, *Geophysical Research Letters*, *32*(20), https://doi.org/10.1029/2005GL024083.

Kappler, K. N., D. D. Schneider, L. S. MacLean, and T. E. Bleier (2017), Identification and classification of transient pulses observed in magnetometer array data by time-domain principal component analysis filtering, *Earthquake Science*, *30*(4), 193–207, https://doi.org/10.1007/s11589-017-0191-6.

Kappler, K. N., D. D. Schneider, L. S. MacLean, T. E. Bleier, and J. J. Lemon (2019), An algorithmic framework for investigating the temporal relationship of magnetic field pulses and earthquakes applied to California, *Computers & Geosciences*, *133*, 104,317, https://doi.org/10.1016/j.cageo.2019.104317.

Kodama, T., O. A. Molchanov, and M. Hayakawa (2000), NASDA Earthquake Remote Sensing Frontier Research — Feasibility of satellite observation of seismoelectromagnetics, *Advances in Space Research*, *26*(8), 1281–1284, https://doi.org/10.1016/S0273-1177(99)01219-3.

Kopytenko, Y. A., V. S. Ismaguilov, O. A. Molchanov, E. A. Kopytenko, P. M. Voronov, K. Hattori, M. Hayakawa, and D. B. Zaitsev (2002), Investigation of ULF magnetic disturbances in Japan during seismic active period, *Journal of Atmospheric Electricity*, *22*(3), 207–215.

Kopytenko, Y. A., V. S. Ismaguilov, K. Hattori, and M. Hayakawa (2006), Determination of hearth position of a forthcoming strong EQ using gradients and phase velocities of ULF geomagnetic disturbances, *Physics and Chemistry of the Earth, Parts A/B/C*, *31*(4–9), 292–298, https://doi.org/10.1016/j.pce.2006.02.004.

Kopytenko, Y. A., V. S. Ismaguilov, K. Hattori, and M. Hayakawa (2012), Anomaly disturbances of the magnetic fields before the strong earthquake in Japan on March 11, 2011, *Annals of Geophysics*, *55*(1), https://doi.org/10.4401/ag-5260.

Kosterin, N. A., V. A. Pilipenko, and E. M. Dmitriev (2015), On Global Ultralow Frequency Electromagnetic Signals Prior to Earthquakes, *Geophysical research*, *16*(1), 24–34 (in Russian).

Kozyreva, O. V., and V. A. Pilipenko (2020), On the Relationship of Geomagnetic Disturbances and Seismic Activity for Alaska Region, *Geophysical research*, *21*(1), 33–49, https://doi.org/10.21455/gr2020.1-3 (in Russian).

Kozyreva, O. V., V. A. Pilipenko, E. E. Marshalko, E. Y. Sokolova, and M. N. Dobrovolsky (2022), Monitoring of Geomagnetic and Telluric Field Disturbances in the Russian Arctic, *Applied Sciences*, *12*(8), 3755, https://doi.org/10.3390/app12083755.

Kuznetsova, V. G., V. E. Maksimchuk, Y. M. Gorodysky, and T. A. Klimkovich (2005), Anomalous Effects in the Geomagnetic Field in Relation to the Seismic Regime of the Carpathians, *Izvestiya*, *Physics of the Solid Earth*, *41*(3), 213–237.

Li, Q., A. Schekotov, T. Asano, and M. Hayakawa (2015), On the Anomalies in ULF Magnetic Field Variations Prior to the 2008 Sichuan Earthquake, *Open Journal of Earthquake Research*, *04*(02), 55–64, https://doi.org/10.4236/ojer.2015.42005.

Lockner, D. A., M. J. S. Johnston, and J. D. Byerlee (1983), A mechanism to explain the generation of earthquake lights, *Nature*, *302*(5903), 28–33, https://doi.org/10.1038/302028a0.

Love, J. J., and A. Chulliat (2013), An International Network of Magnetic Observatories, *EOS, Transactions American Geophysical Union*, *94*(42), 373–374, https://doi.org/10.1002/2013EO420001.

Love, J. J., and J. N. Thomas (2013), Insignificant solar-terrestrial triggering of earthquakes, *Geophysical Research Letters*, *40*(6), 1165–1170, https://doi.org/10.1002/grl.50211.

Marchuk, R., A. Potapov, and V. Mishin (2022), Synchronous globally observable ultrashort-period pulses, *Solnechno-Zemnaya Fizika*, *8*(2), 52–60, https://doi.org/10.12737/szf-82202207.

Martinez-Bedenko, V. A., V. A. Pilipenko, K. Shiokawa, and V. A. Kasimova (2023), Search for Pulsed Ultralow-Frequency Electromagnetic Earthquake Precursors, *Geophysical Research*, *24*(2), 5–24, https://doi.org/10.21455/gr2023.2-1 (in Russian).

Masci, F., and J. N. Thomas (2015), Are there new findings in the search for ULF magnetic precursors to earthquakes?, *Journal of Geophysical Research: Space Physics*, *120*(12), https://doi.org/10.1002/2015ja021336.

Mazur, N. G., E. N. Fedorov, V. A. Pilipenko, and K. E. Borovleva (2024), Electromagnetic ULF fields on the earth's surface and in the ionosphere from an underground seismic source, *Izvestiya*, *Physics of the Solid Earth*, (2).

Menk, F. W., and C. L. Waters (2013), *Magnetoseismology: Ground-Based Remote Sensing of Earth's Magnetosphere*, Wiley, https://doi.org/10.1002/9783527652051.

Molchanov, O. A., and M. Hayakawa (1995), Generation of ULF electromagnetic emissions by microfracturing, *Geophysical Research Letters*, *22*(22), 3091–3094, https://doi.org/10.1029/95gl00781.

Molchanov, O. A., Y. A. Kopytenko, P. M. Voronov, E. A. Kopytenko, and other (1992), Results of ULF magnetic field measurements near the epicenters of the Spitak (Ms = 6.9) and Loma Prieta (Ms = 7.1) earthquakes: Comparative analysis, *Geophysical Research Letters*, *19*(14), 1495–1498, https://doi.org/10.1029/92gl01152.

Molchanov, O. A., M. Hayakawa, and V. A. Rafalsky (1995), Penetration characteristics of electromagnetic emissions from an underground seismic source into the atmosphere, ionosphere, and magnetosphere, *Journal of Geophysical Research: Space Physics*, *100*(A2), 1691–1712, https://doi.org/10.1029/94ja02524.

Molchanov, O. A., A. Y. Schekotov, E. Fedorov, G. G. Belyaev, M. S. Solovieva, and M. Hayakawa (2004), Preseismic ULF effectand possible interpretation, *Annals of Geophysics*, *47*(1), https://doi.org/10.4401/ag-3265.

Naumov, A. P. (1999), Impulsive low-frequency seismo-magnetic signals in geomagnetic variations as an earthquake prediction tool, *Volcanology & Seismology*, *20*, 743–752.

Nosikova, N. S., V. A. Pilipenko, and S. L. Shalimov (2023), On the Magnetic Effects Caused by the Earthquake of March 16, 2022 in Japan, *Izvestiya*, *Physics of the Solid Earth*, *59*(5), 815–820, https://doi.org/10.1134/S1069351323050075.

Odintsov, S., K. Boyarchuk, K. Georgieva, B. Kirov, and D. Atanasov (2006), Long-period trends in global seismic and geomagnetic activity and their relation to solar activity, *Physics and Chemistry of the Earth*, *Parts A/B/C*, *31*(1–3), 88–93, https://doi.org/10.1016/j.pce.2005.03.004.

Ouyang, X. Y., M. Parrot, and J. Bortnik (2020), ULF Wave Activity Observed in the Nighttime Ionosphere Above and Some Hours Before Strong Earthquakes, *Journal of Geophysical Research: Space Physics*, *125*(9), https://doi.org/10.1029/2020JA028396.

Parrot, M., and M. Lil (2015), DEMETER results related to seismic activity, *Radio Science Bulletin*, *355*, 18–25, https://doi.org/10.23919/URSIRSB.2015.7909470.

Petraki, E., D. Nikolopoulos, C. Nomicos, J. Stonham, and other (2015), Electromagnetic Pre-earthquake Precursors: Mechanisms, Data and Models-A Review, *Journal of Earth Science & Climatic Change*, *06*(01), https://doi.org/10.4172/2157-7617.1000250.

Picozza, P., L. Conti, and A. Sotgiu (2021), Looking for Earthquake Precursors From Space: A Critical Review, *Frontiers in Earth Science*, *9*, https://doi.org/10.3389/feart.2021.676775.

Pilipenko, V., O. Kozyreva, E. Fedorov, M. Uspensky, and K. Kauristie (2016), Latitudinal amplitude-phase structure of MHD waves: STARE radar and image magnetometer observations and modeling, *Solnechno-Zemnaya Fizika*, *2*(3), 41–51, https://doi.org/10.12737/19418.

Pulinets, S., and D. Davidenko (2014), Ionospheric precursors of earthquakes and Global Electric Circuit, *Advances in Space Research*, *53*(5), 709–723, https://doi.org/10.1016/j.asr.2013.12.035.

Rabeh, T., M. Miranda, and M. Hvozdara (2009), Strong earthquakes associated with high amplitude daily geomagnetic variations, *Natural Hazards*, *53*(3), 561–574, https://doi.org/10.1007/s11069-009-9449-1.

Rouet-Leduc, B., C. Hulbert, N. Lubbers, K. Barros, C. J. Humphreys, and P. A. Johnson (2017), Machine Learning Predicts Laboratory Earthquakes, *Geophysical Research Letters*, *44*(18), 9276–9282, https://doi.org/10.1002/2017GL074677.

Schekotov, A. Y., and M. Hayakawa (2017), *ULF/ELF electromagnetic phenomena for short-term earthquake prediction*, LAP LAMBERT Academic Publishing.

Schekotov, A. Y., O. A. Molchanov, K. Hattori, E. N. Fedorov, and other (2006), Seismo-ionospheric depression of the ULF geomagnetic fluctuations at Kamchatka and Japan, *Physics and Chemistry of the Earth, Parts A/B/C*, *31*(4–9), 313–318, https://doi.org/10.1016/j.pce.2006.02.043.

Schekotov, A. Y., O. A. Molchanov, M. Hayakawa, E. N. Fedorov, V. N. Chebrov, and other (2008), About possibility to locate an EQ epicenter using parameters of ELF/ULF preseismic emission, *Natural Hazards and Earth System Sciences*, *8*(6), 1237–1242, https://doi.org/10.5194/nhess-8-1237-2008.

Schekotov, A. Y., E. N. Fedorov, Y. Hobara, and M. Hayakawa (2013), ULF Magnetic Field Depression as a Possible Precursor to the 2011/3.11 Japan Earthquake, *Journal of Atmospheric Electricity*, *33*(1), 41–51, https://doi.org/10.1541/jae.33.41.

Schekotov, A. Y., D. Chebrov, M. Hayakawa, G. Belyaev, and N. Berseneva (2020), Short-term earthquake prediction in Kamchatka using low-frequency magnetic fields, *Natural Hazards*, *100*(2), 735–755, https://doi.org/10.1007/s11069-019-03839-2.

Serita, A., K. Hattori, C. Yoshino, M. Hayakawa, and N. Isezaki (2005), Principal component analysis and singular spectrum analysis of ULF geomagnetic data associated with earthquakes, *Natural Hazards and Earth System Sciences*, *5*(5), 685–689, https://doi.org/10.5194/nhess-5-685-2005.

Sgrigna, V., A. Buzzi, L. Conti, P. Picozza, C. Stagni, and D. Zilpimiani (2008), The ESPERIA satellite project for detecting seismo-associated effects in the topside ionosphere. First instrumental tests in space, *Earth, Planets and Space*, *60*(5), 463–475, https://doi.org/10.1186/BF03352813.

Shiokawa, K., Y. Katoh, Y. Hamaguchi, Y. Yamamoto, T. Adachi, and other (2017), Ground-based instruments of the PWING project to investigate dynamics of the inner magnetosphere at subauroral latitudes as a part of the ERG-ground coordinated observation network, *Earth, Planets and Space*, *69*(1), https://doi.org/10.1186/s40623-017-0745-9.

Simpson, J. F. (1967), Solar activity as a triggering mechanism for earthquakes, *Earth and Planetary Science Letters*, *3*, 417–425, https://doi.org/10.1016/0012-821X(67)90071-4.

Smirnov, V. B., and A. D. Zavyalov (2012), Seismic response to electromagnetic sounding of the Earth's lithosphere, *Izvestiya, Physics of the Solid Earth*, *48*(7–8), 615–639, https://doi.org/10.1134/S1069351312070075.

Sobisevich, A. L., K. K. Kanonidi, L. E. Sobisevich, and D. G. Gridnev (2009a), On a class of electromagnetic disturbances preceding strong earthquakes, *Seismic Instruments*, *46*(3), 228–233, https://doi.org/10.3103/s0747923910030047.

Sobisevich, A. L., L. E. Sobisevich, K. K. Kanonidi, and D. V. Likhodeev (2017), Gravimagnetic perturbations preceding earthquakes, *Doklady Earth Sciences*, *475*(2), 891–894, https://doi.org/10.1134/s1028334x17080086.

Sobisevich, L. E. (2020), Seismogravitational processes and gravitomagnetic disturbances accompanying geophysical catastrophes, *Geofizika*, *1*, 70–76 (in Russian).

Sobisevich, L. E., K. K. Kanonidi, and A. L. Sobisevich (2009b), Ultra low-frequency electromagnetic disturbances appearing before strong seismic events, *Doklady Earth Sciences*, *429*(2), 1549–1552, https://doi.org/10.1134/s1028334x09090281.

Sobisevich, L. E., K. K. Kanonidi, and A. L. Sobisevich (2010a), Observations of ultra-low-frequency geomagnetic disturbances reflecting the processes of the preparation and development of tsunamigenic earthquakes, *Doklady Earth Sciences*, *435*(2), 1627–1632, https://doi.org/10.1134/S1028334X10120160.

Sobisevich, L. E., K. K. Kanonidi, and A. L. Sobisevich (2010b), Ultra low-frequency electromagnetic variation observed prior to development of an earthquake followed by tsunami, *Geophysical Journal*, *32*(4), 152–157.

Sobisevich, L. E., A. L. Sobisevich, and K. K. Kanonidi (2012), Anomalous geomagnetic disturbances induced by catastrophic tsunamigenic earthquakes in the region of Indonesia, *Geophysical Journal*, *34*(5), 22–37, https://doi.org/10.24028/gzh.0203-3100.v34i5.2012.116661.

Sobisevich, L. E., K. K. Kanonidi, A. L. Sobisevich, and O. I. Miseyuk (2013), Geomagnetic disturbances in the geomagnetic field's variations at stages of preparation and implementation of the Elazig (March 8, 2010) and M 5.3 (January 19, 2011) earthquakes in Turkey, *Doklady Earth Sciences*, *449*(1), 324–327, https://doi.org/10.1134/s1028334x13030069.

Sobolev, G. A., N. A. Zakrzhevskaya, and E. P. Kharin (2001), On the Relation Between Seismicity and Magnetic Storms, *Izvestiya*, *Physics of the Solid Earth*, *37*(11), 917–927.

Sorokin, V. M., E. N. Fedorov, A. Y. Schekotov, O. A. Molchanov, and M. Hayakawa (2004), Depression of ULF geomagnetic pulsation related to ionospheric irregularities, *Annals of Geophysics*, *47*(1), 191–198.

Sorokin, V. M., , A. K. Yashchenko, and V. A. Novikov (2019), A possible mechanism of stimulation of seismic activity by ionizing radiation of solar flares, *Earthquake Science*, *32*(1), 26–34, https://doi.org/10.29382/eqs-2019-0026-3.

Spivak, A. A., and S. A. Ryabova (2019), Geomagnetic variations during strong earthquakes, *Izvestiya*, *Physics of the Solid Earth*, (6), 3–12, https://doi.org/10.31857/S0002-3337201963-12.

Stothers, R. B. (1990), A search for long-term periodicities in large earthquakes of southern and coastal central California, *Geophysical Research Letters*, *17*(11), 1981–1984, https://doi.org/10.1029/gl017i011p01981.

Straser, V., G. Cataldi, and D. Cataldi (2015), Solar wind ionic and geomagnetic variations preceding the Md8.3 Chile earthquake, *New Concepts in Global Tectonics Journal*, *3*(3), 394–399.

Surkov, V. V., and M. Hayakawa (2006), ULF geomagnetic perturbations due to seismic noise produced by rock fracture and crack formation treated as a stochastic process, *Physics and Chemistry of the Earth*, *Parts A/B/C*, *31*(4–9), 273–280, https://doi.org/10.1016/j.pce.2006.02.019.

Surkov, V. V., and V. A. Pilipenko (1997), Magnetic effects due to earthquakes and underground explosions: a review, *Annals of Geophysics*, *40*(2), https://doi.org/10.4401/ag-3904.

Surkov, V. V., V. A. Pilipenko, and A. K. Sinha (2018), Possible mechanisms of co-seismic electromagnetic effect, *Acta Geodaetica et Geophysica*, *53*(1), 157–170, https://doi.org/10.1007/s40328-018-0211-6.

Sycheva, N. A., L. M. Bogomolov, and V. N. Sychev (2011), On geoeffective solar flares and variations of the seismic noise level, *Izvestiya*, *Physics of the Solid Earth*, *47*(3), 207–222, https://doi.org/10.1134/S1069351310101027.

Tanskanen, E. I. (2009), A comprehensive high-throughput analysis of substorms observed by IMAGE magnetometer network: Years 1993–2003 examined, *Journal of Geophysical Research: Space Physics*, *114*(A5), https://doi.org/10.1029/2008JA013682.

Tarasov, N. T. (1997), Changes in the seismicity of the crust under electrical action, *Doklady Akademii Nauk*, *353*(4), 542–545 (in Russian).

Tarasov, N. T., N. V. Tarasova, A. A. Avagimov, and V. A. Zeigarnik (1999), The effect of high energy electromagnetic pulses on seismicity in central Asia and Kazakhstan, *Volcanology & Seismology*, *21*(4), 627–639.

Tarasov, N. T., N. V. Tarasova, A. A. Avagimov, and V. A. Zeigarnik (2001), The Effect of Electromagnetic Impacts on Seismicity over the Bishkek Geodynamic Test Ground, *Russian Geology and Geophysics*, *42*(10), 1641–1649.

Thomas, J. N., J. J. Love, and M. J. S. Johnston (2009a), On the reported magnetic precursor of the 1989 Loma Prieta earthquake, *Physics of the Earth and Planetary Interiors*, *173*(3–4), 207–215, https://doi.org/10.1016/j.pepi.2008.11.014.

Thomas, J. N., J. J. Love, M. J. S. Johnston, and K. Yumoto (2009b), On the reported magnetic precursor of the 1993 Guam earthquake, *Geophysical Research Letters*, *36*(16), https://doi.org/10.1029/2009GL039020.

Tsutsui, M. (2005), Identification of earthquake epicenter from measurements of electromagnetic pulses in the Earth, *Geophysical Research Letters*, *32*(20), https://doi.org/10.1029/2005GL023691.

Walker, S. N., V. Kadirkamanathan, and O. A. Pokhotelov (2013), Changes in the ultra-low frequency wave field during the precursor phase to the Sichuan earthquake: DEMETER observations, *Annales Geophysicae*, *31*(9), 1597–1603, https://doi.org/10.5194/angeo-31-1597-2013.

Wang, Z., C. Zhou, S. Zhao, X. Xu, M. Liu, Y. Liu, L. Liao, and X. Shen (2021), Numerical Study of Global ELF Electromagnetic Wave Propagation with Respect to Lithosphere–Atmosphere–Ionosphere Coupling, *Remote Sensing*, *13*(20), 4107, https://doi.org/10.3390/rs13204107.

Warden, S., L. MacLean, J. Lemon, and D. Schneider (2020), Statistical Analysis of Pre-earthquake Electromagnetic Anomalies in the ULF Range, *Journal of Geophysical Research: Space Physics*, *125*(10), https://doi.org/10.1029/2020JA027955.

Yagova, N. V., A. K. Sinha, V. A. Pilipenko, E. N. Fedorov, R. Holzworth, and G. Vichare (2019), ULF electromagnetic noise from regional lightning activity: Model and observations, *Journal of Atmospheric and Solar-Terrestrial Physics*, *182*, 223–228, https://doi.org/10.1016/j.jastp.2018.12.005.

Zakrzhevskaya, N. A., and G. A. Sobolev (2002), On the Seismicity Effect of Magnetic Storms, *Izvestiya*, *Physics of the Earth*, *38*(4), 249–261.

Zakrzhevskaya, N. A., and G. A. Sobolev (2004), The Effects of Magnetic Storms with an Abrupt Start on Seismicity in Different Regions, *Volcanology & Seismology*, (3), 63–75 (in Russian).

Zeigarnik, V. A., L. M. Bogomolov, and V. A. Novikov (2022), Electromagnetic Earthquake Triggering: Field Observations, Laboratory Experiments, and Physical Mechanisms - A Review, *Izvestiya*, *Physics of the Solid Earth*, *58*(1), 30–58, https://doi.org/10.1134/S1069351322010104.

Zettergren, M. D., and J. B. Snively (2015), Ionospheric response to infrasonic-acoustic waves generated by natural hazard events, *Journal of Geophysical Research: Space Physics*, *120*(9), 8002–8024, https://doi.org/10.1002/2015JA021116.

Zhang, X., X. Shen, S. Zhao, L. Yao, X. Ouyang, and J. Qian (2014), The characteristics of quasistatic electric field perturbations observed by DEMETER satellite before large earthquakes, *Journal of Asian Earth Sciences*, *79*, 42–52, https://doi.org/10.1016/j.jseaes.2013.08.026.

Zhima, Z., R. Yan, J. Lin, Q. Wang, Y. Yang, and other (2022), The Possible Seismo-Ionospheric Perturbations Recorded by the China-Seismo-Electromagnetic Satellite, *Remote Sensing*, *14*(4), 905, https://doi.org/10.3390/rs14040905.

Zhu, K., M. Fan, X. He, D. Marchetti, K. Li, Z. Yu, C. Chi, H. Sun, and Y. Cheng (2021), Analysis of Swarm Satellite Magnetic Field Data Before the 2016 Ecuador (Mw = 7.8) Earthquake Based on Non-negative Matrix Factorization, *Frontiers in Earth Science*, *9*, https://doi.org/10.3389/feart.2021.621976.

Russian Journal of Earth Sciences

Special Issue: "25th anniversary of the Russian Journal of Earth Sciences"

The Cyclostratigraphy of the Eastern Paratethys Konkian: Zelensky Section (Taman Peninsula)

Yu. V. Rostovtseva

Geophysical Center of the Russian Academy of Sciences (GC RAS), Moscow, Russia

* **Correspondence to:** Yuliana V. Rostovtseva, yurostovtseva@gcras.ru

Abstract: The Eastern Paratethys Konkian sedimentary succession of the Zelensky section (Taman peninsula, Russia) was investigated by cyclostratigraphy methods based on magnetic susceptibility measurements. Cyclostratigraphy is a new scientific direction in stratigraphy and sedimentology, the purpose of which is to identify astronomical cyclicity for the reconstruction geochronology using high-precision technologies. Time series analysis (Lomb-Scargle and REDFIT periodograms, wavelet) revealed statistically significant signals corresponding most likely to long-term insolation periodicities in studied sediments. In the deep-water Konkian sediments of the Zelensky section, the signal at 3.3 m corresponds to the 100-kyr eccentricity cycle. The astronomically tuned these sediments result in an average sedimentation rate of about 3.3 cm/kyr with the duration of accumulation of the Sartaganian and Veselyankian beds about 200 kyr. The obtained cyclostratigraphic results generally do not contradict the new data about the possible duration of the Konkian (Kartvelian, Sartaganian and Veselyankian beds) of about 750 kyr [*Palcu et al.*, 2017].

Keywords: Eastern Paratethys, Konkian, Taman peninsula, Zelensky section, cyclostratigraphy, magnetic susceptibility.

Citation: Rostovtseva Yu. V. (2024), The Cyclostratigraphy of the Eastern Paratethys Konkian: Zelensky Section (Taman Peninsula), *Russian Journal of Earth Sciences*, Vol. 24, ES1011, https://doi.org/10.2205/2024ES000900

Research Article

Received: 15 October 2024
Accepted: 15 January 2024
Published: 29 February 2024

1. Introduction

It is often the term cyclostratigraphy understood as a subdiscipline of stratigraphy that uses the cyclicity of sediments to subdivide and correlate sedimentary strata [*Gladenkov, Yu. B.*, 2004]. However, there are other interpretations of the term. According to [*Hilgen et al.*, 2012], cyclostratigraphy is a new scientific direction in stratigraphy and sedimentology, the purpose of which is to identify, characterize, correlate, and interpret cyclic changes in sedimentary successions, thereby reconstructing geochronology using high-precision technologies. In this case, the priority is the definition of astronomical cyclicity, globally appearing and reflected in the structure of sedimentary rocks. Analysis of the astronomical cyclicity primarily evaluates fluctuations in the Milankovitch cycles. These fluctuations in insolation significantly influence climate conditions, the variability of which is reflected in the action of different sedimentation factors, leading to the accumulation of sediments differing in lithology. The duration of the Milankovitch cycles can be different, depending on the orbital parameters, and vary from the first tens to hundreds of thousands of years, as well as amount to millions of years. One of the features of these cyclostratigraphic studies is the possibility to analyze also monotonic sedimentary successions, in which there is no clear alternation of different rock types. For these cyclostratigraphic studies, a generally accepted methodology has been developed [*Weedon*, 2003]. These cyclostatigraphic studies allow dating of rocks and estimation of sedimentation rates.

The Neogene sediments, including the Konkian rocks, of the Eastern Paratethys are much less studied by cyclostratigraphic methods. In this paper, the astronomical cyclicity of the Konkian sediments of the Eastern Paratethys (Zelensky section) will be considered, which is important when studying basins whose stratigraphy is based on complexes of endemic fauna, the regional correlation of which is difficult due to this.

2. Material and Methods

The objects of cyclostratigraphic studies were the Konkian sediments, which were exposed in the Zelensky section of the Taman Peninsula (Russia) (Figure 1). In the Zelensky section (N 45°13′54.6″; E 36°65′21.7″), Konkian deposits about 22–23 m thick are represented by clays containing separate interbeds of carbonate rocks (up to 0.2–0.3 m). According to the micropaleontological data, the studied sediments are divided into Kartvelian (about 16 m), Sartaganian (about 2–2.5 m), and Veselyankian (about 4–4.5 m) beds [*Palcu et al.*, 2017; *Vernigorova, Yu. V. et al.*, 2006]. The Konkian sediments of the Zelensky section accumulated in relatively deep-water environment [*Rostovtseva, Yu. V. et al.*, 2019]. According to the new data [*Palcu et al.*, 2017], the Konkian stage is distinguished in the volume of Kartvelian, Sartaganian and Veselyankian beds.

The cyclostratigraphic studies were based on measurements of rock magnetic susceptibility. The magnetic susceptibility was measured in situ with a "KT-5" portable magnetic susceptibility meter with a sensitivity of 10^{-5} SI units (Geofyzika BRNO, Czech Republic). Three measurements at each point were made every 20 cm across the strike of the layers. In total, 345 determinations have been obtained for Zelensky section. Average values of the magnetic susceptibility were obtained from three measurements made at each sampling point. These average data were taken as the basis for the statistical analysis. Furthermore, these average values were logarithmically transformed before the trend along the section was removed. For the statistics, the program PAST [*Hammer et al.*, 2001] was used for spectral analysis (Lomb–Scargle periodograms) including REDFIT [*Schulz and Mudelsee*, 2002] and wavelet analysis. The frequency values of the Lomb–Scargle and REDFIT periodograms were then transformed into the depth-domain to indicate the statistically relevant cycles.

The main mineral carrying of primary magnetization is magnetite in the Konkian sediments of Zelensky section [*Palcu et al.*, 2017].

According to paleomagnetic data, the studied Konkian sediments, including Kartvelian, Sartaganian, and Veselyankian beds, are characterized by the presence of three intervals of reversed and normal polarity [*Palcu et al.*, 2017] (Figure 2).

3. Results

The magnetic susceptibility (K) of the Zelensky section sediments varies from 0.060×10^{-3} to 0.240×10^{-3} SI (average 0.150×10^{-3} SI) (Figure 2). Spectral analysis of the magnetic susceptibility data from this section revealed the presence of two well-defined peaks. The REDFIT analysis supports the peak at 3.3 m, passing the 95% and 99% confidence interval, indicating the reliability of the orbitally calibrated record. Another peak at 14.3 m, passing through the 95% confidence interval, is observed on the REDFIT periodogram (Figure 3a). This peak is only 1.5 times smaller than the total thickness of the section, making its use less valid. The peak values were determined based on statistical processing of the magnetic susceptibility data both for the whole section and for the sediments of the Veselyankian and Sartaganian beds as well as the top of Kartvelian beds. The spectral analysis of the data from the lower part of Kartvelian beds did not reveal a strong periodicity.

In the lower part of Kartvelian beds, along with clays, there are microbial carbonate interlayers associated with the development of benthic cyanobacterial communities [*Rostovtseva, Yu. V. et al.*, 2019]. The Sartaganian and Veselyanskian beds contain separate carbonate interlayers consisting mainly of nannoplankton (coccolith). Different sedimentation regimes of microbial and nannoplanktonic carbonate rocks as well as clays may be reflected in the orbitally calibrated record, making interpretation difficult. Taking this into account, it is assumed that the data related to the upper part of the section (to the Sartaganian and Veselyankian beds) are the most validity to estimate the duration of accumulation of the studied sediments by cyclostratigraphic methods.

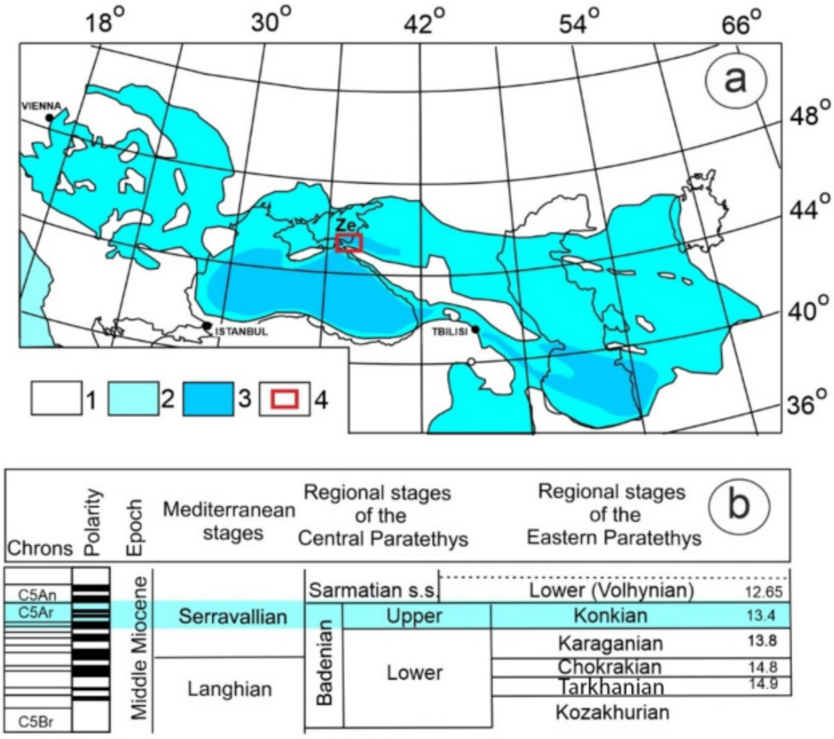

Figure 1. Paratethys during the last large marine transgression in the Middle Miocene (in the Konkian), modified after (*Studencka et al.*, 1998) (a) and scheme of correlation of the Paratethys Lower-Middle Miocene divisions with the Mediterranean stratigraphic scale (b). Land zones (1), shallow-water (2), deep-water (3), location of the study area (Ze – the Zelensky section) (4).

The repetitive signal is also clearly visible in the wavelet analysis for the sediments of the Veselyankian and Sartaganian beds as well as the top of Kartvelian beds (Figure 3b).

4. Discussion

Stratigraphy. One of the problems of stratigraphy of the Neogene of the Eastern Paratethys is the determination of the age of the Miocene and Pliocene regional stages boundaries, as well as the correlation of these regional stages with the Geologic Time Scale (GTS). The duration of the stratigraphic units, including the Konkian, are particularly debated. The Konkian rocks contain flora and fauna of complexes, indicating that these sediments accumulated during the connection the Eastern Paratethys with marine waters (the last large marine transgression in the Middle Miocene). Due to this, the study of the Konkian sediments is very importance.

According to [*Nevesskaja et al.*, 2004], the Konkian Regional Stage includes Sartaganian and Veselyankian beds, which reflect the stage-by-stage onset of marine transgression. According to other scientists [*Andrusov*, 1903; *Merklin*, 1953; *Palcu et al.*, 2017; *Popov et al.*, 2016], the Konkian Regional Stage should also include Pholadidae or Kartvelian beds, which some researchers consider as part of the Karaganian [*Nevesskaja et al.*, 2004] or propose to distinguish them as a separate regional stage [*Il'ina*, 2000; *Jgenti and Maissuradze*, 2016]. At the same time, there is an opinion that the established units of the Konkian Regional Stage are only facies types of sediments without a consistent stratigraphic position [*Belokrys*, 1987; *Vernyhorova*, 2017]. The presence of problems in stratigraphic division of Konkian sediments makes it difficult to select the necessary intervals of the section for cyclostratigraphic studies, as well as to provide regional correlations.

Based on the presence of mollusk fauna, microfauna, and nannoplankton of undivided NN6–NN7 zones, it is assumed that the Konkian regional stage of the Eastern Paratethys corresponds to the lower Serravallian of the Mediterranean and the upper Badenian (Kosovian) of the Central Paratethys [*Hilgen et al.*, 2012; *Popov et al.*, 2013]. There are no absolute

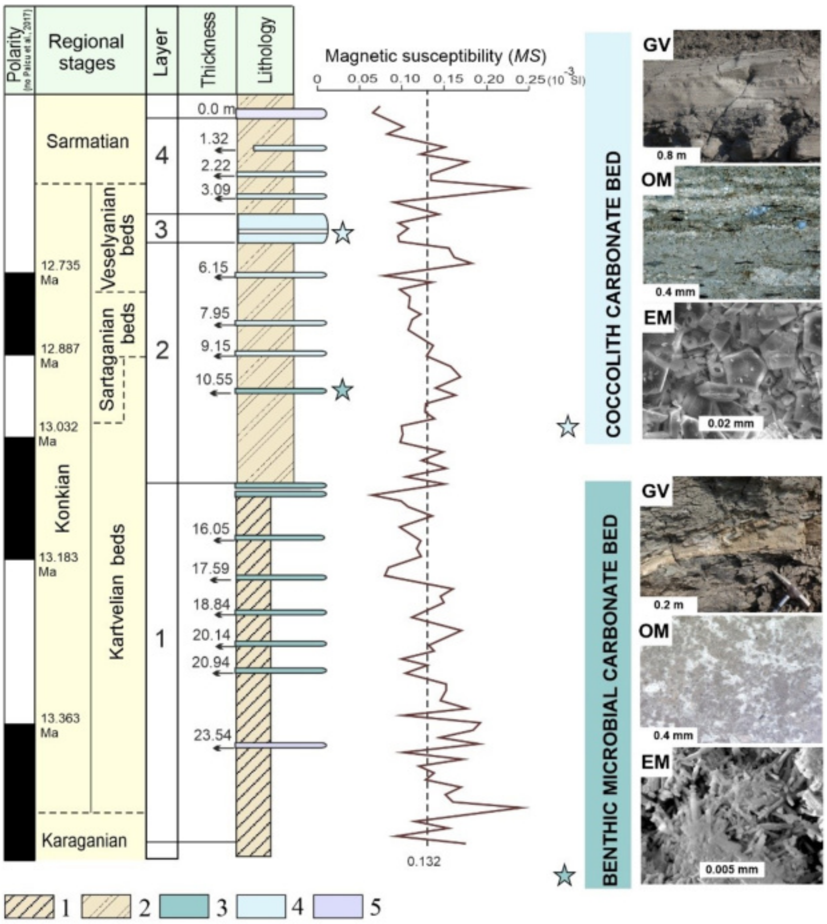

Figure 2. Lithological column, the results of the magnetic susceptibility (MS) measurements and main types of carbonate rocks of the studied Konkian sediments. Stratigraphic subdivision, polarity and possible age dating of rocks according to (*Palcu et al.*, 2017). 1–2 – weakly calcareous (1) and calcareous (2) clays; 3–5 carbonates: microbial (3), coccolith (4), and strongly dolomitized (5). Carbonate beds: general view (GV), in thin section (OM), under an electron microscope (EM).

dates of the Konkian deposits. It is proposed that the accumulation of the Konkian sediments could occur from 13.8–13.4 to 13.0–12.1 Ma [*Nevesskaja et al.*, 2004; *Palcu et al.*, 2017; *Popov et al.*, 2013]. The maximum estimates of this regional stage duration are no more than 1,7 Ma [*Hilgen et al.*, 2012; *Nevesskaja et al.*, 2004; *Popov et al.*, 2013]. According to new data [*Palcu et al.*, 2017], obtained on relatively deep-water middle Miocene sediments in the Zelensky section (Taman Peninsula), the upper and lower boundaries of the Konkian Regional Stage (including Veselyankian, Sartaganian or Kartvelian Beds) are dated to 12.65 and 13.4 Ma, respectively. It is believed that Veselyankian and Sartaganian beds generally correspond to the middle part of the C5Ar chrone (C5Ar.2n, C5Ar.2r, C5Ar.1n, and the lower C5Ar.1r); they accumulated within ~240 kyr (approximately from 12.89 to 12.65 Ma) with a sedimentation rate of approximately 2.2 cm/kyr. The Konkian sediments in the Eastern Paratethys, including the Kartvelian, Sartaganian, and Veselyankian beds, accumulated during ~750 kyr.

Astronomical forcing. The spectral analysis suggests the signals at 3.3 and 14.3 m, which very likely is an astronomical cyclicity imprint in studied sediments. The ratio between the observed periodicities is 1 : 4 (1 : 4.3), which correlates with long-term insolation variations associated with 24-kyr and 100-kyr cycles (precession and eccentricity). If the signal at 3.3 m corresponds to the 24-kyr precession cycle, the duration of accumulation of Sartaganian and Veselyanian beds with the total thickness of about 6–7 m is about 50 ka. In this case, the sedimentation rate was about 12–14 cm/1000 years. If we consider this

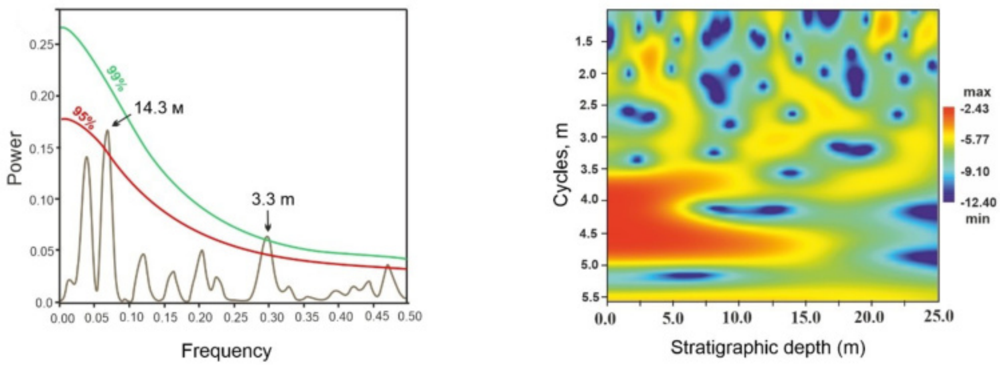

(a) (b)

Figure 3. REDFIT spectral analysis (a) and wavelet analysis (b) of the magnetic susceptibility data from Konkian sediments of Zelensky section (the Taman Peninsula).

signal as a record of 100-kyr eccentricity cycle, the Sartaganian and Veselyankian beds were deposited at an average rate of 3.3 cm/kyr for about 200 ka. In this case, the obtained values are well consistent with new published data [*Palcu et al.*, 2017]. However, it should be noted that these are rather low values of sedimentation regims, which are generally not typical for the intracontinental paleobasins. Apparently, this can be explained by the difference in the rates of accumulation of clayey and carbonate sediments, among which microbial calcareous layer might differ in a duration formation.

5. Conclusion

Based on spectral analysis and frequency-selective filtering of magnetic susceptibility data, the influence of astronomical cycles could be detected in Konkian sediments of the Zelensky section (Taman Peninsula, Russia). Spectral analysis revealed a likely 100-kyr eccentricity cycles.

The relatively deep-water Konkian sediments of the Zelensky section are characterized by low sedimentation rates (3.3 cm/kyr) and the presence of a record of astronomical cyclicity, possibly related to eccentricity changes in insolation.

According to the cyclostratigraphic results, the accumulation duration of the Sartaganian and Veselyanian beds in the Zelensky section is about 200 kyr.

If the Kartvelian, Sartaganian and Veselyanian beds are biofacies (not substage) in the Konkian sediments of the Eastern Black Sea region, these beds could have appeared in the Konkian at different times. In this case, the duration of accumulation of these beds may be different depending on the conditions of sedimentation in certain parts of the paleobasin. Considering these and other problems in the stratigraphy of the Konkian, the study of the astronomical cyclicity of these sediments should be continued on the example of other sections of the Eastern Paratethys.

The obtained cyclostratigraphic results generally do not contradict the new data about the possible duration of the Konkian (Kartvelian, Sartaganian and Veselyankian beds) of about 750 kyr [*Palcu et al.*, 2017].

Acknowledgments. This research was funded by budgetary funding of the Geophysical Center of RAS, adopted by the Ministry of Science and Higher Education of the Russian Federation (project 075-00764-22-00). Alena Rybkina and Alexsandra Rylova are thanked for their field support and fruitful discussions.

References

Andrusov, N. (1903), Geological research at the Taman Peninsula, *Materials for the Geology of Russia*, *21*(2), 257–383 (in Russian).

Belokrys, L. S. (1987), On the main criterion for the regional stratigraphic division of Miocene deposits from the Black Sea-Caspian basin, in *Collection Scientific Works: Stratigraphy of the Cenozoic of the Northern Black Sea and Crimea*, pp. 7–20, Dnepropetrovsk State University, Dnepropetrovsk (in Russian).

Gladenkov, Yu. B. (2004), *Biosphere stratigraphy (stratigraphic problems in the early XXI century)*, GEOS (in Russian), EDN: QKDTIX.

Hammer, O., D. A. T. Harper, and P. D. Ryan (2001), Past: paleontological statistics software package for education and data analysis, *Palaeontologia Electronica*, *4*(1), 1–9.

Hilgen, F. J., L. J. Lourens, J. A. Van Dam, A. G. Beu, A. F. Boyes, R. A. Cooper, W. Krijgsman, J. G. Ogg, W. E. Piller, and D. S. Wilson (2012), *The Neogene Period*, pp. 923–978, Elsevier, https://doi.org/10.1016/B978-0-444-59425-9.00029-9.

Il'ina, L. B. (2000), On the regional Konkian Stage (Middle Miocene) in the Eastern Paratethys, *Stratigraphy and Geological Correlation*, *8*(4), 372–377.

Jgenti, E. M., and L. S. Maissuradze (2016), *Karaganian, Kartvelian, and Konkian Regional Stages in Georgia: Evolution of Mollusks and Foraminifers and Their Stratigraphic Significance*, National museum of Georgia, Tbilisi (in Russian).

Merklin, R. L. (1953), Stages of development of the Konkian basin in the Miocene of the south of the USSR, *Bulletin of the Moscow Society of Naturalists*, *28*(3), 89–91 (in Russian).

Nevesskaja, L. A., E. I. Kovalenko, E. V. Beluzhenko, S. Popov, I. Goncharova, G. Danukalova, I. J. Zhidovinov, A. V. Zaitsev, A. S. Zaztrozhnov, L. B. Ilyina, T. Pinchuk, N. S. Pismennaya, A. Agadjanyan, A. V. Lopatin, and V. M. Trubikhin (2004), *Explanatory Note to the Unified Regional Stratigraphic Scheme of Neogene Deposits in the Southern European Part of Russia*, Paleontological Institute RAS, Moscow (in Russian).

Palcu, D. V., L. A. Golovina, Y. V. Vernyhorova, S. V. Popov, and W. Krijgsman (2017), Middle Miocene paleoenvironmental crises in Central Eurasia caused by changes in marine gateway configuration, *Global and Planetary Change*, *158*, 57–71, https://doi.org/10.1016/j.gloplacha.2017.09.013.

Popov, S. V., M. A. Akhmetiev, L. A. Golovina, I. A. Goncharova, E. P. Radionova, N. Yu. Filippova, and V. M. Trubichin (2013), Neogene Regiostage Stratigraphic Scale of the South Russia: Current State and Perspectives, in *General Stratigraphic Scale of Russia: Current State and Ways of Perfection. All-Russian conference. Moscow, May 23–25, 2013*, pp. 356–539, GIN RAS, Moscow (in Russian).

Popov, S. V., Yu. V. Rostovtseva, N. Y. Fillippova, L. A. Golovina, E. P. Radionova, I. A. Goncharova, Yu. V. Vernyhorova, N. I. Dykan, T. N. Pinchuk, L. B. Iljina, A. V. Koromyslova, T. M. Kozyrenko, I. A. Nikolaeva, and L. A. Viskova (2016), Paleontology and stratigraphy of the Middle-Upper Miocene of the Taman Peninsula: Part 1. Description of key sections and benthic fossil groups, *Paleontological Journal*, *50*(10), 1039–1206, https://doi.org/10.1134/S0031030116100014.

Rostovtseva, Yu. V., A. I. Rybkina, and A. Yu. Sokolova (2019), The Depositional Setting of the Konkian Sediments of the Taman Peninsula, *Moscow University Geology Bulletin*, *74*(1), 50–55, https://doi.org/10.3103/S0145875219010101.

Schulz, M., and M. Mudelsee (2002), REDFIT: estimating red-noise spectra directly from unevenly spaced paleoclimatic time series, *Computers & Geosciences*, *28*(3), 421–426, https://doi.org/10.1016/S0098-3004(01)00044-9.

Vernigorova, Yu. V., L. A. Golovina, and I. A. Goncharova (2006), On the characteristics of the Konkian deposits of the Taman Peninsula, *Biostratigraphic Criteria for Subdivision and Correlation of Phanerozoic Deposits of Ukraine*, pp. 231–242 (in Russian).

Vernyhorova, Y. V. (2017), Middle Miocene (Konkian of the Eastern Paratethys) foraminifera assemblages from the Southern Ukraine, in *7 th International Workshop "Neogene of Central and South Eastern Europe"*, https://doi.org/10.13140/RG.2.2.34298.90560.

Weedon, G. P. (2003), *Time-Series Analysis and Cyclostratigraphy: Examining Stratigraphic Records of Environmental Cycles*, Cambridge University Press, https://doi.org/10.1017/CBO9780511535482.

R of J E S

Russian Journal of Earth Sciences

Special Issue: “25th anniversary of the Russian Journal of Earth Sciences”

Мировые сейсмические сети и каталоги землетрясений

А. Д. Гвишиани[1,2], Б. В. Дзеранов[1,3,*], А. А. Скоркина[4], Б. А. Дзебоев[1,3]

[1]Геофизический центр Российской академии наук, г. Москва, Россия
[2]Институт физики Земли им. О.Ю. Шмидта Российской академии наук, г. Москва, Россия
[3]Геофизический институт Владикавказского научного центра Российской академии наук, г. Владикавказ, Россия
[4]Институт теории прогноза землетрясений и математической геофизики Российской академии наук, г. Москва, Россия
* **Контакт:** Б. В. Дзеранов, b.dzeranov@gcras.ru

Статья посвящена обзору функционирующих в настоящее время сейсмологических агентств, создаваемых, развиваемых и поддерживаемых ими сейсмических мониторинговых сетей, а также производимых каталогов землетрясений. Особое внимание сфокусировано на международных и национальных сейсмологических центрах и сейсмических сетях. Исторический экскурс о первых наблюдениях, выполняемых сейсмическими сетями, дополняет картину. Рассмотрены базовые параметры основных сейсмических сетей и принципы функционирования сейсмологических центров. Обсуждены ключевые характеристики сейсмических каталогов, определяющие критерии их качества. Приведен системно-аналитический подход к решению актуальной задачи создания наиболее полных и представительных каталогов землетрясений с унифицированной магнитудной шкалой путем интегрирования в изучаемом регионе воедино данных из международных, национальных и региональных каталогов.

Ключевые слова: сейсмические сети; сейсмологические агенства; каталоги землетрясений; представительная магнитуда; шкала магнитуд; полнота каталога, объединение каталогов землетрясений.

Цитирование: Гвишиани А. Д., Дзеранов Б. В., Скоркина А. А., Дзебоев Б. А. Мировые сейсмические сети и каталоги землетрясений // Russian Journal of Earth Sciences. — 2024. — Т. 24. — ES1012. — DOI: 10.2205/2024es000901

Введение

Каталоги землетрясений являются основным интегральным результатом сейсмического мониторинга. Они составляют основу для проведения большинства современных исследований, направленных на изучение сейсмического режима региона, построение оценок сейсмической опасности и сейсмического риска. Каталоги позволяют, в том числе, изучать и оценивать частоту возникновения сильных землетрясений в рассматриваемом сейсмоактивном регионе. Информация о расположении зон возможных очагов землетрясений (ВОЗ), являющаяся центральной при проведении работ по оценке сейсмической опасности, в значительной степени базируется на данных о произошедших ранее землетрясениях [*Wang*, 2010]. Таким образом, сейсмический мониторинг и формируемые на его базе каталоги землетрясений являются основополагающими компонентами современных сейсмологических исследований.

Первые прототипы современного регистрирующего сейсмического оборудования появились еще в конце XIX века [*Dewey and Byerly*, 1969]. Тем не менее, началом инструментальных сейсмологических наблюдений принято считать 1904–1906 годы, когда начали внедряться сейсмометры Вихерта и Голицына [*Agnew*, 2002; *Aki and Richards*, 2002]. Тогда же появились методы, позволяющие на записи «смещение-время» не просто

Получено: 15 октября 2023 г.
Принято: 15 января 2024 г.
Опубликовано: 29 февраля 2024 г.

идентифицировать землетрясение, но и определить его параметры и энергию [*Голицын*, 1912]. В 30-х годах XX века благодаря работам Ч. Рихтера основной мерой энергии землетрясения становится магнитуда [*Richter*, 1935].

Первые мониторинговые наблюдения, выполняемые сейсмическими сетями, были реализованы в Японии и Калифорнии в 20-е годы XX века [*Gutenberg*, 1932; *Wadati*, 1928]. Это позволило получить региональные зависимости амплитуд от расстояния [*Wadati*, 1928; 1931]. Изучение таких зависимостей по региональному каталогу землетрясений [*Gutenberg*, 1932] привело к повсеместному введению магнитуды [*Richter*, 1935].

У нас в стране идея создания первой сейсмической сети была высказана И. В. Мушкетовым в 1888 г. [*Minina*, 2019]. За ее создание взялся академик Б. Б. Голицын, с именем которого связано становление инструментальных сейсмологических наблюдений. В 1906 г. им был разработан электромагнитный сейсмограф, представляющий собой фундаментальную инновацию в сейсмометрии. Б. Б. Голицыным было предложено создание в России сейсмических станций двух классов: для регистрации удаленных (телесейсмических) и близких сильных (региональных) землетрясений [*Minina*, 2019].

Несмотря на стремительное увеличение количества сейсмических станций в мире начиная с 1904–1906 гг., две первые стандартизованные сети начали развиваться только в 1956–1958 гг. Это советская Единая сеть сейсмических наблюдений (ЕССН) [*Кондорская и Федорова*, 1996] и американская World-Wide Standardized Seismograph Network (WWSNN) [*Kisslinger and Howell*, 2003; *Oliver and Murphy*, 1971]. Целью их создания, в первую очередь, являлся взаимный контроль ядерных взрывов.

Первоначально сейсмические станции вели запись в аналоговом виде. С годами произошел, почти полностью, переход на цифровой формат регистрации. С развитием средств связи и передачи данных сейсмические сети перестали ограничиваться локальными масштабами. На сегодняшний день сейсмические сети могут быть как национальными или региональными, так и глобальными. Основное различие между ними заключается в масштабе исследования, пространственном разрешении, количестве, качестве и разнообразии получаемых данных и скорости их обработки [*Гвишиани и др.*, 2023; *Havskov and Alguacil*, 2004].

Настоящий обзор посвящен краткому представлению мировых сейсмических сетей и их сейсмологических центров, ведущих мониторинг и изучение землетрясений в планетарном масштабе. Иными словами, здесь идет речь о глобальных и крупных региональных сетях, получающих данные о землетрясениях всего земного шара для некоторого магнитудного порога. При этом, базовое финансирование этих сетей и их центров осуществляется отдельными странами или группами стран. К ним относятся Российская Федерация, Китайская Народная Республика, Соединенные Штаты Америки, Франция, Япония, Европейские страны, входящие в EMSC или ORFEUS. Отдельно следует здесь упомянуть Организацию Договора о всеобщем запрещении ядерных испытаний (CTBTO), являющуюся самостоятельной международной организацией.

1. Сейсмические сети и сейсмологические центры

На сегодняшний день самым крупным сейсмологическим центром в мире является IRIS (Incorporated Research Institutions for Seismology) — консорциум из более чем 125 университетов США. Центр ведет исследования в области сейсмического мониторинга и распространения сейсмологических данных. В IRIS поступают данные с более чем 8 тыс. сейсмических станций из всех стран мира (https://www.iris.edu) (дата обращения: 26.12.2023). В 2023 г. произошло слияние IRIS с UNAVCO (некоммерческий консорциум, созданный для расширения использования методов геодезии в геологических исследованиях). Образованная в результате объединения организация называется Консорциум EarthScope.

Говоря о других наиболее крупных и важных мировых сейсмических сетях, необходимо упомянуть сеть американской Геологической службы USGS (The United States Geological Survey). В ее состав входят: Глобальная сейсмографическая сеть GSN (Global

Seismographic Network), Передовая национальная сейсмическая система ANSS (Advanced National Seismic System) и Национальный центр информации о землетрясениях NEIC (The National Earthquake Information Center).

Отметим также европейскую сеть ORFEUS (Observatories and Research Facilities for European Seismology), французскую глобальную сеть широкополосных сейсмологических станций GEOSCOPE (French Global Network of Seismological Broadband Stations), сеть японского метеорологического агентства JMA (Japan Meteorological Agency), китайский центр сейсмических сетей CENC (China Earthquake Networks Center), сеть Единой геофизической службы Российской академии наук (ФИЦ ЕГС РАН), а также сеть Организации Договора о всеобъемлющем запрещении ядерных испытаний CTBTO (The Comprehensive Nuclear-Test-Ban Treaty Organization).

Приведем базовые характеристики основных сейсмических сетей и сейсмологических центров.

(1.1) Единая геофизическая служба Российской академии наук (ФИЦ ЕГС РАН, http://www.ceme.gsras.ru/new/ssd_news.htm) является базовой организацией, осуществляющей сейсмический мониторинг на территории Российской Федерации. Она является преемницей первой стандартизованной сейсмической сети в мире — ЕССН (Единая система сейсмических наблюдений СССР). Датой ее образования считается 4 января 1963 г., когда в г. Обнинске была создана Центральная геофизическая обсерватория (ЦГО) «Москва» Института физики Земли им. О. Ю. Шмидта АН СССР.

В настоящее время ФИЦ ЕГС РАН имеет иерархическую структуру и включает в себя следующие филиалы:

- Центральное отделение, г. Обнинск (68 станций), код сети OBGSR;
- Лаборатория сейсмического мониторинга Воронежского кристаллического массива, г. Воронеж (11 станций), код сети OBGSR: VMGSR;
- Алтае-Саянский филиал, г. Новосибирск (89 станций), код сети ASGSR;
- Камчатский филиал, г. Петропавловск-Камчатский (97 станций), код сети KAGSR;
- Сахалинский филиал, г. Южно-Сахалинск (59 станций), код сети SAGSR;
- Магаданский филиал, г. Магадан (16 станций), код сети NEGSR;
- Дагестанский филиал, г. Махачкала (17 станций), код сети DAGSR;
- Северо-Осетинский филиал, г. Владикавказ (13 станций), код сети NOGSR;
- Кольский филиал, г. Апатиты (9 станций), код сети KOGSR;
- Байкальский филиал, г. Иркутск (51 станция), код сети BAGSR;
- Якутский филиал, г. Якутск (23 станции), код сети YAGSR;
- Бурятский филиал, г. Улан-Удэ (9 станций), код сети BUGSR.

Отметим, что ФИЦ ЕГС РАН тесно сотрудничает и использует данные ряда сейсмологических центров, функционирующих на базе российских научных организаций:

- Горный институт Уральского отделения РАН, г. Пермь (5 станций), код сети MIRAS;
- Архангельская сейсмическая сеть, г. Архангельск (8 станций), код сети FCIAR;
- Институт динамики геосфер РАН, г. Москва (4 станции), код сети IDG.

Схема расположения станций ФИЦ ЕГС РАН показана на рис. 1.

ФИЦ ЕГС РАН ведет фундаментальные научные и прикладные исследования в области сейсмологии и других смежных разделов геофизики. Совместно с Росгидрометом РФ выполняются исследования, направленные на предупреждение о цунами на Дальнем Востоке. В рамках Договора о всеобъемлющем запрещении ядерных испытаний (CTBTO) обеспечивается функционирование 9 сейсмических станций международной системы мониторинга, осуществляется мониторинг вулканической активности на Камчатке, и др.

Результаты сейсмического мониторинга, выполняемого ФИЦ ЕГС РАН, ежегодно публикуются в сборниках «Землетрясения Северной Евразии» (http://www.gsras.ru/zse) [*ФИЦ ЕГС РАН*, 2023b] и «Землетрясения в России» (http://eqru.gsras.ru) [*ФИЦ ЕГС РАН*, 2023a]. Следует отметить, что сейсмичность Российской Федерации в этих

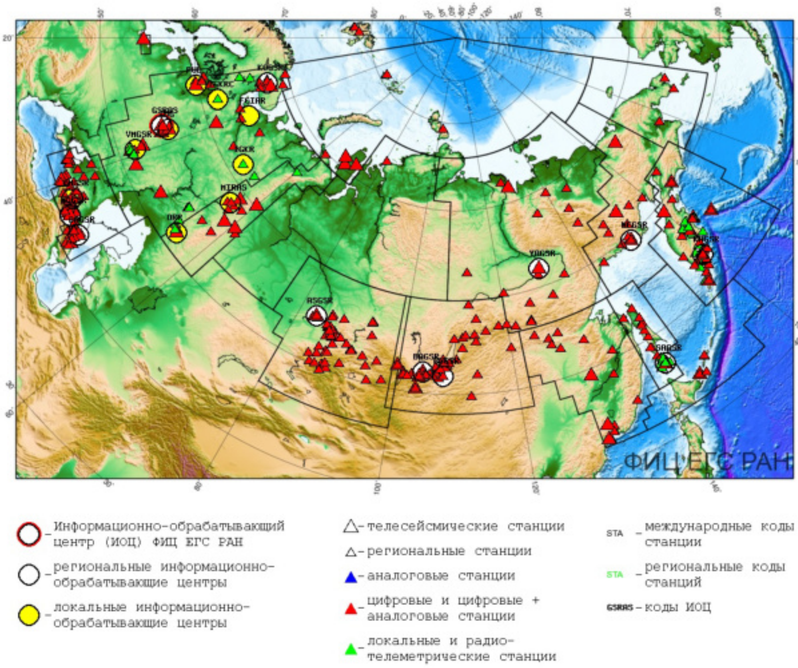

Рис. 1. Расположение сейсмических станций ФИЦ ЕГС РАН (http://eqru.gsras.ru/index.php?inc=main, дата обращения: 26.12.2023).

сборниках представлена в виде набора следующих отдельных каталогов, с перекрывающимися зонами ответственности региональных филиалов:

– Северный Кавказ;
– Восточно-Европейская платформа, Урал и Западная Сибирь;
– Арктика;
– Алтай и Саяны;
– Прибайкалье и Забайкалье;
– Приамурье и Приморье, Сахалин и Курило-Охотский регион;
– Якутия;
– Северо-Восток России и Чукотка;
– Камчатка и Командорские острова.

Такое разбиение обусловлено преемственностью деления территории СССР на XIV подрегионов на основе генеральной сейсмотектонической общности, принятой при составлении [*Новый каталог сильных землетрясений на территории СССР с древнейших времен до 1975 г.* 1977] выдающимися советскими сейсмологами Н. В. Кондорской и Н. В. Шебалиным. Необходимо отметить, что в советский период при составлении ежегодников «Землетрясения в СССР» использовалось еще более подробное деление на регионы.

На сайте ФИЦ ЕГС РАН (http://www.gsras.ru/new/ssd_news.htm) ведется оперативное информирование о произошедших землетрясениях, а также организован онлайн доступ к сейсмическим каталогам и волновым формам.

(1.2.1) Глобальная сейсмографическая сеть (Global Seismographic Network (GSN), https://www.usgs.gov/programs/earthquake-hazards/gsn-global-seismographic-network) — постоянно действующая сеть современных цифровых сейсмических станций, соединенных телекоммуникационной сетью, служащая многоцелевым научным центром и социальным ресурсом для целей мониторинга. Сеть является глобальной преемницей одной из первых стандартизованных сетей WWSNN и состоит из 150 сейсмических станций (рис. 2), относительно равномерно покрывающих поверхность Земли. Отметим, что 12 станций расположены на территории России и обслуживаются ФИЦ ЕГС РАН.

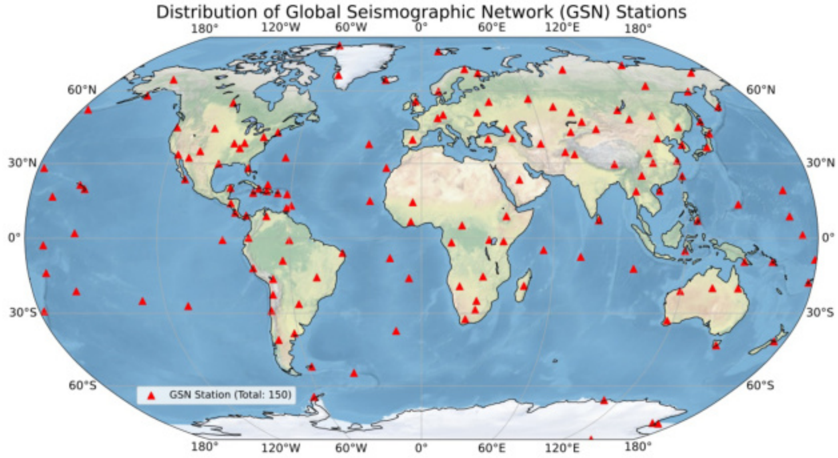

Рис. 2. Расположение сейсмических станций сети GSN (https://www.usgs.gov/programs/earthquake-hazards/gsn-global-seismographic-network, дата обращения: 26.12.2023).

Доступ к данным сети GSN можно получить на сайте IRIS. В рамках IRIS на долю GSN приходится относительно небольшой объем данных, но глобально распределенная сеть широкополосных сейсмоприемников с низким уровнем шума делает эти данные ценными. Количество станций в GSN остается относительно постоянным в течение долгого времени. Это позволяет сосредоточиться на улучшении качества существующих станций [*Ringler et al.*, 2019].

(1.2.2) Передовая национальная сейсмическая система (Advanced National Seismic System (ANSS), https://www.usgs.gov/programs/earthquake-hazards/anss-advanced-national-seismic-system) была учреждена Геологической службой США (USGS) в 2000 г. На данный момент она является основной организацией, занимающейся координацией сейсмологических исследований, а также сейсмическим мониторингом в США. В рамках своей мониторинговой деятельности ANSS включает в себя Национальную сейсмическую сеть, Национальный центр информации о землетрясениях (NEIC), Национальный проект сильных движений и 15 региональных сейсмических сетей, управляемых USGS и ее партнерами [*U.S. Geological Survey*, 2017]. Большая часть станций ANSS оснащена одновременно широкополосными сейсмометрами и сейсмометрами сильных движений. Региональные сети состоят из плотно расположенных станций в сейсмоактивных районах для регистрации достаточно слабых землетрясений и повышения точности определения их характеристик.

По результатам своей деятельности ANSS формирует комплексный каталог ANSS Comprehensive Catalog (ComCat). Он содержит параметры очагов землетрясений и другую информацию, полученную от сетей, входящих в ANSS. Каталог ComCat также интегрирует информацию о параметрах очагов землетрясений из каталогов Centennial Catalog и Global Centroid Moment Tensor Catalog. Новые и обновленные данные добавляются в каталог динамически по мере того, как источники публикуют или обновляют продукты. Доступ к ComCat осуществляется через страницу онлайн-поиска (https://earthquake.usgs.gov/data/comcat), на которой пользователь может выбрать интересующие его землетрясения по широкому спектру критериев.

(1.2.3) Национальный центр информации о землетрясениях (National Earthquake Information Center (NEIC), https://www.usgs.gov/programs/earthquake-hazards/national-earthquake-information-center-neic), расположенный в городе Голден, штат Колорадо (США), создан в 1966 г. в составе USGS. В рамках своей деятельности NEIC решает три основные задачи:

– Максимально быстрое и возможно точное определение координат эпицентра и магнитуды всех значительных землетрясений, происходящих в мире. NEIC оперативно распространяет эту информацию среди заинтересованных национальных и международных агентств, исследователей и широкой общественности.

– Сбор и предоставление ученым и общественности обширной базы сейсмических данных для научных исследований. NEIC является национальным центром данных и архивом информации о землетрясениях.
– Проведение исследовательской работы по улучшению возможностей регистрации землетрясений и пониманию механизма землетрясений [*Benz*, 2017].

(1.3.1) Европейско-Средиземноморский сейсмологический центр (Euro-Mediterranean Seismological Centre (EMSC), https://www.emsc-csem.org) основан в 1975 г. Европейской сейсмологической комиссией (ESC). Он представляет собой некоммерческую организацию, объединяющую 84 института из 55 стран мира. Россию в организации представляет ФИЦ ЕГС РАН. В 1987 г. Совет Европы наделил EMSC полномочиями основной организации, обеспечивающей Европейскую систему оповещения по основным опасностям (https://www.emsc-csem.org/#2, дата обращения: 26.12.2023). EMSC формирует каталоги, пользуясь данными ORFEUS, накапливаемыми в настоящее время в GFZ Potsdam. К данным организован удаленный доступ с помощью пакета ObsPy [*Beyreuther et al.*, 2010]. Последнее дает возможность строить унифицированные модели сейсмичности для территории Европы [*Kotha et al.*, 2020], покрытой несколькими десятками отдельных сетей [*Cauzzi et al.*, 2021].

(1.3.2) Французская глобальная сеть широкополосных сейсмологических станций (French Global Network of broad band seismic stations (GEOSCOPE), http://geoscope.ipgp.fr) — созданная в 1982 г. сеть из 35 широкополосных сейсмических станций для решения задачи глобального инструментального мониторинга (рис. 3). Станции работают непрерывно и передают данные в режиме реального времени, что позволяет использовать их, в том числе, центрами оповещения о цунами. Данные большинства станций поступают в центр данных Парижского института физики Земли и архивируются после проверки [*Roult et al.*, 2013]. GEOSCOPE предоставляет данные и информацию о землетрясениях, произошедших в мире, с магнитудой более 5.5–6.0. Аналогичная информация может быть предоставлена для более слабых землетрясений, например, произошедших во Франции или в европейско-средиземноморском регионе. На сайте GEOSCOPE можно получить доступ к каталогам землетрясений начиная с 2006 г.

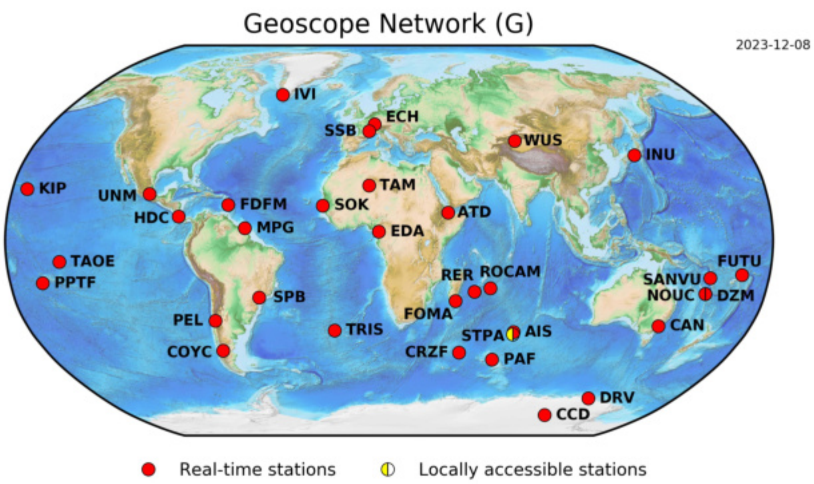

Рис. 3. Расположение широкополосных станций глобальной сети GEOSCOPE (http://geoscope.ipgp.fr, дата обращения: 26.12.2023).

(1.4) Сети сейсмического мониторинга Японии. Высокая сейсмическая активность Японии обусловила значительную плотность сетей сейсмического мониторинга, их разнообразие и высокую степень аппаратной оснащенности. Дополнительный импульс развитию сетей придали разрушительные землетрясения, произошедшие в Кобе в 1995 г.

и Тохоку в 2011 г. [*Ozawa et al.*, 2011]. Оба события были классифицированы как природные катастрофы, принесшие убытки порядка нескольких сотен миллиардов долларов. Организацией и обслуживанием сетей сейсмических наблюдений на территории Японии занимается Национальный исследовательский институт наук о Земле и устойчивости к стихийным бедствиям (National Research Institute for Earth Science and Disaster Resilience (NIED), https://www.bosai.go.jp/e). В число японских сейсмических сетей входят: K-NET, KiK-net, Hi-net и F-net [*Aoi et al.*, 2020]. Кроме того, создана сеть V-net для мониторинга вулканической активности. После землетрясения Тохоку 2011 г. на дне океана были развернуты сети S-net и DONET для оперативной регистрации подводных землетрясений и связанных с ними цунами [*Aoi et al.*, 2020].

В целях раннего предупреждения о землетрясениях и цунами сейсмические данные передаются в режиме реального времени в Японское метеорологическое агентство (Japan Meteorological Agency (JMA), https://www.jma.go.jp/jma/indexe.html). Следует отметить, что JMA создает и развивает как свои сейсмические сети, так и участвует в развитии указанных выше сетей. JMA играет важную роль в предоставлении странам северо-западной части Тихоокеанского региона прогнозной информации о цунами.

(1.4.1) K-NET (Kyoshin Network, https://www.kyoshin.bosai.go.jp/kyoshin/docs/overview_kyoshin_index_en.html**)** — общенациональная сеть мониторинга сильных движений, состоящая из более чем 1000 сейсмических станций, равномерно покрывающих территорию Японию через каждые 20 км. Сеть K-NET функционирует с июня 1996 года.

(1.4.2) KiK-net (Kiban Kyoshin Network https://www.kyoshin.bosai.go.jp/kyoshin/docs/overview_kyoshin_index_en.html**)** — сеть мониторинга сильных движений, состоящая из пар сейсмографов, установленных на поверхности земли и в скважине вместе с сейсмометрами высокой чувствительности (Hi-net). Такие пары приборов установлены примерно в 700 пунктах по территории всей Японии.

(1.4.3) Hi-net (https://www.hinet.bosai.go.jp/summary) — сеть высокочувствительных сейсмографов для мониторинга микроземлетрясений, состоящая из почти 800 станций со средним расстоянием между ними 20 км. Сейсмометры установлены в забое скважин на глубине 100–3500 м для снижения шума, создаваемого ветром, морскими волнами и деятельностью человека.

(1.4.4) F-net (https://www.fnet.bosai.go.jp) — сеть из 70 широкополосных станций, предназначенная для оперативного определения характеристик землетрясений. Сейсмометры устанавливаются в глубине штольни, где температура и давление стабильны. Это позволяет измерять колебания грунта в широком диапазоне частот. Записи сети позволяют получать информацию о механизмах очагов землетрясений и структуре Земли.

(1.4.5) V-net (https://www.vnet.bosai.go.jp) — сеть наблюдений за 16 вулканами с целью разработки прогнозов извержений и смягчения рисков от вулканической опасности. Пункты наблюдения оборудованы несколькими типами приборов, в том числе, скважинными сейсмометрами, скважинными наклономерами, GPS приемниками и широкополосными сейсмометрами.

(1.4.6) S-net (https://www.seafloor.bosai.go.jp) — сеть наблюдений за дном океана, состоящая из 150 пунктов наблюдения, расположенных от острова Хоккайдо до префектуры Тиба. Каждый пункт оборудован сейсмометрами и датчиками давления воды для наблюдения за подводными землетрясениями и цунами. Регистрируемые данные передаются на наземные станции по оптоволоконному кабелю и поступают в NIED в режиме реального времени.

(1.4.7) DONET (https://www.seafloor.bosai.go.jp) — сеть наблюдений за дном океана, состоящая из 51 станции у г. Куманонада и пролива Кии. На станциях установлен широкий спектр приборов для мониторинга землетрясений и цунами. Сеть спроектирована так, чтобы ее можно было легко расширить, заменить или добавить станции и приборы. Данные передаются в исследовательские институты и университеты в режиме реального времени.

Измерения в режиме реального времени с помощью сетей наблюдения за дном океана S-net и DONET увеличивают заблаговременность предупреждений о подводных землетрясениях и предоставляют оперативную и точную информацию о цунами.

(1.5) Центр сейсмических сетей Китая (The China Earthquake Networks Center (CENC), https://www.cenc.ac.cn) основан 18 октября 2004 г. CENC наделен полномочиями оперативного руководства и управления национальной сейсмической сетью Китая CSN (Chinese Seismic Network). Сегодня CSN состоит из сейсмографической сети, сети сильных движений и инженерно-сейсмометрической сети — всего 4082 станции (рис. 4). Отметим, что сейсмографическая сеть охватывает всю континентальную часть Китая, а две другие сети расположены в сейсмоопасных зонах. Все станции Китая обслуживаются 31-м региональным центром, функционирующими под управлением CENC [*Dai and An*, 2020].

Рис. 4. Расположение станций сети CSN [*Dai and An*, 2020]. Красным обозначены сейсмографические станции, черным — станции сильных движений, зеленым — станции инженерно-сейсмометрической сети.

(1.5.1) Сейсмографическая сеть (The Seismographic Network) насчитывает 1107 станций, в том числе 166 национальных и 941 региональную. Национальные станции в основном оснащены 120-секундными сверхширокополосными сейсмометрами (некоторые станции имеют сверхширокополосные 360-секундные сейсмометры), которые используются для мониторинга глобальной сейсмичности. На региональных станциях преимущественно установлены широкополосные сейсмометры 60-х годов для мониторинга региональной сейсмической активности. Различия в плотности расположения станций в разных регионах Китая связаны со степенью экономического развития и плотностью населения. Этим объясняется более плотное размещение станций на востоке Китая по сравнению с его западной частью. Данные от станций в реальном времени передаются в CENC через региональные центры.

(1.5.2) Сеть сильных движений (The Strong Motion Network) состоит из 1965 станций, оснащенных акселерометрами (2g) для регистрации ускорений в ближней зоне. При этом, только 393 станций передают данные в CENC в режиме реального времени через сетевой центр.

(1.5.3) Сеть инструментов интенсивности (The Intensity Instrument Network) состоит из 1010 станций, распределенных по территориям шести провинций: Пекин, Тяньцзинь, Хэбэй, Сычуань, Юньнань и Фуцзян. В сочетании со станциями других сетей Китая они используются для оперативного оповещения об интенсивности и тестирования раннего предупреждения о землетрясениях. Чтобы улучшить возможности мониторинга сильных землетрясений в приграничных районах Китая и во всем мире в режиме, близком к реальному, CENC обменивается сейсмическими данными с глобальной сейсмографической сетью GSN. Отметим, что кроме этого, CENC обменивается данными с Корейской метеорологической администрацией (Korea Meteorological Administration (KMA), https://www.kma.go.kr/neng). При возникновении землетрясения магнитудой выше 5,0 CENC отправляет данные волновых форм с 20 национальных станций на FTP-сервер IRIS.

(1.6) Организация Договора о всеобъемлющем запрещении ядерных испытаний (Comprehensive Nuclear-Test-Ban Treaty Organization (CTBTO), https://www.ctbto.org*)* основана в 1996 г. и включает 50 основных и 120 вспомогательных сейсмических станций, расположенных по всему миру. Как было отмечено выше, на территории России расположены 9 станций CTBTO, обслуживаемых ФИЦ ЕГС РАН. Отметим, что система мониторинга также включает 11 гидроакустических, 60 инфразвуковых и 80 радионуклидных станций (рис. 5). Станции сети CTBTO регистрируют данные, которые передаются для анализа в международный центр обработки данных в Вене. Результаты анализа отправляются государствам-участникам Организации [*Coyne et al.*, 2012].

Рис. 5. Схема международной системы мониторинга CTBTO (https://www.ctbto.org/our-work/ims-map, дата обращения: 26.12.2023).

2. Сейсмологические агентства и проекты планетарного масштаба

Кроме регулярных сейсмических сетей существуют сейсмологические агентства и проекты, которые, не обладая собственными сетями, агрегируют и обрабатывают данные других сетей и создают соответствующие каталоги и бюллетени землетрясений. К перечню таковых в первую очередь необходимо отнести Международный сейсмологический центр (ISC), The Global Centroid-Moment-Tensor (GCMT) и SCARDEC.

Международный сейсмологический центр (The International Seismological Centre (ISC), http://www.isc.ac.uk*)* основан в 1964 г. как независимая международная организация, в которую входят многие страны, включая Российскую Федерацию. Организации, представляющие страны-участницы в ISC, ежегодно платят членские взносы. ISC было создано при содействии ЮНЕСКО в качестве преемника ISS (International Seismological Summary). Целью ISC является сбор, архивирование и обработка сейсмических данных, бюллетеней станций и сетей. ISC осуществляет подготовку и распространение бюллетеня с непрерывной окончательной сводкой сейсмичности в мире. Данные ISC обладают высокой степенью достоверности, но поступают с большим запаздыванием. Бюллетень базируется на информации, поступающей от более 130 сейсмических сетей и центров данных, расположенных по всему миру. Кроме того, ISC совместно с NEIC/USGS ведет международный реестр сейсмических станций. Совместно с IASPEI (Международная ассоциация сейсмологии и физики недр Земли, http://www.iaspei.org) в ISC ведется справочный список событий, включающий информацию о 12 090 землетрясениях и взрывах (с записями волновых форм на региональных и/или телесейсмических расстояниях), зарегистрированных с высокой точностью с 1959 по 2020 гг.

В течение почти 50 лет данные ISC являются общепринятым окончательным источником сейсмологической информации. Они используются учеными во всем мире для оценки сейсмической опасности, тектонических исследований и построения глобальных и региональных томографических и других геофизических моделей. Бюллетень ISC лежит в основе таких хорошо известных продуктов, как глобальная одномерная скоростная модель ak135 [*Kennett and Engdahl*, 1991; *Kennett et al.*, 1995], а также каталоги EHB [*Engdahl et al.*, 2020; *International Seismological Centre*, nodate; *Weston et al.*, 2018] и Centennial [*Engdahl and Villaseñor*, 2002]. Источник данных ISC представляет собой важный критерий контроля качества для СТВТО. Кроме того, он является базой для построения глобальной модели риска землетрясений (GEM) [*Storchak et al.*, 2015].

Глобальный тензор центроид-моментов (The Global Centroid-Moment-Tensor (GCMT), www.globalcmt.org***)*** — проект, основанный в Гарвардском университете США в 1982 г. До 2006 г. он назывался Гарвардский проект CMT. В 2006 г. деятельность проекта CMT переместилась в Колумбийский университет Нью-Йорка. С этого времени исследовательская работа продвигается под названием The Global Centroid-Moment-Tensor. Проект CMT финансируется Национальным научным фондом США [*Woodhouse and Deuss*, 2015].

Каталог GCMT является важным источником информации, обобщающим глобальные сейсмические процессы за последние 40 лет. Создание каталога GCMT было трудоемкой работой, занявшей несколько десятилетий и позволившей получить высококачественный ресурс о размерах и ориентации очагов землетрясений. Определение механизма CMT в настоящее время осуществляется для всех землетрясений с $Mw \geqslant 5{,}0$. В каталогах землетрясений магнитуды, рассчитанные GCMT, имеют соответствующий индекс в обозначении. На сегодняшний день каталог GCMT включает данные о параметрах более 40 000 землетрясений [*Woodhouse and Deuss*, 2015].

База данных временных очаговых функций (Source Time Functions Database (SCARDEC), http://scardec.projects.sismo.ipgp.fr***)*** — веб-ресурс, содержащий: определения сейсмического момента, моментной магнитуды, механизма очага и временной функции очага для сильных землетрясений. Расчеты произведены с помощью одноименного метода (SCARDEC), основанного на деконволюции объемных волн [*Vallée et al.*, 2010]. Вариант автоматизации методики был предложен в 2011 г. [*Vallée et al.*, 2010] и в настоящее время применяется рутинно ко всем землетрясениям магнитудой выше 5,8, содержащимся в каталоге NEIC-PDE с 1992 г. База данных постоянно обновляется и пополняется на сервере Парижского института физики Земли (IPGP). Данные, начиная с 2014 года, можно визуализировать на веб-сайте GEOSCOPE.

Основной целью применения методики SCARDEC является оперативное получение более точных оценок моментных магнитуд, особенно для поверхностных сильных землетрясений (с $Mw > 7{,}0$–$7{,}5$, в том числе потенциально цунамигенных). Известно, что для таких землетрясений становится существенным вклад очагового процесса, а сам очаг не может быть представлен точечным источником (каким очаг землетрясения представляется в методе GCMT). Таким образом, в отличии от GCMT, в методе SCARDEC временная функция очага (производная сейсмического момента по времени) определяется, а не фиксируется. Это позволяет, в том числе, получить первые оценки того, насколько стремительно и равномерно развивался очаговый процесс во времени.

Оценки моментных магнитуд SCARDEC могут отличаться от оценок GCMT на −0.2 магнитудных единиц.

3. Каталоги землетрясений, их параметры и характеристики

Современное увеличение количества сейсмических станций привело к необходимости модернизации процесса обработки сейсмических данных. Первоначально, в эпоху установки одиночных станций (первые десятилетия XX века), основным результатом являлся бюллетень, который включал в себя информацию о типе сейсмических фаз, наблюдаемых на записи, и их параметрах: времена вступления, четкость вступления, знак вступления, амплитуда, период. В это время весьма распространенным методом определения местоположения землетрясения являлся «метод определения по одной станции». Однако достаточно скоро пришло понимание, что бюллетени с разных станций должны анализироваться совместно, что реализовал Дж. Милн, положив начало Международному сейсмологическому бюллетеню (International Seismological Summary, 1899–1912), правоприемником которого принято считать Международный сейсмологический центр.

В настоящее время обработка сейсмических данных осуществляется только по сети станций (региональной или глобальной), что позволило улучшить точность определения гипоцентра, а главное, автоматизировать сам процесс обработки. С другой стороны, стоит отметить, что существенно сократился объем сохраняемой информации с индивидуальных записей, как, например, качество вступления, тип фазы (первые вступления P не всегда интерпретируются как Pn, Pg), количество телесейсмических фаз и т. д. Распространенные ранее бюллетени сейчас часто сменяют каталоги землетрясений, которые выпускают сейсмологические агентства, полученные по разному набору исходных данных. В целом можно сказать, что современные алгоритмы обработки сейсмологических данных являются гибкими и не унифицированными, продолжают модернизироваться, а вместе с этим будет продолжать варьироваться и качество итогового результата — бюллетеня и/или каталога, соответственно.

Отметим, что качество каталога землетрясений зависит от таких функциональных характеристик регистрирующей сети и различных параметров, как: особенности регистрирующего оборудования, апертура сейсмической сети, процедуры локации (в том числе, скоростная модель) и определения магнитуд (в том числе, модель затухания сейсмических волн) и др. Все это, включая неоднородность времени регистрации сейсмических сетей, является причиной наблюдаемых отличий в данных о землетрясениях, представленных в различных каталогах.

Одной из центральных характеристик каталогов землетрясений является магнитуда представительной регистрации (представительная магнитуда) Mc [*Mignan et al.*, 2011]. Магнитуда Mc представляет собой минимальную магнитуду, выше которой надежно регистрируются все землетрясения для заданной пространственно-временной области [*Mignan and Woessner*, 2012]. Она является ключевым параметром, отражающим эффективность сейсмической сети, т. е. ее регистрирующих возможностей. Для анализа каталога строят график повторяемости землетрясений [*Wiemer*, 2000]. На нем значение Mc будет соответствовать началу его линейной части [*Vorobieva et al.*, 2013]. По наклону графика повторяемости (b-value) делается вывод об уровне сейсмичности региона. Чем больше значение параметра b, тем больше пропорция землетрясений малых магнитуд относительно больших.

Другой, часто проблемной, важной характеристикой каталогов землетрясений является шкала магнитуд. Она различается видом сейсмической волны, использованной для ее расчета.

Идея логарифмической шкалы магнитуд землетрясений была впервые предложена еще Чарльзом Рихтером в 1930-х годах для оценки силы землетрясений, происходящих в Южной Калифорнии [*Richter*, 1935]. Оценка магнитуды производилась с использованием относительно высокочастотных данных с близлежащих сейсмических станций. Такая шкала обозначалась M_L, где L маркирует локальную магнитуду. Впоследствии ее стали называть шкалой Рихтера, или локальной (региональной) магнитудой. С развитием сейсмических сетей стало очевидно, что разработанная Рихтером шкала магнитуд действительна только для определенных диапазонов магнитуд и расстояний [*Richter*, 1935].

В число наиболее распространенных в настоящее время типов магнитуд, определяемых ведущими мировыми сейсмическими агентствами, входят введенные Бено Гутенбергом в 1945 г. [*Gutenberg*, 1945]:

– Ms — магнитуда по поверхностным волнам Релея и Лява;
– mb — магнитуда по объемным волнам.

Необходимо отметить, что в своих работах Гутенберг первоначально стыковал шкалы Ms и mb с M_L так, чтобы при $M_L = 5{,}0$, Ms и mb также были равны 5,0. Так реализовывалась идея привести региональные и телесейсмические магнитуды к единой шкале. Однако было обнаружено, что шкалы по-разному характеризуют разные диапазоны магнитуд.

– Mw — моментная магнитуда, предложена Хиро Канамори в 1977 г. Она основана на сейсмическом моменте землетрясения. Mw наиболее тесно связана с энергией, выделившейся при землетрясении, и дает более надежные оценки для очень сильных землетрясений [*Kanamori*, 1977].

В первые годы после введения магнитуды Mw появились надежды, что она станет универсальной магнитудной шкалой. Однако, результаты последних исследований [*Di Giacomo et al.*, 2021] показывают, что широкое применение Mw все еще не позволило на всем диапазоне магнитуд перейти к однородной универсальной магнитудной шкале, базирующейся на Mw.

В СССР была широко распространена оценка энергетического класса землетрясения — K, предложенная в 1964 Т. Г. Раутиан как десятичный логарифм энергии, высвободившейся при землетрясении. Энергетический класс является удобным параметром для слабых и средних землетрясений и может легко быть пересчитан в магнитуду с помощью соответствующих формул [*Rautian et al.*, 2007]. Оценка силы землетрясений в энергетических классах до сих пор проводится на территории России и в постсоветском пространстве.

Планировалось, что оценка энергетического класса станет физическим параметром вместо безразмерной оценки магнитуды. Однако в [*Абубакиров и др.*, 2018] было показано, что, несмотря на тесную связь с физическим параметром (энергией сейсмических волн), оценки класса, по сути, являются такими же оценками магнитуд.

4. Интегрирование каталогов землетрясений

Одной из базовых составляющих сейсмического районирования является использование оптимального, представительного каталога землетрясений исследуемого региона. Однако в силу различных конфигураций мониторинговых сетей и методов обработки записей сейсмические агентства могут пропускать (не регистрировать) землетрясения, которые зафиксированы (локализованы) сетями других агентств. При этом информация о слабых событиях сосредоточена преимущественно в региональных каталогах. Таким образом, наиболее полную информацию обо всех произошедших землетрясениях можно получить только интегрированием (объединением) нескольких существующих для этого региона каталогов в единый. Такое объединение сейсмических данных из различных достоверных источников позволяет увеличить полноту и представительность сейсмических событий в интегрированном каталоге землетрясений.

В процессе объединения каталогов землетрясений необходимо возникает задача идентификации и удаления образующихся дублей (записей, в одном или разных каталогах, возможно относящихся к одному событию). Для целей интегрирования (системного объединения) каталогов землетрясений в [*Vorobieva et al.*, 2022] была создана формализованная методика, использующая авторскую модификацию метода ближайшего соседа [*Zaliapin and Ben-Zion*, 2013; 2016]. Отметим, что особенность созданного в [*Vorobieva et al.*, 2022] математического метода заключается в том, что он дает возможность разделять возникающие дубли и афтершоки с высоким уровнем достоверности. Последнее является сложной задачей распознавания образов, т. к. и те и другие являются событиями, близкими в пространстве и времени.

Эффективность использования созданной методики продемонстрирована в [*Vorobieva et al.*, 2022] на примере объединения каталогов ANSS и JMA афтершоковой последовательности японского землетрясения Тохоку 2011 г. [*Ozawa et al.*, 2011]. Выбор объединяемых в [*Vorobieva et al.*, 2022] подкаталогов сейсмических событий связан с существующими у многих сейсмологических сетей сложностями регистрации ранних афтершоков. Последние содержат важную информацию о физических механизмах, лежащих в основе возникновения землетрясений и постсейсмической деформации вокруг зоны разлома. По итогам интегрирования данных в каталоге ANSS было обнаружено более 700 событий, отсутствующих в каталоге JMA. Большинство из них произошло в начале афтершоковой последовательности землетрясения Тохоку.

В 2021–2023 гг. в [*Gvishiani et al.*, 2022; *Vorobieva et al.*, 2023a,b] А. Д. Гвишиани, П. Н. Шебалиным, И. А. Воробьевой, Б. А. Дзебоевым и их соавторами впервые создан наиболее полный и представительный интегральный каталог землетрясений Арктической зоны Российской Федерации (АЗРФ), включая срединно-океанические хребты Гаккеля и Книповича, а также архипелаг Шпицберген (рис. 6). В интегральном каталоге впервые выполнена унификация магнитудной шкалы. Каталог включает в себя интегрированные данные о землетрясениях из региональных каталогов ФИЦ ЕГС РАН (Якутия, Северо-восток России и Чукотка, Камчатка, Арктика, Восточно-Европейская платформа и Шпицберген), регионального каталога Архангельской сейсмической сети, регионального каталога западного сектора АЗРФ [*Морозов и др.*, 2023] и данных ISC.

Каталог содержит информацию о 45 793 сейсмических событиях за период 1962–2022 гг. Он опубликован в свободном доступе на сайте Мирового центра данных по физике твердой Земли (http://www.wdcb.ru/arctic_antarctic/arctic_seism_4.html, дата обращения: 26.12.2023). Необходимо отметить, что в процессе сборки объединенного каталога территория АЗРФ была разбита на три части (I — Восточный сектор [*Gvishiani et al.*, 2022]; II — Западный сектор [*Vorobieva et al.*, 2023a]; III — хребты Гаккеля и Книповича, архипелаг Шпицберген [*Vorobieva et al.*, 2023b]). На первом этапе объединенные (интегральные) каталоги создавались отдельно для каждой из этих трех частей АЗРФ. Во-первых, это было связано как с пространственным разделением сейсмичности в АЗРФ, так и со сложностью построения во всем регионе корреляционных соотношений между различными магнитудами с целью унификации магнитудной шкалы. Во-вторых, такое разделение АЗРФ было продиктовано, в том числе, разнообразием и сложностью тектонических структур, включающих границу Евразийской и Североамериканской плит.

В 2024 г. И. А. Воробьевой, А. Д. Гвишиани, Б. А. Дзебоевым и Б. В. Дзерановым в [*Vorobieva et al.*, 2024] был создан наиболее полный и представительный интегральный каталог землетрясений Осетинского сектора Большого Кавказа с унифицированной магнитудной шкалой. Каталог представляет собой объединение (интегрирование) данных о землетрясениях из каталогов ФИЦ ЕГС РАН (Кавказ, Северный Кавказ и Грузия), каталога Кавказа, подготавливаемого ранее Институтом геофизики АН Грузинской ССР, и каталога ISC. Интегрированный каталог содержит информацию о 16 285 событиях за период 1962–2022 гг. Авторская унифицированная магнитудная шкала, сведенная к «proxi-Mw», является однородной. Каталог выложен в открытый доступ на сайте Мирового центра данных по физике твердой Земли (http://www.wdcb.ru/sep/seismology/Ossetia/Ossetia.html, дата обращения: 26.12.2023). Отметим, что в результате создания интегрированного каталога существенно пополнено начало афтершоковой последовательности Рачинского землетрясения 29.04.1991 г. с $M = 7{,}0$ [*Арефьев и др.*, 2006], являющегося сильнейшим зарегистрированным на Кавказе.

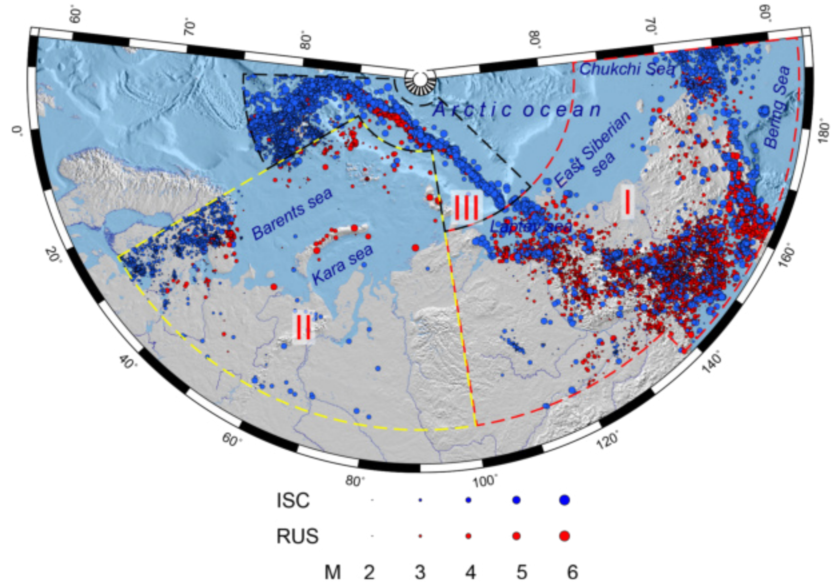

Рис. 6. Объединенный каталог землетрясений Арктической зоны Российской Федерации. I — Восточный сектор; II — Западный сектор; III — хребты Гаккеля и Книповича, архипелаг Шпицберген.

5. Обсуждение

В статье представлен обзор основных мировых и крупных национальных сейсмологических агентств и функционирующих под их управлением сейсмических сетей и центров данных. Также в обзоре рассмотрены базовые характеристики, определяющие критерии качества как записей о сейсмических событиях, так и каталогов землетрясений в целом. Необходимо отметить, что благодаря международному сотрудничеству сейсмологического сообщества в последние десятилетия начал активно развиваться процесс глобализации, выражающийся в том, что одни и те же сейсмические станции входят в состав разных сетей [*Гвишиани и др.*, 2022]. Например, около 30 станций сети GSN одновременно входят в состав сети СВТВО, а 12 являются частью сети ФИЦ ЕГС РАН.

Вопрос стандартизации появления сопровождающей информации о работающих и появляющихся сейсмических сетях до сих пор остается открытым. Несмотря на поступающие начиная с 1912 г. (Б. Голицин) предложения о создании расширенного паспорта сейсмической станции [*Haslinger et al.*, 2022], особенно актуального для возможности анализировать данные приборов регистрации сильных движений, и присвоение уникальных кодов сейсмическим сетям [*Suarez et al.*, 2008], не всегда удается восстановить необходимую информацию, например, о скоростном строении верхних 30 м под станцией, о переносе станции (пусть и не значительном, то есть до 1 км), замене типа оборудования или способа установки и т. п. К сожалению, эти задачи предстоит решать ретроспективно.

Проблема стандартизации касается не только сейсмических сетей, но и итогового результата — каталогов землетрясений. История инструментальных сейсмологических наблюдений насчитывает уже более века. За это время количество сейсмических станций во всем мире выросло до нескольких десятков тысяч. От сейсмологов-пионеров, создававших и развивавших первые мониторинговые сети, сейсмология пришла к сотням международных, национальных и региональных сейсмологических агентств и центров. На фоне такого бурного и стремительного развития все еще остается актуальной и не до конца разрешенной задачей — создание, для конкретного сейсмоактивного региона, наиболее полного представительного каталога землетрясений с однородной магнитудной шкалой. Как уже было отмечено в работах [*Gvishiani et al.*, 2022; *Vorobieva et al.*, 2013;

Vorobieva et al., 2024; 2022; 2023a,b] был сделан существенный шаг вперед в процессе решения этой важной проблемы сейсмологии и оценки сейсмической опасности.

На глобальном уровне задачу решает ISC путем объединения данных о сейсмических событиях от множества мировых сетей и агентств. ISC на периодической основе формирует выверенный бюллетень землетрясений (Reviewed ISC Bulletin). В процессе его формирования автоматический алгоритм решает, какие события в базе данных ISC заслуживают рассмотрения аналитиками ISC. Решение основывается на максимальном значении из всех зарегистрированных магнитуд для данного сейсмического события. Необходимо отметить, что проходят проверку все землетрясения с $M \geqslant 3{,}5$, события с $2{,}5 \leqslant M < 3{,}5$ проверяются выборочно, а с $M < 2{,}5$ — не рассматриваются. Обычно аналитики пересматривают примерно 20% всех событий в базе данных ISC — в настоящее время от 3500 до 5000 в месяц. Работа выполняется с задержкой, примерно, 24 месяца, чтобы обеспечить наиболее полный сбор информации от сетей и центров обработки данных по всему миру. Такой подход гарантирует высокое качество проведенного анализа и полученного результата. В то же время каталог ISC поступает с большим запозданием. Это не позволяет использовать его в исследованиях, требующих результатов в текущем времени, или даже достаточно оперативно. Более того, ISC не работает с волновыми формами, а значит качество каталогов ISC всегда будет ограничено качеством поступающих бюллетеней от различных агентств.

Как следует из [*Gvishiani et al.*, 2022; *Vorobieva et al.*, 2024; 2023a,b], информация о слабых землетрясениях большей частью содержится в региональных каталогах. Например, в каталоге ISC отсутствует целый ряд событий, информация о которых имеется в региональных каталогах ФИЦ ЕГС РАН. Таким образом системный подход, предложенный в [*Vorobieva et al.*, 2022], является эффективным инструментом для создания представительных каталогов землетрясений с унифицированной (авторской) магнитудной шкалой.

Отметим, что формирование наиболее полных объединенных каталогов, содержащих всю известную информацию о слабых землетрясениях, позволит получать локальные оценки коэффициентов закона повторяемости и параметра закона продуктивности землетрясений [*Shebalin et al.*, 2020]. Эти оценки будут определять регионально повторяемость событий разной силы, баланс между количеством больших и малых событий и фрактальную размерность носителя сейсмичности. Все это может позволить уточнить оценки сейсмической опасности и сейсмического риска. Последнее важно для оптимизации возможных экономических потерь и затрат на мероприятия по их предотвращению.

Благодарности. Работа выполнена в рамках государственных заданий Геофизического центра РАН, Института физики Земли им. О. Ю. Шмидта РАН и Института теории прогноза землетрясений и математической геофизики РАН, утвержденных Минобрнауки России.

В работе использовались данные и сервисы, предоставленные ЦКП «Аналитический центр геомагнитных данных» Геофизического центра РАН (http://ckp.gcras.ru).

Список литературы

Абубакиров И. Р., Гусев А. А., Гусева Е. М. *и др.* Массовое определение моментных магнитуд Mw и установление связи между Mw и Ml для умеренных и слабых Камчатских землетрясений // Физика Земли. — 2018. — № 1. — С. 37—51. — DOI: 10.7868/S0002333718010039.

Арефьев С. С., Рогожин Е. А., Быкова В. В. *и др.* Глубинная структура очаговой зоны Рачинского землетрясения по сейсмотомографическим данным // Физика Земли. — 2006. — № 1. — С. 30—44.

Гвишиани А. Д., Добровольский М. Н., Дзеранов Б. В. *и др.* Большие данные в геофизике и других науках о Земле // Физика Земли. — 2022. — № 1. — С. 3—34. — DOI: 10.31857/S0002333722010033.

Гвишиани А. Д., Панченко В. Я., Никитина И. М. Системный анализ Больших Данных для наук о Земле // Вестник Российской академии наук. — 2023. — Т. 93, № 6. — С. 518—525. — DOI: 10.31857/S0869587323060087.

Голицын Б. Б. Лекции по сейсмометрии. — СПб : Типография Императорской Академии Наук, 1912. — 654 с.

Кондорская Н. В., Федорова И. В. Сейсмические станции Единой системы сейсмических наблюдений СССР (ЕССН): На 01.01.90. — Москва : ОИФЗ РАН, 1996. — 36 с.

Морозов А. Н., Ваганова Н. В., Асминг В. Э. *и др.* Сейсмичность западного сектора Российской Арктики // Физика Земли. — 2023. — № 2. — С. 115—148. — DOI: 10.31857/S0002333723020096.

Новый каталог сильных землетрясений на территории СССР с древнейших времен до 1975 г. / под ред. Н. В. Кондорская, Н. В. Шебалин. — Наука, 1977. — 536 с.

ФИЦ ЕГС РАН. Землетрясения России в 2021 году. — 2023a.

ФИЦ ЕГС РАН. Землетрясения Северной Евразии. — 2023b.

Agnew D. C. History of seismology // International Handbook of Earthquake and Engineering Seismology. — Elsevier, 2002. — P. 3–11. — DOI: 10.1016/S0074-6142(02)80203-0.

Aki K., Richards P. G. Quantitative Seismology. — 2nd ed. — Sausalito, CA : University Science Books, 2002. — 723 p.

Aoi S., Asano Y., Kunugi T., *et al.* MOWLAS: NIED observation network for earthquake, tsunami and volcano // Earth, Planets and Space. — 2020. — Vol. 72, no. 1. — DOI: 10.1186/s40623-020-01250-x.

Benz H. Building a National Seismic Monitoring Center: NEIC from 2000 to the Present // Seismological Research Letters. — 2017. — Vol. 88, 2B. — P. 457–461. — DOI: 10.1785/0220170034.

Beyreuther M., Barsch R., Krischer L., *et al.* ObsPy: A Python Toolbox for Seismology // Seismological Research Letters. — 2010. — Vol. 81, no. 3. — P. 530–533. — DOI: 10.1785/gssrl.81.3.530.

Cauzzi C., Bieńkowski J., Custódio S., *et al.* ORFEUS Services and Activities to Promote Observational Seismology in Europe and beyond // EGU General Assembly. — 2021. — DOI: 10.5194/egusphere-egu21-6119.

Coyne J., Bobrov D., Bormann P., *et al.* CTBTO: Goals, Networks, Data Analysis and Data Availability // New Manual of Seismological Observatory Practice 2 (NMSOP2). — Deutsches GeoForschungsZentrum GFZ, 2012. — DOI: 10.2312/GFZ.NMSOP-2_ch17.

Dai G., An Y. China Earthquake Administration: Chinese Seismic Network // Summary of the Bulletin of the International Seismological Centre. — 2020. — Vol. 54, no. 2. — P. 28–40. — DOI: 10.31905/XWIVRBRI.

Dewey J., Byerly P. The Early History of Seismometry (to 1900) // Bulletin of the Seismological Society of America. — 1969. — Vol. 59, no. 1. — P. 183–287.

Di Giacomo D., Harris J., Storchak D. A. Complementing regional moment magnitudes to GCMT: a perspective from the rebuilt International Seismological Centre Bulletin // Earth System Science Data. — 2021. — Vol. 13, no. 5. — P. 1957–1985. — DOI: 10.5194/essd-13-1957-2021.

Engdahl E. R., Di Giacomo D., Sakarya B., *et al.* ISC-EHB 1964–2016, an Improved Data Set for Studies of Earth Structure and Global Seismicity // Earth and Space Science. — 2020. — Vol. 7, no. 1. — DOI: 10.1029/2019EA000897.

Engdahl E. R., Villaseñor A. Global seismicity: 1900–1999 // International Handbook of Earthquake Engineering and Seismology. — Elsevier, 2002. — P. 665–690. — DOI: 10.1016/S0074-6142(02)80244-3.

Gutenberg B. Travel time curves at small distances, and wave velocities in southern California // Gerlands Beitrage zur Geophysik. — 1932. — Vol. 35. — P. 6–45.

Gutenberg B. Magnitude determination for deep-focus earthquakes // Bulletin of the Seismological Society of America. — 1945. — Vol. 35, no. 3. — P. 117–130. — DOI: 10.1785/BSSA0350030117.

Gvishiani A. D., Vorobieva I. A., Shebalin P. N., *et al.* Integrated Earthquake Catalog of the Eastern Sector of the Russian Arctic // Applied Sciences. — 2022. — Vol. 12, no. 10. — P. 5010. — DOI: 10.3390/app12105010.

Haslinger F., Basili R., Bossu R., *et al.* Coordinated and Interoperable Seismological Data and Product Services in Europe: the EPOS Thematic Core Service for Seismology // Annals of Geophysics. — 2022. — Vol. 65, no. 2. — P. DM213. — DOI: 10.4401/AG-8767.

Havskov J., Alguacil G. Seismic networks // Modern Approaches in Geophysics. — Springer Netherlands, 2004. — P. 211–257. — DOI: 10.1007/978-1-4020-2969-1_8.

International Seismological Centre. Searching the ISC-EHB Bulletin. — DOI: 10.31905/PY08W6S3. — URL: https://www.isc.ac.uk/isc-ehb/search/.

Kanamori H. The energy release in great earthquakes // Journal of Geophysical Research. — 1977. — Vol. 82, no. 20. — P. 2981–2987. — DOI: 10.1029/JB082i020p02981.

Kennett B. L. N., Engdahl E. R. Traveltimes for global earthquake location and phase identification // Geophysical Journal International. — 1991. — Vol. 105, no. 2. — P. 429–465. — DOI: 10.1111/j.1365-246X.1991.tb06724.x.

Kennett B. L. N., Engdahl E. R., Buland R. Constraints on seismic velocities in the Earth from traveltimes // Geophysical Journal International. — 1995. — Vol. 122, no. 1. — P. 108–124. — DOI: 10.1111/j.1365-246X.1995.tb03540.x.

Kisslinger C., Howell B. F. Seismology and physics of the Earth's interior in the US (1900–1960) // International Handbook of Earthquake and Engineering Seismology. Part B. — San Diego : Academic Press, 2003.

Kotha S. R., Weatherill G., Bindi D., *et al.* Spatial Variability of Source and Attenuation Characteristics in Large Ground-Motion Datasets // EGU General Assembly. — 2020. — DOI: 10.5194/egusphere-egu2020-5187.

Mignan A., Werner M. J., Wiemer S., *et al.* Bayesian Estimation of the Spatially Varying Completeness Magnitude of Earthquake Catalogs // Bulletin of the Seismological Society of America. — 2011. — Vol. 101, no. 3. — P. 1371–1385. — DOI: 10.1785/0120100223.

Mignan A., Woessner J. Estimating the magnitude of completeness for earthquake catalogs. — Community Online Resource for Statistical Seismicity Analysis, 2012. — DOI: 10.5078/corssa-00180805.

Minina E. V. Formation and development of seismological research in Russia // IOP Conference Series: Earth and Environmental Science. — 2019. — Vol. 350, no. 1. — P. 012009. — DOI: 10.1088/1755-1315/350/1/012009.

Oliver J., Murphy L. WWNSS: seismology's global network of observing stations // Science. — 1971. — Vol. 174. — P. 254–261.

Ozawa S., Nishimura T., Suito H., *et al.* Coseismic and postseismic slip of the 2011 magnitude-9 Tohoku-Oki earthquake // Nature. — 2011. — Vol. 475, no. 7356. — P. 373–376. — DOI: 10.1038/nature10227.

Rautian T. G., Khalturin V. I., Fujita K., *et al.* Origins and Methodology of the Russian Energy K-Class System and Its Relationship to Magnitude Scales // Seismological Research Letters. — 2007. — Vol. 78, no. 6. — P. 579–590. — DOI: 10.1785/gssrl.78.6.579.

Richter C. F. An instrumental earthquake magnitude scale // Bulletin of the Seismological Society of America. — 1935. — Vol. 25, no. 1. — P. 1–32. — DOI: 10.1785/BSSA0250010001.

Ringler A. T., Steim J., Wilson D. C., *et al.* Improvements in seismic resolution and current limitations in the Global Seismographic Network // Geophysical Journal International. — 2019. — Vol. 220, no. 1. — P. 508–521. — DOI: 10.1093/gji/ggz473.

Roult G., Montagner J.-P., Romanowicz B., *et al.* The GEOSCOPE Program: Progress and Challenges during the Past 30 Years // Seismological Research Letters. — 2013. — Vol. 84, no. 2. — P. 250–250. — DOI: 10.1785/0220120193.

Shebalin P. N., Narteau C., Baranov S. V. Earthquake productivity law // Geophysical Journal International. — 2020. — Vol. 222, no. 2. — P. 1264–1269. — DOI: 10.1093/gji/ggaa252.

Storchak D. A., Di Giacomo D., Engdahl E. R., *et al.* The ISC-GEM Global Instrumental Earthquake Catalogue (1900–2009): Introduction // Physics of the Earth and Planetary Interiors. — 2015. — Vol. 239. — P. 48–63. — DOI: 10.1016/j.pepi.2014.06.009.

Suarez G., Eck T. van, Giardini D., *et al.* The International Federation of Digital Seismograph Networks (FDSN): An Integrated System of Seismological Observatories // IEEE Systems Journal. — 2008. — Vol. 2, no. 3. — P. 431–438. — DOI: 10.1109/jsyst.2008.2003294.

U.S. Geological Survey. Advanced National Seismic System—Current status, development opportunities, and priorities for 2017-2027. — 2017. — 32 p. — DOI: 10.3133/cir1429.

Vallée M., Charléty J., Ferreira A. M. G., *et al.* SCARDEC: a new technique for the rapid determination of seismic moment magnitude, focal mechanism and source time functions for large earthquakes using body-wave deconvolution: Wave deconvolution and earthquake parameters // Geophysical Journal International. — 2010. — Vol. 184, no. 1. — P. 338–358. — DOI: 10.1111/j.1365-246X.2010.04836.x.

Vorobieva I., Narteau C., Shebalin P., *et al.* Multiscale Mapping of Completeness Magnitude of Earthquake Catalogs // Bulletin of the Seismological Society of America. — 2013. — Vol. 103, no. 4. — P. 2188–2202. — DOI: 10.1785/0120120132.

Vorobieva I. A., Dzeboev B. A., Dzeranov B. V., *et al.* Integrated Earthquake Catalog of the Ossetian Sector of the Greater Caucasus // Applied Sciences. — 2024. — Vol. 14, no. 1. — P. 172. — DOI: 10.3390/app14010172.

Vorobieva I. A., Gvishiani A. D., Dzeboev B. A., *et al.* Nearest Neighbor Method for Discriminating Aftershocks and Duplicates When Merging Earthquake Catalogs // Frontiers in Earth Science. — 2022. — Vol. 10. — DOI: 10.3389/feart.2022.820277.

Vorobieva I. A., Gvishiani A. D., Shebalin P. N., *et al.* Integrated Earthquake Catalog II: The Western Sector of the Russian Arctic // Applied Sciences. — 2023a. — Vol. 13, no. 12. — P. 7084. — DOI: 10.3390/app13127084.

Vorobieva I. A., Gvishiani A. D., Shebalin P. N., *et al.* Integrated Earthquake Catalog III: Gakkel Ridge, Knipovich Ridge, and Svalbard Archipelago // Applied Sciences. — 2023b. — Vol. 13, no. 22. — P. 12422. — DOI: 10.3390/app132212422.

Wadati K. Shallow and deep earthquakes // Geophysical Magazine. — 1928. — Vol. 1. — P. 162–202.

Wadati K. Shallow and deep earthquakes, 3rd paper // Geophysical Magazine. — 1931. — Vol. 4. — P. 231–283.

Wang Z. Seismic Hazard Assessment: Issues and Alternatives // Pure and Applied Geophysics. — 2010. — Vol. 168, no. 1/2. — P. 11–25. — DOI: 10.1007/s00024-010-0148-3.

Weston J., Engdahl E. R., Harris J., *et al.* ISC-EHB: reconstruction of a robust earthquake data set // Geophysical Journal International. — 2018. — Vol. 214, no. 1. — P. 474–484. — DOI: 10.1093/gji/ggy155.

Wiemer S. Minimum Magnitude of Completeness in Earthquake Catalogs: Examples from Alaska, the Western United States, and Japan // Bulletin of the Seismological Society of America. — 2000. — Vol. 90, no. 4. — P. 859–869. — DOI: 10.1785/0119990114.

Woodhouse J. H., Deuss A. Theory and Observations - Earth's Free Oscillations // Treatise on Geophysics. — Elsevier, 2015. — P. 79–115. — DOI: 10.1016/B978-0-444-53802-4.00002-6.

Zaliapin I., Ben-Zion Y. Earthquake clusters in southern California I: Identification and stability // Journal of Geophysical Research: Solid Earth. — 2013. — Vol. 118, no. 6. — P. 2847–2864. — DOI: 10.1002/jgrb.50179.

Zaliapin I., Ben-Zion Y. A global classification and characterization of earthquake clusters // Geophysical Journal International. — 2016. — Vol. 207, no. 1. — P. 608–634. — DOI: 10.1093/gji/ggw300.

Russian Journal of Earth Sciences

World Seismic Networks and Earthquake Catalogs

A. D. Gvishiani[1,2], B. V. Dzeranov[1,3,*], A. A. Skorkina[4], B. A. Dzeboev[1,3]

[1]Geophysical Center of the Russian Academy of Sciences, Moscow, Russia
[2]Schmidt Institute of the Physics of the Earth Russian Academy of Sciencies, Moscow, Russia
[3]Geophysical Institute, Vladikavkaz Scientific Center RAS, Vladikavkaz, Russia
[4]Institute of Earthquake Prediction Theory and Mathematical Geophysics of the Russian Academy of Sciences, Moscow, Russia

****Correspondence to:** Boris Dzeranov, b.dzeranov@gcras.ru

This paper is devoted to the review of currently functioning seismological agencies, seismic monitoring networks created, developed and supported by them, as well as earthquake catalogs produced. Particular attention is focused on international and national seismological centers and seismic networks. A historical insight about the first observations made by seismic networks completes the picture. The basic parameters of the main seismic networks and the principles of functioning for seismological centers are considered. The key characteristics of seismic catalogs that determine the criteria for their quality are discussed. The system-analytical approach to solving the urgent problem of creating the most complete and representative earthquake catalogs with a unified magnitude scale by integrating data from international, national and regional catalogs in the studied region is presented.

Received: 15 October 2023
Accepted: 15 January 2024
Published: 29 February 2024

Keywords: seismic networks; seismological agencies; earthquake catalogs; representative magnitude; magnitude scale; catalog completenes, merging earthquake catalogs.

Citation: Gvishiani A. D., Dzeranov B. V., Skorkina A. A., Dzeboev B. A. (2024), World Seismic Networks and Earthquake Catalogs, *Russian Journal of Earth Sciences*, 24, ES1012, https://doi.org/10.2205/2024es000901

References

Abubakirov I. R., Gusev A. A., Guseva E. M., *et al.* Mass determination of moment magnitudes Mw and establishing the relationship between Mw and ML for moderate and small Kamchatka earthquakes // Izvestiya, Physics of the Solid Earth. — 2018. — Vol. 54, no. 1. — P. 33–47. — DOI: 10.1134/s1069351318010019.

Agnew D. C. History of seismology // International Handbook of Earthquake and Engineering Seismology. — Elsevier, 2002. — P. 3–11. — DOI: 10.1016/S0074-6142(02)80203-0.

Aki K., Richards P. G. Quantitative Seismology. — 2nd ed. — Sausalito, CA : University Science Books, 2002. — 723 p.

Aoi S., Asano Y., Kunugi T., *et al.* MOWLAS: NIED observation network for earthquake, tsunami and volcano // Earth, Planets and Space. — 2020. — Vol. 72, no. 1. — DOI: 10.1186/s40623-020-01250-x.

Arefiev S. S., Rogozhin E. A., Bykova V. V., *et al.* Deep structure of the Racha earthquake source zone from seismic tomography data // Izvestiya, Physics of the Solid Earth. — 2006. — Vol. 42, no. 1. — P. 27–40. — DOI: 10.1134/s1069351306010034.

Benz H. Building a National Seismic Monitoring Center: NEIC from 2000 to the Present // Seismological Research Letters. — 2017. — Vol. 88, 2B. — P. 457–461. — DOI: 10.1785/0220170034.

Beyreuther M., Barsch R., Krischer L., *et al.* ObsPy: A Python Toolbox for Seismology // Seismological Research Letters. — 2010. — Vol. 81, no. 3. — P. 530–533. — DOI: 10.1785/gssrl.81.3.530.

Cauzzi C., Bieńkowski J., Custódio S., *et al.* ORFEUS Services and Activities to Promote Observational Seismology in Europe and beyond // EGU General Assembly. — 2021. — DOI: 10.5194/egusphere-egu21-6119.

Coyne J., Bobrov D., Bormann P., *et al.* CTBTO: Goals, Networks, Data Analysis and Data Availability // New Manual of Seismological Observatory Practice 2 (NMSOP2). — Deutsches GeoForschungsZentrum GFZ, 2012. — DOI: 10.2312/GFZ.NMSOP-2_ch17.

Dai G., An Y. China Earthquake Administration: Chinese Seismic Network // Summary of the Bulletin of the International Seismological Centre. — 2020. — Vol. 54, no. 2. — P. 28–40. — DOI: 10.31905/XWIVRBRI.

Dewey J., Byerly P. The Early History of Seismometry (to 1900) // Bulletin of the Seismological Society of America. — 1969. — Vol. 59, no. 1. — P. 183–287.

Di Giacomo D., Harris J., Storchak D. A. Complementing regional moment magnitudes to GCMT: a perspective from the rebuilt International Seismological Centre Bulletin // Earth System Science Data. — 2021. — Vol. 13, no. 5. — P. 1957–1985. — DOI: 10.5194/essd-13-1957-2021.

Engdahl E. R., Di Giacomo D., Sakarya B., *et al.* ISC-EHB 1964–2016, an Improved Data Set for Studies of Earth Structure and Global Seismicity // Earth and Space Science. — 2020. — Vol. 7, no. 1. — DOI: 10.1029/2019EA000897.

Engdahl E. R., Villaseñor A. Global seismicity: 1900–1999 // International Handbook of Earthquake Engineering and Seismology. — Elsevier, 2002. — P. 665–690. — DOI: 10.1016/S0074-6142(02)80244-3.

Golitsyn B. Lectures on seismometry. — St. Petersburg : Imperial Academy of Sciences, 1912. — 654 p.

GS RAS. Earthquakes in Northern Eurasia. — 2023a.

GS RAS. Earthquakes in Russia in 2021. — 2023b.

Gutenberg B. Travel time curves at small distances, and wave velocities in southern California // Gerlands Beitrage zur Geophysik. — 1932. — Vol. 35. — P. 6–45.

Gutenberg B. Magnitude determination for deep-focus earthquakes // Bulletin of the Seismological Society of America. — 1945. — Vol. 35, no. 3. — P. 117–130. — DOI: 10.1785/BSSA0350030117.

Gvishiani A. D., Dobrovolsky M. N., Dzeranov B. V., *et al.* Big Data in Geophysics and Other Earth Sciences // Izvestiya, Physics of the Solid Earth. — 2022a. — Vol. 58, no. 1. — P. 1–29. — DOI: 10.1134/s1069351322010037.

Gvishiani A. D., Panchenko V. Y., Nikitina I. M. Big Data System Analysis for Geosciences // Herald of the Russian Academy of Sciences. — 2023. — Vol. 93, no. 6. — P. 518–525. — DOI: 10.31857/S0869587323060087.

Gvishiani A. D., Vorobieva I. A., Shebalin P. N., *et al.* Integrated Earthquake Catalog of the Eastern Sector of the Russian Arctic // Applied Sciences. — 2022b. — Vol. 12, no. 10. — P. 5010. — DOI: 10.3390/app12105010.

Haslinger F., Basili R., Bossu R., *et al.* Coordinated and Interoperable Seismological Data and Product Services in Europe: the EPOS Thematic Core Service for Seismology // Annals of Geophysics. — 2022. — Vol. 65, no. 2. — P. DM213. — DOI: 10.4401/AG-8767.

Havskov J., Alguacil G. Seismic networks // Modern Approaches in Geophysics. — Springer Netherlands, 2004. — P. 211–257. — DOI: 10.1007/978-1-4020-2969-1_8.

International Seismological Centre. Searching the ISC-EHB Bulletin. — DOI: 10.31905/PY08W6S3. — URL: https://www.isc.ac.uk/isc-ehb/search/. https://www.isc.ac.uk/isc-ehb/search/.

Kanamori H. The energy release in great earthquakes // Journal of Geophysical Research. — 1977. — Vol. 82, no. 20. — P. 2981–2987. — DOI: 10.1029/JB082i020p02981.

Kennett B. L. N., Engdahl E. R. Traveltimes for global earthquake location and phase identification // Geophysical Journal International. — 1991. — Vol. 105, no. 2. — P. 429–465. — DOI: 10.1111/j.1365-246X.1991.tb06724.x.

Kennett B. L. N., Engdahl E. R., Buland R. Constraints on seismic velocities in the Earth from traveltimes // Geophysical Journal International. — 1995. — Vol. 122, no. 1. — P. 108–124. — DOI: 10.1111/j.1365-246X.1995.tb03540.x.

Kisslinger C., Howell B. F. Seismology and physics of the Earth's interior in the US (1900–1960) // International Handbook of Earthquake and Engineering Seismology. Part B. — San Diego : Academic Press, 2003.

Kondorskaya N. V., Fedorova I. V. Seismic stations of the Unified Survey of Seismic Observation of the USSR (USSO) as of 01.01.1990. — Moscow : IPE RAS, 1996. — 36 p.

Kotha S. R., Weatherill G., Bindi D., *et al.* Spatial Variability of Source and Attenuation Characteristics in Large Ground-Motion Datasets // EGU General Assembly. — 2020. — DOI: 10.5194/egusphere-egu2020-5187.

Mignan A., Werner M. J., Wiemer S., *et al.* Bayesian Estimation of the Spatially Varying Completeness Magnitude of Earthquake Catalogs // Bulletin of the Seismological Society of America. — 2011. — Vol. 101, no. 3. — P. 1371–1385. — DOI: 10.1785/0120100223.

Mignan A., Woessner J. Estimating the magnitude of completeness for earthquake catalogs. — Community Online Resource for Statistical Seismicity Analysis, 2012. — DOI: 10.5078/corssa-00180805.

Minina E. V. Formation and development of seismological research in Russia // IOP Conference Series: Earth and Environmental Science. — 2019. — Vol. 350, no. 1. — P. 012009. — DOI: 10.1088/1755-1315/350/1/012009.

Morozov A. N., Vaganova N. V., Asming V. E., *et al.* Seismicity of the Western Sector of the Russian Arctic // Izvestiya, Physics of the Solid Earth. — 2023. — Vol. 59, no. 2. — P. 209–241. — DOI: 10.1134/s106935132302009x.

New Catalog of Strong Earthquakes in the USSR from Ancient Times through 1977 / ed. by N. V. Kondorskaya, N. V. Shebalin. — Translated, Published by World Data Center A for Solid Earth Geophysics, 1982. — 608 p.

Oliver J., Murphy L. WWNSS: seismology's global network of observing stations // Science. — 1971. — Vol. 174. — P. 254–261.

Ozawa S., Nishimura T., Suito H., *et al.* Coseismic and postseismic slip of the 2011 magnitude-9 Tohoku-Oki earthquake // Nature. — 2011. — Vol. 475, no. 7356. — P. 373–376. — DOI: 10.1038/nature10227.

Rautian T. G., Khalturin V. I., Fujita K., *et al.* Origins and Methodology of the Russian Energy K-Class System and Its Relationship to Magnitude Scales // Seismological Research Letters. — 2007. — Vol. 78, no. 6. — P. 579–590. — DOI: 10.1785/gssrl.78.6.579.

Richter C. F. An instrumental earthquake magnitude scale // Bulletin of the Seismological Society of America. — 1935. — Vol. 25, no. 1. — P. 1–32. — DOI: 10.1785/BSSA0250010001.

Ringler A. T., Steim J., Wilson D. C., *et al.* Improvements in seismic resolution and current limitations in the Global Seismographic Network // Geophysical Journal International. — 2019. — Vol. 220, no. 1. — P. 508–521. — DOI: 10.1093/gji/ggz473.

Roult G., Montagner J.-P., Romanowicz B., *et al.* The GEOSCOPE Program: Progress and Challenges during the Past 30 Years // Seismological Research Letters. — 2013. — Vol. 84, no. 2. — P. 250–250. — DOI: 10.1785/0220120193.

Shebalin P. N., Narteau C., Baranov S. V. Earthquake productivity law // Geophysical Journal International. — 2020. — Vol. 222, no. 2. — P. 1264–1269. — DOI: 10.1093/gji/ggaa252.

Storchak D. A., Di Giacomo D., Engdahl E. R., *et al.* The ISC-GEM Global Instrumental Earthquake Catalogue (1900–2009): Introduction // Physics of the Earth and Planetary Interiors. — 2015. — Vol. 239. — P. 48–63. — DOI: 10.1016/j.pepi.2014.06.009.

Suarez G., Eck T. van, Giardini D., *et al.* The International Federation of Digital Seismograph Networks (FDSN): An Integrated System of Seismological Observatories // IEEE Systems Journal. — 2008. — Vol. 2, no. 3. — P. 431–438. — DOI: 10.1109/jsyst.2008.2003294.

U.S. Geological Survey. Advanced National Seismic System—Current status, development opportunities, and priorities for 2017-2027. — 2017. — 32 p. — DOI: 10.3133/cir1429.

Vallée M., Charléty J., Ferreira A. M. G., *et al.* SCARDEC: a new technique for the rapid determination of seismic moment magnitude, focal mechanism and source time functions for large earthquakes using body-wave deconvolution: Wave deconvolution and earthquake parameters // Geophysical Journal International. — 2010. — Vol. 184, no. 1. — P. 338–358. — DOI: 10.1111/j.1365-246X.2010.04836.x.

Vorobieva I., Narteau C., Shebalin P., *et al.* Multiscale Mapping of Completeness Magnitude of Earthquake Catalogs // Bulletin of the Seismological Society of America. — 2013. — Vol. 103, no. 4. — P. 2188–2202. — DOI: 10.1785/0120120132.

Vorobieva I. A., Dzeboev B. A., Dzeranov B. V., *et al.* Integrated Earthquake Catalog of the Ossetian Sector of the Greater Caucasus // Applied Sciences. — 2024. — Vol. 14, no. 1. — P. 172. — DOI: 10.3390/app14010172.

Vorobieva I. A., Gvishiani A. D., Dzeboev B. A., *et al.* Nearest Neighbor Method for Discriminating Aftershocks and Duplicates When Merging Earthquake Catalogs // Frontiers in Earth Science. — 2022. — Vol. 10. — DOI: 10.3389/feart.2022.820277.

Vorobieva I. A., Gvishiani A. D., Shebalin P. N., *et al.* Integrated Earthquake Catalog II: The Western Sector of the Russian Arctic // Applied Sciences. — 2023a. — Vol. 13, no. 12. — P. 7084. — DOI: 10.3390/app13127084.

Vorobieva I. A., Gvishiani A. D., Shebalin P. N., *et al.* Integrated Earthquake Catalog III: Gakkel Ridge, Knipovich Ridge, and Svalbard Archipelago // Applied Sciences. — 2023b. — Vol. 13, no. 22. — P. 12422. — DOI: 10.3390/app132212422.

Wadati K. Shallow and deep earthquakes // Geophysical Magazine. — 1928. — Vol. 1. — P. 162–202.

Wadati K. Shallow and deep earthquakes, 3rd paper // Geophysical Magazine. — 1931. — Vol. 4. — P. 231–283.

Wang Z. Seismic Hazard Assessment: Issues and Alternatives // Pure and Applied Geophysics. — 2010. — Vol. 168, no. 1/2. — P. 11–25. — DOI: 10.1007/s00024-010-0148-3.

Weston J., Engdahl E. R., Harris J., *et al.* ISC-EHB: reconstruction of a robust earthquake data set // Geophysical Journal International. — 2018. — Vol. 214, no. 1. — P. 474–484. — DOI: 10.1093/gji/ggy155.

Wiemer S. Minimum Magnitude of Completeness in Earthquake Catalogs: Examples from Alaska, the Western United States, and Japan // Bulletin of the Seismological Society of America. — 2000. — Vol. 90, no. 4. — P. 859–869. — DOI: 10.1785/0119990114.

Woodhouse J. H., Deuss A. Theory and Observations - Earth's Free Oscillations // Treatise on Geophysics. — Elsevier, 2015. — P. 79–115. — DOI: 10.1016/B978-0-444-53802-4.00002-6.

Zaliapin I., Ben-Zion Y. Earthquake clusters in southern California I: Identification and stability // Journal of Geophysical Research: Solid Earth. — 2013. — Vol. 118, no. 6. — P. 2847–2864. — DOI: 10.1002/jgrb.50179.

Zaliapin I., Ben-Zion Y. A global classification and characterization of earthquake clusters // Geophysical Journal International. — 2016. — Vol. 207, no. 1. — P. 608–634. — DOI: 10.1093/gji/ggw300.